technische universität
dortmund

Dissertation

From Oxygen to Extended Organic Molecules: The Role of Electron Correlation in Molecule-Surface Interactions on 3*d*-Ferromagnetic Metals

submitted in partial fulfillment of the
requirements for the degree of

Dr. rer. nat.

to the Faculty of Physics at
TU Dortmund University, Germany

by

David Janas

Dortmund, June 2025

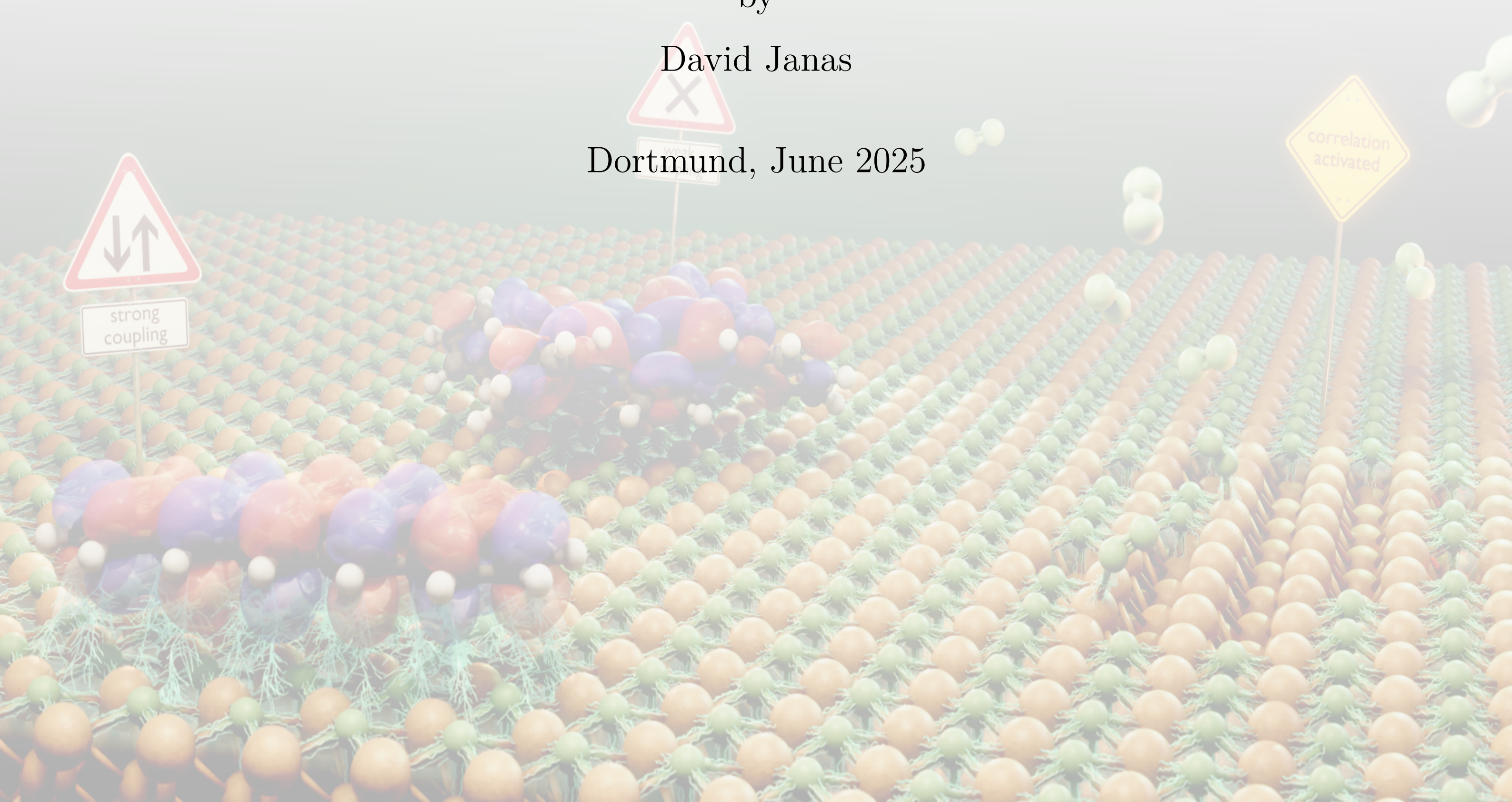

Accepted by the Faculty of Physics at TU Dortmund University, Germany.

Day of the oral examination: 22 October 2025

Examination board:

Prof. Dr. Mirko Cinchetti

Prof. Dr. Carsten Westphal

Prof. Dr. Benjamin Stadtmüller

Prof. Dr. Kevin Kröninger

Dr. Bärbel Siegmann

From Oxygen to Extended Organic Molecules: The Role of Electron Correlation in Molecule-Surface Interactions on $3d$-Ferromagnetic Metals

Kurzfassung

Im Rahmen dieser Dissertation wird untersucht, wie elektronische Korrelationen die Wechselwirkung zwischen atomaren bzw. molekularen Adsorbaten und ferromagnetischen Übergangsmetalloberflächen beeinflussen, wobei Fe(100) als Modelloberfläche dient. Ferromagnetische $3d$-Metalle wie Eisen spielen eine zentrale Rolle sowohl in der Oberflächenphysik als auch in angewandten Bereichen wie der Spintronik, der Katalyse und organisch-anorganischen Hybridsystemen. Bestehende Modelle wie das Newns–Anderson-Modell und das d-Band-Modell liefern zwar nützliche Konzepte zum Verständnis von Molekül–Oberflächen-Wechselwirkungen, vernachlässigen jedoch in der Regel elektronische Korrelationen — ein zentrales Merkmal ferromagnetischer $3d$-Metalle — und gehen oft von einer räumlich homogenen Kopplung aus, die bei großen organischen Molekülen nicht mehr gültig ist.

Um diese Einschränkungen zu überwinden, wird eine Kombination aus spin- und impulsaufgelöster Photoemissionsspektroskopie, Rastersondenmikroskopie sowie fortgeschrittener elektronischer Strukturtheorie eingesetzt, um Molekül–Metall-Grenzflächen systematisch zu untersuchen. Dabei kommen sowohl die Dichtefunktionaltheorie mit effektiven Hubbard-Korrekturen (DFT+U) als auch die Dynamische Molekularfeldtheorie (DMFT) zur Anwendung, um elektronische Korrelationseffekte angemessen zu beschreiben. Ausgehend von der Chemisorption atomaren Sauerstoffs zeigt die Arbeit, dass Adsorbate die elektronische Korrelation in der Fe-Oberflächenschicht verstärken können. Dies führt zu einer energetischen Verengung der d-Bänder, einer Reduktion der Austauschaufspaltung und zum Auftreten spinabhängiger Lebensdauereffekte in den sauerstoffbezogenen Zuständen. Diese Modifikationen — typische Kennzeichen von Vielteilchenwechselwirkungen — beeinflussen wiederum maßgeblich die nachfolgende Moleküladsorption.

Darauf aufbauend wird die Adsorption von Pentacen auf einer sauerstoffpassivierten Fe-Oberfläche (Fe–O) untersucht. Hier führt die zuvor erwähnte, korrelationsinduzierte Modifikation der Substrat-d-Bandstruktur zu einem Übergang von schwacher zu starker Molekül–Metall-Kopplung. Ein recheneffizienter Ansatz wird entwickelt, um die durch DMFT offenbarte Renormalisierung der d-Bänder mithilfe der DFT+U-Methodik mit einem gezielt gewählten U_{eff}-Wert nachzubilden. Auf dieser Grundlage wird ein erweitertes d-Band-Modell eingeführt, das die besondere Rolle der Fe-d_{z^2}-Orbitale bei der Kopplung an die erweiterten π-Systeme organischer Moleküle hervorhebt.

Abschließend wird die Adsorption metallierter Tetraphenylporphyrine (ZnTPP und NiTPP) auf Fe–O untersucht. Diese Moleküle bleiben elektronisch entkoppelt, zeigen jedoch messbare konformationelle Verformungen. Mittels Photoemissions-Orbitaltomographie (POT) wird aufgezeigt, wie sich Molekülgeometrie und Orbitalanordnung über Mono- und Mehrlagenfilme hinweg entwickeln. POT etabliert sich dabei als leistungsfähige impulsaufgelöste Methode zur Untersuchung sowohl der elektronischen Struktur als auch der molekularen Konformation.

Insgesamt entwickelt diese Arbeit ein korrelationsbewusstes Verständnis hybrider Grenzflächen auf ferromagnetischen Substraten. Sie zeigt, dass elektronische Korrelation und Orbitalhybridisierung miteinander verknüpfte Phänomene sind, die gemeinsam die elektronischen und geometrischen Eigenschaften von Molekül–Metall-Systemen bestimmen. Die Ergebnisse liefern wichtige Impulse für zukünftige Entwicklungen in der Katalyse, der molekularen Elektronik und in spinbasierten Technologien.

Abstract

This thesis investigates how electron correlation shapes the interaction between atomic and molecular adsorbates and ferromagnetic transition metal surfaces, using Fe(100) as a model substrate. Ferromagnetic $3d$ metals such as iron are central to surface science and applied fields like spintronics, catalysis, and organic–inorganic hybrid systems. While existing models such as the Newns–Anderson framework and the d-band model provide useful concepts to understand molecule–surface interactions, they typically neglect electron correlation — a key feature of $3d$ ferromagnets — and often assume spatially uniform coupling, which breaks down for large organic adsorbates.

To address these limitations, a combination of spin- and momentum-resolved photoemission spectroscopy, scanning probe microscopy, and advanced electronic structure calculations is used to systematically probe molecule–metal interfaces. This includes both density functional theory with effective Hubbard corrections (DFT+U) and dynamical mean-field theory (DMFT), which allow for a more accurate description of electron correlation effects. Starting from the chemisorption of atomic oxygen, the work demonstrates that adsorbates can enhance electron correlation in the Fe surface layer, leading to an energetic narrowing of the Fe d-bands, reduced exchange splitting, and the appearance of spin-dependent lifetime effects in oxygen-related states. These modifications — signatures of many-body interactions — in turn affect how subsequent molecular adsorption proceeds.

Building on this, the thesis examines pentacene adsorption on an oxygen-passivated Fe surface (Fe–O). Here, the aforementioned correlation-induced changes in the substrate d-band structure drive a transition from weak to strong molecule–metal coupling. A computationally efficient approach is developed to emulate the d-band renormalization revealed by DMFT using the DFT+U formalism with a tailored value of U_{eff}. Expanding on these findings, an extended d-band model is introduced that emphasizes the pivotal role of Fe d_{z^2} orbitals in coupling to the extended π-systems of organic molecules.

Finally, the adsorption of metalated tetraphenylporphyrins (ZnTPP and NiTPP) on Fe–O is explored. These molecules remain decoupled electronically, but exhibit measurable conformational distortions. Using photoemission orbital tomography (POT), the thesis reveals how molecular geometry and orbital alignment evolve across mono- and multilayer films. POT is thereby established as a powerful momentum-resolved probe of both electronic structure and molecular conformation.

Altogether, this work advances a correlation-aware framework for understanding hybrid interfaces on ferromagnetic substrates. It shows that electron correlation and orbital hybridization are interconnected phenomena that jointly determine the electronic and geometric properties of molecule–metal systems. These findings carry important implications for future developments in catalysis, molecular electronics, and spin-based technologies.

Contents

Introduction

The ferromagnetic $3d$ transition metals — particularly iron — occupy a central position in both fundamental surface science and applied technologies. Their unique combination of partially filled d-states and intrinsic spin polarization [1] makes them indispensable across three major fields: spintronics, heterogeneous catalysis, and organic–inorganic hybrid systems.

In spintronics, ferromagnetic metals act as spin-polarized electrodes that enable key device functionalities such as *giant magnetoresistance* (GMR) [2, 3] and *tunneling magnetoresistance* (TMR) [4–6], forming the foundation of technologies like spin valves, magnetic sensors, and non-volatile memory [7, 8]. These effects have revolutionized magnetic data storage and paved the way for fast, energy-efficient components in next-generation information processing [9]. Moreover, the integration of ferromagnetic electrodes with organic semiconductors defines the field of organic spintronics [10], where molecule–ferromagnet interfaces give rise to hybrid states with exotic spin-dependent properties [11–13]. These interfaces, in which molecular orbitals couple to the spin-split electronic states of the metal, can exhibit spin polarization [14], magnetic anisotropy [15, 16], and other intriguing emergent behaviors — even the occurrence of ferromagnetism in actually non-magnetic compounds [17, 18] — that have earned them the nickname *spinterfaces* [19, 20]. A central advantage of organic molecules in this context is their intrinsically long spin relaxation times — often reaching tens to hundreds of milliseconds under ideal conditions [21] — due to the weak spin–orbit coupling and low hyperfine interaction in their light-element scaffolds [22]. These values exceed those typically observed in inorganic semiconductors and metals by several orders of magnitude [23], underscoring the potential of molecular systems for robust spin transport and information storage [24].

At the molecular scale, such coupling not only governs spin transport, which manifests as measurable spin polarization in nanoscale TMR experiments [14, 25, 26], but also profoundly alters the magnetic properties of the underlying substrate. Adsorption of small molecules such as CO, or of π-conjugated systems like fullerenes, can steer the magnetization direction in ultrathin films [15, 16], enhance local exchange interactions leading to magnetic hardening [26, 27], induce Dzyaloshinskii–Moriya interactions [28, 29] — as observed for oxygen on Ni surfaces [30] — or stabilize magnetic skyrmions in hydrogenated Fe double layers [31].

While these spin-dependent phenomena highlight the sensitivity of ferromagnetic surfaces to interfacial coupling, a parallel line of research explores their role in chemical reactivity [32, 33]. In heterogeneous catalysis, ferromagnetic transition metals serve as active surfaces for key chemical transformations, like the synthesis of ammonia [34] or electrocatalytic conversion processes, which are essential, for the production of green fuels [35]. In 1931, the deployment of iron-based catalysts in the Haber–Bosch process [36] — a milestone achieved by Carl Bosch in 1931, which paved the way for industrial ammonia synthesis — was awarded with the Nobel price and remains among the most consequential technological advances of the 20th century [37]. Subsequent conceptual developments, including Linus Pauling's bonding theory [38] and

Gerhard Ertl's atomically resolved investigations of catalytic reactions [39–43], established a modern framework for surface chemistry rooted in orbital hybridization, adsorbate–substrate coupling, and the emergent concept of the surface chemical bond [44].

To rationalize molecule–surface interactions, theoretical models such as the Newns–Anderson framework [45, 46] and the d-band model of Hammer and Nørskov [47, 48] have proven invaluable. These approaches capture complex adsorption phenomena through simple, physically meaningful descriptors — such as the position and width of the d-band relative to the adsorbate frontier orbitals [48–51] — to explain trends in adsorption strength, electronic structure, and catalytic activity [52–54]. However, the applicability of these models is fundamentally limited in two key respects. First, they neglect electron correlation, an intrinsic property of $3d$ ferromagnetic metals [55, 56], which can narrow the d-band, reduce exchange splitting, and thereby possibly alter hybridization behavior [57, 58]. Moreover, they do not account for how adsorbates themselves may influence the strength or nature of electronic correlations at the surface. Second, these models were originally based on small, reactive adsorbates (*e.g.*, H, O, CO [47, 52, 59]), where the assumption of spatially uniform coupling between adsorbate and substrate states is reasonably valid. In contrast, large organic molecules consist of many atoms and span lateral dimensions far exceeding the atomic spacing of the substrate. As a result, the molecule–surface interaction becomes inhomogeneous, with site-dependent coupling strengths and possible conformational adjustments. Under these conditions, the simplifying assumptions underlying traditional models break down, and their application becomes more nebulous.

This thesis addresses these gaps by investigating how electron correlation modifies the electronic structure of ferromagnetic surfaces and mediates their interaction with atomic and molecular adsorbates. Using Fe(100) as a model ferromagnetic substrate, the work spans interaction regimes from simple monoatomic chemisorption to extended organic–metal hybrid interfaces. A combination of spin- and momentum-resolved photoemission spectroscopy, scanning probe microscopy, and advanced electronic structure calculations — including *Hubbard-corrected density functional theory* (DFT+U) [60, 61] and *dynamical mean-field theory* (DMFT) [62] — is used to unravel and interpret the nature of the electronic coupling at these interfaces. Particular attention is paid to how *hybrid interface states* (HISs) emerge from correlated substrates, how traditional models must be revised, and how such insights might guide the design of materials for catalysis, electronics, and spin-based applications.

Furthermore, by employing *photoemission orbital tomography* (POT) [63, 64] to investigate not only the electronic structure but also the adsorption geometry and conformational properties of porphyrin molecules — essential in biological processes such as oxygen transport and photosynthesis [65, 66] — this work bridges model surface science and real-world function, elucidating how molecular geometry and electronic characteristics are interlinked within this versatile molecular class.

Thesis Structure

- **Chapter 1** introduces the theoretical foundations of electronic structure in molecules, surfaces, and interfaces. It provides an overview over the different interaction regimes and the corresponding key models for molecule–surface interactions, ranging from physisorption to strong chemisorption.

- **Chapter 2** outlines the experimental and computational methods employed in this thesis. It includes concise descriptions of sample preparation techniques, characterization tools such as AES, LEED, and STM, and an introduction to the DFT framework.
- **Chapter 3** focuses on photoemission techniques used to resolve the band structure and electronic properties of surfaces and interfaces. It presents the fundamental principles of photoemission and key concepts underlying PES, covering core methods including XPS, UPS, and ARPES. Special emphasis is placed on momentum-resolved photoemission microscopy, including its spin-resolved variant, which serves as a central technique throughout the thesis. The concept of POT is introduced as a powerful method for reconstructing molecular orbitals and determining adsorption geometries from momentum maps obtained in momentum-resolved experiments.
- **Chapter 4** presents the chemisorption of atomic oxygen on Fe(100), demonstrating how electron correlation is enhanced upon adsorption. This leads to significant modifications of the Fe *d*-bands and lays the groundwork for understanding more complex hybrid interfaces.
- **Chapter 5** explores the adsorption of pentacene on the oxygen-passivated Fe(100)–$p(1\times1)$O (Fe–O) surface. Building directly on Chapter 4, it reveals the formation of hybrid interface states driven by correlation-induced modifications of the Fe *d*-states. A refined d_{z^2}-band model is introduced to describe the coupling between molecular orbitals of extended organic adsorbates and the correlated metal substrate.
- **Chapter 6** focuses on tetraphenylporphyrins (ZnTPP and NiTPP) adsorbed on Fe–O surfaces, where they remain electronically decoupled from the substrate. POT is extended to investigate more complex molecular distortions, and conformational changes are traced across mono- and multilayer films, establishing a connection between geometric distortions and the electronic structure of the molecules.
- **Chapter 7** concludes the thesis by summarizing the main findings and discussing broader implications for interface design in correlated systems. An outlook is offered on the potential of correlation-aware interface engineering for future studies in catalysis, spintronics, and molecular electronics.

Each results chapter (Chapters 4–6) is structured around clear scientific questions, introduced at the outset and addressed through a combination of experimental observations and theoretical interpretation. Concluding remarks summarize the key insights and underscore their relevance in the broader context of surface and interface science.

1 Theoretical Background

1.1 Electronic Structure of Atoms, Molecules, and Surfaces

The electronic structure of matter is fundamental to understanding its chemical and physical behavior. At the most basic level, atoms feature discrete energy levels derived from the quantization of their electronic orbitals [38]. When atoms combine to form molecules, these atomic orbitals hybridize into bonding and antibonding *molecular orbitals* (MOs), as illustrated in Fig. 1.1. Bonding states are energetically stabilized due to an in-phase overlap of atomic orbitals, which increases the electron density between the nuclei. Antibonding states, in contrast, result from out-of-phase combinations, leading to a nodal plane and energetic destabilization. The resulting molecular orbitals determine the electronic properties of the molecule and play a central role in its interaction with other molecules or surfaces.

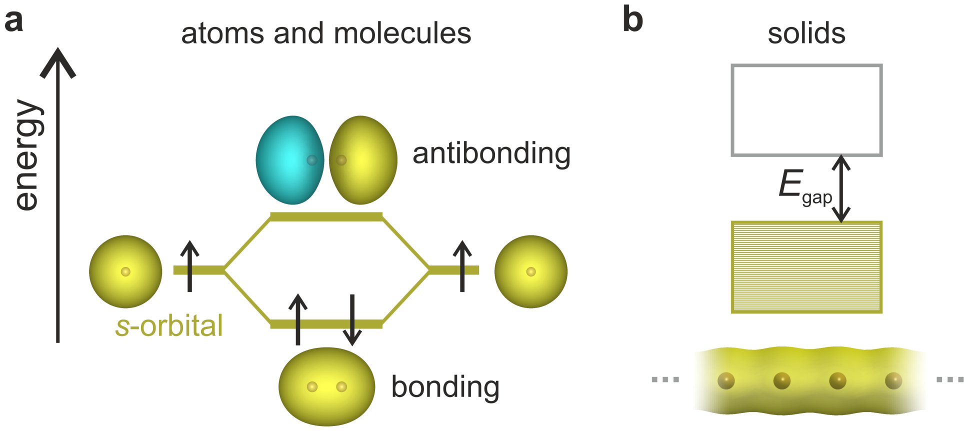

Figure 1.1: Fundamental electronic structure of molecules and solids. **(a)** Hybridization of wave functions of single atoms leads to the formation of bonding and antibonding molecular states, which is an important concept for the bond formation in molecules [67, 68]. **(b)** Electronic structure of an exemplary inorganic semiconductor (top). Due to the overlap of a quasi-infinite number of orbitals (bottom), the energy levels form quasi-continuous bands, which can be separated by energy gaps.

In solids, the picture evolves dramatically. As countless atoms are brought together in a periodic lattice, their atomic orbitals overlap extensively, forming energy bands instead of discrete levels. These bands, separated by an energy gap (E_{gap}), govern the electrical and optical properties of the solid*. Semiconductors, for example, exhibit band gaps in the range of 1–3 eV [69], allowing

---

*Note that the illustration starting from 1s orbitals and ending in a band gap, as it is depicted in Fig. 1.1, is not physically accurate, but merely a conceptual sketch.

them to interact with visible and infrared light. This makes them suitable for a wide range of electronic applications, including light-based energy harvesting and information processing. As shown in Fig. 1.1b, these energy gaps are analogous to the gaps found in molecules, where the discrete separation between bonding and antibonding states mirrors the *valence band* (VB) and *conduction band* (CB) of a solid.

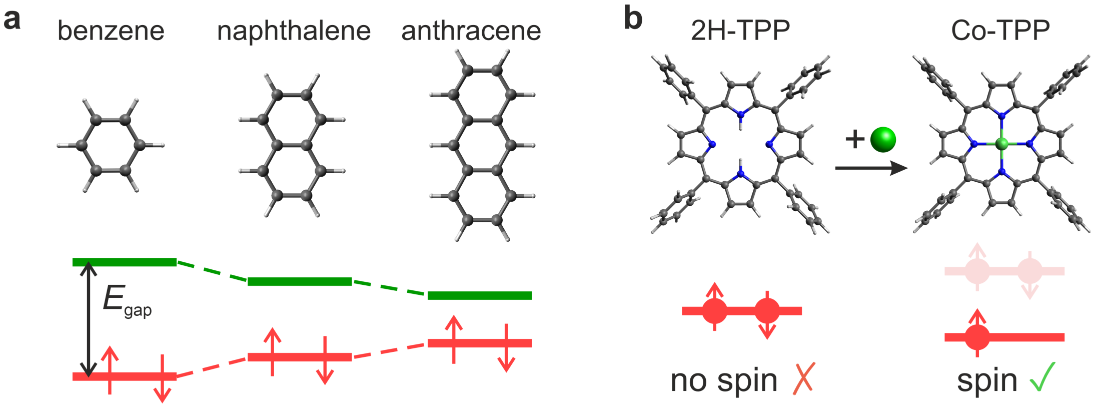

Figure 1.2: Illustration on the tunability and diversity of organic semiconductors. **(a)** Relation between energy gap of acene molecules and the number of carbon rings. As more rings are added, the energy gap between the frontier orbitals shrinks, allowing access to a wide range of different band gaps by changing the molecular compound. **(b)** In more complex molecules, such as the depicted porphyrins, magnetic properties can be introduced on demand by incorporating or substituting the central metal ion.

Thus, organic molecules offer a unique opportunity to emulate the functionality of solids while also providing key advantages and pathways for extending their capabilities. In *organic semiconductor*s (OSCs), E_{gap} is determined by the molecular structure and can be tuned by altering chemical composition, conjugation length, or molecular packing, as depicted in Fig. 1.2a. This tunability extends beyond the electronic gap, and also includes magnetic properties (see Fig. 1.2b), which can be precisely engineered by modifying the molecular composition. Unlike inorganic materials, OSCs are flexible, lightweight, and environmentally friendly, as their processing does not require resource-intensive methods like etching [70].

Furthermore, molecules are inherently more adaptable than crystalline solids. Their electronic states are sensitive to their environment, allowing for custom tailoring of properties such as charge transport, light absorption, and emission. This flexibility makes them ideal for applications in photovoltaics, *organic light-emitting diode*s (OLEDs), and molecular spintronics, where control and design are paramount.

1.2 Fundamental Properties of Organic Molecules

OSCs are materials based on π-conjugated molecules or polymers, predominantly composed of carbon atoms along with lighter elements such as nitrogen, hydrogen, and oxygen. These molecules exhibit alternating single and double bonds in a structure known as conjugation. The carbon atoms are sp^2-hybridized, forming strong covalent σ-bonds in the molecular plane, while the remaining p_z orbitals overlap to create π-bonds [71]. The *highest occupied molecular orbital* (HOMO) typically corresponds to the occupied π-bonding state, while the *lowest unoccupied molecular orbital* (LUMO) is associated with the unoccupied π^*-antibonding state. Since σ-bonds are significantly stronger than π-bonds, organic molecules remain stable even when their antibonding π^*-orbitals (bonding π-orbitals) are populated (depopulated), as occurs during optical excitations or charge injection [71].

In polyatomic molecules, the effective potential experienced by an electron arises from the combined influence of the atomic nuclei and other electrons [72]. While electrons in inner energy shells are strongly localized near the nuclei, the outer regions exhibit merged potential wells where atomic orbitals interact to form delocalized MOs. The uppermost region of this potential corresponds to the vacuum level (E_{vac}). The energy difference between the HOMO and the vacuum level define the ionization potential (IP), while the separation between the LUMO and the vacuum level corresponds to the electron affinity (EA). A simplified scheme of the potential well is sketched in Fig. 1.3.

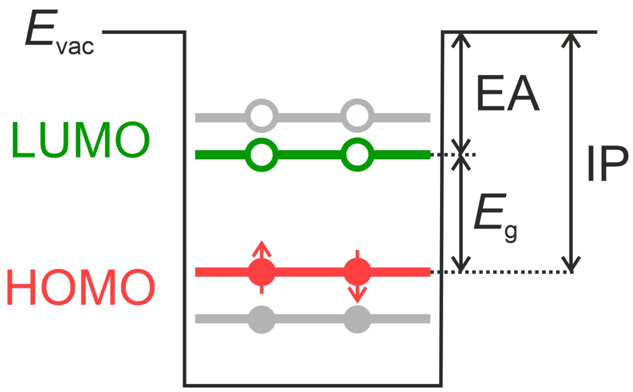

Figure 1.3: Simplified sketch of the electronic structure of an isolated molecule. Red dots represent electrons filling the HOMO level (red line) while green circles illustrate unfilled states of the LUMO level (green line). The gap (E_{gap}) is defined by the HOMO and LUMO (green line) distance, or as the difference between IP and EA.

The electronic structure of OSCs is conceptually similar to inorganic semiconductors, with the HOMO serving as the VB and the LUMO as the CB. The bandgap, which determines their electronic and optical properties, generally exceeds 1.5 eV, making OSCs inherently insulating. However, just as inorganic semiconductors, the conductivity of OSCs can be significantly enhanced by doping with oxidizing or reducing agents [73]. Oxidizing substances remove electrons from the molecules, acting as p-dopants, whereas reducing agents introduce n-doping through electron donation [74]. While solids and metals are characterized by bands and highly delocalized charges that move almost freely through the material, charge carriers in organics are strongly localized travelling only incoherently by hopping from one molecule to another [75].

This and the much stronger electron-phonon coupling present in OSCs renders inorganic semiconductor charge transfer models inadequate, even in cases where band-like transport is partly present

[75]. Owing to this strong electron-phonon coupling, charged states on individual molecules are stabilized by significant lattice deformations. Such quasi-particle states of phonon-dressed charges are called polarons.

Understanding the origin of these polaronic states requires recognizing that the equilibrium geometry of the ionized state differs from the neutral ground state. This difference arises because exciting a molecule involves transferring one of its electrons from a bonding to an antibonding orbital. As a result, the overall electron density between atomic cores decreases, leading to increased equilibrium atomic distances [76].

Thus, a vertical Franck-Condon transition, such as the one presented in Fig. 1.4 with an associated energy $E_{\mathrm{IP,v}}$, is followed by geometric relaxation into the excited ground state ${E^*}_0$, resulting in an energy gain E_{rel}. Conversely, transitioning from the ground state to the relaxed ionized state necessitates the adoption of a distorted state, demanding the distortion energy E_{dis}. Geometric relaxation becomes favorable when the energy difference $E_{\mathrm{IP,v}} - E_{\mathrm{IP,d}} = \Delta\epsilon$ surpasses the distortion energy E_{dis}. This energy difference instigates a local lattice distortion around the charge: the polaron. The binding energy of this polaron state, given by $\Delta\epsilon - E_{\mathrm{dis}} = E_{\mathrm{rel}}$, is generally favorable in organic molecules, thereby effectively narrowing the energy gap [74].

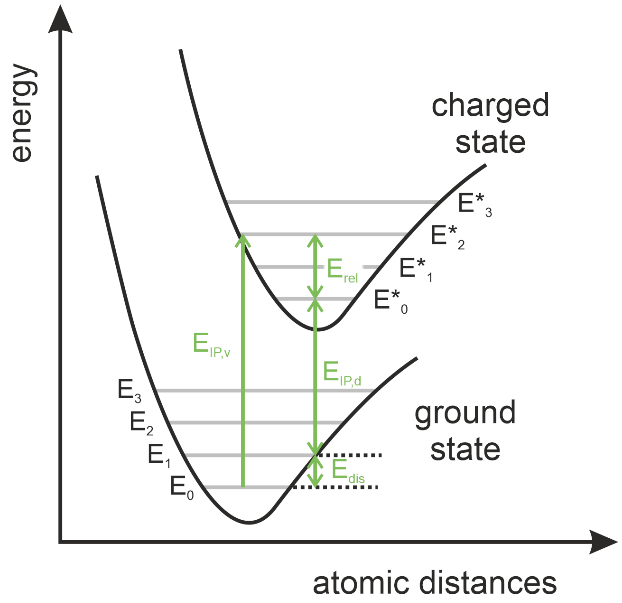

Figure 1.4: Energy diagram of the Franck-Condon principle. Black curves depict the potential energy curves of the ground state and the ionized state of an organic molecular complex. Grey horizontal lines indicate vibrational energy levels, corresponding to vibrational modes such as stretching, bending or torsional motions of molecular bonds. Adapted from [74].

In this process, the ionized state's frontier molecular levels shift as follows: the HOMO is elevated by $\Delta\epsilon$, while the LUMO is reduced by the same amount as depicted in Fig. 1.5a-c. This charge-induced deformation suggests that polaron formation is energetically preferred in most organic semiconductors. However, it is crucial to note that this does not confer a metallic character since the half-occupied level remains localized within the energy gap [74].

The introduction of another charge to the molecule presents two potential outcomes: 1) In the case of a molecular thin film, the new charge forms an additional polaron elsewhere on the molecular lattice, or 2) it occupies the singly unoccupied state of the pre-existing polaron, thus creating a bipolaron. The formation of bipolarons implies that the Coulomb repulsion between the two placed charges is smaller than the energy gained by the interaction with the lattice. However, since the lattice relaxation around two charges is stronger than the deformation induced by a single charge, the electronic states of bipolarons are further separated from the initial HOMO-LUMO states, as presented in the energy diagram in Fig. 1.5b,c.

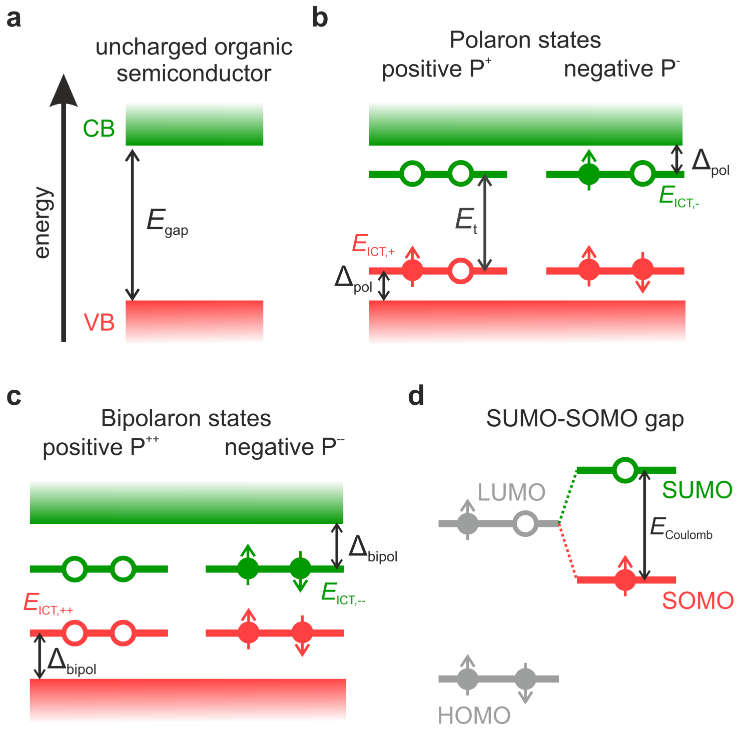

Figure 1.5: Schematic band structure of an organic semiconducting film illustrating the role of ionization processes. **(a)** In the neutral state, the valence band (VB) and conduction band (CB) are separated by an energy E_{gap}, corresponding approximately to the HOMO-LUMO gap. **(b)** When the molecule is ionized, polarons are formed with energy levels that lie within the gap of the neutral molecule. The separation between these polaronic states determines the gap for electronic transport, E_{t}. **(c)** If an additional charge of the same sign is added to an already ionized molecule, bipolarons are formed, leading to further shifted energy levels. In (b) and (c), $\mathit{\Delta}_{\text{pol}}$ and $\mathit{\Delta}_{\text{bipol}}$ denote the polaron and bipolaron binding energies, respectively. **(d)** One-electron diagram for a singly charged molecule. The electrostatic field induced by the added charge creates a Coulomb barrier, hindering the addition of further charges. This barrier results in a splitting into singly occupied (SOMO) and singly unoccupied (SUMO) molecular orbitals.

Generally, this renders bipolarons thermodynamically more stable than two separated polarons. Since a bipolaron is occupied by two charges of opposite spin, their net spin is zero. Both types of charged states, polarons and bipolarons, can contribute to the charge transport in organic materials and have been elucidated to explain the transport properties of different organic semiconductors. The similarities between bipolarons and Cooper pairs in superconductors makes them a fascinating research topic, particularly since the discovery of superconductivity in highly doped K_3C_{60} samples [77, 78], which can even be achieved at room temperature by resonant excitation with light [79, 80].

However, owing to the mentioned strong Coulomb repulsion present in the case of a bipolaron, its formation is rarely observed in adsorbed monolayer films, and instead the single charge ionization state (polaron) is stabilized, giving rise to a Mott-Hubbard-like electronic structure [81, 82]. The molecular frontier orbital structure is now comprised of a *singly occupied molecular orbital* (SOMO) and its counterpart *singly unoccupied molecular orbital* (SUMO), which are separated by a Coulomb gap E_{Coulomb}, as schematically depicted in Fig. 1.5d [82–84]. Noteworthy, the emerging Coulomb gap can reach values on the order of 1 eV, significantly altering the charge injection properties of the OSC material and preserving its semiconducting character [82, 84].

So far, we have only considered intramolecular changes due to the ionization of individual molecules, however, placing a charge onto a molecule does not only affect the geometry of the charged molecule itself, but also elicits a response from the molecular environment. Such a response includes variations of the distances between neighboring molecules, *i.e.*, polarons that distort the whole molecular lattice [76], and even more influential: the formation of polarization clouds at organic/inorganic interfaces [85–87]. While the former plays a key role in organic crystals, it is generally less significant at interfaces and is therefore not explicitly considered. The latter, by contrast, has a huge impact on the energy level alignment of organic thin films, particularly in the monolayer range.

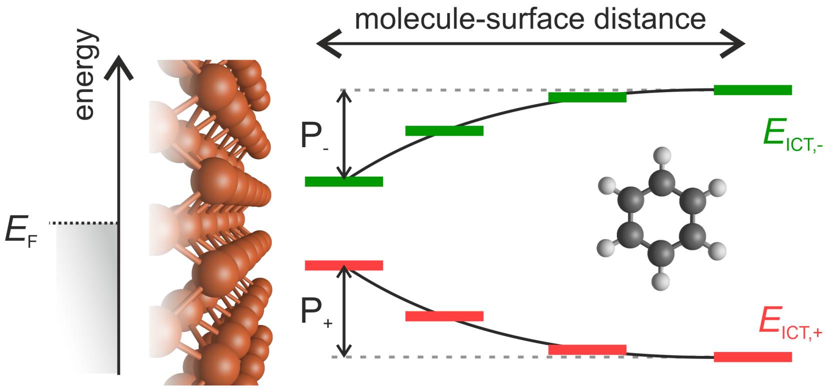

Figure 1.6: Transport gap renormalization due to surface polarization effects. Polarization clouds in the metal screen and stabilize the charged molecular states, reducing the transport gap. As the metal-molecule distance decreases, the screening becomes more effective.

For example, when an ionized molecule is placed on a metal surface, the change in potential due to the charged adsorbate is immediately felt by the electrons inside the metal and their delocalized nature allows them to reply instantaneously, acting as self-consistent polarization clouds [85, 87]. The formation of such polarization clouds is associated with the energy P_+ for clouds surrounding cations (holes) and P_- for anions (electrons) [87]. This additional correlation energy further stabilizes the added hole or electron, reducing the HOMO-LUMO gap by the combination $P = P_+ + P_-$, leading to a renormalized HOMO-LUMO transport gap of E_t = IP–EA–P as illustrated in Fig. 1.6. In comparison to the gas phase this renormalization of the molecular levels is predicted to be as large as several eV [86].

Since the underlying Coulomb interactions are long-range, the polarization clouds can extend over many lattice constants, depending on the materials, while P itself depends on the proximity to surfaces and interfaces. For thin organic films on metal surfaces this leads to variations in the experimentally determined transport gaps (E_t) for varying film thicknesses. For single layers the polarizability is increased due to the vicinity of the metal and its high polarizability, which screens the molecular ions more effectively. However, with increasing thickness, the influence of the metal on the topmost layer is reduced (this layer is the one effectively probed in UPS, IPES and STM/STS experiments) and the polarizability of the environment decreases. Thus, surface layers that are well-separated from the metal exhibit an increased transport gap as only the underlying molecular layer can screen the localized charges, and no polarizability from the vacuum side is expected [87].

Hence, in organic materials charge carriers must not only be considered as quasiparticles called polarons, but rather polarons surrounded by polarization clouds [87]. In practice, the molecular orbitals can be obtained using specifically tuned functionals in *density functional theory* (DFT) calculations [71, 82], to obtain realistic values for the HOMO-LUMO gap. Effects such as the screening by the environment, geometric relaxations and vibronic effects can be taken into account either by calculations or by fitting theoretical results to the experimentally obtained transport gap (obtained through experiment) [71, 82]. In the latter case this is done by rigidly shifting the unoccupied and occupied molecular orbitals to match experimental results.

Notably, the formation of polarization clouds is also possible in electronically hard materials such as oxides. However, due to strong ionic bonding and concomitantly strong localization of the electrons and holes, the polarization clouds are also of polaronic nature and therefore linked to ionic displacements [88, 89]. Thus, the resulting screening is significantly less effective compared to the one on metal surfaces [82]. Consequently, the insertion of ultrathin dielectric barriers (few monolayers) can be used to effectively tune the metal-organic distance, and thereby tailor the screening capacity of the metal substrate, which ultimately affects the energy level alignment [90].

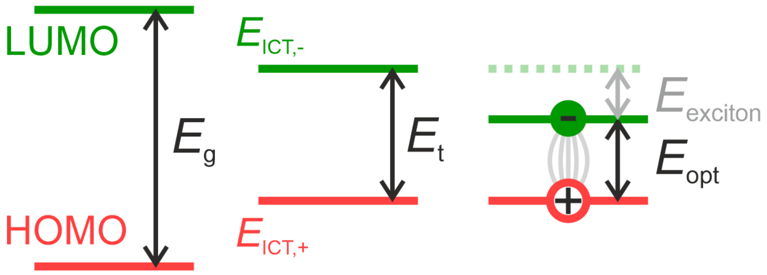

Figure 1.7: Energy gaps in OSC. The energy E_gap represents the HOMO-LUMO gap of the unperturbed gas-phase molecule (left). The transport gap E_t corresponds to the energy distance of the singly charged states (middle), while the optical gap E_opt is further reduced by the exciton binding energy (right).

From Fig. 1.7 one can see that E_t inside an undoped organic material is given by the distance between the two polaronic states $E_{\mathrm{ICT},+}$, and $E_{\mathrm{ICT},\text{-}}$, *i.e.*, the energy that is necessary to create a separated electron-hole pair. This gap can be few eV smaller than the gas phase HOMO-LUMO gap, however, it still exceeds the optical gap of OSC by $\sim 1\,\mathrm{eV}$ [91]. Unlike the transport excitation, optical excitation does not induce free charge carriers in the HOMO and LUMO levels, it rather corresponds to the formation of (strongly localized) electron-hole pairs, called excitons [91, 92]. The energy spectrum of these quasiparticles is characterized by a hydrogen like series of well-defined states within the HOMO-LUMO gap, as illustrated in Fig. 1.7 [92]. Due to the weak electrostatic van der Waals forces between individual molecules, the excitonic states in OSC are strongly localized, meaning that both electron and hole are located either on the same molecular site (Frenkel exciton) or on neighboring molecules (charge transfer exciton).

Consequently, the exciton binding energies in OSC ($\approx 100 - 1000\,\mathrm{meV}$) are generally higher than the ones of delocalized Mott-Wannier excitons in inorganic semiconductors ($\approx 10 - 100\,\mathrm{meV}$). While the latter excitonic states are usually unstable at elevated temperatures, the strongly localized excitons in OSC tend to be stable even at room temperature [92, 93]. Despite the fact that optical excitations do not correspond to free charge carrier excitations, the induced variations in the local charge distributions, due to exciton formation, have direct influence on the transport-related polaronic excitations and both are strongly interwoven in OSC [92].

1.3 Interaction Regimes for Molecules on Surfaces

In contrast to a solid, where the periodic potential leads to a band-like structure in the energy dispersion, the electronic structure of a molecule (or an atom) consists of separate molecular levels with well-defined energies. However, when a molecule adsorbs on a metallic substrate, the mutual metal–molecule interaction can induce significant changes in the electronic structure of the two constituents depending on the degree of interaction. This degree is usually characterized by the adsorption energy ΔE, which denotes the energy that is necessary to remove an adsorbed molecule from the substrate at $T = 0\,\mathrm{K}$ [94].

Typically, one distinguishes between two interaction regimes, the physisorption regime and the chemisorption regime, whereby the latter is usually divided in weak and strong chemisorption. In the physisorption regime the molecule–substrate interaction is weak and originates from van der Waals forces, which arise due to the mutual formation of dipoles in the electron clouds that surround adsorbate and surface atoms [33]. Chemical bonds can generally be excluded in this interaction regime. Because of the weak interaction, which typically leads to adsorption energies in the range of $0.1\,\mathrm{eV}$ to $1.0\,\mathrm{eV}$, the molecules maintain their gas-phase-like electronic character and only a renormalization of the HOMO-LUMO gap is observed, owing to the polarizability of the surface. This is schematically shown in Fig. 1.8a,b. Physisorption can occur for adsorption on inert or on passivated surfaces [13], with a molecule/substrate distance of typically $\gtrsim 3\,\text{Å}$ [20, 95]. Despite the absence of chemical bonds, charge transfer between the substrate and the molecular adlayer is still possible by integer amounts via tunneling.

On substrates that are more reactive instead, *i.e.* on metals, where chemical bonds and partial charge transfer occur at the interface, we fall in the chemisorption regime. Aside from structural

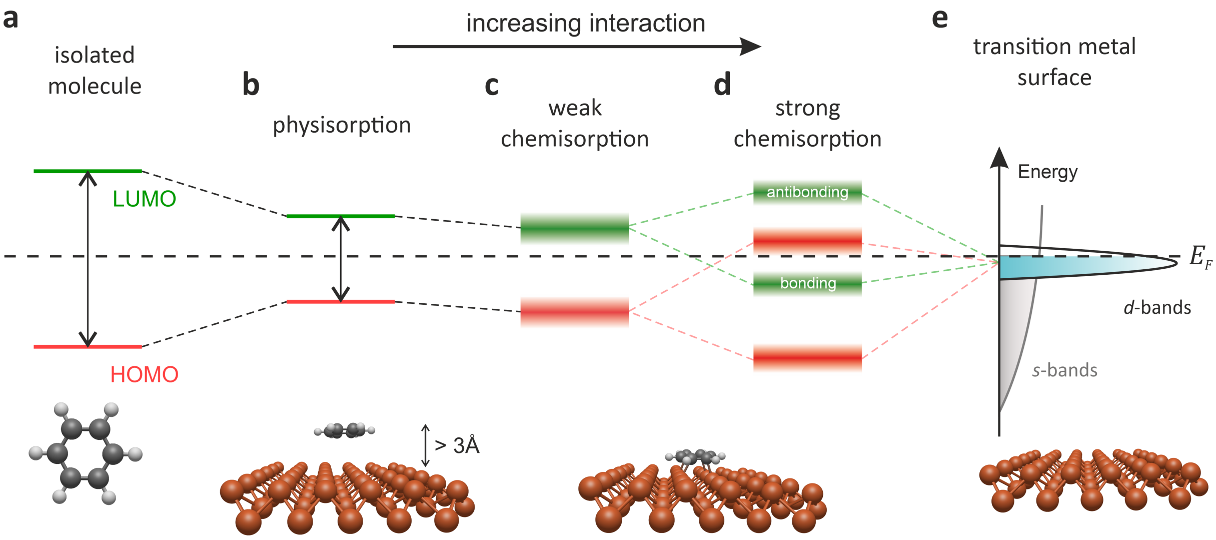

Figure 1.8: Evolution of molecular electronic states with increasing interaction between molecule and a transition metal surface. **(a)** For an isolated molecule the HOMO (red) and LUMO (green) are separated by a distinct energy gap. **(b)** In the case of physisorption, molecular orbitals are left almost unperturbed, however, the polarizability of the surfaces leads to a reduction of the HOMO-LUMO gap. **(c)** Weak chemisorption leads to the formation of chemical bonding, resulting in a finite lifetime of the molecular states, broadening and shifting them in energy. **(d)** Strong chemisorption occurs when molecular states hybridize with the narrow *d*-bands of the metal surface, resulting in the formation of bonding and antibonding metal-molecule states. **(e)** Prototypical electronic structure of a transition metal surface, featuring partially occupied *d*-states and broad *sp*-bands.

deformations of the molecular complex, chemisorption can also give rise to a plethora of alterations in the molecule's electronic structure such as new hybrid states with mixed metal-molecule character, so-called *hybrid interface state*s (HISs).

An important model to rationalize the electronic structure of chemisorbed systems is the Newns-Anderson model [45, 46], where in addition to ΔE also the bandwidth W of the overlapping substrate metal band plays a decisive role. This model is best understood in the two limiting cases of weak and strong chemisorption, represented by $W/\Delta E \gg 1$ and $W/\Delta E \ll 1$, respectively.

Weak chemisorption emerges for surfaces with broad bands, typically *sp*-bands width a width of $W \approx 10\,\text{eV}$ [13]. Here, hybridization can facilitate a partial transfer of charges between the molecule and the substrate and further leads to a finite lifetime τ of the molecular state, which in turn gives rise to a Lorentzian broadening $\Gamma = \hbar/\tau$ of the sharp molecular levels. This behavior is presented in Fig. 1.8c [52].

In contrast, strong chemisorption is also a result of hybridization, but with electrons originating from narrow *d*- or *f*-bands, which typically have a width of $W \approx 1\,\text{eV}$ [13]. Here, alongside the already mentioned renormalization, the strong interaction can cause the molecular states to split into bonding and antibonding resonances — analogous to the combination of atomic orbitals [67] — as depicted in Fig. 1.8d,e. Based on the energy positions of these newly formed states, it can occur that some of the formerly unoccupied orbitals become partially filled if they fall below the Fermi level, due to the ensuing electron transfer from the substrate to the molecular layer. This process is called *electron backdonation.* On the contrary, some of the initially occupied orbitals can also become partially unfilled as electrons are transferred in the opposite direction (from the molecule to the substrate), which is referred to as *electron donation.*

Since in the *density of states* (DOS) of a transition metal, both types of bands (broad *sp*- and narrow *d*-bands) exist and contribute to the bonding, both need to be taken into account for an adequate description of the bond energy. A model that does so is the *d*-band model by Hammer and Nørskov [47, 48]. Here, the adsorption energy is divided in two sub contributions

$$\Delta E = \Delta E_{sp} + \Delta E_{d}, \tag{1.1}$$

to describe the bonding ΔE_{sp} due to interaction with the delocalized *sp*-electrons, and the additional bonding ΔE_d arising from coupling to the *d*-states.

Within the picture of the *d*-band model, the coupling between the adsorbate electronic states and the metal states is a two-step process: firstly, interaction with the *sp*-bands causes the adsorbate state to shift and broaden energy. Subsequently, coupling of the renormalized states with the metal *d*-bands induces the emergence of split bonding and antibonding states producing an electronic structure like the one depicted in Fig. 1.8d [33]. While ΔE_{sp} dominates the bond strength, as it is negative and according to amount larger than ΔE_d, its value does generally not depend on the metal [33]. Thus, variations in the adsorption energy can be grasped by considering the properties of the metal *d*-bands only. In this simplified one-electron picture, that addresses the adsorbate–substrate problem from a purely energetic point-of-view, the adsorption energy is mainly determined by the center of the metal *d*-band, the relative energy positions of the renormalized adsorbate states and their coupling strength to the metal the *d*-band [33].

Notably, the *d*-band center is directly linked to the filling of the *d*-shell and consequently for transition metals, a weaker bond strength is observed for elements farther to the right in the periodic table, while an enhanced chemical reactivity is observed when going from 5*d* to 4*d* over to 3*d* transition metals. The first trend can be understood by considering that an increased *d*-band filling lowers the *d*-band center, shifting the antibonding resonances below the Fermi level. This leads to their occupation and, consequently, to weaker bonding. A similar weakening occurs when bonding resonances are pushed above the Fermi level [53].

The second trend is a consequence of the Pauli repulsion and the fact that the spatial extension of the *d* orbitals decreases when going from 5*d* to 4*d* down to 3*d* states. Since the Pauli principle mandates that two electrons cannot be in the same state, the adsorbate states must become orthogonal to the metal *d* states, which raises their kinetic energy [53]. This repulsion increases for a larger overlap of the corresponding orbitals. As a result, gold — which has the most extended *d*-states of the noble metals — is considered the least reactive and therefore the noblest of all metals [47].

Models like the Newns-Anderson and the *d*-band model are invaluable tools to rationalize the electronic structure of adsorbates on metal surfaces. They successfully explain the observed adsorption behavior and catalytic activity of single atoms and monomers, such as CO or ethylene, on various metals [51, 59, 96]. Despite their simplicity, some of the qualitative conclusions regarding interaction regimes and adsorption trends maintain their validity, even when extended to larger organic molecules.

Based on these insights, several models have been introduced to provide simplified descriptions of organic–inorganic interfaces across different interaction regimes, which we will discuss in the following. Finally, we return to the formalism of the Newns–Anderson model and present it in a more rigorous manner.

1.4 Energy Level Alignment at Interfaces

In the previous chapter, we have introduced the interaction regimes occurring at metal–organic interfaces depending on the degree of chemical bonding. Based on the type of interaction, the energy positions of the frontier orbitals can differ significantly compared to when the molecule is in the gas phase. This arrangement of the molecular levels is referred to as energy level alignment and it is undoubtedly one of the most important quantities of a metal–organic interface, as it determines the charge injection properties, which crucially affect the performance of organic-based devices. Until today, no universal model exist that can predict the energy level alignment reliably for all the various interaction strengths, however, different models have been applied successfully for certain regimes that capture the dominant physical and chemical processes occurring at the distinct interface.

1.4.1 Physisorption without Charge Transfer: The Schottky-Mott Limit

The most straightforward method to predict how the frontier orbital levels of an organic compound energetically align is achieved by simply aligning the vacuum levels (E_{vac}) of the two constituents as sketched in Fig. 1.9a. This approach is referred to as Schottky-Mott model and it excludes any sort of chemical interaction and is therefore valid for physisorbed systems (non-reactive molecules on inert surfaces), where no hybridization is expected such as *ex situ* prepared interfaces of non-reactive molecules on inert surfaces like Gold [71].

In this limiting case, the decisive quantities on the molecular side are the ionization potential (IP) and the electron affinity (EA), which denote the distances between E_{vac} and the HOMO and LUMO, respectively. While the IP determines the energy that is needed to remove an electron from an isolated molecule, EA represents the required energy for adding an electron to the isolated molecule. However, as mentioned earlier, the actual energies that are relevant for ionizing a molecule are the energies of the *integer charge transfer* (ICT) states rather than the exact HOMO and LUMO positions. Therefore, we introduce the renormalized electron affinity and renormalized ionization potential, EA* and IP*, respectively. In this simplified picture we neglect any polarization effects from the environment, although such effects can readily be included by starting from the renormalized HOMO-LUMO gap.

The other crucial parameter that defines where the frontier orbitals fall energetically is the substrate work function Φ_{sub}. Following the energy diagram presented in Fig. 1.9b, the barriers

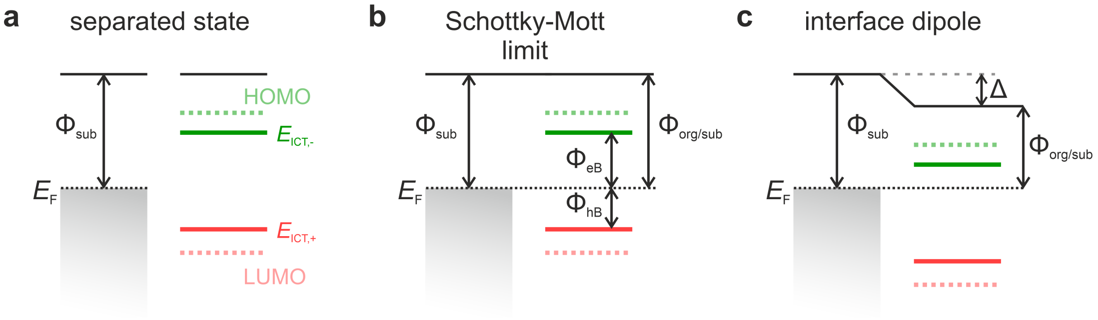

Figure 1.9: Energy level alignment at metal-organic interfaces without charge transfer. **(a)** In the separated state, the substrate work function ($\mathit{\Phi}_{\text{sub}}$) is defined by the distance between Fermi level (E_{F}) and vacuum level. The molecular energy levels, including the HOMO and LUMO, are unaffected by the substrate. **(b)** In the Schottky-Mott limit, the vacuum level of the substrate and the OSC align, and the injection barriers for holes ($\mathit{\Phi}_{\text{hB}}$) and electrons ($\mathit{\Phi}_{\text{eB}}$) are determined by the *integer charge transfer* (ICT) states ($E_{\text{ICT,+}}$ and $E_{\text{ICT,-}}$) of the organic material. **(c)** The presence of an interface dipole ($\mathit{\Delta}$) alters the effective work function of the combined metal-molecule system ($\mathit{\Phi}_{\text{org/sub}}$), shifting the molecular energy levels and influencing the charge injection efficiency at the interface.

for injecting charges, either electrons or holes, from the substrate into the organic molecule are given via the two following expressions:

$$\mathit{\Phi}_{\text{eB}} = \mathit{\Phi}_{\text{sub}} - \text{EA}^* \tag{1.2}$$

$$\mathit{\Phi}_{\text{hB}} = \text{IP}^* - \mathit{\Phi}_{\text{sub}}. \tag{1.3}$$

From these formulas, it is evident that the charge injection barriers depend on the substrate work function, suggesting a fully predictable and controllable energy level alignment for a sufficiently high degree of work function tunability.

However, it became evident early on that the orbital alignment at most interfaces differs from this prediction, owing to the fact that the adsorption process is often accompanied by the formation of an additional interface dipole, which alters the work function and ultimately the energy level alignment.

In case of a metal surface, one important contribution to this interface dipole arises due to the Pauli interaction with the molecular electrons. To visualize this, we first introduce the Jellium model, which is a simple model to predict the electron density near a metallic surface, by assuming a constant density of positive charges with a sharp potential step at the surface. Solving the self-consistent equations for the electron density [97, 98], reveals that the electron density exceeds beyond the crystal surface up to a distance of several Å [99]. The scheme of the Jellium model potential and the corresponding electron density are depicted in Fig. 1.10.

Consequently, the spilling-out of electrons leads to the emergence of an electric dipole barrier $\mathit{\Delta\Phi}$, which hinders the electrons from inside the solid from escaping. This dipole barrier is directly to the metal work function, which is given via the relation

$$\mathit{\Phi}_{\text{sub}} = \mathit{\Delta\Phi} - \mu, \tag{1.4}$$

where μ denotes the chemical potential of the infinite bulk system [97]. Since the orientation of the crystal surface determines its atomic density, it also affects the charge carrier density. Therefore, higher work functions are observed for surface orientations with more densely packed structures, *i.e.*, the (111) orientation of Ag exhibits a higher work function than the (100) surface [100]. However, upon adsorption, the ensuing Pauli repulsion due to the presence of the adsorbate electrons pushes the electrons spilling-out from the surface back into the solid. This leads to a reduction of the surface dipole; hence, this contribution of the interface dipole is negative, and it reduces the work function of the final system. This is the first contribution to the interface dipole and due to its nature, this effect is called the push-back effect.

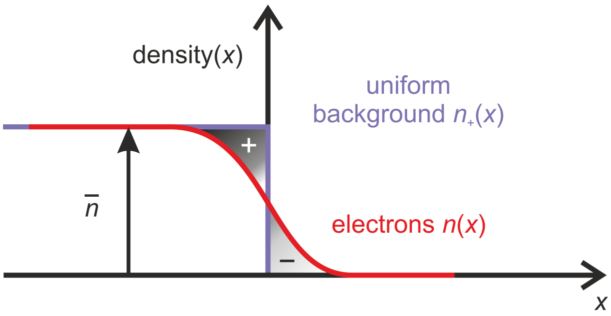

Figure 1.10: Electron density distribution at a metallic surface modeled using the Jellium approximation. Adapted from [97].

While it plays an important role on metallic surfaces, it is generally far less relevant on oxide surfaces, which are electronically hard materials with strongly localized electrons. The second contribution to the interface dipole arises due to any electric dipole moment on the molecule. Such a dipole can be intrinsic to the molecule or induced by the interaction with the surface, *e.g.* due to conformational changes of the molecule. In contrast to the push-back-related dipole, this one can be either negative or positive depending on the direction of the dipole, thus, it can change its sign depending on the adsorption geometry.

Taking into account the resulting interface dipole $\Delta = \Delta_{\mathrm{push}} + \Delta_{\mathrm{dipole}}$, the injection barriers are now given via

$$\Phi_{\mathrm{eB}} = \Phi_{\mathrm{sub}} - \mathrm{EA}^* - \Delta \tag{1.5}$$

$$\Phi_{\mathrm{hB}} = \mathrm{IP}^* - \Phi_{\mathrm{sub}} + \Delta. \tag{1.6}$$

The illustrated energy diagram in Fig. 1.9c showcases how the presence of an interface dipole modifies the expected energy level alignment as predicted by the Schottky-Mott model. This adjustment is a first pivotal step towards bridging the gap between the theoretical predictions of the Schottky-Mott model and the empirical observations.

Moreover, an insightful observation from Fig. 1.9 reveals that any variation in the clean substrate's initial work function, Φ_{sub} induces a proportional and rigid shift in the final work function of the system, $\Phi_{\mathrm{org/sub}}$, yielding a linear relationship with the slope of $S = \mathrm{d}\Phi_{\mathrm{org/sub}}/\mathrm{d}\Phi_{\mathrm{sub}} = 1$. This relation is not affected by the interface dipole and is generally referred to as vacuum level alignment. As we will see in the next section, this kind of energy level alignment modelling is only valid if the ICT states do not cross the Fermi level.

1.4.2 Non-Hybridized Interfaces with Charge Transfer: Integer Charge Transfer and Capacitor Models

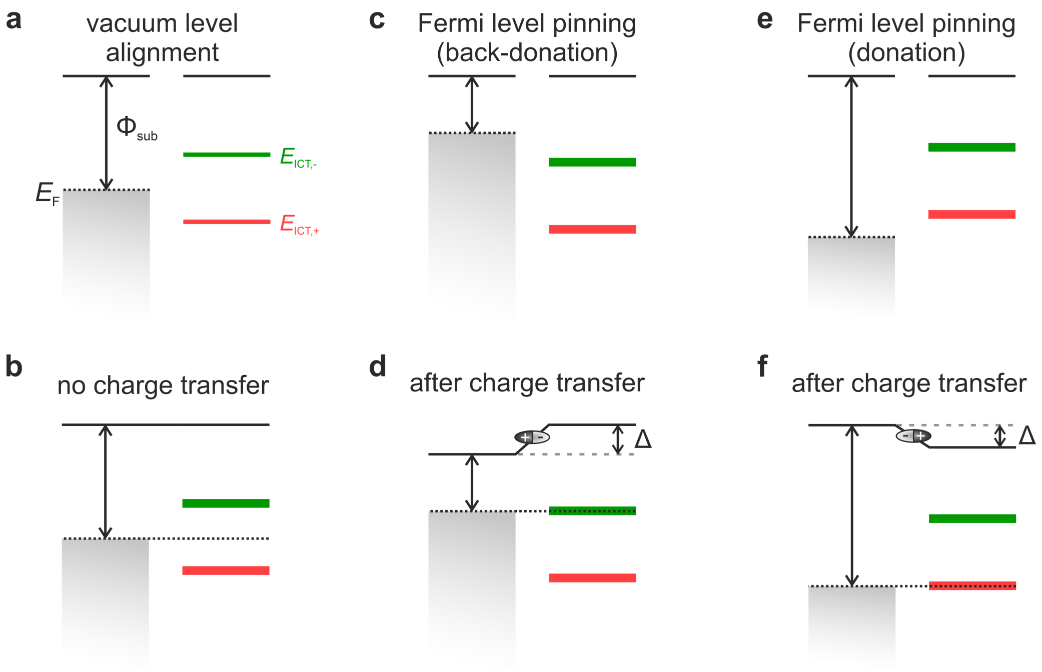

Figure 1.11: Schematic illustration of energy level alignment within the ICT model. Panels **(a)**,**(c)**,**(e)** show vacuum level alignment for three cases: **(a)** neither HOMO nor LUMO cross the Fermi level, **(c)** the HOMO lies above E_F, and **(e)** the LUMO lies below E_F. Panels **(b)**,**(d)**,**(f)** show the corresponding situations after possible charge transfer took place. While no charge transfer occurs in **(b)**, leading to preserved vacuum level alignment, electron transfer in **(d)** and **(f)** results in pinning of the respective frontier orbital at E_F and the formation of an interface dipole Δ.

Having explored the intricacies of the Schottky-Mott model and the role of interface dipoles in determining energy level alignments, it becomes evident that the interaction between organic molecules and surfaces is multifaceted. While the aforementioned models provide a first insights into the energetic landscape, they primarily focus on the static alignment of energy levels during the absence of charge transfer.

However, many devices, *e.g.* OLEDs or organic-based transistors, rely on molecules being in an ionized state. As initially discussed, charging molecules can have a significant influence on the energetic landscape of their frontier orbitals. This brings us to the integer charge transfer model, a framework that focuses on the mechanisms of charge exchange between adsorbed molecules and substrates if hybridization at the interface is negligible. Due to the absence of hybridization, charge transfer is only possible by integer amounts. This scenario is common for interfaces formed by non-reactive molecules on metal surfaces that are passivated by thin dielectric films (*e.g.* by oxides), on semiconductor surfaces, or, if the interaction is weak enough, on inert metals.

In order to understand the conditions under which integer charge transfer can occur, we start by considering the case of vacuum level alignment discussed in Section 1.4.1, however, for simplicity we assume that the interface dipole $\Delta = 0$. As elaborated previously, in this case where the dipole-corrected work function lies between the values of $E_{\mathrm{ICT,-}}$ and IP, *i.e.*, $E_{\mathrm{ICT,-}} < \Phi_{\mathrm{sub}} < E_{\mathrm{ICT,+}}$, the interface constituents will not exchange any charges (see Fig. 1.11a,b). However, this situation changes when one of the ICT states crosses the Fermi level, *i.e.*, one of the two conditions $E_{\mathrm{ICT,-}} > \Phi_{\mathrm{sub}}$ or $E_{\mathrm{ICT,+}} < \Phi_{\mathrm{sub}}$ is met. These situations are depicted in Fig. 1.11c, and Fig. 1.11e, respectively. Now, charge flow across the interface will set in to minimize the energy of the composite system. This charge transfer, however, is accompanied by an additional interface dipole Δ_{CT}, resulting in a total dipole of $\Delta = \Delta_{\mathrm{push}} + \Delta_{\mathrm{dipole}} + \Delta_{\mathrm{CT}}$. Note, that in Fig. 1.11 we assumed $\Delta_{\mathrm{push}} + \Delta_{\mathrm{dipole}} = 0$. The sign of the dipole contribution Δ_{CT} depends on the direction in which the charge transfer takes place.

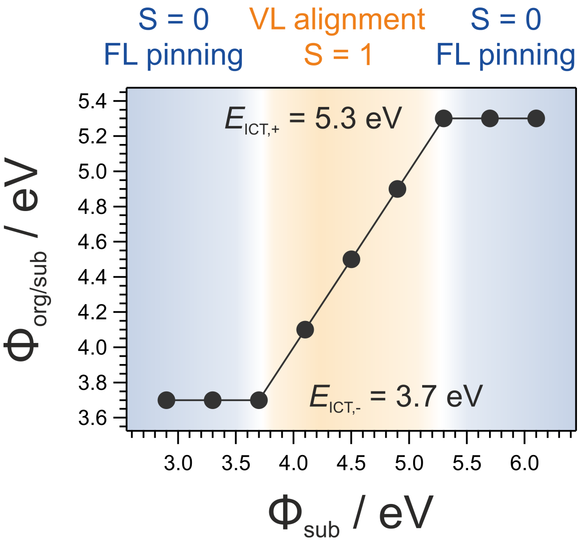

Figure 1.12: Predicted relation between the work function of the hybrid-molecule system and the initial work function of the pristine susbtrate for fixed ICT state energies (same molecule). Blue shaded areas highlight regions where charge transfer pins the frontier orbitals to the Fermi level, resulting in a constant Φ, while no charge transfer occurs in the orange region. Concept adapted from [71].

In case of electron transfer into the molecular adlayer (back-donation), it would increase the interface dipole, hence it would be positive, while in the case of no charge transfer it would simply be zero. Ultimately, this dipole shifts the crossing ICT states towards the Fermi level keeping them fixed at E_{F}, as presented in Fig. 1.11d,f. Due to this fixed alignment of the frontier states with respect to the Fermi energy, this mechanism is referred to as *Fermi level pinning*. Combining this information with the one from the previous chapter, we find that sweeping the work function Φ_{sub} should result in a step-ramp-like behavior of $\Phi_{\mathrm{org/sub}}$, as it is shown in Fig. 1.12.

In general, the ICT model also provides a good approximation for organic adsorbates on semiconducting surfaces, where a similar universal trend in energy level alignment — driven by potential equilibration — has been observed [101–104]. However, deviations can emerge when the $E_{\mathrm{ICT,-}}$ and $E_{\mathrm{ICT,+}}$ states energetically overlap with the valence and conduction bands, respectively. These deviations arise from the fundamentally different nature of the tunneling charge carriers at passivated metals versus semiconducting surfaces. While in the former case, charges originate from the delocalized free electron gas of the metal, in semiconductors they are strongly localized, being associated with dopants and defects [84, 105].

Due to this localized character, charge transfer across the organic–semiconductor interface leads to the formation of a space-charge region that can extend substantially into the bulk. The resulting electrostatic potential gradient induces band bending [106, 107], thereby contributing to the aforementioned deviations from the idealized ICT scenario.

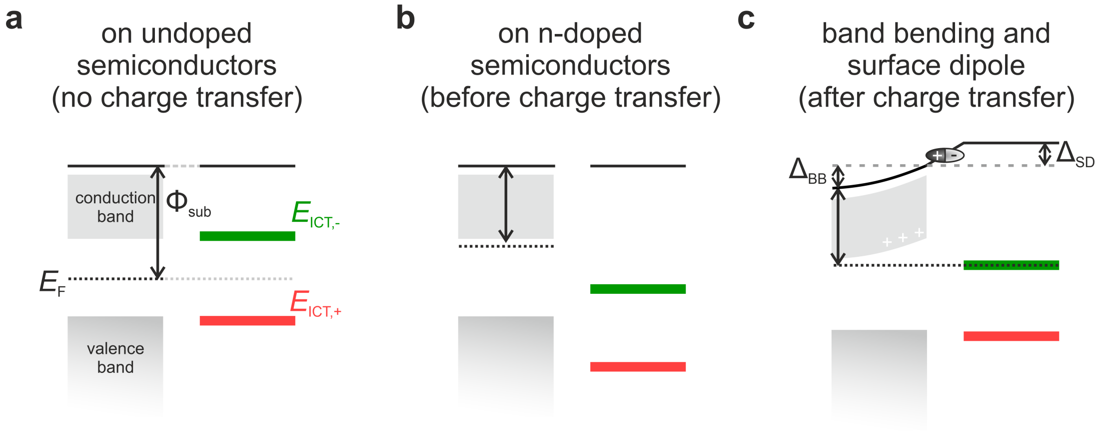

Figure 1.13: Scheme of the ICT model on semiconducting surfaces. Energy diagrams for an OSC (acceptor) on **(a)** an unoped semiconductor without charge transfer, **(b)** an n-doped semiconductor where the LUMO falls below the Fermi level before charge transfer is taken into account. **(c)** When charge transfer takes place, this creates a space-charge region, which results in band bending of the semiconductor bands. Notably, the alignment presented in (b), with one of the frontier orbitals inside the gap between valence and conduction band is referred to as type-II band alignment in semiconductor heterojunctions. This type of alignment is favorable for the formation of interlayer excitions between the inorganic substrate and the organic adlayer with long life times.

Therefore, the interface dipole due to charge transfer on semiconducting substrates Δ_{CT}, is often divided into a band bending contribution Δ_{BB} (*i.e.*, the long-range potential variation within the bulk) and a surface dipole contribution Δ_{SD}. A sketch of the energy level alignment, illustrating these phenomena on top of undoped as well as an n-doped semiconductors, is shown in Fig. 1.13.

Note that a limited availability of charge carriers, *e.g.* due to insufficient concentration of dopants, can also restrict charge transfer and reduce band bending, thereby further altering the energy level alignment [84, 106].

While the ICT model can reliably predict the occurrence of charge transfer on passivated metal surfaces, it does not provide intuitive access to the amount of charge that is transferred and how this charge is distributed. To address this problem and in agreement with experimental findings, Hurdax *et al.* have proposed a simple capacitor model [108, 109].

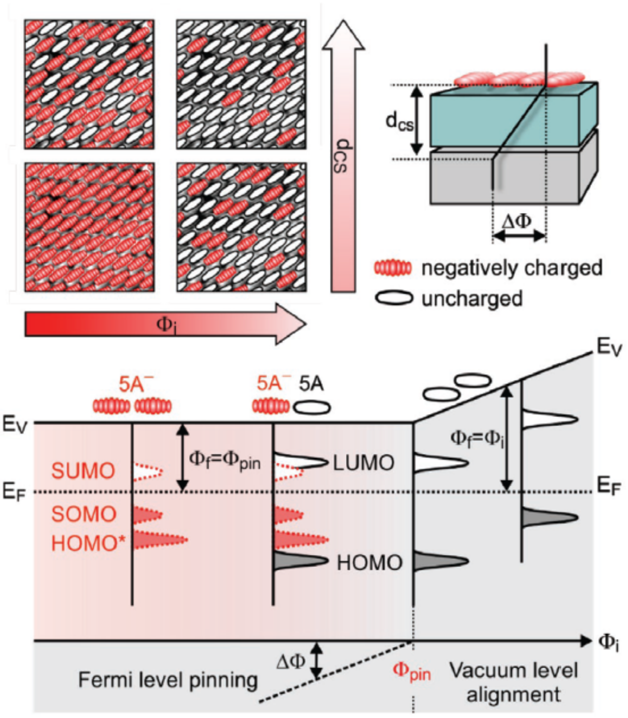

Figure 1.14: Relation between integer charge transfer and energy level alignment at interfaces with thin dielectric films on metallic surfaces. In order to achieve Fermi level pinning, an equilibrium distribution of charged and uncharged molecules established at the surface. This behavior is described by the capacitor model, which considers the potential difference across the dielectric film ($\Delta\Phi$), and the charge separation distance (d_{CS}). By modifying the work function of the dielectric barrier, it is possible to transition from integer charged molecules to neutral molecules, *i.e.*, from Fermi level pinning to vacuum level alignment. Reproduced from [108], licensed under CC BY 4.0.

Within the capacitor model it is assumed that both charged and neutral molecular species can coexist on the surface and that their balance controls the potential equilibration in the Fermi level pinning regime. Hence, when the initial work function of the substrate Φ_{sub} is modified beyond its critical values where charge transfer is activated ($E_{\mathrm{ICT,-}} > \Phi_{\mathrm{sub}}$ or $E_{\mathrm{ICT,+}} < \Phi_{\mathrm{sub}}$), a gradual variation in the ratio of charged and uncharged molecules sets in. This variation is proportional to the potential difference across the dielectric thin film induced by the charged molecules, expressed by $\Delta\Phi = \Phi_{\mathrm{org/sub}} - \Phi_{\mathrm{sub}}$.

On a macroscopic level, this behavior resembles the electrostatic relation of a capacitor:

$$\Delta\Phi = \frac{\sigma(d_{\mathrm{diel}} + d_0)}{\epsilon_0\epsilon_r} = \frac{\sigma d_{\mathrm{cs}}}{\epsilon_0\epsilon_r}. \tag{1.7}$$

Here $\Delta\Phi$ is in eV and σ, the homogeneous 2D charge density induced by the molecular monolayer, is in C × cm^{-2}. The latter is given by n/A, where n is the fraction of charged molecules ($n_{\mathrm{charged}}/n_{\mathrm{total}}$) and A the area per molecule; both quantities are experimentally accessible. The dielectric constant of the dielectric barrier is given by ϵ_r and ϵ_0 is the vacuum permittivity. The parameter d_{cs} describes the charge separation distance, which is given by the thickness of the dielectric film d_{diel} and d_0, the height of the transferred charge (and its mirror) above (below) the dielectric. A summary of the capacitor model is presented in Fig. 1.14.

This model describes well systems, where charges originate predominantly from the underlying metal, but is less suitable for systems where defects or gap states define the electronic properties [105, 108].

1.4.3 Weak Chemisorption: The Induced Density of Interface States (IDIS) Model

The previously discussed models have solely focused on the energy level alignment of organic-based interfaces, where chemical bonds, *i.e.* the hybridization of wave functions is negligible. While this approximation is generally valid when the substrate is non-conductive, hence, it does not have any states available for hybridization in the energy range of the molecular frontier orbitals and the resulting molecule-substrate distance is large, this approximation is usually not applicable for *in situ* prepared organic films atop clean metal surfaces.

Already in early studies by Hill *et al.* [85], probing the frontier electronic structure of various molecules atop a variety of metal surfaces, clear deviations from the expected slopes of $S = 1$ (vacuum level alignment) or $S = 0$ (Fermi level pinning) were revealed. It was observed that in most cases the extracted slope parameter would lie somewhere in between these ideal values of $S = 0$ and $S = 1$, taking on seemingly continuous values within this range [85].

In order to understand this phenomenon, one has to consider that in the case of metals, a significant amount of DOS is present near the Fermi level and thus, when looking from the perspective of the Newns-Anderson model, hybridization between those states and the frontier molecular orbitals is likely to occur. Based on this model (see Details in Section 1.4.5), it follows that weak or moderate chemical interaction between the molecule and the substrate will cause a Lorentzian broadening of the molecular levels, creating a local DOS in the HOMO-LUMO gap.

Based on this local *induced density of interface states* (IDIS), Vazquez *et al.* proposed the so-called IDIS model of energy level alignment, which takes into account weak to moderate hybridization effects between metal surfaces and the organic adlayer [110, 111].

Due to the continuity of electronic states in the former gap, fractional charge transfer for any value of Φ_{sub} is enabled, not being restricted by a critical work function value, where the frontier states cross the Fermi level. Instead, according to the IDIS model, charge transfer will take place until E_{F} of the metal aligns with the so-called *charge neutrality level* (CNL) of the molecule. The CNL is defined as the energy up to which the DOS of the adsorbate must be integrated in order to obtain the amount of charge in the neutral molecule. For each molecule the CNL is calculated by imposing charge neutrality conditions: the total electronic charge below the CNL integrates to the number of occupied molecular states [112].

Importantly, the CNL does not describe the molecular charge transfer after contact, it rather presents the organic Fermi level for the molecule in proximity to a metal before charge transfer is considered [111].

Within the IDIS model, it is possible to break down the energy level alignment into two main steps. In the first step, the molecule approaches the surface and the emerging interface dipole as well as polarization effects result in a provisional energy level alignment of the Fermi level and the frontier molecular levels.

In a second step, the system will relax through charge transfer attempting to align E_F and CNL. The direction of charge transfer is determined by the relative position of E_F and CNL. If the CNL lies above the Fermi energy, electrons will flow from the molecule to the metal (donation), and if the CNL falls below E_F, electrons will flow from the metal to the molecular adsorbate (back-donation). In either case, the dipole $\mathit{\Delta}_\mathrm{CT}$ set up by the charge rearrangement will tend to bring the CNL closer to E_F. The final dipole across the interface is given via $\mathit{\Delta}_\mathrm{tot} = \mathit{\Delta}_\mathrm{push} + \mathit{\Delta}_\mathrm{CT} + \mathit{\Delta}_\mathrm{dip}$.

How closely the CNL and Fermi level are able to align depends on the available density of states near E_F, determining how much charge can be accommodated. This availability is described by the Screening parameter $S = \mathrm{d}\mathit{\Phi}_\mathrm{org/sub}/\mathrm{d}\mathit{\Phi}_\mathrm{sub}$, which captures how the work function changes upon molecular deposition, depending on the initial work function of the substrate. In terms of the IDIS model, the screening parameter S is further defined as $S = \frac{1}{1+4\pi e^2 D(E_\mathrm{F})\delta}$, where $D(E_\mathrm{F})$ is the density of gap states at the Fermi energy, and δ is the effective distance between metal and OSC. The additional dipole due to charge transfer from or to the IDIS is $\mathit{\Delta}_\mathrm{CT} = (1 - S)(\mathit{\Phi}_\mathrm{sub} - \mathit{\Delta}_\mathrm{push} - E_\mathrm{CNL}))$. We consider $\mathit{\Delta}_\mathrm{CT}$ to be positive when electrons are transferred from the metal to the molecule. Combining the charge transfer dipole with the previous dipole contributions yields $\mathit{\Delta}_\mathrm{tot} = \mathit{\Delta}_\mathrm{push} + \mathit{\Delta}_\mathrm{CT} = (1 - S)(\mathit{\Phi}_\mathrm{sub} - E_\mathrm{CNL}) + S \cdot \mathit{\Delta}_\mathrm{push}$.

A screening parameter of $S = 0$ indicates that the DOS is sufficiently large to accommodate or provide all the charge necessary to align the CNL and E_F through charge transfer $D(E_\mathrm{F}) \rightarrow \infty$ in the second definition of S). In this situation, a change in the substrate work function $\mathit{\Phi}_\mathrm{sub}$ will result in no appreciable shift of E_F with respect to CNL, since charge transfer will produce an opposite dipole that exactly compensates for the work function shift. In such a scenario, one says the molecule is pinned to the Fermi level.

Conversely, a screening parameter of $S = 1$ indicates a total absence of IDIS, meaning there is no DOS in the molecular gap, and thus no charge flow that could align the CNL and E_F ($D(E_\mathrm{F}) \rightarrow 0$). A change in work function will simply shift E_F within the gap by the same amount, yielding a slope parameter of $S = 1$. A scenario where $S = 1$ and $\mathit{\Delta} = 0$ (vacuum level alignment) corresponds to the previously described Schottky-Mott limit [72, 111, 113].

In practice, IDIS modelling of an interface is carried out in four steps [71]:

1) The renormalized molecular orbitals are obtained using a suitable theoretical or a mixed experimental-theoretical approach.

2) After obtaining the molecular orbitals and corresponding energies, the IDIS at the organic/metal interface is calculated. Considering only interaction between molecular orbitals and the metal states located close to the Fermi level, the Lorentzian energy broadening $\mathit{\Gamma}_i$ due to hybridization for each molecular orbital energy E_i is calculated.

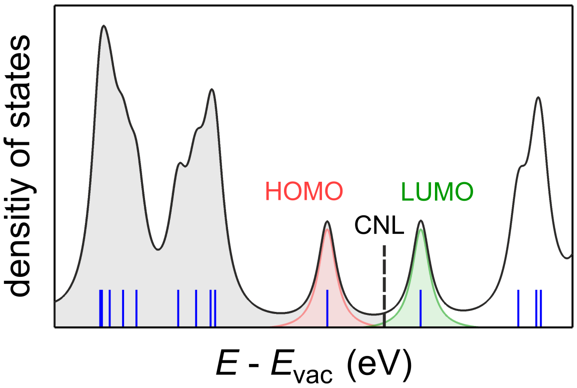

Figure 1.15: Basic concept of the IDIS model. Blue bars represent the energies of molecular orbitals. Applying Lorentzian broadening to the indicated states results in a set of resonance that, when summed up, create the IDIS. Peak areas that correspond to the HOMO and LUMO are highlighted in red and green, respectively. The CNL is marked by the black dashed line.

3) The total DOS for the organic molecule is obtained by adding the broadened contributions from all the molecular orbitals. The broadening will strongly depend on the molecule-substrate distance δ, and the broadening itself ultimately affects the DOS $D(E_{\mathrm{F}})$. Hence, the slope parameter S depends both directly and indirectly on δ, explaining how even small variations in the substrate-molecule distance can evoke large modifications in S, and hence in the energy level alignment.

4) Having obtained the now-modified DOS for the molecules at the interface, the final step in the IDIS model is to calculate the CNL by imposing charge neutrality conditions, resulting in the final IDIS, exemplary depicted in Fig. 1.15.

1.4.4 Strongly Chemisorbed Interfaces: Density Functional Theory and Beyond

Having discussed the physisorption and weak chemisorption regimes—where organic molecules retain their electronic and structural integrity to a large extent, we now turn to the final and most complex case: strong chemisorption. While physisorption is governed by weak van der Waals forces and weak chemisorption already introduces limited hybridization and charge transfer, strong chemisorption involves the formation of true chemical bonds between molecular orbitals and substrate states. This can lead to a profound reorganization of the molecular frontier levels, and even a breakdown of the molecular identity. The molecule is no longer simply adsorbed, but instead a hybridized interface is formed with the substrate.

Despite many efforts to describe this regime within generalized models of level alignment, strong chemisorption remains the least tractable and most system-specific interaction regime. No universal model exists that can reliably predict the interfacial electronic structure in this case, and the conceptual tools that work in the weak-coupling limit often fail entirely.

One of the primary obstacles in understanding strong chemisorption is the alteration of the molecular structure itself. Strong chemical bonding can significantly modify both the geometry and the electronic properties of the adsorbed molecules [114]. These changes are rarely uniform and often affect only specific regions of the molecule — typically those in direct contact with the substrate — resulting in local distortions, symmetry breaking, and in some cases a complete reorganization of the frontier orbitals. In addition to molecular deformation, such interactions frequently induce changes in the substrate itself. While weakly bound systems may exhibit only subtle surface relaxations [88], strong chemisorption can lead to much more pronounced effects — including significant atomic rearrangements and even large-scale surface reconstructions [115] — as the molecule perturbs both the local electronic environment and the atomic structure of the surface.

A particularly striking example is C_{60} on TM surfaces like Cu(111) or Fe(100), where the fullerene does not only adsorb on a flat surface, but instead induces the formation of nanoscale indentations, effectively embedding itself into the substrate [116, 117]. Such reconstructions cannot be anticipated from weak-coupling models and dramatically alter the nature of the interface. These structural responses, on both sides of the interface, are highly system-specific and depend sensitively on the chemical identity of the adsorbate and the surface.

In addition to these structural transformations, strong chemisorption often gives rise to electronic changes that are not easily anticipated. For example, in the case of nickel porphyrins (NiTPP) on Cu(100), hybridization leads not only to a broadening of the LUMO, but to a partial occupation of several higher-lying unoccupied orbitals, including the LUMO+3 [114]. Such behavior is clearly incompatible with models based on rigid level alignment, which assume weak perturbations to the molecular spectrum.

Finally, hybridization in the strong coupling regime may also be subject to more subtle constraints: recent studies have shown that the formation of hybrid interface states depends not only on energy and spatial overlap, but also on momentum compatibility between molecular orbitals and the substrate band structure [118, 119]. While this momentum matching is not a dominant factor in most systems, it adds an additional layer of selectivity that becomes relevant for large, delocalized orbitals with well-defined momentum patterns — such as those found in planar π-conjugated molecules [118, 119]. These combined effects (local structural rearrangement, orbital reordering, and momentum-selective hybridization) highlight why strong chemisorption remains fundamentally difficult to describe using universal models.

Given these complexities, computational methods, like DFT, have become indispensable tools for studying chemisorbed interfaces [95, 114, 120]. DFT allows detailed insights into electronic structure and energy alignment, usually far beyond the reach of empirical or qualitative models, treating each interface on its own terms, accounting for the precise atomic structure, charge redistribution, and hybridization patterns. In particular, DFT enables the prediction of structural relaxation, charge transfer, and orbital hybridization effects that empirical models cannot capture.

However, DFT is not a universal solution. One of its intrinsic limitations is a systematic underestimation of the energy gap between occupied and unoccupied states. This is not a result of poor parameter choices, but a fundamental shortcoming of the method itself [121, 122]. It affects both inorganic semiconductors and organic molecules and leads to HOMO–LUMO gaps that are significantly smaller than experimental values. While such deviations may be acceptable for qualitative insights, they limit the predictive power of DFT in accurately determining level alignment, dissociation energies of molecular ions, and charge transfer processes at interfaces [123].

Moreover, the mean-field character of DFT imposes additional limitations, particularly in systems where electron correlation plays a significant role. A prominent example is the failure to accurately describe materials with localized electronic states, such as the partially filled *d*-orbitals of transition metals. In such cases, many-body effects beyond the standard DFT treatment can critically shape the electronic structure at the interface. More advanced approaches like *dynamical mean-field theory* (DMFT) are designed to capture such phenomena, but their computational cost and the lack of detailed experimental input often preclude their use in realistic interface models [124]. As a result, correlated materials remain challenging to describe reliably within theoretical frameworks. Details about the theoretical framework and the DFT methodology used in this thesis are given in Section 2.3.

Despite the complexity of molecule–metal interfaces involving large organic adsorbates, and the practical as well as conceptual limitations of first-principles methods, simplified theoretical models continue to play a valuable role. While they do not capture the full structural or electronic richness of extended systems, such models offer an intuitive and often mathematically rigorous framework for understanding key aspects of chemisorption [45, 46, 125]. One of the most influential examples is the aforementioned Newns–Anderson model, originally developed to describe the interaction of single atomic adsorbates with metallic surfaces.

Although its original scope does not include large π-conjugated molecules, the model nonetheless captures the essential physics of level hybridization, spectral broadening, and energy renormalization at these interfaces [95, 126, 127]. As such, it provides a microscopic foundation for interpreting adsorption-induced changes in the electronic structure. In this thesis, we revisit and empirically adapt the Newns–Anderson model, with the aim of describing molecule–metal coupling in systems involving large organic adsorbates, where strong chemisorption and electron correlation render the original atomic assumptions insufficient.

1.4.5 The Newns–Anderson Model: Hybridization and Resonance Formation

The Newns–Anderson model describes the hybridization of a single adsorbate orbital, arising from an atom or molecule, with the continuum of states at a solid surface [45]. It provides a physically transparent and analytically tractable framework for understanding how a discrete adsorbate state $|a\rangle$ with energy ε_a evolves when interacting with a continuum of metallic states $|k\rangle$, where $k = 1, 2, \ldots, n$ [33].

The following expression defines the Hamiltonian for the adsorbate–metal system in second quantization [45]:

$$\hat{H} = \varepsilon_a \, \hat{c}_a^\dagger \hat{c}_a + \sum_k \varepsilon_k \, \hat{c}_k^\dagger \hat{c}_k + \sum_k \left(V_{ak} \, \hat{c}_k^\dagger \hat{c}_a + V_{ak}^* \, \hat{c}_a^\dagger \hat{c}_k \right), \tag{1.8}$$

The projection of the DOS on the adsorbate orbital is given by:

$$n_a(\varepsilon) = \sum_i |\langle \phi_i | a \rangle|^2 \delta(\varepsilon - \varepsilon_i), \tag{1.9}$$

where $|\phi_i\rangle$ and ε_i are the eigenstates and eigenvalues of the full Hamiltonian [33]. Newns realized that this expression could be recast following the conceptual work by Anders, as [33, 45]:

$$n_a(\varepsilon) = \frac{1}{\pi} \cdot \frac{\Delta(\varepsilon)}{(\varepsilon - \varepsilon_a - \Lambda(\varepsilon))^2 + \Delta(\varepsilon)^2}, \tag{1.10}$$

where $\Delta(\varepsilon) = \pi V^2 \rho_m(\varepsilon)$ is the weighted DOS of the metal and $\Lambda(\varepsilon)$ its Hilbert transform ($\rho_m(\varepsilon)$ is the metal DOS):

$$\Lambda(\varepsilon) = \frac{\mathcal{P}}{\pi} \int \frac{\Delta(\varepsilon')}{\varepsilon - \varepsilon'} \, d\varepsilon'. \tag{1.11}$$

In the case of a constant metal DOS, *i.e.* $\rho_m(\varepsilon) = \text{const.}$, $\Lambda(\varepsilon)$ vanishes and the adsorbate state is described by a Lorentzian distribution:

$$n_a(\varepsilon) = \frac{1}{\pi} \cdot \frac{\Delta_0}{(\varepsilon - \varepsilon_a)^2 + \Delta_0^2}, \tag{1.12}$$

Hence, coupling to the continuum of metal states results in a finite lifetime, leading to a broadened but unshifted adsorbate resonance, as assumed in earlier sections.

If the DOS is a broad semi-ellipse, which is generally a valid approximation for *sp*-bands, the above formula Eq. (1.10) describes the same broadening, however, the finite width of the DOS now induces an additional downward shift (to higher binding energies) of the adsorbate resonance. Notably, this renormalization process corresponds to the first step in the *d*-band model, capturing the interaction between the adsorbate level and the metal *sp* bands. The correct resonance energy ε_{res} is found by solving:

$$\varepsilon_{\text{res}} = \varepsilon_a + \Lambda(\varepsilon_{\text{res}}),^{\dagger} \tag{1.13}$$

which is done graphically in Fig. 1.16a.

In contrast, when solving Eq. (1.13) for a sharp and narrow semi-elliptic DOS, characteristic of *d*-bands, the resonance condition may yield multiple solutions, resulting in a split lineshape of the adsorbate-projected DOS (see Fig. 1.16b).

[†] Alternatively, due to the linearity of the Hilbert transform, an equivalent expression of this equation is $\frac{1}{V^2}(\varepsilon - \varepsilon_a) = \Lambda_{\text{DOS}}(\varepsilon)$, where $\Lambda_{\text{DOS}}(\varepsilon)$ is the Hilbert transform of the actual metal DOS $\rho_m(\varepsilon)$.

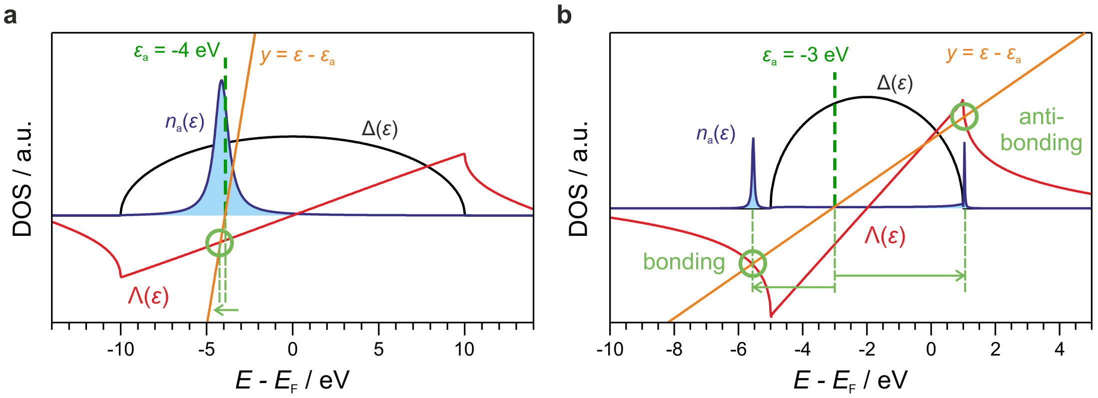

Figure 1.16: Projected DOS $n_a(\varepsilon)$ for an adsorbate state coupled to a surface with a semielliptic DOS. **(a)** Coupling to broad *sp*-like states leads to a renormalization of the adsorbate resonance, shifting it to lower energies. **(b)** A sharper surface DOS resembling narrow *d*-bands results in multiple intersections between the Hilbert transform of the metal DOS and the adsorbate function, indicating a splitting into bonding and antibonding resonances. Concept adapted from [33].

This splitting is a direct consequence of hybridization and reflects the formation of bonding and antibonding hybrid states, analogous to the level scheme in molecular orbital theory [67], and serves as an unambiguous fingerprint of strong chemical bonding. While the Newns–Anderson model is not directly applicable to extended organic molecules, where spatial variations typically prevent a uniform description of coupling, its underlying physical principles remain valid. In this thesis, the Newns–Anderson framework is therefore employed as a conceptual tool to interpret key aspects of hybridization, particularly in comparison with first-principles results from DFT and beyond.

2 Experimental Methods

2.1 Sample Preparation and Surface Characterization

2.1.1 Thin Film Deposition

One of the fundamental requirements of nanoscience — and of advancing technological applications more broadly — is the ability to fabricate thin films with precise control over growth down to the atomic scale. This capability is particularly crucial in the context of the perpetual miniaturization in technology, as famously anticipated by Moore's law [128, 129]. Among the most established approaches to achieve such atomically controlled growth is the thermal evaporation of materials, a concept devised already in 1850 by Michael Faraday [130, 131]. In this process, a material (typically in solid or liquid form) is transformed into the vapor phase by the addition of thermal energy [132]. The vapor subsequently condenses onto a suitably prepared substrate, enabling the bottom-up fabrication of heterostructures and layered devices [132, 133]. In the following, we will briefly discuss two of the most prominent thermal evaporation techniques, both of which have been employed for thin film fabrication in the present thesis: electron-beam (e-beam) evaporation and Knudsen cell evaporation. These methods represent widely used standards for the controlled growth of high-quality thin films in surface and interface science.

Beam Evaporation: Focused Energy for Precision Growth

Electron beam (e-beam) evaporation is a physical vapor deposition technique that utilizes a high-energy electron beam to evaporate source materials under *ultra-high vacuum* (UHV) conditions. The electrons, generated by thermionic emission from a filament are accelerated by an electric field, directing them onto the target material, as depicted in Fig. 2.1. The localized heating causes the material to melt and vaporize. The resulting particle vapor is ejected from the evaporator cell and ultimately condenses on a substrate to form a thin film. Instead of the presented rod-like evaporant, also evaporation from a crucible containing the evaporant is possible. The crucibles for e-beam evaporation are usually made from metals with extremely high melting points such as molybdenum or tantalum.

This method is particularly advantageous for depositing materials with high melting points, such as metals, ceramics, and oxides, which are challenging to process using conventional thermal evaporation. The high energy of the electron beam allows for rapid evaporation, while the vacuum environment minimizes contamination and ensures high-purity films. Before the evaporator is used for thin film preparation, it undergoes thorough degassing by operating under low evaporation conditions for several hours. Additionally, the evaporators are water-cooled to prevent heating

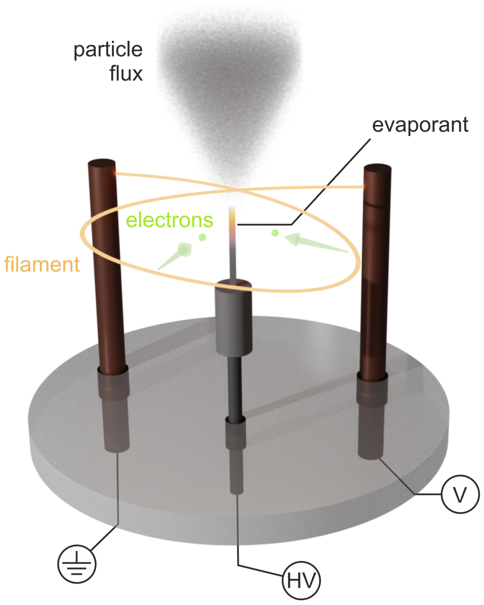

Figure 2.1: Sketch of the key components of an electron beam evaporator.

of the surrounding metal parts and to minimize thermally induced desorption of unwanted gas particles.

Key benefits of e-beam evaporation include precise control over the deposition rate, film thickness, and uniformity. By carefully tuning parameters such as beam current, substrate temperature, and deposition rate, it is possible to achieve films with excellent crystallinity and minimal defects. Throughout the growth, the current produced by some of the ionized particles of the evaporant can be used to monitor the deposition rate.

Organic Sublimation: Knudsen Cell Evaporation

The deposition of organic materials requires a different approach due to their lower thermal stability compared to inorganic compounds. Knudsen cell evaporation, a specialized technique for organic sublimation, offers a gentle yet effective means of depositing thin films of organic molecules.

Knudsen cells operate on the principle of thermal sublimation. The organic material, typically in powder form, is placed in a small crucible inside the Knudsen cell. The cell is resistively heated to a temperature high enough to induce sublimation without decomposition. The resulting vapor exits the cell through a small orifice and travels to the substrate, where the molecules adsorb onto the surface and form a thin film.

One of the key advantages of Knudsen cell evaporation is its ability to preserve the molecular structure of organic compounds during deposition. This makes it an indispensable tool for the creation of devices that utilize organic semiconductors, where the integrity of the material determines device performance. Furthermore, the low deposition rates typical of this technique enable controlled layer-by-layer growth, which is essential for creating heterostructures and interfaces with monolayer precision.

Complementary Roles and Applications

While e-beam evaporation and organic sublimation serve different material classes, their combined use often proves synergistic in advanced material fabrication. For instance, e-beam evaporation can be used to deposit metallic contacts or metal oxide buffer layers, while Knudsen cell evaporation is ideal for depositing the active organic layers in devices such as organic photovoltaics or LEDs. The integration of these techniques enables the precise engineering of high-quality films and multilayer systems, where both inorganic and organic components are essential.

2.1.2 Auger Electron Spectroscopy (AES)

Auger electron spectroscopy (AES) is a widely used technique for analyzing the elemental composition of surfaces with remarkable sensitivity and specificity. The method is based on the detection of Auger electrons, which are emitted through a multi-step electronic relaxation process known as the Auger effect. The effect is named after Pierre Victor Auger [134], who first observed and explained the respective phenomenon, although there exists some controversy about possible overlooked contributions by Lise Meitner [135, 136]. The Auger process and the corresponding energy diagram are depicted in Fig. 2.2. It occurs when an atom, excited by an incident electron beam (or by light), undergoes a core-level ionization of the X shell ($X = \mathrm{K}$ in Fig. 2.2a). To stabilize the ionized state, an electron from a higher energy level $Y\,(\mathrm{L}_1)$ transitions to fill the vacancy, and the excess energy from this transition is transferred to another electron in the Z ($\mathrm{L}_{2,3}$) shell of the atom (Fig. 2.2b). The second electron, now energized, is ejected from the atom as an Auger electron. The kinetic energy of the emitted Auger electron is determined by the energy levels of the specific atom from which it originates, leading to the expression [137, 138]:

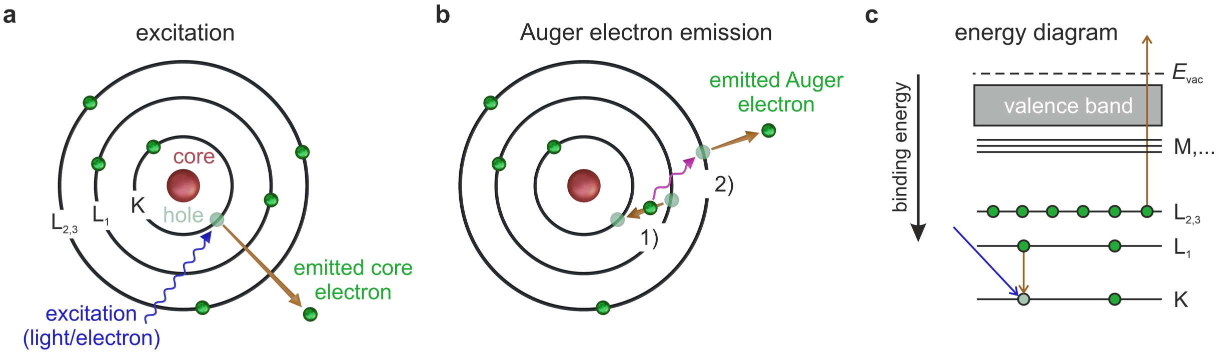

Figure 2.2: **(a)**,**(b)** Principles behind the Auger process and **(c)** the corresponding energy diagram.

$$E_{\mathrm{kin}} = E_X - E_Y - E_Z - \varDelta U - \varPhi, \tag{2.1}$$

where Φ is the work function, and ΔU a correction term accounting for energetic changes due to the doubly ionized final state. An energy diagram illustrating the exemplary KLL Auger process is displayed in Fig. 2.2c. This dependence on atomic energy levels makes the Auger process element-specific, with the exception of hydrogen and helium, which do not produce Auger electrons. By analyzing the kinetic energy distribution of these electrons, AES provides a detailed fingerprint of the elements present at or near the surface of a material. While less straightforward, AES also allows for a qualitative assessment of oxidation states and chemical environments by comparing shifts in peak energies with available reference data sets [139, 140].

AES is typically performed using a focused electron beam to induce the Auger effect, while an electron energy analyzer is used to measure the energies of the emitted Auger electrons. The resulting spectra display sharp peaks corresponding to the characteristic energies of the elements present, enabling qualitative and quantitative surface analysis. Overall, this sensitivity to surface composition makes AES an invaluable tool for the study of thin films, coatings, and surface reactions.

2.1.3 Low Energy Electron Diffraction (LEED)

Low energy electron diffraction (LEED) is a fundamental technique for investigating the atomic structure of crystalline surfaces [138]. The method relies on the diffraction of low-energy electrons, typically in the range of 20–200 eV, when they interact with the periodic arrangement of atoms at a material's surface. For a more comprehensive overview of the method and its theoretical background, see for example refs. [138, 141]. Due to the low penetration depth of these electrons, LEED is highly surface-sensitive, providing information exclusively about the outermost atomic layers of a material.

In a typical LEED experiment, a beam of monochromatic electrons is directed toward the surface of a sample. As the electrons interact with the periodic potential of the surface atoms, a fraction of them is elastically back-scattered, producing a diffraction pattern that reflects the symmetry and periodicity of the surface lattice. This pattern is projected onto a fluorescent screen, where the positions and intensities of the diffraction spots provide direct information about the surface structure, including lattice constants, reconstructions, and adsorbate arrangements. The basic components of a LEED apparatus are depicted in Fig. 2.3a, together with an exemplary LEED pattern in Fig. 2.3b. LEED is particularly powerful for analyzing ordered surfaces, as the sharpness and intensity of the diffraction spots are directly related to the degree of surface order and cleanliness. By comparing experimental diffraction patterns with theoretical simulations, the exact atomic arrangement of the surface can be determined with high accuracy. This makes LEED an indispensable tool in surface science, especially for characterizing surfaces, thin films, and surface reconstructions.

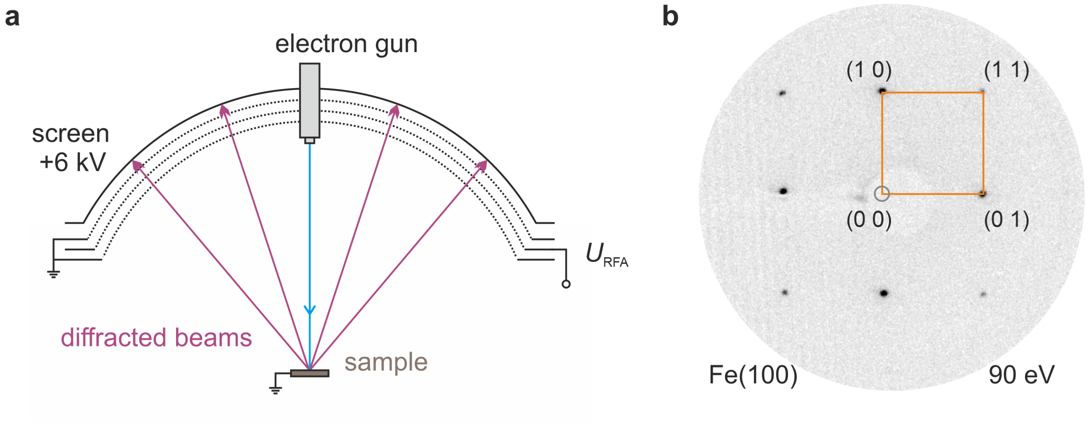

Figure 2.3: Basic principle of a LEED apparatus. **(a)** Schematic depiction of a LEED setup. Redrawn from [138]. **(b)** Exemplary LEED pattern recorded of the square lattice of a Fe(100) surface. The first occurring diffraction spots are indicated, along with the electron kinetic energy used during the measurement.

2.2 Scanning Tunneling Microscopy and Spectroscopy (STM/STS)

The *scanning tunneling microscope* (STM) is one of the most important techniques in modern surface science, revolutionizing the way we experience matter by enabling the visualization of individual molecules and even atoms. Invented by Gerd Binnig and Heinrich Rohrer at the IBM research laboratory in Zürich in 1981, this groundbreaking tool became the flagship technique of nanoscience and earned them the 1986 Nobel Prize in Physics [142].

Beyond its pioneering achievement of resolving surface topographies with sub-Å resolution, STM has evolved into an exceptionally versatile experimental platform [143, 144]. Today, it is not only used to image individual atoms and molecules but also to manipulate them [145, 146], enabling the realization of single-molecule nano-devices [147] and even the atomic control over chemical reactions [148]. A particularly striking extension is the application of an additional radio-frequency AC field to the STM junction, which enables coherent spin control in single-atom electron spin resonance experiments [149]. This merges the atomic spatial resolution of STM with the energy resolution of magnetic resonance spectroscopy. Moreover, by coupling STM with ultrafast laser pulses, time-resolved measurements with simultaneous spatial and temporal resolution become feasible [150, 151]. When combined with synchrotron radiation, STM even reaches chemical sensitivity through *x-ray absorption spectroscopy* (XAS) with atomic spatial resolution [152]. By integrating the dimensions of space, spin, time, and elemental specificity, STM has redefined how we probe and manipulate the fundamental building blocks of materials.

A basic STM consists of several essential components, which are depicted in Fig. 2.4a [142]. At its core is a probe tip, which scans the surface of the sample by measuring the tunneling current generated between the tip and the surface. Precise control of the tip's position is achieved using piezoelectric transducers, which allow movement in three mutually perpendicular directions: x, y, and z. The x and y directions scan the surface laterally, while the z-direction adjusts the distance between the tip and the sample. During measurement, the tip and sample are separated

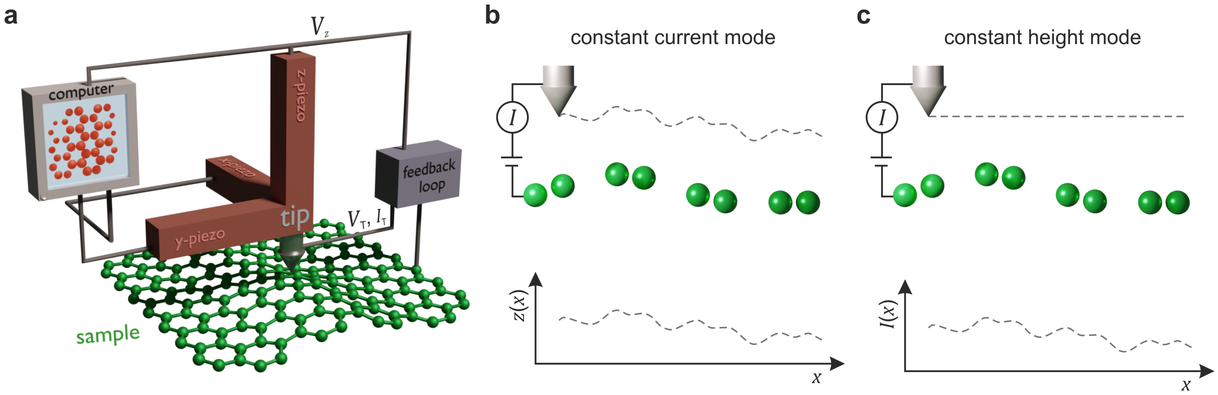

Figure 2.4: Technical realization of a scanning tunneling microscope. **(a)** Illustration of the basic components of an STM. The STM can be operated either in the **(b)** constant current mode, or the **(c)** constant height mode.

by only a few Å, allowing their wavefunctions to overlap [153]. When a bias voltage V is applied between the tip and the sample, a tunneling current (I) is established. The direction of the current depends on the sign of the bias voltage. Conventionally, a positive bias voltage ($V > 0$) corresponds to tunneling from the occupied states of the tip to the unoccupied states of the sample. Conversely, a negative bias voltage ($V < 0$) indicates tunneling from the occupied states of the sample into the unoccupied states of the tip.

In constant current mode (see Fig. 2.4b), the tunneling current is maintained at a constant value by adjusting the z-position of the tip via a feedback loop [142, 153]. When the measured current exceeds a reference value, the feedback loop withdraws the tip; when it falls below the reference, the tip moves closer. This process generates a two-dimensional map of $z(x, y)$, which represents the surface contour [154]. The data can then be visualized as a topographic plot. Alternatively, in constant height mode (see Fig. 2.4c), the z-position remains fixed while the tunneling current is recorded as the tip scans the surface laterally. This method produces a current map, $I(x, y)$, which contains similar information to the constant current mode but is better suited for extremely flat surfaces. It also allows faster data acquisition, as no adjustments to the z-piezo are required [153].

From a quantum mechanical perspective, the tunneling current can be estimated using the principles of tunneling through a potential barrier. For a one-dimensional potential $U(\vec{r}) = U(z)$, the Schrödinger equation is given by [153]:

$$-\frac{\hbar^2}{2m}\nabla^2\psi(\vec{r}) + U(z)\psi(\vec{r}) = E\psi(\vec{r}), \tag{2.2}$$

where $\hbar$ is the reduced Planck constant and m the electron mass. For this expression, the wave function can be separated as:

$$\psi(\vec{r}) = \psi_{\|}(x, y)\psi_z(z), \tag{2.3}$$

and the energy as:

$$E = E_{\|} + E_z, \tag{2.4}$$

where $E_\parallel = \frac{\hbar^2 k_\parallel^2}{2m}$.

Inside the barrier only the decaying term is relevant, thus:

$$\psi_z(z) \propto e^{-\kappa z}, \tag{2.5}$$

where the decay constant κ is:

$$\kappa = \sqrt{\frac{2m}{\hbar^2}(U_0 - E_z)} = \sqrt{\frac{2m}{\hbar^2}\left(U_0 - E + \frac{\hbar^2 k_\parallel^2}{2m}\right)} = \sqrt{\frac{2m}{\hbar^2}(\Phi - E) + k_\parallel^2}. \tag{2.6}$$

Close to E_F and for small applied voltages ($e \cdot V \ll \Phi$), κ determines the rapid decay of the tunneling current with increasing tip-sample distance. This results in an extreme surface sensitivity of STM, with the tunneling current decreasing by an order of magnitude for every 1 Å increase in z [153, 154]. The tunneling of a sample state ψ_n with energy E_n inside the sample, from the metal surface to the tip, is visualized in Fig. 2.5. The work function ϕ represents the minimum energy needed to remove an electron from the metal into vacuum. When a small bias V is applied, electronic states in the sample with energies E_n in the range from E_F to $E_\mathrm{F} - e \cdot V$ can tunnel into the tip, with the transmission probability given by $T = e^{-2\kappa z}$ [153, 154].

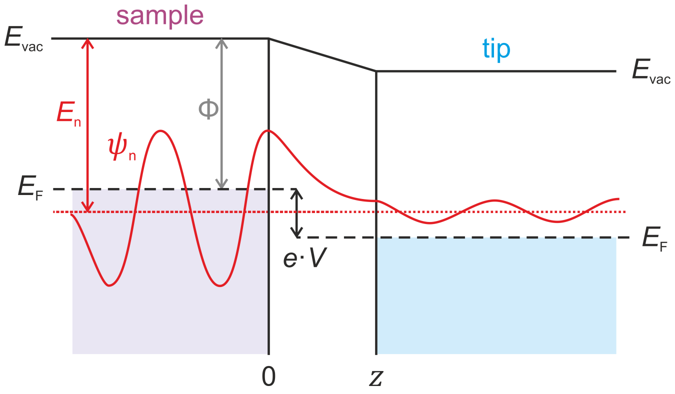

Figure 2.5: Schematic illustration of electron tunneling in scanning tunneling microscopy (STM). A sample state ψ_n with energy E_n tunnels from the sample (left) to the tip (right) through the vacuum barrier. The work function Φ represents the energy required to remove an electron from the metal into vacuum. When a small bias voltage V is applied, electronic states within the energy range $E_\mathrm{F} - e \cdot V$ to E_F contribute to the tunneling current. The probability of tunneling is determined by the decay constant κ. Adapted from [153].

Probing the Electronic Structure in STS

For a more detailed description of the tunneling process, Bardeen's tunneling theory provides the foundation for the widely-used Tersoff-Hamann model [153, 155]. This model approximates the STM tip as a spherical potential well with a radius of curvature R and a center at $\vec{r_0}$ (see Fig. 2.6) [155]. The distance between the tip and the sample is defined by the parameter d. In this framework, the tip wavefunction is treated as an s-wave, simplifying the calculation of the tunneling current. The model predicts that the tunneling conductance ($G = I/V$) is proportional to the *local density of states* (LDOS) at E_F and $\vec{r_0}$:

$$G \propto \rho(E_\mathrm{F}, \vec{r_0}), \tag{2.7}$$

where $\rho(E_\mathrm{F}, \vec{r_0})$ is the LDOS at the Fermi energy and tip position $\vec{r_0}$ [153, 155].

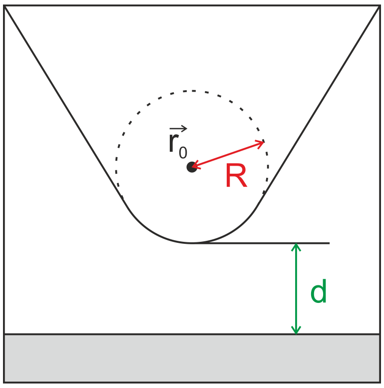

Figure 2.6: Schematic representation of the tip-sample geometry in the Tersoff-Hamann model [155]. The tip is approximated as a locally spherical structure with radius R centered at position $\vec{r_0}$. The dashed circle represents the effective curvature of the tip. The tip-sample separation is denoted d. Adapted from [155].

Under specific conditions — such as a spherically symmetric tip state, a constant tip density of states over the energy range of interest, and minimal variation of the sample LDOS within $k_\mathrm{B}T$ — the Tersoff–Hamann model can be extended to finite bias [153], *i.e.*:

$$G \propto \rho(E_\mathrm{F} - e \cdot V, \vec{r_0}). \tag{2.8}$$

Consequently, STS allows for the measurement of the energy-resolved local density of states (LDOS), by recording the differential conductivity as the applied bias voltage is swept across a defined range [156, 157]. However, careful background subtraction is essential for ensuring quantitative accuracy of the spectra. Normalizing $\mathrm{d}I/\mathrm{d}V$ spectra by the measured conductance (I/V) is a simple and effective approach [157], though it does not account for variations in the DOS of the tip [158]. Advanced corrections may be necessary for precise LDOS measurements [159]. By acquiring spatially resolved $\mathrm{d}I/\mathrm{d}V$ maps, STM can directly visualize the real-space distribution of surface electronic states [160, 161], as well as the molecular orbitals of individual adsorbates [90, 162]. In the latter case, the observed intensity patterns can be directly compared to Kohn–Sham orbitals obtained from density functional theory (DFT). It is also important to recognize that STM is inherently sensitivity to electronic states with small in-plane momentum ($k_\parallel$), since the tunneling current is dominated by contributions from states near the $\overline{\Gamma}$-point of the *Brillouin zone* (BZ) [163–165]. This presents a fundamental contrast to photoemission spectroscopy, which accesses a broader momentum range. Awareness of this difference can be crucial when interpreting or correlating data from both techniques.

2.3 Density Functional Theory (DFT)

DFT is one of the most widely used computational methods in quantum mechanics for predicting the electronic properties of atoms, molecules, and solids. It provides an efficient framework for solving the many-electron Schrödinger equation by expressing the total energy as a functional of the electron density.

The Many-Body Problem and the Born-Oppenheimer Approximation

The fundamental challenge in quantum mechanics is solving the time-independent Schrödinger equation for a system of N interacting electrons and M nuclei:

$$\hat{H}\Psi(\mathbf{R},\mathbf{r}) = E\Psi(\mathbf{R},\mathbf{r}), \tag{2.9}$$

where $\mathbf{R}$ represents the nuclear coordinates, $\mathbf{r}$ the electronic coordinates, and $\Psi(\mathbf{R},\mathbf{r})$ is the many-body wavefunction [166]. The full Hamiltonian consists of kinetic and interaction terms:

$$\hat{H} = -\sum_I \frac{\hbar^2}{2M_I}\nabla_I^2 - \sum_i \frac{\hbar^2}{2m}\nabla_i^2 + \sum_{i<j}\frac{e^2}{|\mathbf{r}_i - \mathbf{r}_j|} - \sum_{i,I}\frac{Z_I e^2}{|\mathbf{r}_i - \mathbf{R}_I|} + \sum_{I<J}\frac{Z_I Z_J e^2}{|\mathbf{R}_I - \mathbf{R}_J|}. \tag{2.10}$$

This equation is computationally intractable for large systems. The Born-Oppenheimer approximation simplifies the problem by assuming that nuclei are much heavier than electrons and can be treated as stationary. This reduces the problem to solving the electronic Schrödinger equation in a fixed nuclear potential, involving only the second, third, and fourth terms [167]:

$$\hat{H}_{\text{el}}\Psi_{\text{el}}(\mathbf{r}) = E_{\text{el}}\Psi_{\text{el}}(\mathbf{r}). \tag{2.11}$$

However, even in this simplified form, the many-body electron-electron interaction remains a major computational challenge.

The Hohenberg-Kohn Theorems and the Concept of DFT

DFT replaces the many-electron wavefunction $\Psi(\mathbf{r}_1, \mathbf{r}_2, ..., \mathbf{r}_N)$ with the electronic density $\rho(\mathbf{r})$, reducing the problem from $3N$ dimensions to only three. The foundation of DFT is established by the Hohenberg-Kohn theorems [168]:

> 1) The ground-state electronic density $\rho(\mathbf{r})$ uniquely determines all the ground-state properties of the system, including the total energy and the many-electron wave function.
>
> 2) The exact ground-state electron density minimizes the total energy functional $E[\rho]$ and this variational minimum corresponds to the solution of the Schrödinger equation.

Thus, instead of solving the full Schrödinger equation, one can simply obtain the ground-state properties of an interacting electron system by minimizing $E[\rho]$ with respect to $\rho(\mathbf{r})$. This is the central idea of DFT. However, while the existence of the correct $E[\rho]$ is guaranteed by the Hohenberg-Kohn theorem, its exact form is unknown [169].

The Kohn-Sham Equations

Since the actual form of $E[\rho]$ is not known, Kohn and Sham introduced an auxiliary system of non-interacting electrons that reproduce the same ground-state density as the interacting system [170]. The total energy functional is decomposed as [169]:

$$E[\rho] = T_s[\rho] + E_{\text{ext}}[\rho] + E_H[\rho] + E_{\text{xc}}[\rho], \tag{2.12}$$

where [169]:

- $T_s[\rho]$ is the kinetic energy of the non-interacting electrons,
- $E_{\text{ext}}[\rho]$ is the external potential energy,
- $E_H[\rho]$ is the classical Hartree energy describing electron-electron Coulomb repulsion, and
- $E_{\text{xc}}[\rho]$ is the exchange-correlation energy, which contains all many-body effects beyond Hartree theory.

The Hartree potential treats the electron-electron interaction in a mean-field manner and therefore includes a so-called self-interaction contribution. This leads to a well-known deficiency of DFT: the tendency to over-delocalize electrons. The origin of this self-interaction lies in the fact that the electron described by the Kohn-Sham equation also contributes to the total density, thereby experiencing an unphysical Coulomb interaction with itself. Among other contributions, the attempted correction of this self-interaction error is included in the exchange-correlation functional [169].

The single-particle Kohn-Sham equations take the form [166, 169]:

$$\left[-\frac{\hbar^2}{2m}\nabla^2 + V_{\text{eff}}(\mathbf{r})\right]\psi_i(\mathbf{r}) = \epsilon_i \psi_i(\mathbf{r}), \tag{2.13}$$

where the effective potential is given by:

$$V_{\text{eff}}(\mathbf{r}) = V_{\text{ext}}(\mathbf{r}) + V_H(\mathbf{r}) + V_{\text{xc}}(\mathbf{r}). \tag{2.14}$$

This formulation reduces the many-body problem to a set of single-particle equations, which can be solved self-consistently. However, the quality of the resulting calculations is influenced by how closely the employed exchange-correlation functional approximates the unknown exact one.

Accuracy and Predictive Power of DFT

DFT has been remarkably successful in predicting ground-state properties of molecules and solids, including [171]:

- Total energies and electronic band structures,
- Structural properties such as equilibrium geometries and lattice constants,
- Chemical reactivity and adsorption energies,
- Magnetic properties and spin polarization.

However, the accuracy of DFT depends on the choice of the exchange-correlation functional $E_{\mathrm{xc}}[\rho]$. The most widely used approximations include [167, 169]:

- The *local density approximation* (LDA), which assumes that the exchange-correlation energy at each point in space depends only on the local electron density, as in a uniform electron gas.
- The *generalized gradient approximation* (GGA), which incorporates density gradients for improved accuracy.
- Hybrid functionals, such as B3LYP [172, 173], which mix a fraction of exact Hartree-Fock exchange with GGA exchange-correlation to better capture electron correlation effects.

While DFT provides an excellent balance between accuracy and computational efficiency, it has known limitations, particularly in describing strongly correlated materials, charge transfer excitations, and van der Waals interactions [95, 123, 167]. Extensions such as Hubbard-corrected DFT (DFT+U), the GW approximation, DMFT corrections, and time-dependent DFT (TD-DFT) have been developed to address these shortcomings [60, 124, 174, 175]. In the result chapters, two of these approaches, namely DMFT and DFT+U will be examined in more detail in the context of electron correlation effects at interfaces involving a ferromagnetic Fe surface.

3 Photoemission Techniques for Resolving Electronic Structure

3.1 Photoelectron Spectroscopy (PES)

Photoelectron spectroscopy (PES) is fundamentally based on the photoelectric effect, first observed in 1887 by Heinrich Hertz [176]. Subsequent studies by Hallwachs [177], and Lenard [178] provided further insights, ultimately enabling Albert Einstein to explain the phenomenon in 1905 using the quantum nature of light [179], a concept introduced five years earlier by Max Planck [136]. This discovery marked a major turning point in physics, as it provided direct evidence for the wave-particle duality of light and played a key role in the development of quantum mechanics, formally established in 1926 by Schrödinger [180].

Early attempts to harness the photoelectric effect for analytical applications were hindered by experimental limitations. However, the field experienced a major breakthrough in the 1950s, driven by the work of Kai Siegbahn, who rekindled interest in photoelectron spectroscopy by integrating high-resolution spectrometers into the technique. His contributions paved the way for the development of various spectroscopic methods based on the photoelectric effect, which have since become indispensable for investigating molecules, solids, and surfaces [181]. Recognizing its profound impact on materials science, the Nobel Prize in Physics was awarded in 1981 to Karl Siegbahn for his pioneering work in photoelectron spectroscopy [182]. He not only realized the potential of photoelectrons as a spectroscopic tool but also introduced the concept of *electron spectroscopy for chemical analysis* (ESCA), a milestone that established PES as a cornerstone of modern surface science. Some of its key principles, variants, and applications of PES will be discussed in detail in the following sections.

3.1.1 Core- and Valence-Level Spectroscopy

A schematic overview of a typical PES experiment is shown in Fig. 3.1. By measuring the kinetic energy E_{kin} and emission angles ϕ and θ of photoelectrons emitted after excitation with photons of energy $h\nu$, the binding energy E_{b} of the electrons can be determined via the photoemission equation:

$$E_{\text{kin}} = h\nu - E_{\text{b}} - \varPhi, \tag{3.1}$$

where $\varPhi$ denotes the work function of the material and E_{b} corresponds to the electron binding energy in reference to the Fermi level ($E_{\text{b}} = 0$ at E_{F}) [183].

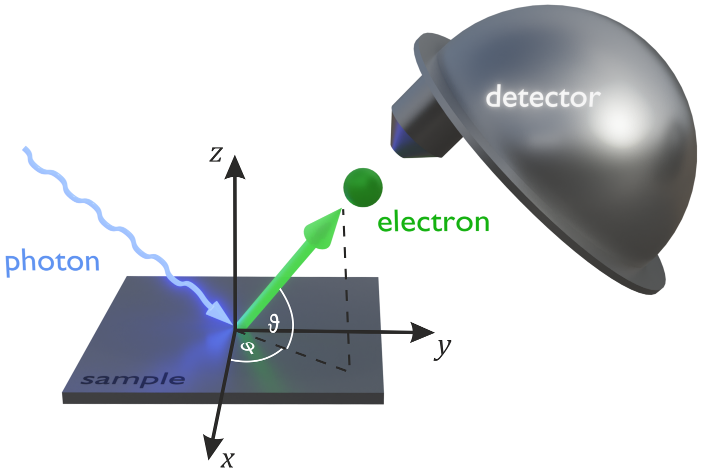

Figure 3.1: Illustration of a standard PES setup.

The relation between the electrons and their energy levels inside a metal, and the corresponding intensity of the photoelectrons as function of the energy $I(E_{\text{kin}})$, the so-called *energy distribution curve* (EDC), is depicted in Fig. 3.2.

The bottom left side sketches the basic spatial distribution of electronic levels inside a typical metal, consisting of strongly localized levels that lie close to the atomic cores (core levels in dark green), and the strongly delocalized valence electrons (light green shaded area) that are allowed to move freely throughout the solid. While the former have rather high binding energies typically ranging from 100 eV to several keV, the latter are located in a rather narrow range of roughly 10 eV below the Fermi energy, which are typically accessed with light sources up to 100 eV [184].

As shown, the EDC is a projection of the density of occupied states $D(E)$ superimposed to a continuous background, which results from inelastically scattered secondary electrons [184]. In general, these electrons can be considered as having lost their initial information about the electronic structure of the solid. However, since the scattering processes are closely linked to the unoccupied density of states, they can, with appropriate theoretical modeling, be exploited to gain insights into the unoccupied electronic structure [185].

According to the different photon energies that are utilized to study either the core or the valnce electrons, PES is generally divided into two different types [183, 184]. The first one is **x-ray photoelectron spectroscopy (XPS)**, which employs x-ray radiation, *i.e.* photons with energies in the range of 100 eV – 10 keV, to probe core-level electrons [183].

These levels appear as sharp peaks at high binding energies in the EDCs and are highly sensitive to the local chemical environment (see Fig. 3.2) [184]. Shifts in core-level binding energies — known as chemical shifts — arise from changes in valence electron density due to processes such as oxidation, reduction, or chemical bonding [138]. For example, oxidation usually shifts core levels to higher binding energies (typically by 1–2 eV) due to reduced screening, while reduction

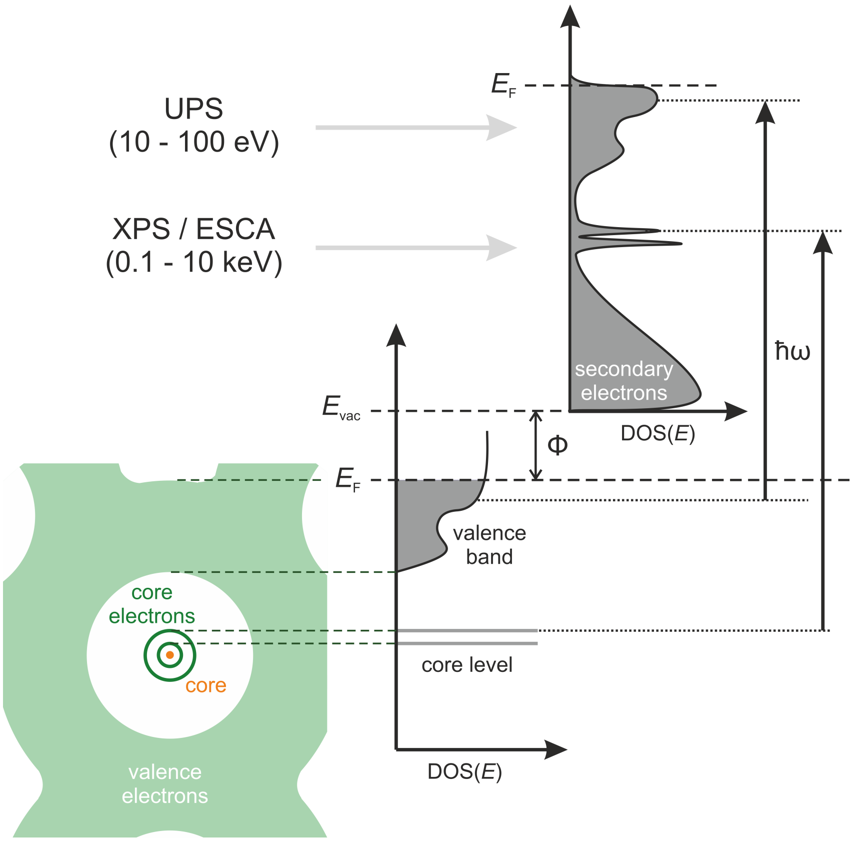

Figure 3.2: Schematic illustration of the relation between the electronic structure of a solid and the EDC obtained in photoemission experiments with a photon energy $\hbar\omega$. The green structure on the left represents the distribution of charge carriers in a solid. Core electrons (dark green) are localized close to the atomic nucleus (core) and form discrete, sharp energy levels. In contrast, valence electrons are more delocalized and contribute to broad energy bands. This underlying electronic structure, shown in the center as a density of states (DOS), is probed in photoemission experiments.

leads to the opposite effect. Such shifts offer a reliable means of distinguishing between metallic and oxidized states in both bulk materials and adsorbed metal-hosting organic complexes [186].

In addition, surface core-level shifts (SCLSs) can occur due to differences between surface and bulk atoms, further extending the information obtainable from XPS [187]. Thanks to its element-specific nature and chemical sensitivity, XPS is widely used to determine composition, oxidation states, and bonding environments [184]. However, the interpretation of spectra can be complicated by overlapping effects, necessitating careful analysis and often theoretical support [138].

In contrast to XPS, **ultraviolet photoelectron spectroscopy (UPS)** utilizes photon energies in the ultraviolet to extreme ultraviolet range ($h\nu \sim 10$–$100\,\mathrm{eV}$), making it particularly well-suited for probing valence electronic states [184].

The measured UPS intensity reflects the energy distribution of occupied states, modulated not only by the DOS but also by transition matrix elements associated with the photoemission process [184, 188, 189]. In systems of weakly-interacting electrons, such as simple metals, the spectral line shape often closely reflects the calculated DOS. However, in materials where electron correlations play a significant role, many-body interactions can substantially modify the spectral features, leading to marked deviations from the ground-state DOS [190].

Beyond providing information on the valence band electronic structure, UPS enables a precise determination of a sample's work function (Φ). By analyzing the secondary electron cutoff, UPS allows for an accurate measurement of Φ [191]. Taken together, these characteristics have established UPS as a standard method for characterizing surface electronic properties and hybridization phenomena at interfaces.

Moreover, when the photoelectron emission angles are resolved — a technique known as *angle-resolved photoelectron spectroscopy* (ARPES) — UPS evolves into a powerful method for mapping the momentum-resolved electronic states. This grants access to one of the most fundamental characteristics of a solid material: its band structure. When combined with pump-probe schemes, time-resolved photoemission enables the exploration of the unoccupied band structure and the dynamics of excited states with femtosecond (fs) and even attosecond (as) time resolution [192, 193]. This ultrafast perspective is essential for studying non-equilibrium phenomena [194, 195], including charge carrier dynamics [196], the relaxation of excitonic excitations [197, 198], and light-induced phase transitions [199].

3.1.2 Three-Step and One-Step Models of Photoemission

A widely used approach for quantitatively understanding the photoemission process and the resulting spectra is the three-step model, introduced by Berglund and Spicer [200, 201]. This model provides a simplified yet effective approximation by dividing the entire process into three independent and sequential stages.

The first step involves the optical excitation of an electron within the solid. According to Fermi's golden rule, the probability of transition between an initial $|\Psi_i\rangle$ and a final state $|\Psi_f\rangle$ is given by [184, 202]:

$$w_{if} = \frac{2\pi}{\hbar} |\langle \Psi_f | \hat{H}^{\text{int}} | \Psi_i \rangle|^2 \cdot \delta(E_{\text{f}} - E_{\text{i}} - h\nu), \tag{3.2}$$

where the operator $\hat{H}^{\text{int}} = \frac{1}{2mc}\left(\vec{A} \cdot \hat{\vec{p}}\right)$ describes the interaction between photon and electron, when local field effects are neglected (valid approximation for lower photon energies) and the δ-function ensures energy conservation [184, 188]. In this model both initial and final state are considered as bands inside the solid. If a dipole transition between two bands is allowed depends on the symmetry of initial and final state and also on the polarization of the incident light [188, 189, 203].

The next step is the propagation of the electron towards the surface. The amount of photoexcited electrons that leave the solid is limited by inelastic scattering, which not only reduces the energy of excited electrons but also makes them lose their initial momentum information (ignoring any potential insight they may carry about the unoccupied states). The decisive quantity for the attenuation is the *inelastic mean free path* (IMFP) λ, which describes the average distance an electron has to travel inside the solid before it scatters inelastically [204]. It is highly dependent on the kinetic energy of the electron, thus, the photon energy but also the binding energy of the investigated electrons have a great influence on the surface sensitivity in PES. The universal curve of the IMFP alongside a selection of the IMFP measured for different metals is shown in Fig. 3.3. The minimum of the curve lies in the range from $50 - 100\,\text{eV}$, where λ is in the order of approximately $2 - 5\,\text{Å}$, which demonstrates why UPS is considered a strongly surface sensitive technique. The third step is the transmission of the electron through the surface into the vacuum, which requires that the final state lies above the vacuum level. As the parallel translational symmetry is conserved during the photoemission process, also the parallel component of the electron's wave vector inside the solid $\vec{k}_{\parallel}^{\text{in}}$ is conserved, and thus $\vec{k}_{\parallel}^{\text{in}} = \vec{k}_{\parallel}^{\text{ex}}$ holds. This relation will be discussed in more detail in the following section (Section 3.1.3).

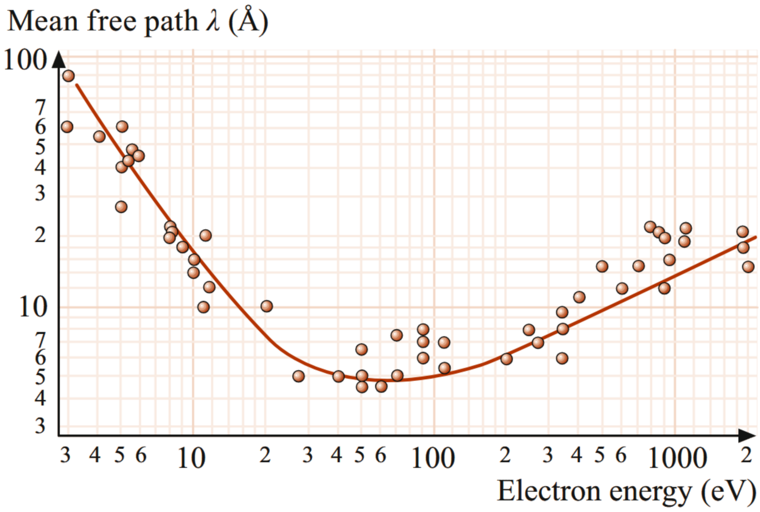

Figure 3.3: Graph of the IMFP as a function of E_{kin}. Often this curve is referred to as universal curve. Reproduced from [205]. © 2023 Springer Nature.

The three-step model provides a valuable description when the three processes do not interfere with each other [206]. In particular, for valence-level spectroscopy, the last two steps are considered less significant, as variations in the photoemission current are mainly determined by the allowed transitions in the solid's band structure [188, 206]. In this model, Fermi's golden rule is applied only to the initial excitation step, treating the subsequent propagation and escape processes separately.

A more rigorous, state-of-the-art, but also more complex approach to calculating photoemission intensities is the one-step model [184]. This formalism accounts for all many-body interactions, including inelastic scattering processes of photoelectrons, providing a quantitative estimation of the photoemission spectral weights [207]. Unlike the three-step model, the one-step approach directly applies Fermi's golden rule to the entire photoemission process, using a more accurate description of the final state. Within the one-step model, the final state is described as a physically accurate time-reversed LEED state. Inside the crystal, it is expressed as a sum of propagating and evanescent Bloch waves, which transition into free-electron-like behavior in vacuum [184]. A direct comparison between the one-step and three-step models is shown in Fig. 3.4.

Notably, under certain approximations, the three-step formalism can be recovered starting from the one-step approach [184]. While applications of the one-step theory to realistic systems have significantly improved in recent years, applying this formalism to more complex systems remains challenging [207].

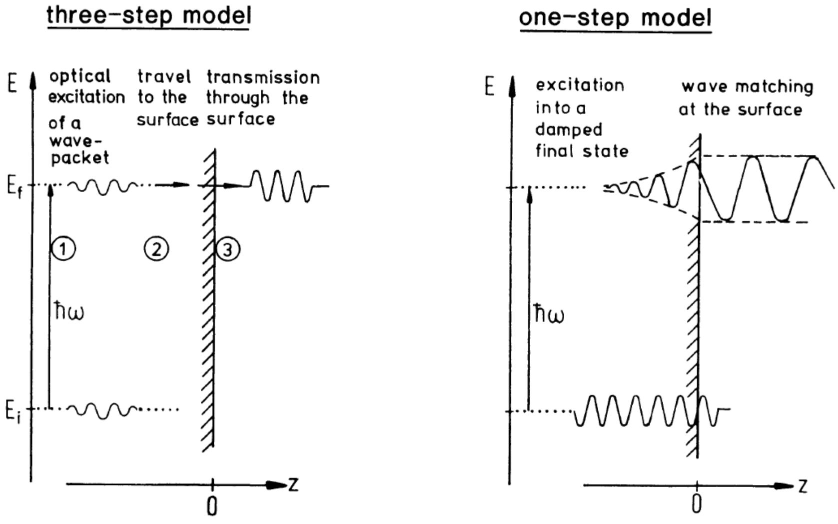

Figure 3.4: Illustration of the three-step and one-step models of photoemission. The three-step model divides the photoemission process into three stages: (1) photoexcitation, (2) electron transport to the surface, and (3) transmission into the vacuum. In the one-step model, all three processes are inherently included in the time-reversed LEED state. Reproduced from [184]. © 2003 Springer Nature.

3.1.3 Angle-Resolved Photoemission and Band Structure Mapping

As indicated earlier, ARPES is the go-to technique for experimentally accessing the band structure of crystalline materials [208, 209]. In the following, we briefly introduce its fundamental principles, beginning with the relationship between the electron's wave vector inside the solid, $\vec{k}^{\text{in}}$, and the detected wave vector of the emitted electron, $\vec{k}^{\text{ex}}$, which is determined from the measured kinetic energy via:

$$E_{\text{kin}} = \frac{\hbar^2 \left(\vec{k}_{\perp}^{\text{ex}^2} + \vec{k}_{\parallel}^{\text{ex}^2}\right)}{2m}, \tag{3.3}$$

where m denotes the electron mass.

The emission angles provide direct access to the momentum components of the emitted electron. The polar angle θ describes the emission direction relative to the surface normal, while the azimuthal angle ϕ defines the in-plane orientation. The corresponding parallel momentum components of the emitted electron are given by:

$$\vec{k}_{\parallel}^{\text{ex}} = \vec{k}^{\text{ex}} \sin(\theta) = \sqrt{\frac{2mE_{\text{kin}}}{\hbar^2}} \sin(\theta) \begin{pmatrix} \cos(\phi) \\ \sin(\phi) \end{pmatrix} . \tag{3.4}$$

This relation establishes how the measured emission angles θ and ϕ determine the electron's momentum components in the surface plane. Fig. 3.1 illustrates this connection, depicting how the emission direction correlates with the momentum components k_x and k_y of the emitted electron.

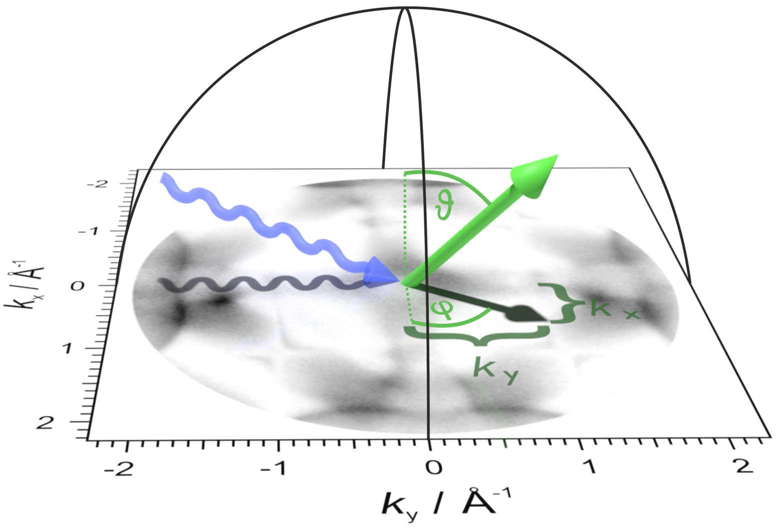

Figure 3.5: Relation between emission angles and momentum components in ARPES. The grayscale map represents the measured photoemission intensity in the k_x-k_y plane at a constant kinetic energy. The blue wavy arrow indicates the incident photon, while the green arrow represents the emitted photoelectron. The k_x and k_y momentum contributions, which are directly linked to the emission direction, are visually highlighted in dark green.

Due to the periodic potential along the surface, the parallel momentum component of the electron is conserved up to a reciprocal lattice vector $\vec{G}_{hk}$:

$$\vec{k}_{\parallel}^{\text{ex}} = \vec{k}_{\parallel}^{\text{in}} + \vec{G}_{hk}. \tag{3.5}$$

This conservation allows a direct mapping of the two-dimensional (2D) surface band structure from the measurable quantities E_{kin}, θ, and ϕ.

While the parallel momentum component is well-defined, the perpendicular momentum component $\vec{k}_{\perp}^{\text{in}}$ is not conserved due to the loss of translational symmetry in this direction. To approximate

$\vec{k}_{\perp}^{\text{in}}$, the free-electron final-state model is frequently employed. This model assumes a parabolic dispersion for the final state and introduces an empirical inner potential V_0, leading to the expression [206]:

$$\vec{k}_{\perp}^{\text{in}} = \sqrt{\frac{2m}{\hbar^2}\left(E_{\text{kin}} + V_0\right) - k_{\parallel}^2}. \tag{3.6}$$

The inner potential V_0 must be determined experimentally, typically by comparing measured ARPES spectra with calculated band structures or by analyzing measurements at varying photon energies. Since the photon energy directly influences the range of accessible $\vec{k}_{\perp}^{\text{in}}$ values, tuning it provides an effective approach for reconstructing the bulk electronic structure [210].

3.2 Photoemission Orbital Tomography (POT) of Molecular Layers

While the previous sections have focused on crystalline solids and the use of ARPES to access their band structure, organic molecular systems present a different set of challenges. In particular, conventional UPS measurements on thin molecular films often suffer from broad and overlapping spectral features, making the identification of individual molecular orbitals challenging [64]. *Photoemission orbital tomography* (POT) offers a unique approach for probing the electronic structure of organic molecules adsorbed on surfaces, making use of the aforementioned momentum-resolved information provided by ARPES [63, 64, 114].

Fundamentals of POT

Within the one-step model of photoemission (Section 3.1.2), the photocurrent $I(k_x, k_y; E_{\text{kin}})$ emitted in a direction (k_x, k_y) results from transitions between occupied molecular orbitals Ψ_i and final states Ψ_f:

$$I(k_x, k_y, E_{\text{kin}}) \propto \sum_i |\langle \Psi_f(k_x, k_y, E_{\text{kin}}) | \vec{A} \cdot \vec{p} | \Psi_i \rangle|^2 \times \delta(E_i + \Phi + E_{\text{kin}} - \hbar\omega). \tag{3.7}$$

A key simplification in POT is the plane-wave final-state approximation, which treats the emitted electron's final state as a free-electron plane wave. This reduces the expression for the photocurrent I_i originating from a specific initial molecular orbital Ψ_i to a direct relation involving the Fourier transform of the respective molecular orbital [63, 211]:

$$I_i(k_x, k_y) \propto |\vec{A} \cdot \vec{k}|^2 \cdot |\tilde{\Psi}_i(k_x, k_y)|^2, \tag{3.8}$$

where $|\vec{A} \cdot \vec{k}|$ is the polarization factor and $|\vec{k}|^2 = {k_x}^2 + {k_y}^2 + {k_z}^2 = \frac{2m}{\hbar^2} E_{\text{kin}}$. The key advantage of this approximation is that the momentum-dependent photocurrent directly reflects the modulus square of the Fourier transform of individual molecular orbitals, allowing their structure to be reconstructed from reciprocal space [63], as illustrated in Fig. 3.6.

As can be shown with mathematical rigor, this approach is valid for large, planar molecules consisting mostly of light atoms, such as hydrogen, carbon, nitrogen, and oxygen, when photoemission is dominated by delocalized π-orbitals [64]. Additionally, for the approximation to hold, the emitted electron's momentum vector $\vec{k}$ should form a small angle with the light polarization vector $\vec{A}$.

Although POT was initially developed for imaging π-orbitals, recent studies have demonstrated that σ-orbitals can also be imaged with this technique, significantly expanding its applicability [212]. This capability is particularly relevant for surface chemical reactions, as σ-orbitals provide direct insight into bond formation and dissociation processes at the molecular periphery, which π-orbitals alone might not capture.

Recently, POT has been used to experimentally resolve an unprecedented number of 38 molecular orbitals within a binding energy range exceeding 10 eV [213]. Such an extensive dataset provides a stringent benchmark for exchange-correlation functionals in DFT, by enabling a direct validation of calculated orbital energies.

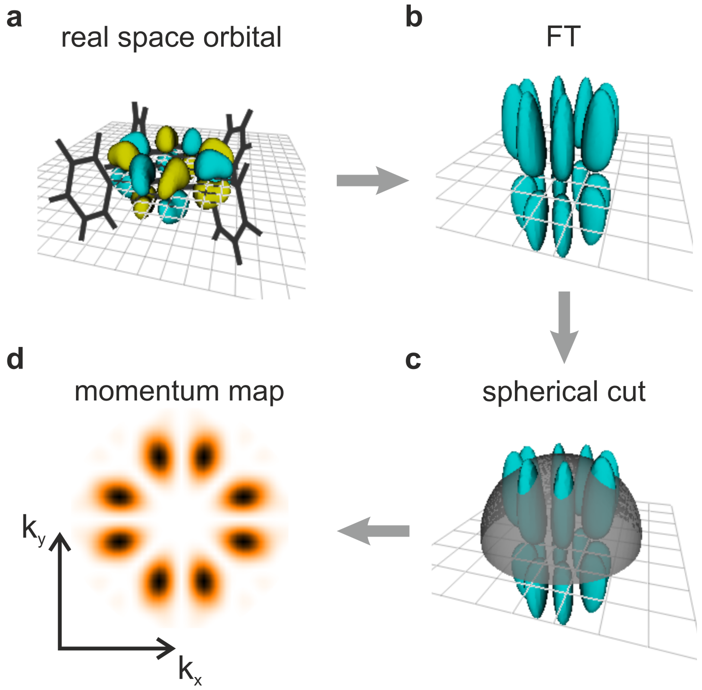

Figure 3.6: Concept of the photoemission orbital tomography approach. In **(a)** the HOMO-1 orbital of a porphyrin molecule is shown and in **(b)** the corresponding FT. By cutting the FT along the isoenergetic hemisphere with radius $k = \sqrt{(2m/\hbar^2)E_{\text{kin}}}$ indicated in **(c)**, the final momentum map, which is presented in **(d)**, is created. This simulated momentum map can ultimately be compared to the experimental data to identify distinct molecular orbitals. Published in [214].

Beyond static orbital imaging, POT has also been extended to time-resolved measurements, allowing the study of ultrafast molecular dynamics. By implementing a femtosecond pump-probe scheme, it has been demonstrated that POT can track the evolution of excited molecular states with both spatial and temporal resolution [215–218].

Another valuable aspect of POT is its ability to detect structural distortions of adsorbed molecules, which typically result from molecule–substrate or intermolecular interactions [219]. This aspect will be explored in more detail in the final chapter of this thesis, where POT is employed to elucidate the conformational changes of adsorbed metalloporphyrins and to examine how these distortions affect the electronic structure.

3.3 Momentum-Resolved Photoemission Microscopy

3.3.1 Real- and Momentum-Space Imaging

Photoelectron emission microscopy (PEEM) is a surface-sensitive technique that utilizes photoelectrons to generate microscopic images of a sample's surface. First demonstrated by E. Brüche in 1933 [220], the technique relies on photoemitted electrons that are extracted from a sample and subsequently projected onto a detector by a system of electrostatic and magnetic lenses [221, 222]. The working principle of a PEEM is illustrated in Fig. 3.7. A strong electrostatic field (typically around 10 keV) between the sample (cathode) and an anode accelerates all the emitted electrons, even those emitted at angles close to ±90°, towards a 2D electron detector. This first electrostatic lens is the so-called cathode or objective lens [223]. While this simple configuration can already produce images with 15 to 40 times magnification, a severe enhancement of the performance can be achieved by adding a subsequent imaging column, which hosts a sets of various electron lenses [222]. The resulting image represents the lateral distribution of photoelectron intensity, allowing for high-resolution surface imaging. Modern aberration-corrected PEEM instruments with sophisticated lens columns can achieve spatial resolutions down to a few nanometers [222, 224]. Due to its high-resolving imaging capabilities, PEEM has been widely applied to study surface phenomena in materials science and catalysis. A pivotal demonstration of its potential came from Ertl's group at the Fritz Haber Institute, where PEEM was used to investigate

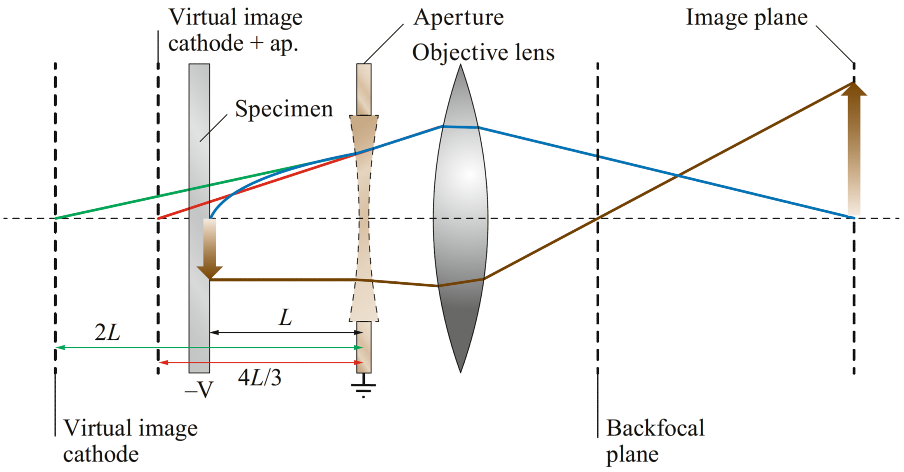

Figure 3.7: Scheme of the cathode lens in typical PEEM instrument. Reproduced from [222]. © 2020 Springer Nature.

oscillatory behavior in gas adsorption on active surfaces during catalytic reactions. Their studies provided real-time visualization of surface chemical dynamics, sparking significant interest in the chemistry community and establishing PEEM as a valuable tool for surface reaction studies [42, 225–227].

Beyond direct real-space imaging, PEEMs can be configured to operate in a momentum-resolved mode, commonly referred to as *momentum microscopy* (MM). In this mode, the instrument provides direct access to the electronic band structure by mapping the momentum distribution of photoemitted electrons. For crystalline samples, the objective lens naturally forms a diffraction pattern in the *back-focal plane* (BFP), indicated in Fig. 3.7 [224]. By incorporating an additional projection lens, this diffraction pattern can be magnified and imaged onto the 2D detector, resolving the parallel momentum components of the photoelectrons. The objective lens is also the most critical component in determining the ultimate $k_{\|}$ resolution, thus precise alingment of the sample with respect to the anode is of utmost importance [223]. When coupled with an energy filter, this configuration enables momentum microscopy to record full momentum distributions at specific kinetic energies, allowing for the reconstruction of complete band structures and Fermi surfaces [228].

MM was first experimentally demonstrated by Kotsugi *et al.* in 2002 [229], using a simple retarding-field electron energy analyzer. Compared to conventional ARPES, which measures momentum along a small azimuthal region at a time, MM enables the simultaneous detection of the entire momentum distribution over a 2π azimuthal range. This results in significantly reduced acquisition times for mapping band structures, while the included microscope functionality allows identifying and selecting small sample regions, making PEEMs extremely versatile for a wide range of materials, from crystalline bulk materials to heterostructures, molecular adlayers, and even microscopic flake samples.

3.3.2 Instrumentation: NanoESCA and KREIOS

For the experiments in this thesis, two complementary momentum microscopes were employed: the NanoESCA PEEM at the Elettra synchrotron in Trieste [230] and the KREIOS 150 MM momentum microscope at the Technical University of Dortmund [195, 196]. While both instruments share the same fundamental working principle and utilize hemispherical energy analyzers for energy dispersion, they differ in design and light source configuration.

Both systems employ hemispherical analyzers for energy filtering. The NanoESCA microscope incorporates a double-hemispherical analyzer, which corrects for spherical aberrations [231], whereas the KREIOS system utilizes a single-hemispherical analyzer with an optimized electrostatic lens design that eliminates the need for additional aberration correction [232]. Notably, the latter also corrects for the nonisochromaticity of electron trajectories — a residual effect that still persists in standard double-hemispherical designs and typically requires post-processing of the data [233]. Despite these structural differences, both instruments follow the same energy-filtering principle. A schematic of the NanoESCA instrument, illustrating its key components — including the PEEM optics, energy filter, and detector system — is shown in Fig. 3.8.

The primary distinction between the two setups lies in their light sources. The NanoESCA microscope operates at the Elettra synchrotron, which offers a tunable photon source spanning a broad range of photon energies and thus covers both the UPS and XPS regimes. This enables photon-energy-dependent studies and permits switching between different light polarizations, including linear (*s*- and *p*-) as well as circular polarization.

In contrast, the KREIOS microscope is based in a laboratory setting and utilizes two primary excitation sources:

1. A gas discharge lamp using helium as an excitation source, providing efficiently photon energies of either 21.2 eV (He I) or 40.8 eV (He II), commonly used for valence band spectroscopy. The lamp is further equipped with a monochromator, which filters unwanted photon energies while reducing the pressure in the experimental chamber during operation by two orders of magnitude and reducing the beam size down to few hundreds of µm.

2. An *extreme ultraviolet* (XUV) *high-harmonic generation* (HHG) source, delivering photons at approximately 30 eV. This pulsed source enables time-resolved measurements via a pump-probe scheme, allowing the study of ultrafast dynamics in molecular and solid-state systems [195].

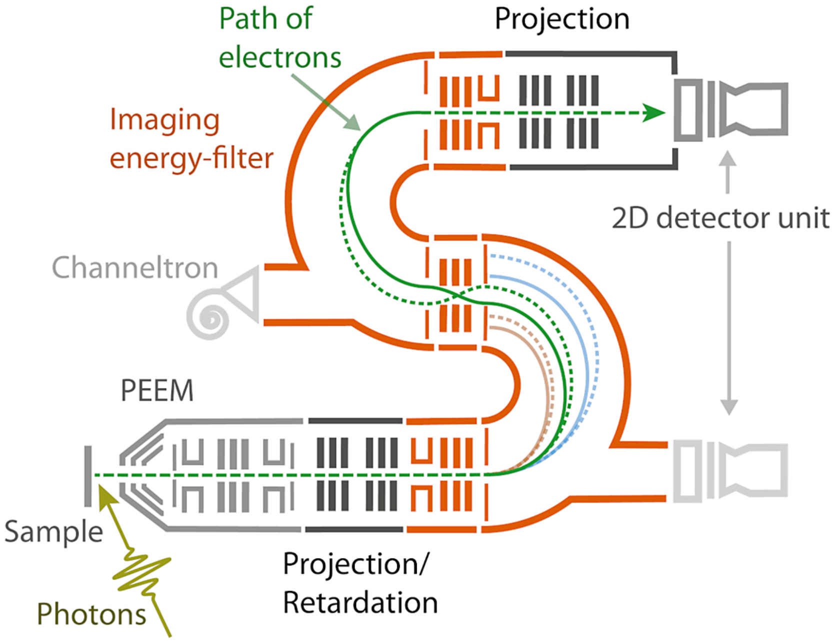

Figure 3.8: Schematic of the NanoESCA momentum microscope. The system includes a PEEM column (the cathode lens sits in the beginning) for magnification and mode-selection, a double-hemispherical analyzer for energy filtering, and a 2D detector for image acquisition. Reproduced from [234].

Together, these instruments offer complementary capabilities, with the synchrotron-based NanoESCA enabling high-energy tunability and polarization control, while the KREIOS system provides laboratory-based access to momentum microscopy, including the potential for time-resolved measurements [195, 196] — although the latter were not utilized in the present thesis.

The NanoESCA further extends its capabilities with spin-resolved measurements, utilizing a dedicated spin filter to probe spin-dependent electronic properties. Both instruments are equipped with hexapod sample stages that allow precise piezo-controlled adjustments of the sample position and cooling via a commercial flow crystoat, which can be operated with liquid nitrogen or helium to reach sample temperatures below 10 K.

3.3.3 Spin-Resolved Momentum Microscopy

A unique feature of the NanoESCA instrument is its capability for spin-resolved photoemission, allowing the measurement of spin-resolved band structures. This capability is essential for exploring the magnetic properties of materials that are otherwise inaccessible in conventional spin-integrated measurements.

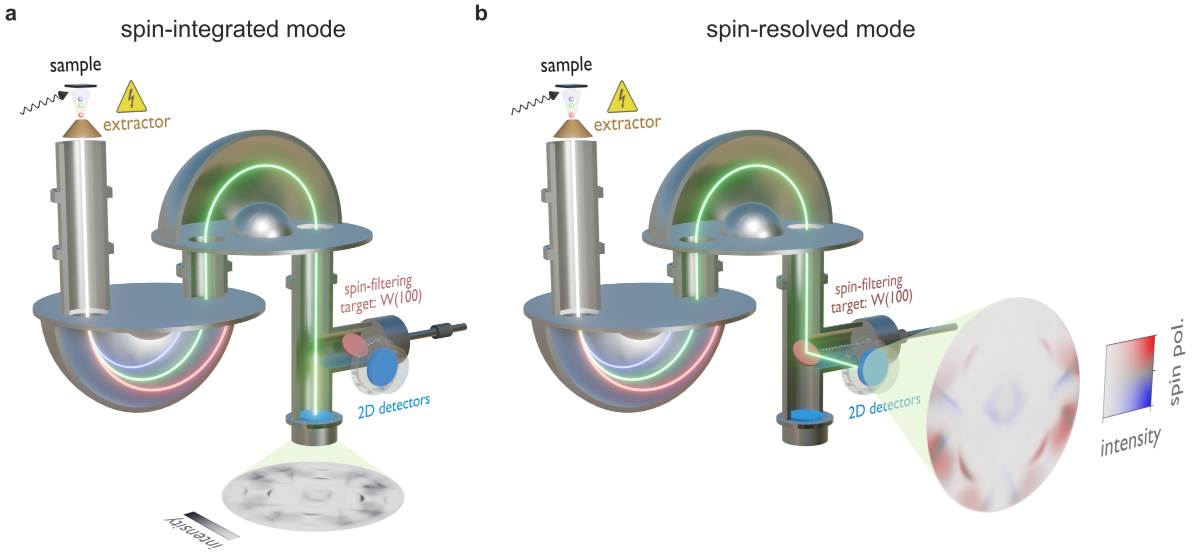

Figure 3.9: Operation modes of the NanoESCA instrument. **(a)** Standard spin-integrated mode, where the photoemitted electrons pass through the hemispherical analyzer and are directly detected. **(b)** Spin-resolved mode, where electrons are further scattered off a W(100) spin-filtering target before detection, enabling spin-sensitive measurements.

The transition between spin-integrated and spin-resolved operation in the NanoESCA instrument is schematically illustrated in Fig. 3.9. In the spin-integrated mode, the momentum distribution of all emitted electrons is detected without spin discrimination, providing a comprehensive overview of the electronic band structure. In contrast, spin-resolved measurements are performed by reflecting electrons at a W(100) spin-filtering target, thereby enabling access to spin-dependent band structure information.

Principles of Spin-Filtering in Momentum Microscopy

In general, spin-polarization measurements in photoemission experiments rely on spin-dependent scattering at a solid-state target. Typical configurations for spin-resolved measurements include Mott detectors [235], *spin-polarized low-energy electron diffraction* (SP-LEED) [236], and low-energy exchange scattering [237]. However, these methods suffer from inherently low efficiency due to the weak probability of spin-dependent scattering and the single-channel working scheme of traditional detectors [238].

The major drawback of conventional spin polarimeters, is their single-channel nature, which significantly limits data acquisition speed and spatial resolution. These constraints make them impractical for modern high-resolution photoemission studies, where high efficiency and parallel detection capabilities are required. The figure of merit, defined as:

$$F = S_{\mathrm{Sh}}^2 \frac{I}{I_0}, \tag{3.9}$$

where S_{Sh} is the Sherman function (a measure of the spin sensitivity of the detector) and I/I_0 is the ratio of scattered to incoming intensity, has remained at approximately 10^{-4} since the introduction of Mott and SPLEED-based polarimeters in the 1980s [238].

To overcome these limitations, the NanoESCA instrument employs a two-dimensional multichannel spin detection scheme based on a W(100) scattering target [239]. This approach dramatically enhances the efficiency of spin-resolved measurements, improving detection rates by up to eight orders of magnitude compared to single-channel detectors. This gain stems from both the intrinsically high efficiency of the W(100) spin filter and the simultaneous multichannel detection of electrons, allowing high-throughput spin-resolved band structure measurements [240].

The spin-filtering mechanism in W(100) is based on spin-dependent reflectivity due to spin-orbit coupling at the crystal surface. When electrons scatter off the W(100) target, their scattering amplitude depends on their spin orientation, leading to an asymmetry in the measured intensity based on spin polarization. This filtering effect is maximized when the crystal is used in a 90° deflection geometry, where the spin quantization axis is normal to the scattering plane [241].

The working principle of the W(100) spin filter is illustrated in Fig. 3.10.

An electrostatic retarding lens deaccelerates the electrons from the analyzer pass energy (typically 100 eV), to the scattering energy, E_{scatt}, ranging between 15 to 90 eV. A reciprocal image is formed at the W(100) target, ensuring that electrons originating from the same point in real space arrive as a parallel beam at the crystal surface [240].

This arrangement preserves the spatial information of the incoming electron beam. Upon specular reflection at 90°, the image is reconstructed using a second symmetrical electrostatic lenses, enabling direct measurement of spin-resolved band structures.

The spin-integrated image can still be obtained by retracting the spin filter from the electron optical path, ensuring identical detector conditions in both modes [238]. The spin-averaged reflectivity and spin sensitivity as a function of scattering energy for W(100) are shown in Fig. 3.10b. The two optimal working points, indicated by vertical dashed lines, lie at scattering

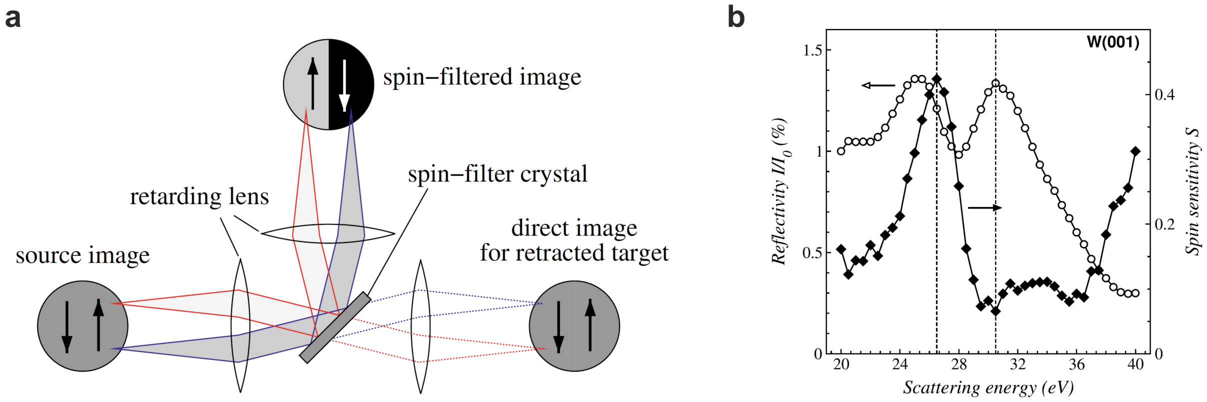

Figure 3.10: **(a)** Schematic representation of the spin-filtering process using a W(100) crystal. Electrons undergo specular reflection at the spin-filter crystal, with spin-dependent scattering leading to a spin-filtered image. The spatial information of the source image is preserved due to parallel beam conditions. The spin-integrated image can still be obtained by retracting the spin-filter crystal from the electron optical path. Reproduced from [240]. © 2011 AIP Publishing. **(b)** Spin-averaged reflectivity (I/I_0, open circles) and spin sensitivity (S_{Sh}, filled diamonds) as a function of electron scattering energy for the W(100) spin filter. The two optimal working points at 26.5 eV and 30.5 eV are highlighted by vertical dashed lines, corresponding to highly asymmetric spin sensitivity regions. Reproduced from [207]. © 2021 Springer Nature.

energies of 26.5 eV and 30.5 eV, where the spin asymmetries reach approximately 42% and 6%, respectively [241].

However, a key limitation of the W(100) spin filter is its relatively short operational lifetime. Contamination from surface adsorption rapidly degrades the crystal quality, typically within a few hours, requiring frequent cleaning. Additionally, the fundamental limit in energy resolution is set by the crystalline quality of the W(100) target [240]. Defects, mosaic structures, and other imperfections can broaden the diffraction pattern and reduce measurement precision. Consequently, careful preparation and the use of high-quality, well-ordered W(100) crystals are essential for optimal performance [241].

To mitigate some of these issues, a novel approach involves using an Ir(100) substrate passivated with a pseudomorphic monolayer of Au. This modification has been shown to enhance efficiency while significantly extending operational lifetimes to several weeks and even months. However, the preparation of such a target requires additional tools for precise Au deposition and maintenance [223].

Noteworthy, a novel approach representing the newest generation of 2D imaging spin filters employs the Fe–O surface as a spin-selective scattering target that combines spin–orbit and exchange scattering within a single system [242]. This advanced design enables the simultaneous detection of two spin-polarization directions using only a single setup. Moreover, with the integration of an additional imaging branch, the configuration could, in principle, be extended to allow full spin-vector resolution [242].

Calculation of the Spin Polarization

The spin polarization $P(x, y)$ and total intensity $I_0(x, y)$ can be determined using intensity measurements at the two optimal spin-filter working points:

$$P(x,y) = \frac{I_l(x,y) - I_h(x,y)}{S_l \cdot I_h(x,y) - S_h \cdot I_l(x,y)} \tag{3.10}$$

$$I_0(x,y) = \frac{S_l I_h(x,y) - S_h I_l(x,y)}{S_l - S_h} \tag{3.11}$$

where I_l, I_h represent the measured intensities at low and high spin-filter working points, normalized to their respective reflectivity references R_l, R_h, while S_l, S_h denote the spin asymmetry functions at these energies [207, 241].

4 Oxygen Chemisorption on Fe(100)

4.1 Introduction: Adsorption and Correlation at Ferromagnetic Surfaces

Ferromagnetism in transition metals such as Fe, Co, and Ni is commonly understood within the framework of the single-particle Stoner model [243], which describes it as arising from a spontaneous spin polarization of the electronic states when the gain in exchange energy outweighs the associated increase in kinetic energy, leading to an exchange splitting between majority and minority spin bands. Within this framework, the exchange interaction is treated using a static mean-field approximation, in which each electron experiences an effective magnetic field generated by the average spin polarization of the other electrons. This mean field leads to an energy splitting between majority and minority spin states, stabilizing the ferromagnetic ground state [244].

When an adsorbate approaches a ferromagnetic surface, its molecular orbitals hybridize with the spin-polarized electronic structure of the metal. As introduced in Section 1.3, this process can be described within the Newns-Anderson and *d*-band models [47, 48, 52], which provide intuitive frameworks for understanding adsorbate–metal interactions. In the case of ferromagnetic substrates, however, the spin-split density of states must be explicitly considered, as the hybridization becomes inherently spin-dependent, leading to distinct bonding and antibonding resonances in the majority and minority spin channels, as depicted schematically in Fig. 4.1 [245]. Analogous to the standard *d*-band model, the adsorption strength and the modification of the substrate's spin-polarized electronic structure are governed by the spin-resolved position and filling of the hybrid states relative to the Fermi energy (E_F), with the majority and minority spin channels considered separately, resulting in a spin-selective hybridization process [245].

The *d*-band model provides a simplified single-particle interpretation of the electronic structure as obtained from spin-polarized DFT, which itself is a single-particle formalism based on an effective spin-dependent potential [47, 246].

While this single-particle description captures many essential aspects, it was recognized early on that $3d$-ferromagnetic transition metals exhibit pronounced electron correlation effects due to the localized nature of their open $3d$-shells, which remain relatively strongly bound to the ionic cores [55, 247–249]. These many-body interactions significantly influence both the electronic and magnetic properties of these materials and cannot be fully captured by mean-field theories such as the Stoner model or standard DFT [250–252]. Correlation effects typically manifest in several key ways: a narrowing of the $3d$-bandwidth, a reduction of the exchange splitting, the appearance of satellite features in excitation spectra at higher binding energies [58, 253–258], and the broadening of electronic bands due to the finite lifetime introduced by many-particle scattering [124, 175]. Given that chemisorption modifies the *d*-band structure by introducing

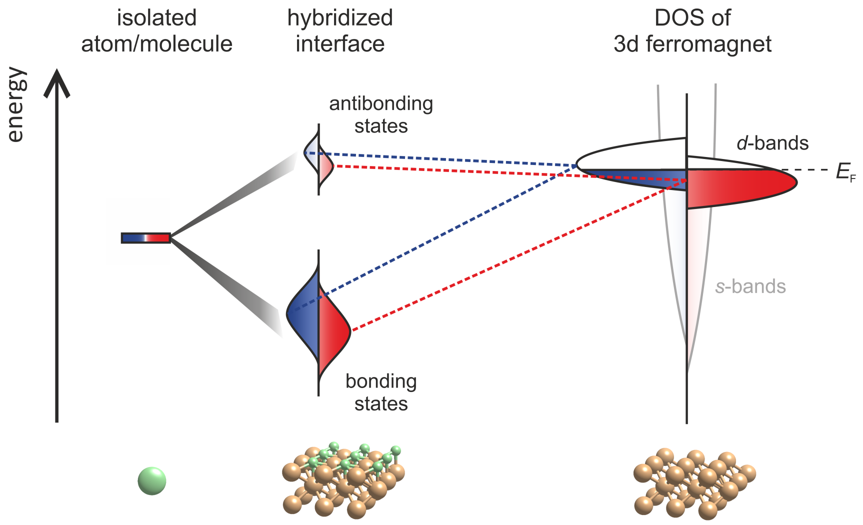

Figure 4.1: Schematic representation of the *d*-band model for adsorption on ferromagnetic surfaces. On the left, an isolated atom or molecule exhibits sharp discrete electronic levels. As the adsorbate approaches the ferromagnetic transition metal surface (right), these levels initially broaden due to weak interaction with the metal states. Upon strong hybridization with the *d*-bands of the metal, the states split into bonding and antibonding adsorbate-metal resonances, as illustrated in the middle for the hybridized interface.

hybridization and altering the occupation and distribution of *d*-states, it is natural to expect that these changes will also affect the strength and character of electron correlation at the surface. Variations in the local *d*-electron configuration could influence the effectiveness of many-body scattering processes, potentially leading to measurable changes in electronic structure and magnetism. However, the specific ways in which adsorption modifies correlation effects remain largely unexplored.

This raises two central questions:

1) How does chemisorption at ferromagnetic surfaces influence electron correlation?

2) What are the resulting consequences for the electronic and magnetic properties of the hybrid interface?

Addressing these questions is the central focus of this chapter.

To explore the phenomenon of adsorbate-induced correlation phenomena, we focus on the model system of oxygen chemisorbed atop *ferromagnetic* (FM) iron, forming an Fe–O reconstruction, where the O atoms occupy the hollow sites of the surface lattice, positioned less than 0.5 Å above the Fe surface atoms. This system serves as an ideal test case due to its well-characterized electronic structure [164, 259–263], its known magnetic properties [259, 261], including its role as a highly effective spin filter in spin-resolved photoelectron spectroscopy experiments [242, 264–266]. Through studying this prototypical hybrid interface, we aim to gain detailed insight into how chemisorption modifies electron correlation at ferromagnetic surfaces and to provide a basis for understanding correlation effects at hybrid interfaces more generally.

4.2 Sample Preparation and Experimental Overview

The Fe(100) thin film investigated in this study was epitaxially grown on a MgO(100) crystal. Initially, the commercial MgO substrate (MaTecK GmbH) was cleaned under UHV conditions by sequential cycles of argon ion sputtering (2 keV Ar^+) and annealing at 870 K for 45 minutes [267]. A 300 nm-thick Fe(100) film was then deposited in-situ via e-beam evaporation using an EFM 3 evaporator by Focus GmbH. This thickness ensures in-plane magnetization along the Fe [001] crystallographic direction (easy axis). Surface cleanliness was maintained by repeated cycles of gentle Ar^+ sputtering at 0.5 keV and annealing at 870 K.

The Fe(100)–$p(1 \times 1)$O surface was prepared by exposing the clean Fe film to 30 L (Langmuir) of O_2 at approximately 820 K. Subsequent annealing at 870 K for 5 minutes ensured the removal of excess oxygen, leading to the formation of the desired surface reconstruction, which was verified by LEED and AES (see Fig. 4.2).

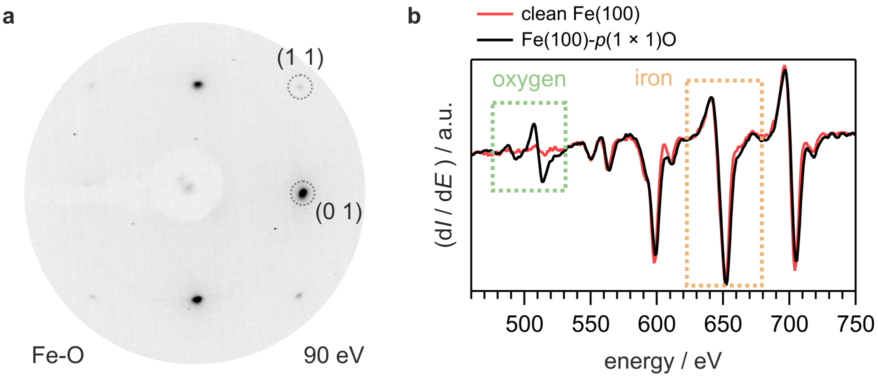

Figure 4.2: Surface characterization of Fe(100)–$p(1 \times 1)$O. **(a)** LEED pattern at 90 eV showing sharp (0 1) and (1 1) diffraction spots, indicative of high crystalline order. **(b)** Differential AES spectra of clean Fe(100) (red) and Fe(100)–$p(1 \times 1)$O (black), confirming successful passivation with oxygen. Only one of the three Fe-related peaks is highlighted.

To investigate the electronic structure, mainly a NanoESCA momentum microscope was utilized, which is equipped with an adjustable W(100) spin-filtering target, allowing the measurements of momentum maps with additional information on the in-plane spin polarization. This instrument enables probing of the electronic and magnetic properties of interfaces with high precision throughout the entire *surface Brillouin zone* (SBZ). To ensure a well-defined magnetic state during the spin-photoemission experiments, the Fe sample was magnetized inside the UHV analysis chamber along the [001] direction using a permanent magnet and measured in remanence. For verification of the measured properties, measurements were also performed upon reversing the magnetization direction.

Theoretical modeling of the Fe(100) and Fe(100)–$p(1 \times 1)$O surfaces was performed by Dr. Andrea Droghetti from Trinity College Dublin, who carried out both DFT and DFT+DMFT calculations. These results are presented throughout this chapter unless stated otherwise.

4.3 Limitations of DFT and the Role of DMFT in Correlated Systems

As mentioned earlier, hybrid interfaces involving FM surfaces are generally described using spin-polarized DFT: a single-particle framework. Fig. 4.3 shows the surface *projected density of states* (PDOS) calculated within DFT (LSDA) for clean Fe(100) and the oxygen-passivated Fe(100)–$p(1 \times 1)$O surface.

While the majority (↑) d-states in Fe(100) (Fig. 4.3a) lie well below the Fermi energy and appear fully occupied, the minority ones (↓) are mostly unoccupied and situated right above E_F, as expected in the Stoner model of ferromagnetism. Note that, while bulk Fe is not considered to exhibit a Stoner gap [244], *i.e.*, a gap between the top of the majority band and the Fermi energy, the situation differs at the surface, where the reduced coordination number can lead to modifications in the electronic structure and enhance magnetic properties [268].

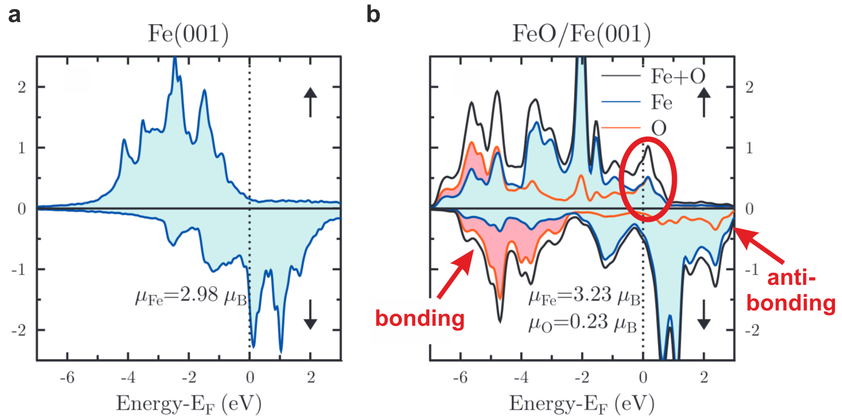

Figure 4.3: Surface PDOS calculated using DFT within the local spin-density approximation (LSDA) for **(a)** clean Fe(100) and **(b)** oxygen-passivated Fe(100)–$p(1\times1)$O. The DOS is projected onto Fe d-orbitals and O p-orbitals. A key feature of the oxygen-passivated surface in b) is the formation of unoccupied states (holes) in the majority spin channel, as highlighted by the red circle, indicating the electronic modifications induced by surface oxidation. Adapted with permission from A. Tange [262]. © 2010 American Physical Society.

Upon oxygen adsorption (see Fig. 4.3b), bonding states with dominant O character emerge in the majority channel between $-7.0\,\mathrm{eV}$ and $-4.0\,\mathrm{eV}$, while the minority bonding states are found between $-6.0\,\mathrm{eV}$ and $-3.0\,\mathrm{eV}$. Antibonding states, primarily associated with Fe, remain near or above the Fermi level and shape the DOS in this region [262]. Beyond the formation of these spin-split hybrid states, oxygen adsorption is also accompanied by a redistribution of the electronic states near the Fermi level, reflecting subtle but critical changes in the occupancy of the Fe d-states.

In the minority spin channel, the DOS at E_F is severely reduced, indicating a trend toward increased insulating behavior. In the majority spin channel, hybridization with the oxygen p-states leads to a partial depletion of the Fe d-states near E_F. While the majority spin channel was previously almost fully occupied, this depletion introduces a finite density of unoccupied states, *i.e.* holes (highlighted by the red circle).

The significance of this hole creation can be understood by recognizing that, in a ferromagnetic metal, electrons propagate through the spin-dependent Stoner mean-field, which is determined by the net spin polarization. In addition, the so-called electronic self-energy accounts for scattering processes in which a single electron interacts with the Fermi sea, exciting another electron from an occupied into an unoccupied state [269]; this process corresponds to the generation of a particle–hole pair [124]. A more detailed discussion of the self-energy concept and its role within dynamical mean-field theory (DMFT) will follow in Section 4.3.1.

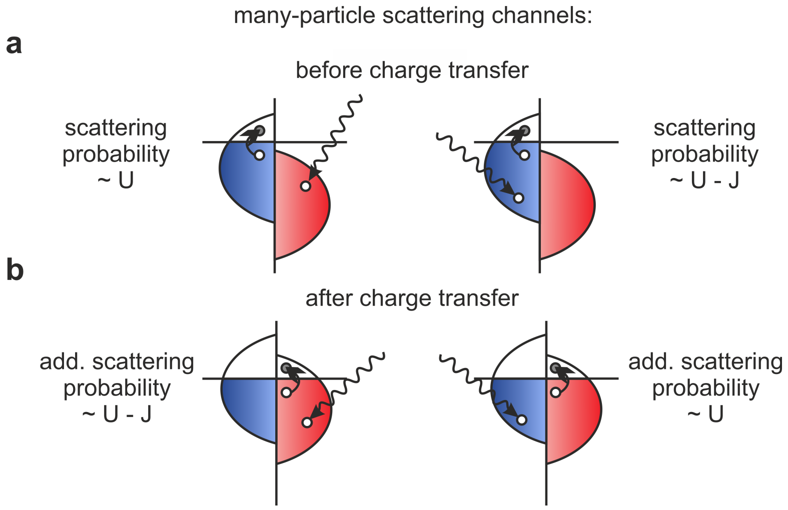

Figure 4.4: Illustration how the presence or absence of holes in one spin channel affects the available many-body scattering channels in ferromagnetic transition metals. **(a)** Surface DOS similar to the one obtained for clean Fe, where no holes are present in the majority spin channel. As a result, excited states in both spin channels can scatter only with particle-hole pairs in the minority states, with scattering being more probable for majority-spin excitations due to spin-dependent scattering preferences. **(b)** Modified DOS for an Fe–O surface, where unoccupied states (holes) appear in the majority spin channel. This enables additional scattering processes within the majority spin channel, severely enhancing correlation effects for minority electrons.

Since the creation of a particle–hole pair requires that both occupied and unoccupied states are available, even subtle changes in the electronic configuration — such as the opening of a small number of holes in an otherwise filled *d*-band — can decisively enhance the rate of many-particle scattering.

In a strong ferromagnetic system like Fe(100), the majority-spin *d*-band is practically completely filled, as illustrated in Fig. 4.4a, and its contribution to the DOS above E_F is nearly zero, while the minority-spin DOS remains large in this energy region. As a result, particle–hole pair creation is suppressed in the majority-spin channel but enabled in the minority-spin channel.

Importantly, the probability of this scattering process is significantly increased when electrons scatter off particle–hole pairs of opposite spin. Due to the absence of holes in the majority-spin channel, majority-spin electrons primarily scatter off minority-spin particle–hole pairs, with a probability that scales with the effective interaction strength U. In contrast, minority-spin electrons scatter off same-spin (minority) particle–hole pairs, but with a reduced effective interaction of $U - J$ (see Fig. 4.4a). Since $U - J < U$, majority-spin electrons are subject to stronger correlation effects than their minority-spin counterparts.

These findings are well established, having been predicted by early DFT+DMFT calculations and supported by experimental observations [57, 254, 255, 270].

Interestingly, this reasoning suggests that modifications to the d-band filling, such as those induced by oxygen chemisorption, can significantly alter spin-dependent scattering rates by introducing additional scattering channels that would otherwise remain inaccessible, as illustrated in Fig. 4.4b. This, in turn, could enhance electron correlation effects, particularly for the minority-spin states, where efficient scattering pathways would previously have been absent.

4.3.1 The Influence of DMFT-Corrections in Simulating Fe(100)

To accurately account for electronic correlations in theoretical simulations, beyond-DFT approaches such as DMFT [62] or many-body perturbation theory (*e.g.*, GW [271], and its extensions like GT or GWT [175, 272]) must be employed. These approaches incorporate the so-called electronic self-energy $\Sigma(E)$, which describes how an electron or hole interacts with its many-body environment, considering exchange and correlation effects beyond the effective single-particle picture of spin-polarized DFT [190, 273]. Self-energy techniques successfully reproduce the key spectral features associated with electronic correlation, including band renormalization, exchange splitting modification, and lifetime broadening, as schematically depicted in Fig. 4.5. However, understanding how these correlation effects evolve upon chemisorption requires a thorough analysis of the electronic structure changes.

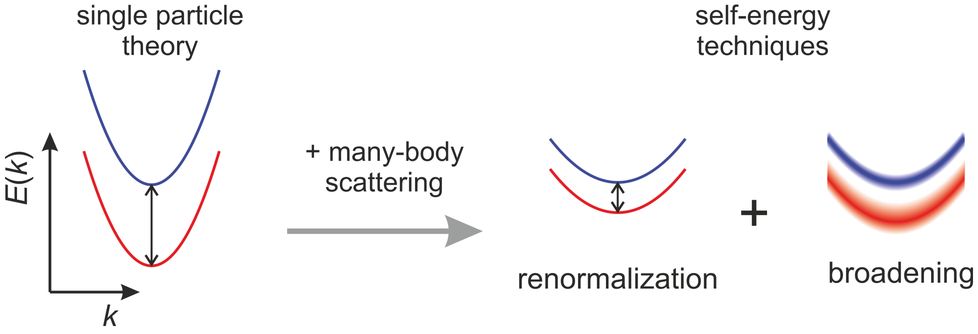

Figure 4.5: Influence of electron correlation in first-principles calculations of ferromagnets. The left side represents the typical single-particle picture from DFT, where sharp bands exhibit strong exchange splitting. When many-body effects are included using self-energy techniques like DMFT (right side), two key effects arise: (1) renormalization of the band structure, accompanied by a reduction in exchange splitting, and (2) broadening of the bands due to finite lifetimes of the renormalized quasiparticle bands.

Here, tailored DMFT calculations, which include second-order terms in the effective electron–electron interaction U and Hund's coupling J between the $3d$ electrons [124, 274], are employed to interpret the experimental data and to assess whether adsorption enhances electron correlation, and how these changes impact the magnetic and electronic structure of hybrid interfaces.

Calculating the Fe(100) Surface With Electron Correlation

To visualize the influence of electron correlation on the Fe(100) surface, a direct comparison is made between the DOS obtained from conventional single-particle DFT and from DFT supplemented with dynamical mean-field theory (DFT+DMFT) corrections. These calculations were performed by Dr. Andrea Droghetti and are here analyzed in direct comparison with the experimental data obtained in the context of this thesis, to elucidate how adsorption modifies the correlated electronic structure of the Fe surface.

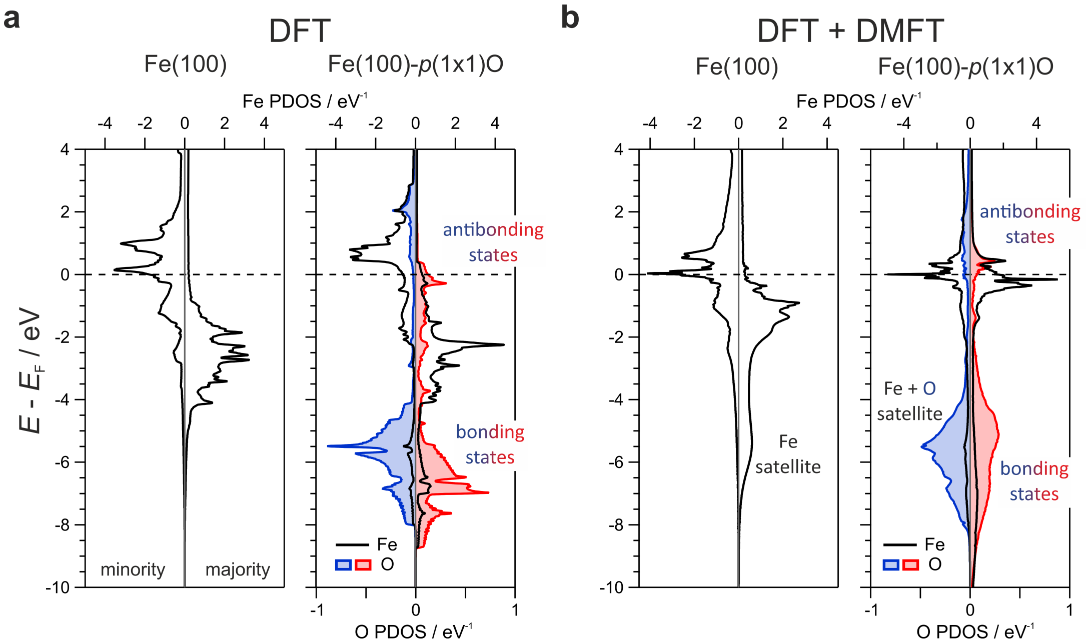

Figure 4.6: PDOS for Fe(100) and Fe(100)–$p(1 \times 1)$O surfaces. **(a)** PDOS of surface Fe atoms (and O atoms where applicable) for Fe(100) and Fe(100)–$p(1\times1)$O, calculated using DFT. **(b)** The same PDOS computed using a combination of DFT and DMFT corrections (DFT+DMFT). In both cases, hybridization between Fe and O states leads to the formation of bonding and antibonding states. The inclusion of many-body effects in DFT+DMFT introduces additional spectral features, including satellite states near −5 eV, which are absent in the pure DFT calculations. Published in [190].

As noted earlier, the DMFT-corrections account for many-body effects by incorporating second-order interactions in both the on-site Coulomb repulsion U and Hund's coupling J between Fe $3d$ electrons [250, 251]. While DMFT neglects spatial electron correlations, it captures dynamical fluctuations in time, making it an effective approach for studying correlation effects in transition metals [248, 252]. Its validity has been confirmed in previous studies, where it successfully reproduced correlation-induced spectral features observed in photoemission experiments [249]. Fig. 4.6 shows the PDOS for Fe(100) and Fe(100)–$p(1 \times 1)$O surfaces, computed within these two approaches.

In the DFT-calculated PDOS (Fig. 4.6a), we observe the characteristic hybridization between Fe *d*- and O *p*-orbitals, as expected from *d*-band theory. Notably, the projections on the O atoms exhibit a strong spin splitting of 2 eV for both the bonding and the antibonding states, mirroring the exchange splitting of the Fe *d*-states.

Next, we account for correlation effects by examining the PDOS from DFT+DMFT, shown in Fig. 4.6b. In the clean Fe(100) surface, correlations move all the electronic states closer to the Fermi energy, resulting in a reduction of the exchange splitting and a narrowing of the Fe *d*-bands. Moreover, a prominent satellite peak emerges at $-5\,\mathrm{eV}$ in the majority spin channel, a clear signature of many-body interactions. The correlation parameters $U = 1.8\,\mathrm{eV}$ and $J = 0.5\,\mathrm{eV}$ used in these calculations are consistent with values previously reported for Fe surfaces [56]. As discussed earlier, the absence of satellite features in the minority DOS indicates that correlation effects are significantly stronger for the majority electrons.

Having established the role of correlation effects in the clean Fe(100) surface, we now examine how these effects evolve upon oxygen adsorption. The density of states (DOS) obtained from DFT+DMFT for the Fe(100)–$p(1 \times 1)$O system is shown on the right in Fig. 4.6b.

Notably, accurately reproducing the experimental spectral features, which are discussed in detail in the next section, requires a substantial adjustment of the correlation parameters U and J. Specifically, the Coulomb U and Hund's exchange J values for the Fe surface atoms in our DMFT calculations need to be increased to $U = 3.0\,\mathrm{eV}$ and $J = 1.1\,\mathrm{eV}$. In contrast, calculations using the same values as for the clean Fe(100) surface ($U = 1.8\,\mathrm{eV}$, $J = 0.5\,\mathrm{eV}$) yield a PDOS that does not capture the experimentally observed spectral features, as shown in Section A.1.

This enhancement of the correlation parameters verifies that oxygen adsorption reduces the effective screening of electron-electron interactions at the Fe surface, leading to an overall increase in electronic correlations. This behavior is consistent with the well-established trend that oxygen, as an electronegative ligand, promotes electronic localization, which in turn raises the effective Coulomb interaction strength [275, 276]. Indeed, transition metal oxides, where such mechanisms dominate, serve as prototypical examples of strongly correlated materials [277, 278]. The larger U for Fe, indicates that the Fe *d*-electrons experience stronger electron-electron interactions in the presence of oxygen.

As reasoned earlier, beyond this increase in the effective interaction U, the second crucial factor influencing electron correlation is the *d*-band filling. In a fully occupied band, electron-hole excitations are suppressed, and correlation effects become negligible regardless of U. However, if the bands become partially filled, electronic interactions also become activated. The degree of correlation is thus closely linked to the occupation of the Fe *d*-orbitals.

In Fe(100)–$p(1 \times 1)$O, the majority-spin 3*d*-orbitals remain nearly filled but exhibit a small hole concentration of approximately 0.1 electrons. This relatively minor reduction in occupancy has profound consequences, as it places the system in a more correlated regime. The increase in U leads to a narrowing of the *d*-bands and a suppression of the exchange splitting, affecting both the majority and minority spin states. Notably, correlation effects in the minority-spin *d*-band are now strong enough to induce a satellite feature, which was absent in pristine Fe(100). Despite these significant changes in electronic structure, the total d-shell occupation of surface Fe atoms remains constant at approximately 6.8 electrons. However, the enhanced correlation leads to a substantial reduction in the local magnetic moment, from 3.2 to $1.8\,\mu_B$.

A quantitative measure of the correlation strength is given by the mass enhancement factor m^*/m, which characterizes the effective mass increase due to many-body interactions relative to the non-interacting band mass m obtained from DFT. In clean Fe(100), the surface Fe d-orbitals exhibit weak correlation, with mass enhancement factors of 1.23 (majority spin) and 1.36 (minority spin). After oxygen adsorption, these values increase to 1.52 and 1.43, respectively; the largest enhancement (1.60) is observed for the spin-up d_{xy} orbital, which, due to its hybridization with O p-states, experiences slight hole doping [190].

Overall, these results demonstrate that oxygen adsorption leads to a transition from a weakly correlated to an intermediate correlated metallic state, underscoring the significant impact of adsorbates on electron correlation effects at metal surfaces. To directly validate these insights, we now turn to the key experimental investigation of the electronic structure of the passivated Fe(100) surface.

4.4 The Role of Oxygen in Shaping the Electronic structure of Fe(100)

4.4.1 The Spin-Integrated Band Structure of the Passivated Fe Surface

With the theoretical foundation of electron correlation effects established, we now turn to their experimental manifestations as revealed by our MM measurements.

To assess the impact of oxygen adsorption, we first compare momentum maps acquired at the Fermi level before and after oxidation. The corresponding maps are presented in Fig. 4.7a,b. For reference, the first SBZ is outlined (gray square), with high-symmetry paths connecting the $\overline{\Gamma}$, $\overline{\mathrm{X}}$, and $\overline{\mathrm{M}}$ points indicated by red lines. The surface normal is aligned along the Cartesian z-axis, while the photon beam incidence plane and magnetization direction $\vec{M}$ lie parallel to the k_y-axis, as marked by the golden and black arrows, respectively.

The electronic structure of pristine Fe(100) exhibits two distinct features within the SBZ, both linked to the d_{xz} and d_{yz} orbitals of bulk iron [279–281]. One of these features extends along the $\overline{\Gamma\mathrm{X}}$ direction (blue), gradually fading near both $\overline{\Gamma}$ and $\overline{\mathrm{X}}$. The other appears along the $\overline{\Gamma\mathrm{M}}$ path, positioned near the $\overline{\mathrm{M}}$-point (orange).

Upon oxygen adsorption, the Fe(100) surface undergoes a transition to the Fe(100)–$p(1 \times 1)$O phase (see Fig. 4.7c), accompanied by significant modifications in its electronic structure [262]. The corresponding momentum map, shown in Fig. 4.7b, reveals substantial changes compared to the pristine surface. The feature along $\overline{\Gamma\mathrm{X}}$ is replaced by a diamond-shaped state near $\overline{\Gamma}$ (blue) and a ring-like structure at the SBZ center (violet). Simultaneously, the state near $\overline{\mathrm{M}}$ (orange) becomes more rounded and pronounced. An additional diamond-shaped feature emerges, connecting the four $\overline{\mathrm{X}}$-points (green).

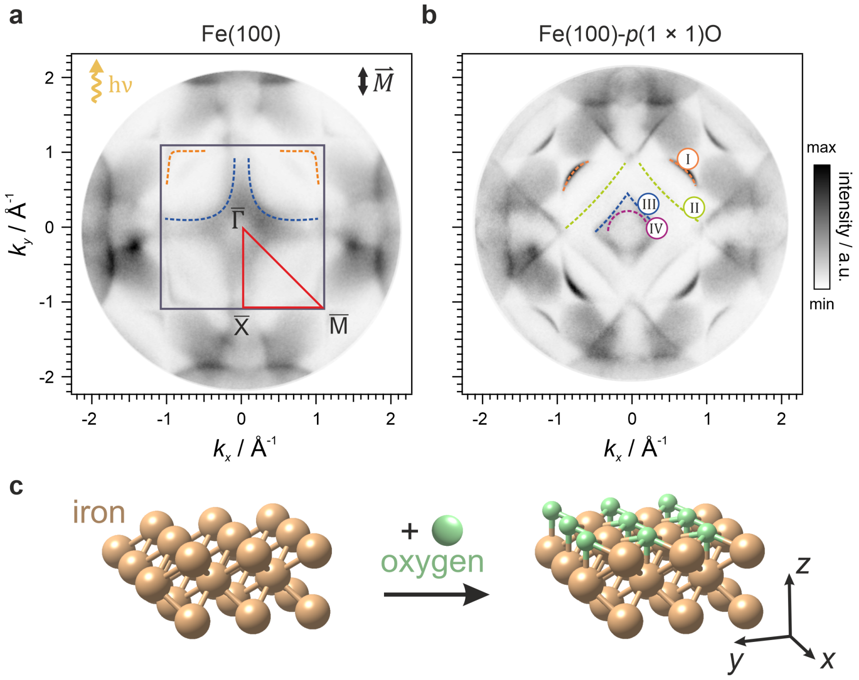

Figure 4.7: Momentum-resolved electronic structure of Fe(100) and Fe(100)–$p(1 \times 1)$O. **(a)**,**(b)** Momentum maps taken at $E = E_\mathrm{F}$ for **(a)** clean Fe(100) and **(b)** oxygen-passivated Fe(100)–$p(1 \times 1)$O. The SBZ is outlined in gray in (a), with red lines marking the high-symmetry directions. The incident light beam (impinging at 66° relative to the surface normal) and the magnetization ($\vec{M}$) are aligned along the k_y-direction. The measurements were performed using p-polarized light with a photon energy of $h\nu = 64\,\mathrm{eV}$. **(c)** Structural models of the Fe(100) surface before (left) and after oxygen adsorption (right). Published in [190].

Notably, all these states appear sharper than those observed for the clean Fe(100) surface. This enhanced definition can be attributed to the substantial narrowing of the d-bands, a direct consequence of increased electron correlation.

The modifications in the electronic structure induced by oxygen adsorption become even more evident when analyzing the energy dispersion of key spectral features along high-symmetry directions. To properly assess these changes, we first establish a baseline by examining the band structure of clean Fe(100). Understanding the dispersion of electronic states provides crucial insight into the role of electron correlations and serves as a reference for interpreting the effects of oxygen passivation.

The experimentally determined band structure of Fe(100) is presented in Fig. 4.8 (top), alongside theoretical calculations performed using DFT+DMFT, *i.e.* with many-body self-energy corrections (bottom). The agreement between experiment and theory is remarkably good, particularly for the band dispersion from E_F to $-2.0\,\mathrm{eV}$, as well as the broad satellite feature at $-6.0\,\mathrm{eV}$, both of which are well captured. Only the overall bandwidth is slightly overestimated, likely due to limitations of the perturbative solver used in the DMFT calculations [190].

These observations underscore the importance of a detailed band structure analysis as a foun-

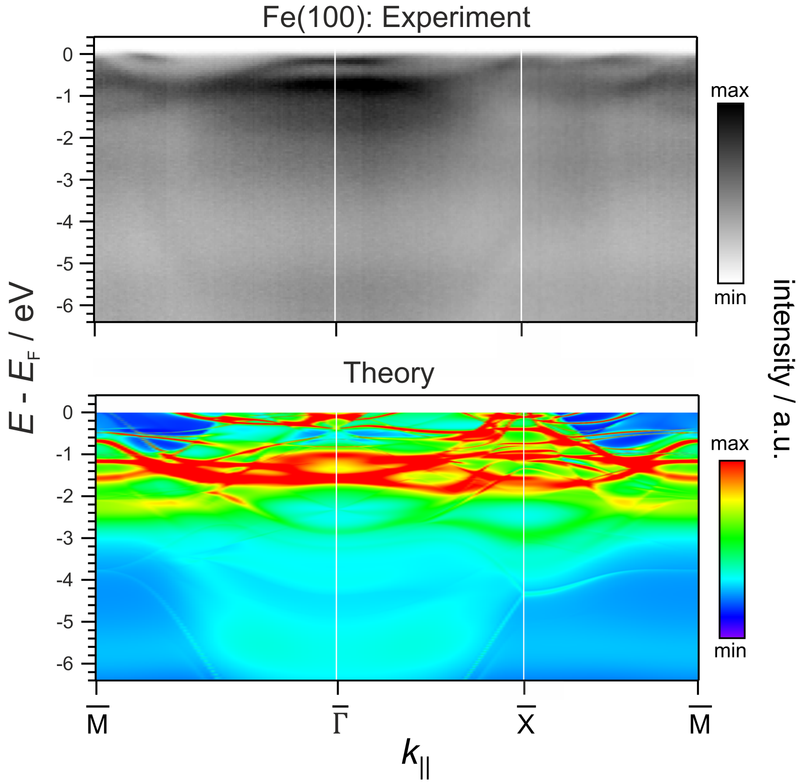

Figure 4.8: Comparison of experimental and theoretical electronic structure of Fe(100). (Top) Measured band structure of clean Fe(100), showing cuts along the $\overline{\mathrm{M}} - \overline{\Gamma} - \overline{\mathrm{X}} - \overline{\mathrm{M}}$ directions. (Bottom) Theoretical spectral function calculated using DFT+DMFT, incorporating electron correlation effects. The computed band structure captures key features observed in the experiment, including band broadening and renormalization effects. The comparison highlights the role of many-body interactions in shaping the electronic structure of Fe(100). Published in [190].

dation for understanding how oxygen adsorption reshapes the electronic states at the interface. Expanding on the preceding discussions, oxygen adsorption generates hybrid states near E_{F}, where Fe d-orbitals mix with antibonding O states, exhibiting strong Fe d character and undergoing significant renormalization due to enhanced electron correlation effects [263].

A complete characterization of the newly formed electronic states requires a systematic examination of the three-dimensional (3D) bulk BZ to ensure an unambiguous assignment. Fig. 4.9 provides an overview of the bulk BZ and the corresponding SBZ, illustrating how different photon energies sample distinct momentum-space regions. By varying the photon energy in MM experiments, we can track the dispersion of electronic states along k_z, enabling a direct distinction between bulk and surface states. Bulk states are expected to exhibit a strong k_z-dependence, while surface and interface states should remain unaffected by changes in photon energy [282].

Contrary to intrinsic surface states, adsorbate-induced states do not necessarily lie within the band gaps of the bulk-projected band structure. However, additional effects influencing photoemission

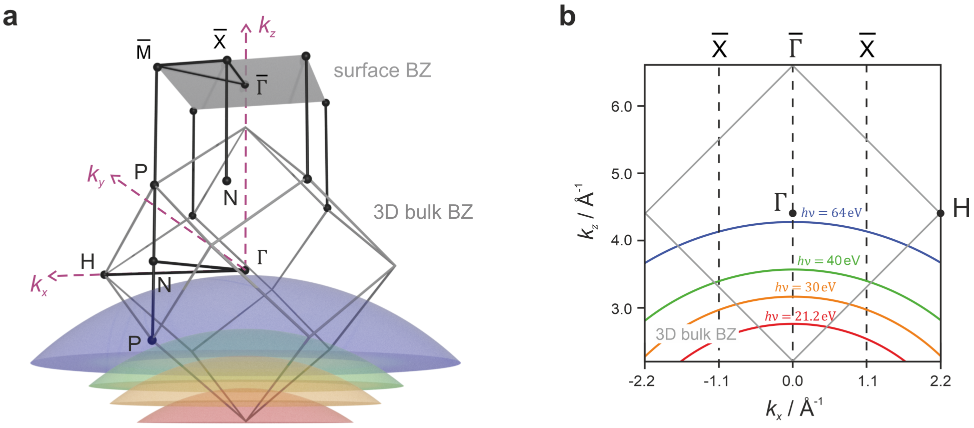

Figure 4.9: Relation between the 3D bulk BZ and the SBZ of Fe(100). **(a)** Schematic representation of the 3D bulk BZ of body-centered cubic (bcc) iron and its relation to the first SBZ of Fe(100). High-symmetry points are indicated, and the four colored spherical surfaces represent iso-energetic cuts corresponding to different photon energies used in photoemission experiments. **(b)** Side view of the 3D BZ, illustrating the cutting planes corresponding to the selected photon energies. These energy-dependent cuts in reciprocal space allow access to different regions of the bulk electronic structure in momentum-resolved photoemission spectroscopy measurements.

intensity can complicate the analysis and potentially lead to misinterpretation [189].

To establish whether distinct photoemission features originate from interface states — often referred to as ”extrinsic surface states” — or from bulk states, three common principles can be applied [138, 282]: (i) When comparing the pristine and passivated Fe surface, states that emerge after passivation can be clearly attributed to the interface. (ii) Because of their two-dimensional nature, surface states should not exhibit k_z-dispersion, in contrast to bulk states that disperse along k_z. Thus, states that remain unchanged across different photon energies are likely to be located at the surface. (iii) A comparison between experimental data and theoretical calculations can provide further insight into the origin of a given state.

To apply this approach, photon-energy-dependent MM measurements were conducted at 64 eV, 40 eV, 30 eV, and 21.2 eV, summarized in Fig. 4.10. These photon energies correspond to different slices through the bulk BZ, as indicated by the colored lines in Fig. 4.9b, which were calculated using the free-electron final state model with an assumed inner potential of $V_0 = 7\,\text{eV}$ [283]. The significant variation in k_z implies that bulk states should exhibit noticeable changes in their spectral appearance across different photon energies, whereas interface states should remain unchanged.

This expectation is confirmed by the experimental results. For clean Fe(100), only a single state, which extends along the $\overline{\Gamma\text{X}}$ path at the Fermi level (highlighted by a brown circle), can be identified as a true surface state, consistent with previous reports [284]. Upon oxygen adsorption, the formation of the Fe(100)–$p(1 \times 1)$O superstructure leads to the disappearance of this Fe(100) surface state, confirming its surface-related origin. Simultaneously, new electronic states emerge,

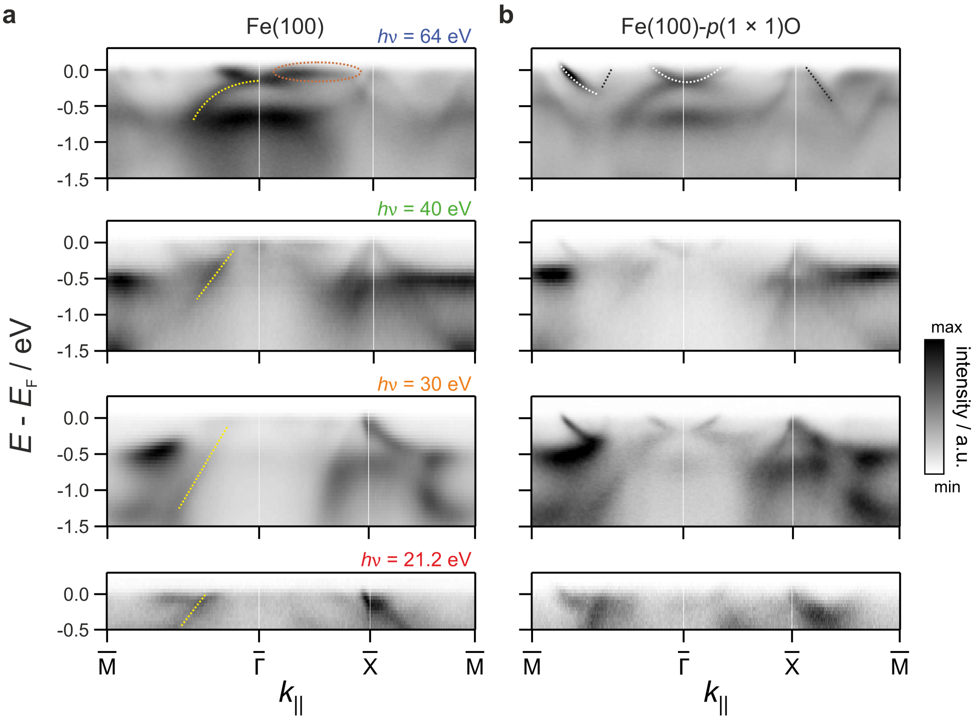

Figure 4.10: Momentum-resolved photoemission band structure of Fe(100) and Fe(100)–$p(1 \times 1)$O. Surface band structure of **(a)** Fe(100) and **(b)** Fe(100)–$p(1 \times 1)$O along the $\overline{\mathrm{M}} - \overline{\Gamma} - \overline{\mathrm{X}} - \overline{\mathrm{M}}$ direction, determined via momentum-resolved photoemission spectroscopy. Measurements were performed at different photon energies (64 eV, 40 eV, 30 eV, and 21.2 eV), enabling sampling across the entire 3D bulk BZ and facilitating the distinction between bulk and surface/interface states. For clean Fe(100), the brown circle highlights a prominent surface state, while the yellow lines highlight bulk bands. These bands exhibit strong dispersion as a function of photon energy. In contrast, the black and white highlighted features on the right, *i.e.* for (Fe(100)–$p(1 \times 1)$O, all remain mostly unchanged across different photon energies, indicating their surface/interface character.

which show no dispersion along k_z, suggesting that they are adsorbate-induced interface states rather than bulk bands.

Having established the interface nature of these states, we now examine the full experimental band structure of Fe(100)–$p(1 \times 1)$O and compare it with theoretical calculations. Fig. 4.11a presents the measured band dispersion along the $\overline{\mathrm{M}} - \overline{\Gamma} - \overline{\mathrm{X}} - \overline{\mathrm{M}}$ direction, revealing not only the previously discussed Fe d-related states near the Fermi level but also new dispersing bands at higher binding energies, corresponding to bonding oxygen states. The latter features were not present in the clean Fe(100) substrate, where only faint parabolic bands were observed alongside the broad satellite resonances. The emergence of these additional bands upon oxidation highlights the strongly hybridized nature of the oxygen p-orbitals at the interface.

To gain further insight into the interfacial electronic properties, we compare the experimental band structure with theoretical calculations incorporating many-body interactions. Fig. 4.11b shows the corresponding momentum-resolved DOS obtained from DFT+DMFT calculations.

The comparison reveals a remarkable agreement between experiment and theory, accurately reproducing the energy positions and dispersion of the observed features.

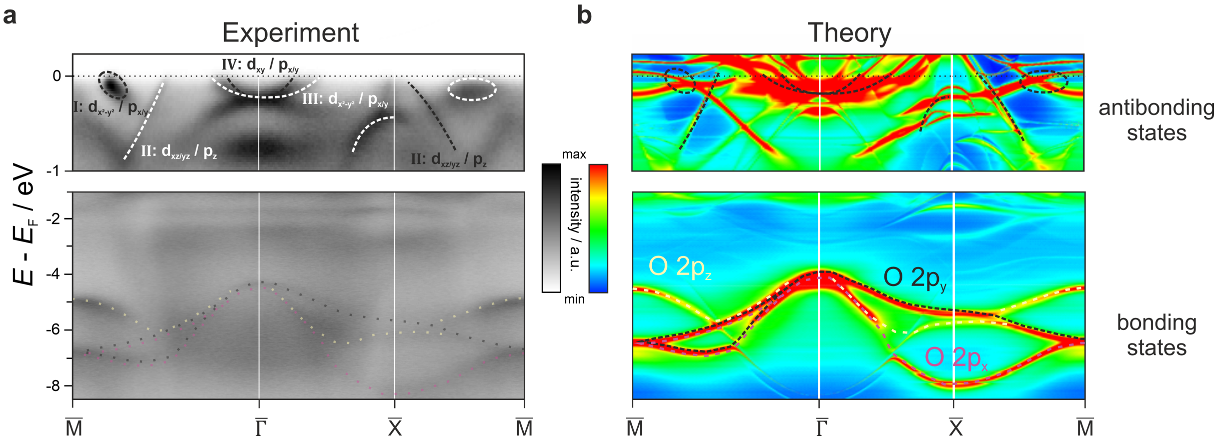

Figure 4.11: Comparison of experimental and theoretical surface band structure of Fe(100)–$p(1 \times 1)$O. **(a)** Momentum-resolved photoemission measurements of the Fe(100)–$p(1 \times 1)$O interface along the $\overline{M} - \overline{\Gamma} - \overline{X} - \overline{M}$ direction, acquired using a photon energy of $h\nu = 64\,\mathrm{eV}$. The upper panel focuses on the near-Fermi-level region (E_F to $-1.0\,\mathrm{eV}$), where key hybridized states are labeled according to their dominant orbital character. The lower panel presents the band structure over a wider energy range ($-1.0\,\mathrm{eV}$ to $-8.5\,\mathrm{eV}$), revealing deeper-lying states. **(b)** Theoretical band structure computed with electron correlation effects included via self-energy corrections. The upper panel shows the near-Fermi-level antibonding states, while the lower panel highlights the bonding states dominated by oxygen $2p$ orbitals. Published in [190].

While the hybridized antibonding states near the Fermi level originate predominantly from Fe d-orbitals, they are therefore quasiparticle states, *i.e.* single-particle-like electronic states that are renormalized by electron correlation effects. As a result, these states are confined to a narrow energy window of approximately 1 eV and exhibit reduced dispersion compared to their counterparts in clean Fe(100).

This behavior is a direct consequence of Fe(100)–$p(1 \times 1)$O being an intermediate correlated system, where dynamical self-energy contributions play a crucial role in determining the electronic structure. The band narrowing observed in experiment reflects an increase in the effective mass ratio m^*/m, induced by stronger electron-electron interactions. Earlier studies speculated that discrepancies between DFT calculations and experimental data might arise from missing correlation effects [263], and later attempts at implementing many-body corrections [266] provided partial improvements. However, these approaches failed to capture the magnitude of many-body interactions, preventing a conclusive description of the physics governing the chemisorbed interface. The present results provide direct experimental evidence that oxygen adsorption enhances electron correlation effects, substantially altering the electronic structure of Fe(100).

Beyond the antibonding hybrid states near the Fermi level, we now turn to the bands at lower energies, centered around $-6\,\mathrm{eV}$. These states exhibit a characteristic parabolic dispersion along the $\overline{XM}$-path (Fig. 4.11a) and can be unambiguously assigned to bonding interactions between the oxygen $2p$ (p_x, p_y, p_z) orbitals and Fe d-orbitals [259, 261]. This assignment is further supported by the orbital- and k-resolved spectral functions presented in Fig. 4.12.

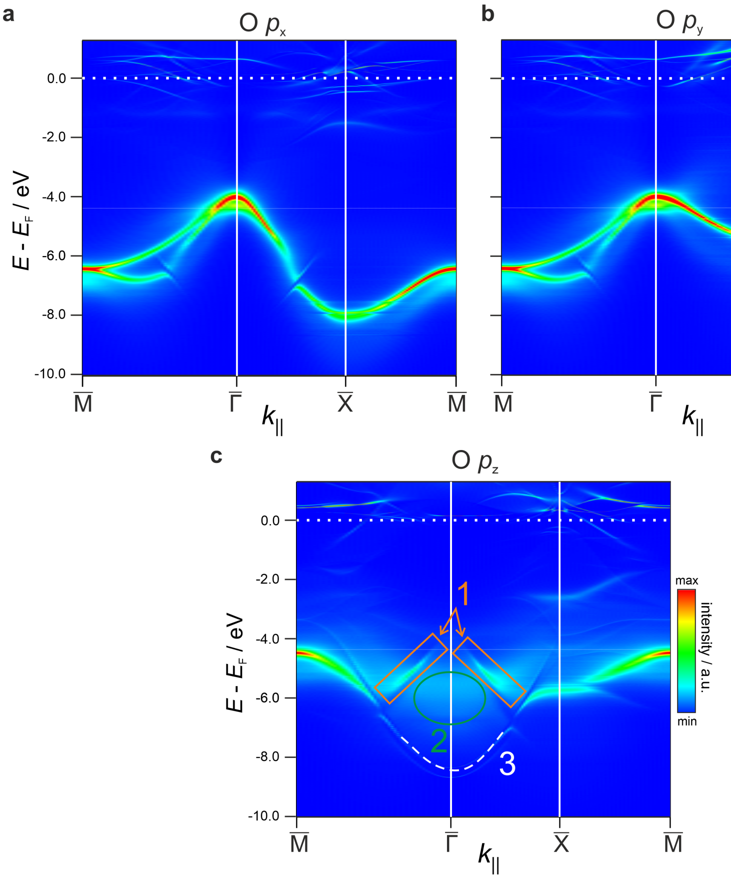

Figure 4.12: Oxygen-projected spectral functions of the Fe(100)–$p(1\times1)$O surface. **(a)–c)** DFT+DMFT spectral function projected onto the oxygen atom of the Fe(100)–$p(1\times1)$O surface, resolved for different oxygen $2p$ orbitals: **(a)** p_x, **(b)** p_y, and **(c)** p_z. The spectral weight distribution reveals the orbital character of the hybridized states. In c), three distinct O p_z-derived features near the zone center are marked: (1) states overlapping with p_x and p_y contributions, (2) a broad satellite-like feature near -6 eV, and (3) a low-energy dispersive band. Published in [190].

Yet, the most striking feature in this energy region is the merging of these sharp bonding states into a broad satellite feature of Fe near the $\overline{\Gamma}$-point. This satellite appears as a diffuse intensity between -5.0 eV and -7.0 eV, and is also clearly visible in the total DOS (Fig. 4.6). Unlike the antibonding states discussed earlier, this satellite feature is a true many-body excitation, which cannot be captured within a simple single-particle band structure description. Its enhancement upon oxygen adsorption is a direct consequence of the strengthening of the effective electron-electron interaction U, which increases the spectral weight in this energy region.

To further assess the role of electron correlations, we compare the experimental findings with different theoretical approaches. Standard DFT calculations within the *local spin density* *approximation* (LSDA) fail to reproduce the experimentally observed band structure (Fig. 4.13, top).

LSDA predicts electronic states broadly distributed across a large energy range, from E_F down to $-8\,\mathrm{eV}$, whereas MM measurements reveal a much narrower spectral weight, confined within a $2\,\mathrm{eV}$ window below the Fermi level. Additionally, LSDA fails to reproduce the distinct satellite at $-6\,\mathrm{eV}$, instead only predicting a band-like features in this energy range.

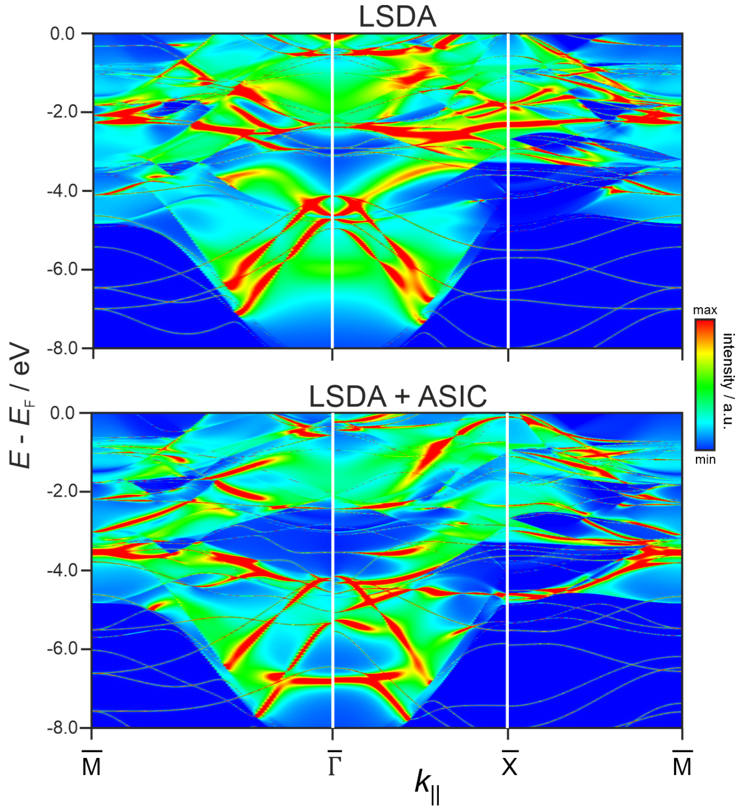

Figure 4.13: Spectral function of the Fe(100)–$p(1 \times 1)$O surface: comparison of LSDA and LSDA+ASIC calculations. (Top) Spectral function of the Fe(100)–$p(1 \times 1)$O surface calculated using DFT within the LSDA approximation. (Bottom) The same spectral function computed using LSDA with the addition of an approximate self-interaction correction (ASIC). Published in [190].

To evaluate whether self-interaction corrections improve the agreement, the *atomic self-interaction correction* (ASIC) method was applied, which has been successfully used for transition metal oxides [16, 17, 26, 27, 30, 31, 120, 285]. However, as shown in the bottom panel of Fig. 4.13, ASIC does not significantly improve the agreement with experiment.

Although some features become slightly sharper, the overall spectral weight remains too broadly dispersed, and the quasiparticle renormalization observed in MM is not reproduced. This failure highlights that static corrections alone are insufficient to describe Fe(100)–$p(1 \times 1)$O, as they do not account for the dynamical electron correlation effects arising from many-particle scattering.

These discrepancies confirm that Fe(100)–$p(1\times1)$O is an intermediate correlated metal, where only dynamical self-energy corrections can accurately describe the experimental electronic structure.

By systematically comparing MM measurements with DMFT-based calculations, we establish that Fe(100)–$p(1\times1)$O exhibits quasiparticle renormalization, suppressed band dispersion, and an enhanced satellite feature, all of which provide direct evidence that oxygen adsorption significantly enhances electron correlations at this interface.

4.4.2 Spin-Resolved Band Structure of Fe(100) and Fe(100)–$p(1\times1)$O

Having assigned the main features of the surface band structure, we now analyze the spin-resolved photoemission data, which provide deeper insight into the magnetic properties of Fe(100)–$p(1 \times 1)$O. Fig. 4.14 presents a comprehensive overview, including a spin-resolved momentum map in Fig. 4.14a and the extracted band structure in Fig. 4.14b.

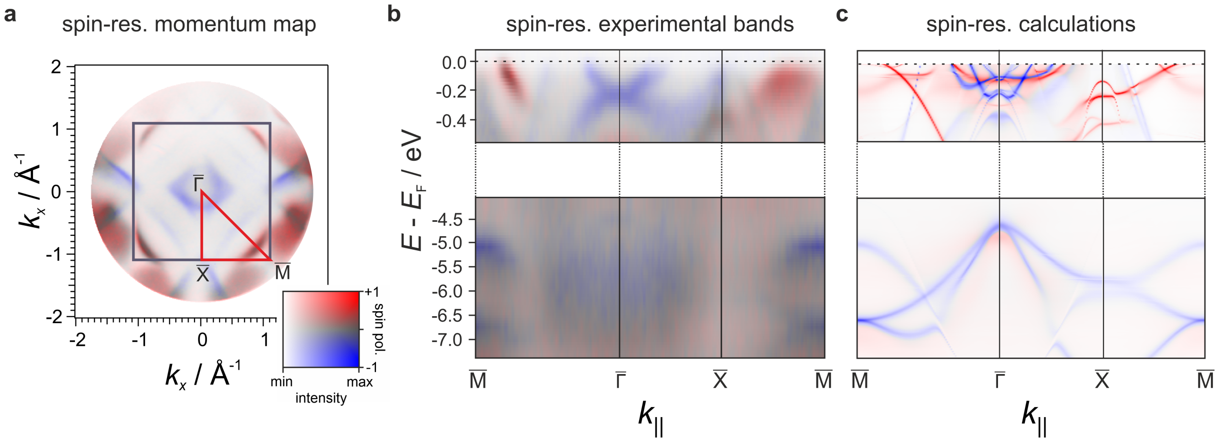

Figure 4.14: Spin-resolved band structure of oxygen-passivated Fe(100)–$p(1\times1)$O. **(a)** Spin-resolved photoemission momentum map near E_F recorded at a photon energy of $h\nu = 64\,\text{eV}$. The color scale represents spin polarization, with blue indicating minority and red indicating majority spin states. The SBZ and high-symmetry directions are indicated. **(b)** Experimentally measured spin-resolved band structure of the Fe(100)–$p(1 \times 1)$O surface, covering the energy regions of the antibonding states (E_F to $-0.5\,\text{eV}$, top panel) and bonding states (-4.0 to $-7.5\,\text{eV}$, lower panel). **(c)** Theoretical spin-polarized band structure computed for the same energy range as (b). The 2D spin polarization color scale applies to (a), (b), and (c). Published in [190].

To simultaneously display both spin polarization and spectral intensity, the color scale follows a two-dimensional representation (Fig. 4.14b, right), where the blue-red color gradient encodes the spin polarization, while color saturation represents the total intensity [223]. These data allow for a direct tracking of the dispersion of both the bonding and antibonding states in the two spin channels, facilitating a meaningful comparison with theoretical calculations. From these measurements, the spin character of the antibonding states near the Fermi level can be directly identified. The states near the center of the SBZ primarily originate from minority-spin electrons (blue regions), while those located near the $\overline{\mathrm{M}}$-point exhibit a strong majority-spin character (red regions).

For a direct comparison, the spin-resolved theoretical band structure is presented alongside the experimental results in Fig. 4.14c. As discussed previously, enhanced electron correlations have a profound impact on the spin-resolved spectra. A particularly striking consequence is the breakdown of the single-particle Stoner model of ferromagnetism in the energy region close to the Fermi level. Unlike the conventional expectation of exchange-split Fe 3*d*-bands, the data reveal no clear exchange splitting.

While some minor discrepancies exist between experiment and theory near the $\overline{\Gamma}$-point, potentially arising from photoemission matrix element effects [189] or the neglect of non-local correlations in DMFT [286], the overall agreement between theoretical and experimental results is remarkably good across most regions of the SBZ. Importantly, despite the heavily reduced exchange splitting of Fe *d*-bands due to oxygen adsorption, the spin polarization of states at E_F remains significant. The former finding challenges earlier assumptions, as previous studies suggested that surface Fe *d*-band characteristics remain mostly unaffected by passivation [259]. This interpretation was consistent with computational predictions at the time, which were based on single-particle approximations.

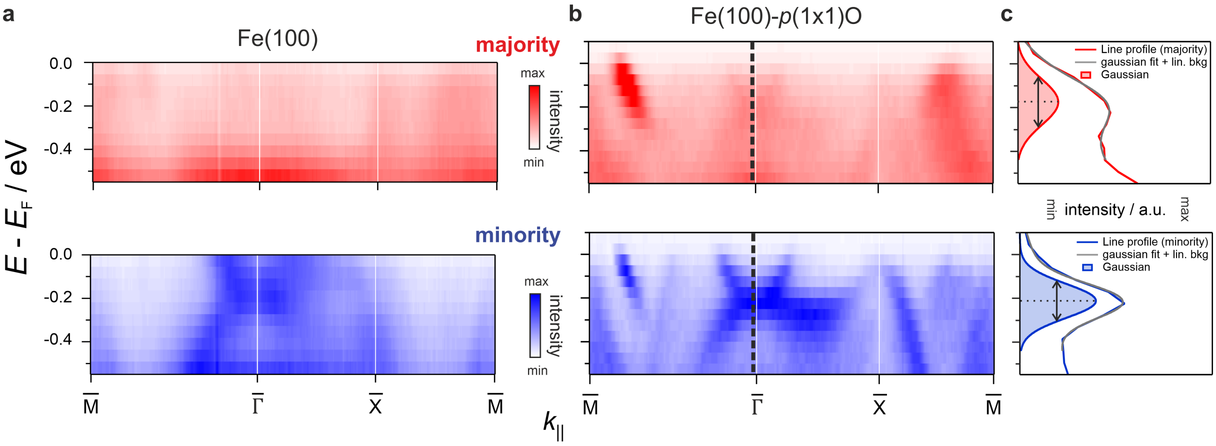

Figure 4.15: Spin-resolved band structure near E_F for Fe(100) and Fe(100)–$p(1\times1)$O. **(a),(b)** Spin-resolved contributions to the experimental band structure near E_F for **(a)** clean Fe(100) and **(b)** Fe(100)–$p(1\times1)$O, measured using *p*-polarized light with a photon energy of $h\nu = 64\,\mathrm{eV}$. Oxygen adsorption modifies the electronic structure, introducing additional features in both spin channels. In (b), two dashed lines near $\overline{\Gamma}$ indicate the positions where EDCs were extracted for further analysis. **(c)** Extracted line profiles from (b), showcasing Gaussian fits with a linear background used to determine the bandwidth and exchange splitting. This fitting procedure enables a precise quantification of the changes induced by oxygen adsorption in the spin-dependent band structure. Published in [190].

Our findings highlight the necessity of combining state-of-the-art spin-resolved photoemission experiments with advanced many-body calculations to correctly disentangle and interpret the complex spin-resolved electronic structure of the Fe–O system.

Next, to perform a more quantitative evaluation based on the experimental data, the two spin contributions can also be examined separately. We begin by presenting spin-resolved data for clean Fe(100) and oxygen-passivated Fe(100)–$p(1 \times 1)$O in the region near the Fermi energy. This comparison provides a direct visualization of how oxygen adsorption modifies the spin-dependent electronic structure.

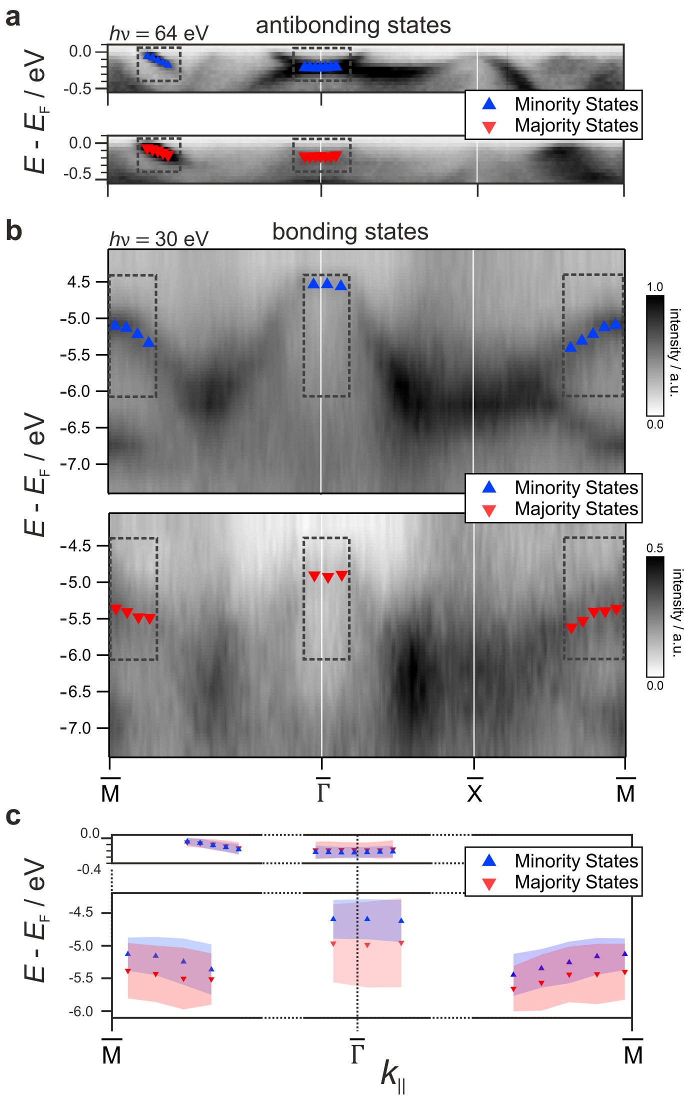

Figure 4.16: Spin-resolved photoemission analysis of bonding and antibonding Fe–O states. **(a),(b)** Separated majority (red) and minority (blue) spin photoemission intensities for the Fe–O interface, showing **(a)** antibonding states and **(b)** bonding states. The peak positions (triangles) were obtained from Gaussian fits to energy distribution curves within the highlighted boxes. To optimize signal detection, antibonding states were recorded using a photon energy of $h\nu = 64\,\mathrm{eV}$, while bonding states were measured at $h\nu = 30\,\mathrm{eV}$. **(c)** Combined summary of the extracted peak positions, including Gaussian widths, to illustrate the spin-dependent energy distribution of both bonding and antibonding Fe–O states along the $\overline{\mathrm{M}} - \overline{\Gamma} - \overline{\mathrm{X}} - \overline{\mathrm{M}}$ direction. Published in [190].

Fig. 4.15 displays the majority (red) and minority (blue) contributions for pristine Fe(100) (Fig. 4.15a) and Fe(100)–$p(1 \times 1)$O (Fig. 4.15b) in a narrow energy window around the Fermi level. For clean Fe(100), the majority-spin channel exhibits almost no intensity close to E_F, whereas distinct features are observed around $\overline{\Gamma}$ in the minority channel. However, oxygen adsorption alters the spin-dependent electronic structure, and leads to a significant redistribution of spectral weight. In the majority-spin channel, states now appear near E_F that coincide energetically with the modified bands in the minority channel. This change reflects the collapse of Stoner-like magnetism as the exchange splitting is severely decreased.

To quantitatively track these changes, line intensity profiles can be extracted from the spin-resolved spectra. The dashed lines in Fig. 4.15b indicate the positions from where the two exemplary line profiles were extracted that are displayed in Fig. 4.15c.

Fitting of these intensity profiles using a Gaussian function with a linear background allows us to determine both the peak position and the energy width of each feature, with the *full width at half maximum* (FWHM) used as a measure of the effective bandwidth. This approach enables a direct and quantitative comparison of the bandwidth and exchange splitting before and after oxygen adsorption.

In the following, we apply this analysis to shed light on the properties of the bonding and antibonding states of the Fe–O surface in both spin channels. Specifically, we perform the band-fitting analysis for distinct momentum regions where features directly linked to oxygen chemisorption become visible. This is illustrated in Fig. 4.16, where line profiles were extracted from the areas highlighted by the dotted boxes and fitted according to the described procedure. Each region was carefully selected to isolate a single spectral feature, ensuring robust extraction of both position and width.

Fig. 4.16 presents the results of this spin-resolved analysis, with panels (a) and (b) showing the separated majority- and minority-spin photoemission intensities for both the antibonding and bonding Fe–O states. To optimize sensitivity to these specific bands, measurements were performed at photon energies of $h\nu = 64\,\mathrm{eV}$ for the antibonding states and $h\nu = 30\,\mathrm{eV}$ for the bonding states. The extracted peak positions and widths are summarized in Table 4.1 and Table 4.2, providing a comprehensive overview of the spin-dependent electronic structure at the oxygen-terminated Fe surface.

Table 4.1: Extracted exchange splitting $\mathit{\Delta}_\mathrm{ex}$ for both bonding and antibonding states at $\overline{\Gamma}$ and $\overline{\mathrm{M}}$.

k-point	state	$\mathit{\Delta}_\mathrm{ex}$ / meV
$\overline{\Gamma}$	antibonding (E_F)	-40 ± 10
$\overline{\mathrm{M}}$	antibonding (E_F)	-10 ± 10
$\overline{\Gamma}$	bonding (O $2p$)	360 ± 30
$\overline{\mathrm{M}}$	bonding (O $2p$)	230 ± 50

To further illustrate these trends, Fig. 4.16c presents a visual summary of the fit results, where the extracted peak positions are plotted, and the average widths for each region are shown as error bars. This direct comparison of band positions and their spin-dependent broadening across different momentum points offers complementary insight to the quantitative values listed in the tables.

Table 4.2: Extracted FWHM values for bonding/antibonding states at $\overline{\Gamma}$ and $\overline{\mathrm{M}}$.

k-point	state	FWHM / meV	
		majority	minority
$\overline{\Gamma}$	antibonding (E_F)	250 ± 20	180 ± 20
$\overline{\mathrm{M}}$	antibonding (E_F)	160 ± 30	140 ± 30
$\overline{\Gamma}$	bonding (O $2p$)	640 ± 50	310 ± 20
$\overline{\mathrm{M}}$	bonding (O $2p$)	420 ± 40	300 ± 50

This analysis reveals two key trends. First, the exchange splitting Δ_ex near E_F collapses upon oxygen adsorption. As a result, the minority-spin features at $\overline{\Gamma}$ shift slightly below their majority-spin counterparts, with a remaining offset of approximately 40 meV. This suppression in exchange splitting provides direct evidence for correlation-driven band renormalization at the oxygen-covered interface. Second, the majority bands systematically exhibit broader linewidths (larger FWHM) compared to the minority bands, indicating a significantly reduced quasiparticle lifetime for majority carriers. This effect is particularly pronounced for the oxygen bonding states: at $\overline{\Gamma}$ the majority bandwidth exceeds 600 meV, roughly twice the width of the minority band.

This spin-dependent broadening is consistently observed at multiple high-symmetry points within the SBZ. At both $\overline{\Gamma}$ and near $\overline{\mathrm{M}}$, bonding majority-spin bands exhibit significantly larger FWHM than their minority counterparts, suggesting that the reduced lifetime of majority carriers is not confined to isolated k-points, but reflects an intrinsic property of the oxygen-terminated Fe surface.

A detailed analysis of the DFT+DMFT results reveals that this lifetime asymmetry originates from the coupling of these states to the Fe-derived satellites — many-body features that are substantially more pronounced in the majority-spin channel. As a result, majority electrons experience faster relaxation than minority electrons, a manifestation of dynamic spin filtering [287], driven by electronic correlations [190].

Notably, as one approaches $\overline{\Gamma}$ and moves to energies further below E_F, the oxygen p_z states begin to directly overlap and merge with the Fe-derived satellite features. This interaction leads to additional broadening and complicates the disentanglement of Fe and O contributions in the measured spectra. This overlap is particularly important because it directly impacts the apparent exchange splitting extracted for the oxygen p_z states: the satellite itself is spin-polarized and contributes additional spectral weight at distinct energies. As a result, the extracted splitting may not reflect a purely oxygen-derived signal. To better assess this effect and to resolve discrepancies in earlier reports, we compare our results to previous spin-resolved photoemission studies conducted at different photon energies.

In particular, Getzlaff *et al.* [261] performed spin-resolved measurements at a photon energy of 21.2 eV and reported an exchange splitting of approximately 250 meV for the oxygen p_z states, which is fully consistent with the values we obtain at 30 eV. In contrast, Johnson *et al.*

[260], who conducted their measurements at 60 eV, reported a much larger exchange splitting of $\Delta_{\mathrm{ex}} \approx 1.3\,\mathrm{eV}$ for the bonding O p_z states at $\overline{\Gamma}$, posing an apparent discrepancy between the two studies.

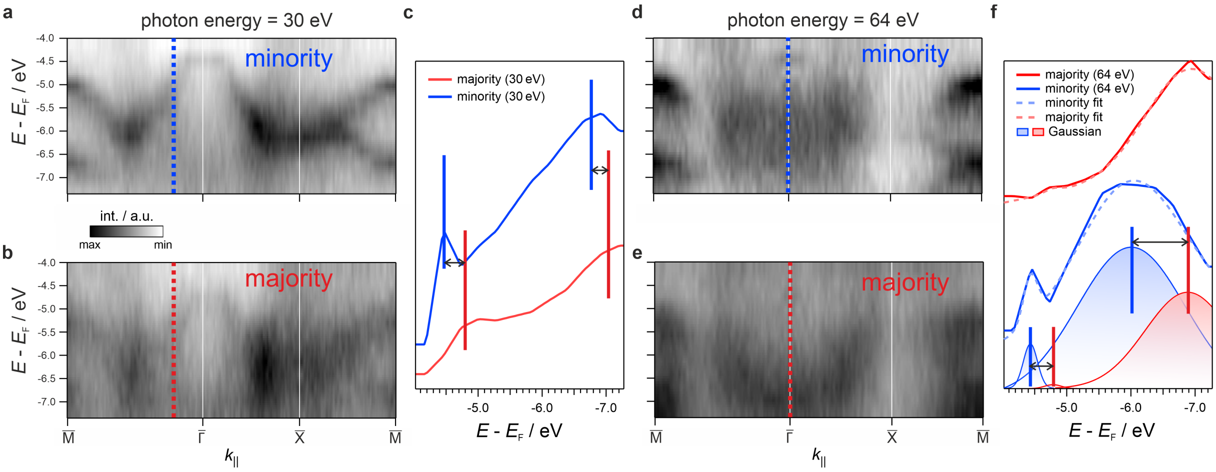

Figure 4.17: Spin-resolved band structure of Fe(100)–$p(1\times1)$O at different photon energies. **(a),(b)** Spin-resolved band structure measured $h\nu = 30\,\mathrm{eV}$, showing **(a)** minority and **(b)** majority spin states. Vertical dashed lines at $\overline{\Gamma}$ indicate the positions where intensity profiles were extracted for further analysis. **(c)** Intensity profiles extracted at $\overline{\Gamma}$ from (a) and (b). Estimated peak positions are indicated by vertical bars. **(d),(e)** Same as (a) and (b), but measured at $h\nu = 64\,\mathrm{eV}$ to focus more on the Fe-related contributions and their spin character. **(f)** Intensity profiles extracted from the 64 eV measurements, fitted with Gaussians and a linear background to determine band positions and spin splitting.

To directly investigate the origin of this difference, we compare spin-resolved measurements at both $h\nu = 30\,\mathrm{eV}$ and $h\nu = 64\,\mathrm{eV}$, allowing us to probe the same states under conditions that either enhance or suppress Fe-derived spectral features due to relative changes in the photoionization cross section. In particular, at a photon energy of $h\nu = 30\mathrm{eV}$ the ratio in cross section is O : Fe = 1.30, which then reduces to O : Fe = 0.55 for energies of $h\nu = 64\,\mathrm{eV}$ [288].

At 30 eV, where oxygen-derived features dominate, we observe exchange splittings fully consistent with Getzlaff's results (see Table 4.1 and Table 4.2). At 64 eV, however, where the relative Fe $3d$ cross section is significantly enhanced, the extracted exchange splitting increases drastically, closely matching the value reported by Johnson *et al.* (see Fig. 4.17). This comparison demonstrates that the apparent exchange splitting is not a purely intrinsic property of the oxygen p_z states, but instead reflects additional contributions from hybridization with the overlapping Fe satellites.

This interpretation is fully supported by our DMFT calculations, which capture both the position and the spin polarization of the Fe satellite. The calculations presented in Fig. 4.18 show that the majority-spin satellite overlaps spectrally with the oxygen p_z states, artificially enhancing the apparent exchange splitting when both contributions are present. This spectral mixing, which becomes pronounced at photon energies that enhance Fe-related intensity, explains the discrepancy between past studies and highlights the essential role of electron correlations in shaping the interfacial electronic structure.

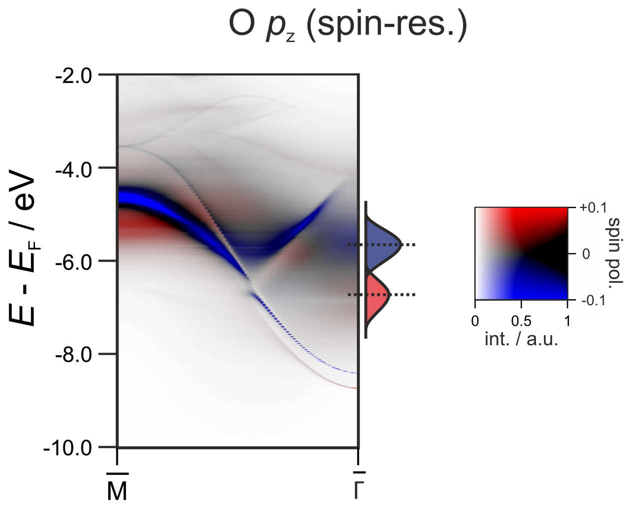

Figure 4.18: Spin-resolved band structure for the O p_z-projected states along the $\overline{\mathrm{M}}$–$\overline{\Gamma}$ direction with enhanced contrast to emphasize the spin polarization of broad resonances. The Gaussians-like curves on the right indicate the approximate peak positions.

4.4.3 Tuning Electron Correlation via Adsorbate Variation

Having illustrated the distinctive role of chemisorption in modifying electron correlation at $3d$ transition-metal ferromagnetic surfaces, the next, broader question concerns how different adsorbates might influence correlation effects at metal surfaces more generally. To systematically address this question, the Fe(100)–$p(1 \times 1)$O system serves as a model platform, where the effect of the adsorbate on the surface Fe atoms is simulated by introducing an external “gate” potential V_g applied to the on-site energy of oxygen. By tuning V_g, the alignment between oxygen-derived states and the Fe d-bands is systematically varied, mimicking the electronic influence of adsorbates with different electronegativities or molecular orbital energies. This approach allows for a controlled study of how the surface electronic structure and correlation strength respond to changes in the adsorbate potential. The case $V_\mathrm{g} = 0\,\mathrm{eV}$ corresponds to the on-site energy predicted by DFT within the LSDA.

Fig. 4.19 summarizes the resulting trends. In panel (a), the spin-resolved and total occupation of the Fe d-orbitals is shown as a function of V_g. Although the variations in occupation are moderate due to the metallic nature of the surface, clear trends emerge. For larger (more positive) V_g, the spin up d-orbitals — especially the in-plane d_{xy} orbital — become depopulated, moving away from full occupancy, while the spin down orbitals gain charge. Conversely, for smaller (more negative) V_g, the spin up orbitals approach full occupancy, and the spin down orbitals become progressively emptied.

These changes in occupation directly influence the correlation strength at the surface. The effective degree of correlation is quantified in Fig. 4.19b through the mass enhancement factor m^*/m, calculated using DFT+DMFT. A clear monotonic increase in m^*/m is observed with increasing V_g, indicating that larger V_g values drive the system into a more correlated regime. Importantly, the increase in correlation occurs even though the parameters U and J are held

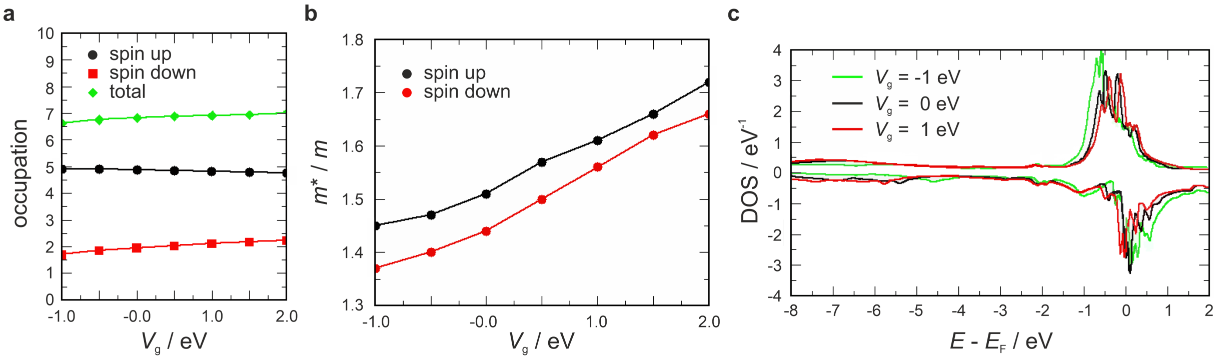

Figure 4.19: Modelling differing adsorbates by adding an on-site gate potential V_g. **(a)** Spin up, spin down, and total DFT occupation of the surface Fe d-orbitals in Fe(100)–$p(1 \times 1)$O as a function of the applied gate potential V_g, which shifts the oxygen on-site energy. **(b)** Effective mass enhancement factor m^*/m obtained from DFT+DMFT calculations as a function of V_g. **(c)** Spin-resolved DOS projected onto the surface Fe atom in Fe(100)–$p(1 \times 1)$O, calculated by DFT+DMFT for three representative values of V_g. Published in [190].

constant at 3.0 eV and 1.1 eV, respectively. This underlines that correlation strength depends not only on the bare interaction parameters, but also sensitively on the degree of orbital filling — a characteristic feature of correlated d-electron systems.

Physically, this enhancement of m^*/m indicates that electrons become increasingly dressed by many-body interactions as V_g increases. This dressing reflects the degree to which single-particle excitations are renormalized due to electron-electron scattering, with shorter quasiparticle lifetimes. In contrast, smaller V_g reduce correlation effects, allowing the electronic structure to approach the single-particle DFT limit, where quasiparticles are longer-lived and less dressed.

The impact of these correlation changes on the density of states (DOS) is shown in Fig. 4.19c, where the spin-resolved DOS projected onto the surface Fe atom is plotted for selected values of V_g. Increasing V_g leads to substantial broadening of the spectral features near the Fermi level and a clear reduction of the spin splitting, both direct consequences of enhanced electron correlations. This correlation-driven reduction in exchange splitting reflects the well-documented competition between local Coulomb interactions and itinerant magnetism, which is particularly relevant at metallic surfaces with adsorbates.

It is important to emphasize that these calculations assume the Fe(100)–$p(1 \times 1)$O adsorption geometry, with oxygen occupying the fourfold hollow sites in a dense monolayer. In practice, the adsorption geometry and resulting superstructure can change significantly with the choice of adsorbate. For example, nitrogen and carbon adsorbates are known to form $c(2\times2)$ reconstructions on Fe(100) [289, 290], corresponding to a lower adatom density compared to the $p(1 \times 1)$ structure. Changes in coverage directly alter the degree of hybridization, modify the charge transfer per surface atom, and thereby influence the correlation strength.

Additionally, different adsorbates may preferentially occupy alternative adsorption sites, such as top or bridge sites, rather than hollow sites. This change in adsorption site affects which Fe d-orbitals participate most strongly in the adsorbate interaction. Adsorption at hollow sites tends to couple more strongly to in-plane orbitals such as d_{xy}, while adsorption at top sites enhances the involvement of out-of-plane orbitals like d_{z^2}. Such variations would alter the specific occupation trends observed here and could shift the balance between spin up and spin down populations in distinct ways — an effect that remains to be explored.

Overall, this analysis highlights that adsorption not only modifies the surface electronic structure through direct charge transfer and hybridization, but also provides a direct and versatile mechanism to tune electronic correlations. The resulting changes in correlation strength — and the associated modification of spin polarization and quasiparticle lifetimes — have direct consequences for molecular spintronic devices, where efficient spin injection relies critically on the interfacial spin polarization. This perspective, incorporating both structural and electronic factors, provides a general and transferable framework for understanding correlation effects at hybrid adsorbate-metal interfaces, extending well beyond the specific Fe(100)–$p(1 \times 1)$O model system considered here.

4.5 Conclusion: Adsorbate-Enhanced Electron Correlation and the Stoner Picture of Band Ferromagnetism

This chapter explored the electronic structure and correlation effects at the interface between oxygen and ferromagnetic Fe(100), demonstrating that adsorbate-induced changes in the DOS of the metal cannot be considered a minor perturbation, but rather a central aspect in understanding such interfaces. The combination of spin-resolved momentum microscopy and many-body theoretical modeling revealed that the oxygen adsorption significantly enhances electronic correlations in the Fe *d*-bands. This leads to a substantial narrowing of the Fe *d*-states near the Fermi energy and a pronounced reduction of the exchange splitting — effects that cannot be captured within a simple Stoner picture of ferromagnetism.

Moreover, correlation induces spin-dependent broadening of electronic bands at larger binding energies, along with the emergence of satellite features, which are clear fingerprints of many-body physics. These results show that adsorption can be used as a tool to tune electronic correlations at metallic surfaces, effectively enabling access to intermediate correlated metallic regimes with distinct properties that would not be realized in clean systems. This finding is of general importance for the description of ferromagnetic metal surfaces and interfaces, particularly in the context of molecular spintronics and heterogeneous catalysis.

A particularly relevant consequence of these correlation effects is their impact on subsequent adsorption processes at such passivated surfaces. In conventional surface science, the *d*-band center model is widely used to rationalize how the electronic structure of a metal surface influences the strength of chemical bonding with adsorbates. In its simplest form, this model assumes that the metal DOS remains largely unaffected by the adsorption process itself, meaning the bonding can be described using a single-particle picture. However, the results of this chapter demonstrate that such an assumption is no longer valid when strong correlation effects are induced by the initial adsorption of oxygen.

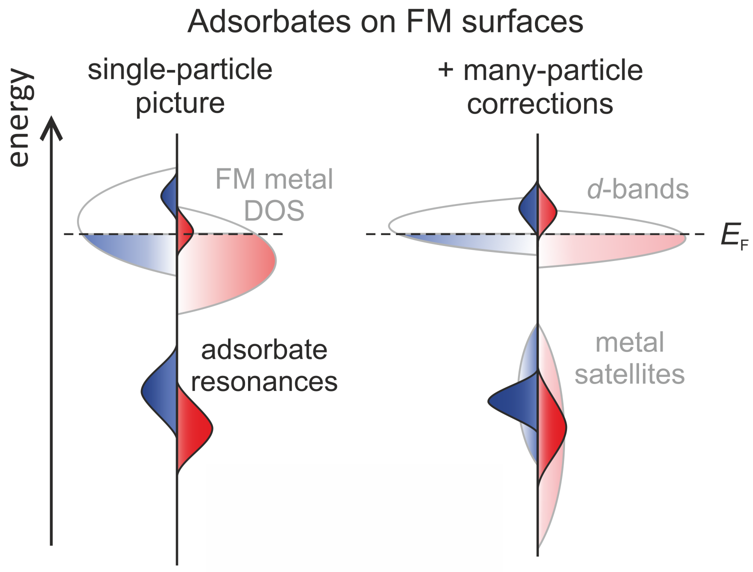

Figure 4.20: Impact of electron correlation on the DOS for adsorbed atoms or molecules hybridized with FM surfaces. The left panel illustrates the single-particle picture based on the *d*-band center model, where the spin-dependent hybridization of atomic oxygen states results in the formation of bonding and antibonding resonances (black lines), while the metal DOS (grey lines) remains largely unaffected. The right panel shows the influence of many-body effects, where electron correlation leads to significant modifications in the metal DOS, including the emergence of satellite features at lower energies and a strong reduction of the exchange splitting near the Fermi energy. Published in [190].

As illustrated in Fig. 4.20, the single-particle *d*-band center model (left panel) describes hybridization between adsorbate states and a largely unperturbed metal DOS. In contrast, the correlated picture (right panel) shows that the metal DOS itself is strongly reshaped by correlation, including the formation of satellite features and a reduction of the exchange splitting. These changes are expected to have direct consequences for the bonding of additional adsorbates on top of this passivated surface, as both the energetic position and the effective width of the hybridizing states will be altered. Therefore, understanding how correlation modifies the Fe *d*-bands is crucial for correctly describing the chemical and magnetic interaction with further adsorbates.

5 Correlation Effects and Bonding at the Pentacene/Fe(100)–$p(1\times1)$O Interface

5.1 Introduction: Chemisorption, Correlation, and the Limits of Traditional Models

The previous chapter demonstrated that oxygen adsorption on Fe(100) enhances correlation effects in the Fe surface layer, leading to a narrowing of the Fe *d*-bands near the Fermi energy and a reduction of the exchange splitting. Notably, recent investigations by Cao *et al.* [32] suggest that such changes in the metal DOS, particularly the reduction of the exchange splitting, can severely increase the reactivity of a ferromagnetic surface. Therefore, the correlation-induced changes in the DOS could counteract the otherwise passivating nature of the oxygen layer, thereby influencing the interaction with subsequently deposited adsorbates.

This raises the central question of this chapter, which is also graphically displayed in Fig. 5.1:

> How do correlation-induced modifications of the Fe electronic structure, triggered by oxygen-passivation, affect the bonding of subsequently deposited adsorbates, in particular organic molecules?

To address this issue, we return to the conceptual foundation of chemisorption as captured by the Newns–Anderson model. This framework predicts that the essential adsorption characteristics of adsorbate/metal interfaces can be derived from two key quantities: **(i)** the metal's density of states (DOS), and **(ii)** the spatial overlap between molecular orbitals and metal states.

And while this model and the related *d*-band model are extremely powerful and successful, they are primarily developed for small adsorbates with localized orbitals, where the hybridization is assumed to be spatially uniform. These assumptions begin to break down for larger organic molecules, such as *pentacene* (5A), which comprise a large number of atoms and cover lateral areas that vastly exceed the atomic spacing of the substrate.

Hence, in such cases, the interaction between the molecule and the surface can no longer be regarded as uniform, but instead becomes sensitive to the local environment experienced by different molecular regions [57, 127]. This naturally raises the question of how the shape and symmetry of molecular orbitals influence the local coupling strength. An early conceptual insight into the importance of orbital structure was provided by Kenichi Fukui [291, 292], who recognized that the spatial distribution and symmetry of molecular orbitals govern how chemical reactions proceed. Although his frontier molecular orbital theory was originally formulated for reactions between isolated molecules, the underlying idea that effective interactions depend on orbital overlap also apply to molecule–surface systems.

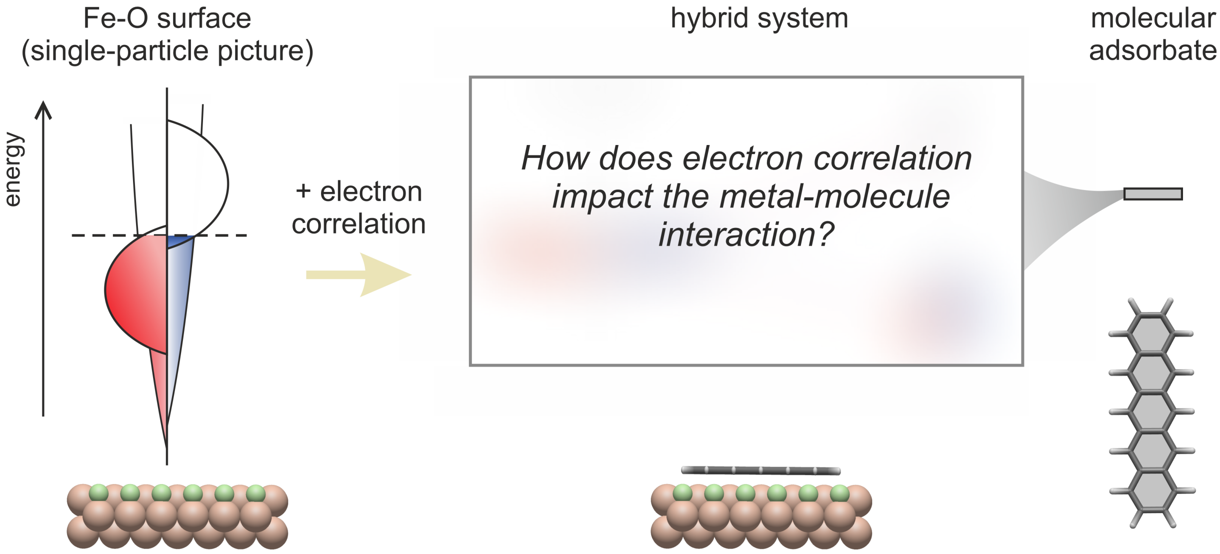

Figure 5.1: Schematic illustration of the central question guiding this chapter. Left: Single-particle schematic of the Fe d-band structure for the Fe–O surface prior to the inclusion of electron correlation. Right: Electronic structure of a typical molecular adsorbate, characterized by sharp energy levels. The key question, highlighted in the center, concerns the nature of the electronic structure of the resulting hybridized interface once correlation-induced d-band renormalization is taken into account.

Of particular relevance are the frontier orbitals, *i.e.* the HOMO and LUMO, whose spatial distribution and energy level alignment with the substrate states determine how hybridization unfolds at the interface. In this chapter, we aim to explore how the frontier orbital structure of extended conjugated molecules dictates their interaction with a correlated Fe–O surface.

Scientific Focus of This Chapter

To investigate the introduced question, this chapter focuses on the adsorption of 5A — a prototypical conjugated organic semiconductor renowned for its high charge-carrier mobility [293] — on the oxygen-passivated Fe(100) surface (Fe–O). Hereby, the Fe–O surface serves as a well-characterized example of a correlation-modified metal surface, while 5A, with its extended π-system and well-characterized frontier orbital structure, represents an ideal model system for exploring hybridization phenomena. The overarching goal is to establish a correlation-aware framework for molecular adsorption that explicitly accounts for the modified electronic structure of the substrate.

This requires a combined experimental and theoretical approach that provides full access to the interfacial properties. To resolve the structural arrangement of the 5A monolayer, we first employ LEED and STM, which together reveal the long-range order and the local adsorption geometry. Building on this foundation, we use POT to probe the occupied electronic structure in momentum space, enabling a direct assignment of molecular orbitals. Although POT is surface-sensitive, it

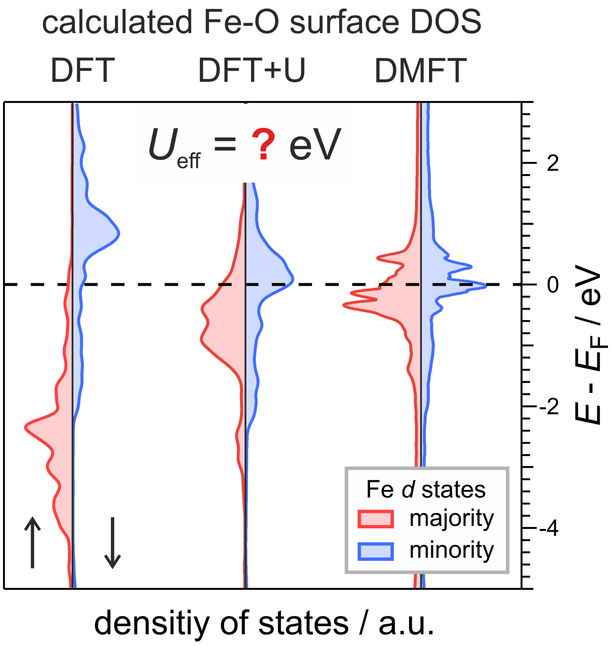

Figure 5.2: Comparison between the Fe d DOS calculated using standard DFT, DFT+U, and DFT+DMFT. In DFT+U, the effective Hubbard parameter U_{eff} is introduced to mimic the correlation-induced band narrowing. However, the optimal value of U_{eff} is not known *a priori* (indicated by the question mark) and must be determined by benchmarking against DMFT. Figure from manuscript currently under review.

captures contributions from both the molecular adlayer and the underlying substrate, providing access to the full interfacial electronic structure.

To complement this perspective, we employ STS combined with spatially resolved differential conductance ($\mathrm{d}I/\mathrm{d}V$) mapping. These techniques offer local access to both occupied and unoccupied states at the single-molecule level, yielding a real-space view of the molecular orbitals of individual molecules. Unlike POT, scanning tunneling techniques are selectively sensitive to the topmost layer, sampling almost exclusively the electronic states of the adsorbed molecule.

Together, these complementary methods create a comprehensive picture of molecular hybridization at the 5A/Fe–O interface, establishing the basis for critically evaluating existing chemisorption models and developing a refined framework that incorporates correlation effects, complexity of conjugated molecules, and spatially non-uniform coupling.

On the theoretical side, the challenge lies in accurately describing the electronic structure of the correlated Fe–O substrate beneath an extended organic layer. While the previous chapter demonstrated that DMFT can capture the influence of electron correlation at the clean Fe–O surface [190], its direct application to systems involving large adsorbates like 5A is computationally prohibitive. The reason lies in the escalating cost of accounting for many-particle scattering processes across all correlated Fe sites beneath the molecule.

To tackle this, we employ the DFT+U method — a computationally efficient extension of standard density functional theory that introduces an effective on-site Coulomb term (U_{eff}) to approximate the impact of local correlation effects in the Fe d-orbitals [60, 61]. However, unlike DMFT, DFT+U remains a purely single-particle approach.

The key idea, therefore, is to benchmark DFT+U against DMFT for the clean Fe–O surface. By tuning the effective Hubbard parameter $U_{\mathrm{eff}} = U - J$, we aim to reproduce the characteristic d-band narrowing and the reduction of the exchange splitting observed in the DMFT results, without explicitly including true many-body physics.

This conceptual approach is illustrated in Fig. 5.2, which compares the Fe d-projected DOS obtained from standard DFT (left) and DMFT (right). In between, an example of a DFT+U DOS is shown, which represents the target electronic structure that an appropriately tuned U_{eff} aims to reproduce. However, to achieve such a meaningful DFT+U description, we must determine the U_{eff} value that brings the DFT+U DOS into quantitative agreement with the DMFT benchmark — a key task that will be discussed in Section 5.3.1.

5.2 Sample Preparation and Experimental Overview

The preparation of the 5A/oxygen-passivated Fe(100) interfaces builds directly on the substrate preparation described in the previous chapter. After obtaining the well-ordered Fe-O substrate following the previously outlined procedures, 5A was deposited from a Knudsen-cell evaporator under UHV conditions ($p < 2 \times 10^{-10}$ mbar). Coverage control was achieved by adjusting the deposition time at a fixed rate, which had been pre-calibrated using a quartz crystal microbalance, yielding well-defined 5A/Fe-O interfaces with 0.5 ML and 1 ML coverage (with 1 ML corresponding to one saturated molecular monolayer). The formation of an ordered molecular layer was confirmed by the emergence of additional diffraction features in the LEED pattern (see Fig. 5.3a) and by the pronounced appearance of carbon-related signals in AES data, while the substrate oxygen and iron signals remained largely unaffected (see Fig. 5.3b). All deposition steps were performed at room temperature.

Momentum-resolved photoemission experiments were conducted at the NanoESCA beamline of the Elettra synchrotron. High-resolution 2D momentum maps were recorded using a NanoESCA momentum microscope operated in momentum mode, with p-polarized synchrotron light at a photon energy of 40 eV. The sample temperature was maintained at 80 K during the measurements, and continuous sample rastering was employed to minimize radiation-induced damage.

STM and STS studies were carried out at two independent *low-temperature* (LT) STM setups. For the 0.5 ML 5A/Fe–O interface, measurements were performed at the University of Duisburg-Essen using a home-built LT STM operating at 77 K, while data for the 1 ML interface were acquired at the CNR-IOM institute in Trieste using a commercial Omicron LT STM at 77 K. Both setups allowed the acquisition of topographic images in constant-current mode, as well as differential conductance ($\mathrm{d}I/\mathrm{d}V$) maps recorded at constant height using lock-in detection. To preserve the surface quality during transfer between preparation and analysis chambers, a dedicated UHV transfer suitcase with a base pressure below 5×10^{-11} mbar was used. The STM measurements on the 1 ML film were performed by Dr. Alessandro Sala and were part of an NFFA-Europe-funded

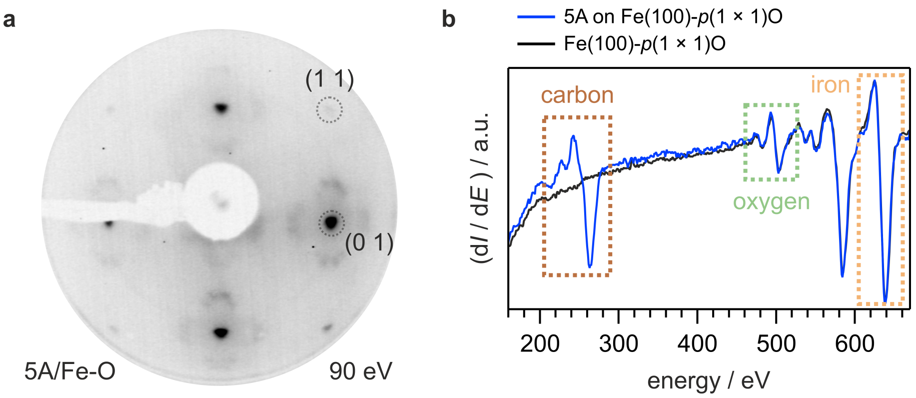

Figure 5.3: Characterization of the 5A/Fe–O interface. **(a)** LEED pattern at 90 eV after deposition of 1 ML 5A, showing additional diffraction features around the (1 0) spots, indicative of long-range molecular order. **(b)** Differential AES spectra before (black) and after (blue) 5A deposition, revealing strong carbon signatures while oxygen and iron signals remain unchanged, confirming the integrity of the Fe–O substrate.

project. The measurements on the 0.5 ML 5A sample were performed by Dr. Mehdi Bouatou in the group of Prof. Gruber (University of Duisburg-Essen).

To ensure sample quality prior to the transfer into the STM setups, complementary momentum-resolved measurements were performed at TU Dortmund using a laser-based momentum microscope equipped with a femtosecond XUV light source operating at 29.7 eV [195, 214].

Theoretical modeling of the 5A/Fe–O interface was performed by Dr. Andreas Windischbacher from the University of Graz in the group of Prof. Puschnig, using DFT combined with an effective Hubbard U_{eff} correction (DFT+U). This approach was calibrated against the reference DMFT data for the Fe–O surface from Dr. Andrea Droghetti, which were discussed in the previous chapter. The gas-phase momentum maps of 5A were generated using the *kMap.py* Software package [211].

5.3 Electronic Structure and Coupling Mechanisms at the Interface

5.3.1 Efficient Modeling of Correlation-Driven d-Band Modifications

The previous chapter demonstrated that oxygen adsorption on Fe(100) induces pronounced changes in the surface electronic structure due to an enhancement of electron correlation, including a substantial narrowing of the Fe d-bands and a reduction in exchange splitting [190]. Capturing this influence of correlation is essential for any meaningful theoretical description of subsequent molecular adsorption at the Fe–O interface.

The most accurate way to describe these correlation effects is DMFT, which explicitly accounts for many-particle scattering processes at each correlated Fe site [190, 280]. While DMFT reliably captures the correlation-driven modifications of the Fe–O electronic structure, its computational cost renders it impractical for systems with large unit cells, such as those required to model organic monolayers like 5A.

To handle this, we adopt the DFT+U approach — an extension of density functional theory (DFT) that introduces an effective on-site Coulomb term (U_{eff}) to modify the occupation-dependent part of the energy functional [60, 61].

DFT+U was developed to improve the description of systems with localized d or f electrons, where standard DFT tends to yield overly broad bands and underestimated band gaps due to over-delocalization of electronic states [60]. This delocalization stems from the self-interaction error — an artifact in which an electron is spurously influenced by the potential of its own charge density, unphysically favoring fractional occupations. By penalizing these fractional occupations, DFT+U restores a more physical electronic structure and corrects the excessive smoothing of the total energy as a function of electron number [61, 294].

This concept is illustrated in Fig. 5.4, which shows how the total energy behaves in different formalisms. In standard DFT (black line), the curvature is too smooth due to the energetic gain from delocalization. The Hubbard correction in DFT+U (blue line) restores the piecewise linear segments expected from exact theory (red dashed line) by disfavoring fractional occupations [61, 123].

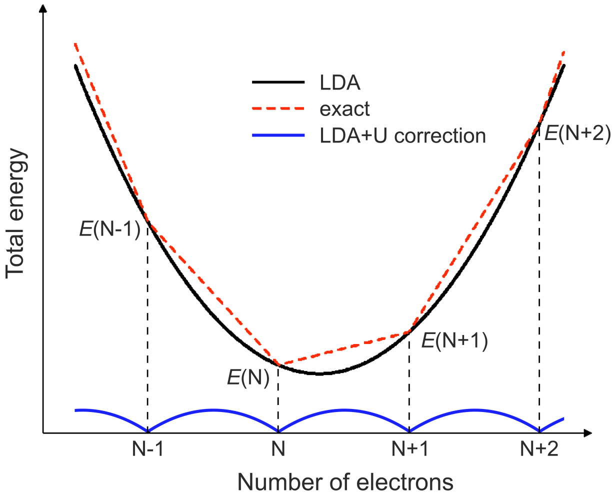

Figure 5.4: Illustration of the spurious curvature problem in DFT and its correction within DFT+U. Standard DFT (black line) over-smooths the energy curvature, while DFT+U (blue) restores the correct curvature by penalizing fractional occupations, approximating the exact behavior (red dashed line). Reproduced from [61]. © 2005 American Physical Society.

In the general case, DFT+U modifies the energy functional through an additional term of the form:

$$E_U = \frac{U}{2} \sum_{I,\sigma} \mathrm{Tr}\left[n_{I\sigma}(1 - n_{I\sigma})\right] \tag{5.1}$$

where $n_{I\sigma}$ denotes the occupation matrix for localized d orbitals at site I and spin σ [294].

To highlight its physical meaning more intuitively, this expression reduces to:

$$E_U = \frac{U}{2}n(1-n) \tag{5.2}$$

for a single site with a single spin-degenerate localized orbital. Here, n denotes the occupation of that orbital, neglecting explicit spin. This simplified quadratic form directly illustrates the core mechanism: the energy penalty vanishes for integer occupations ($n = 0$ or $n = 1$) but is maximized for fractional occupations ($n = 0.5$). The resulting Hubbard-correction corresponds to the blue line in Fig. 5.4, which approximately restores the correct curvature when applied to the LDA total energy (black) [61].

While values for U_{eff} can be derived from first principles [295], DFT+U is often applied in an empirical fashion, where the U_{eff} parameter is tuned to reproduce experimental observables such as band gaps or specific features of the electronic band structure [60, 296, 297]. For strongly correlated systems like transition metal oxides, where metal cations are embedded in ionic lattices, DFT+U is a well-established method for capturing the properties of localized *d*-electrons [60, 61]. Similarly, it has proven effective in organic coordination complexes (*e.g.*, porphyrins and related macrocycles), where transition metal ions are coordinated by planar or three-dimensional ligand fields[*]. In such systems, the U_{eff} correction is likewise applied to the spatially localized *d*-states of the coordinated metal ions, providing a computationally efficient alternative to more sophisticated and costly hybrid functionals, as demonstrated in various studies of porphyrins and related species [299–302].

From a phenomenological perspective, DFT+U increases the energetic separation between occupied and unoccupied states, pushing the former to lower and the latter to higher energies [303]. In semiconductors and insulators, this mechanism helps to correct the typically underestimated band gaps. However, in ferromagnetic transition metals, which are generally weakly to moderately correlated, the situation is more nuanced. In such systems, occupied and unoccupied states differ in spin character, with majority-spin states being largely occupied and minority-spin states less so. Here, applying a conventional positive U_{eff} tends to exaggerate the spin splitting, leading to magnetic properties that deviate more strongly from experiment than those obtained by standard DFT [61, 295, 304].

It is important to stress that DFT+U is not a genuine theory of electronic correlation in the many-body sense. It does not capture dynamical correlations, and cannot reproduce spectral features of purely many-body origin, such as satellite states. Instead, its role in this work is analogous to that of a scissor operator[†] as commonly employed in organic electronic structure calculations [111, 287, 306, 307] — a pragmatic adjustment designed to match a known reference while retaining computational efficiency. In particular, it is used here to emulate the correlation-induced renormalization of the Fe *d*-bands, most notably the reduction in exchange splitting.

---

[*] Ligands are atoms, ions, or molecules that donate electron density to a central metal ion, forming directional coordinate bonds [298].

[†] A scissor operator is a computational correction that rigidly shifts the energy levels in DFT, such as molecular orbitals in organic molecules, to approximate quasiparticle energy alignment and reproduce experimental band gaps [305].

Benchmarking DFT+U Against DMFT

To make this approach reliable, we calibrated U_{eff} by performing DFT+U calculations for the clean Fe–O surface across a range of U_{eff} values and directly comparing the resulting DOS to the reference DMFT result [190]. This benchmarking, summarized in Fig. 5.5, reveals that only negative U_{eff} values reproduce the correlation-induced narrowing and reduced exchange splitting seen in DMFT. In contrast, the positive U_{eff} values typically used for transition metal oxides strongly exaggerate the spin splitting. Based on this calibration, we fix $U_{\mathrm{eff}} = -3.1\,\mathrm{eV}$ for all subsequent DFT+U calculations of the 5A/Fe–O interface. This calibrated framework provides a physically grounded and internally consistent theoretical baseline for interpreting the experimental data and for investigating how correlation-induced modifications of the Fe d states influence molecular adsorption, energy level alignment, and electronic coupling at the interface.

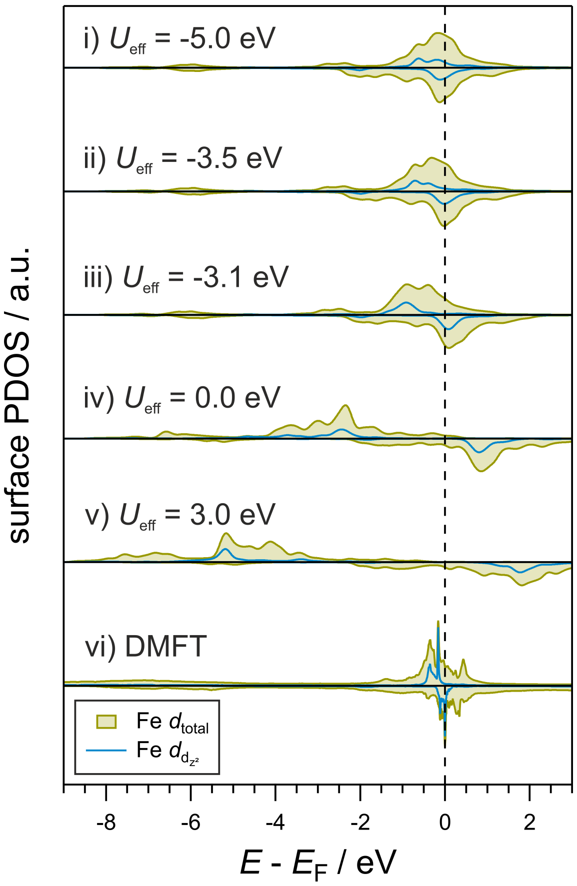

Figure 5.5: Calibration of DFT+U against DMFT for the Fe(100)–$p(1 \times 1)$O surface. Panels (i-v) show the Fe–O DOS calculated using DFT+U for different U_{eff} values, while panel (vi) displays the reference DMFT result. Only negative U_{eff} values (panels ii-iii) reproduce the correlation-induced narrowing and reduced exchange splitting observed in DMFT. Positive U_{eff} (panel v) exaggerates the exchange splitting, illustrating the limitations of conventional DFT+U for ferromagnetic metals. Figure from manuscript currently under review.

5.3.2 Molecular Self-Assembly and Structural Evolution

To unravel the structural evolution of 5A on oxygen-passivated Fe(100)–$p(1 \times 1)$O, we combine the molecular-scale resolution of STM with the large-area sensitivity of LEED. This complementary approach allows us to develop a comprehensive structural model, capturing both the local molecular arrangement and the emergence of long-range order across the self-assembled film. This provides a detailed picture of the structural properties, spanning from molecular to mesoscopic scales.

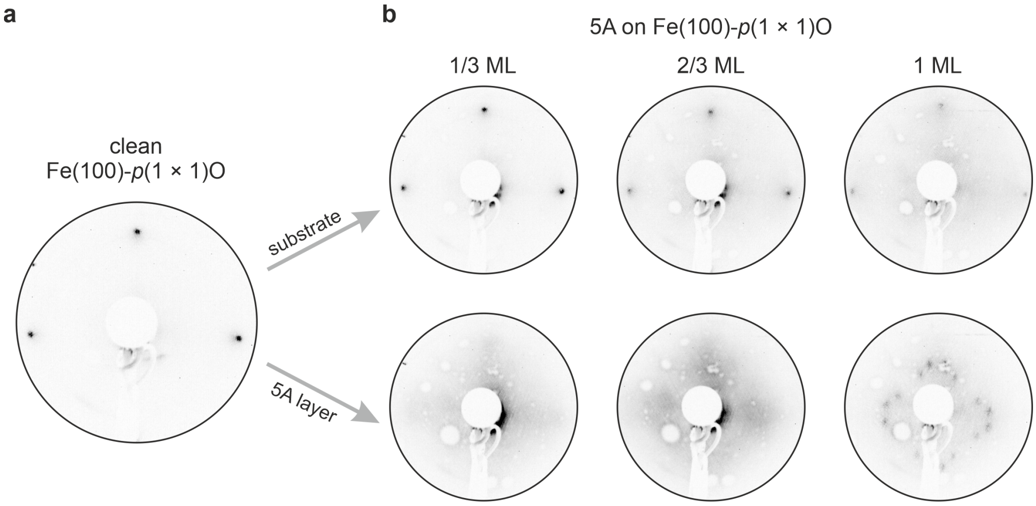

Figure 5.6: Evolution of the LEED pattern during stepwise deposition of 5A on oxygen-passivated Fe(100)–$p(1 \times 1)$O. **(a)** Reference LEED pattern of the clean Fe(100)–$p(1 \times 1)$O substrate, recorded at approximately 50 eV. **(b)** LEED patterns showing the evolution of diffraction spots with increasing 5A coverage. The upper row displays the substrate-related diffraction spots (recorded at 50 eV), while the lower row highlights the molecular superstructure spots (recorded at 15 eV). Data are shown for coverages of 1/3 ML, 2/3 ML, and 1 ML (saturated monolayer). With increasing coverage, the intensity of the substrate spots decreases, but they remain sharp, indicating preservation of the underlying order. Simultaneously, initially diffuse molecular diffraction features appear and gradually sharpen, indicating the development of an ordered molecular superstructure.

Figure 5.6a shows the LEED pattern of the clean Fe(100)–$p(1 \times 1)$O surface, exhibiting the characteristic fourfold symmetry expected for a square Fe(100) surface lattice with an ordered oxygen overlayer. Upon stepwise deposition of 5A molecules, the emergence of additional diffraction spots becomes apparent, as shown in Fig. 5.6b. These molecular diffraction features are initially diffuse at low coverages, but they gradually sharpen with increasing coverage, indicating the formation of long-range molecular order. At the saturation coverage of one monolayer (1 ML), the molecular diffraction spots are sharpest, confirming that the self-assembled monolayer exhibits well-defined structural order.

STM images collected for sub-monolayer coverages (Figure 5.7a and b) provide complementary real-space information on the molecular arrangement. At 0.5 ML coverage, individual 5A molecules are clearly visible and align their long molecular axes parallel to the [001] and [010] directions of the substrate. This alignment already indicates a non-negligible molecule-substrate interaction, guiding the molecular orientation. Notably, even at this low coverage, 5A molecules form locally ordered islands, indicative of a pronounced tendency for self-assembly. The large-scale STM image in Figure 5.7a was recorded at a bias voltage of −2.0 V and a tunneling current of 20 pA, showing one such ordered island.

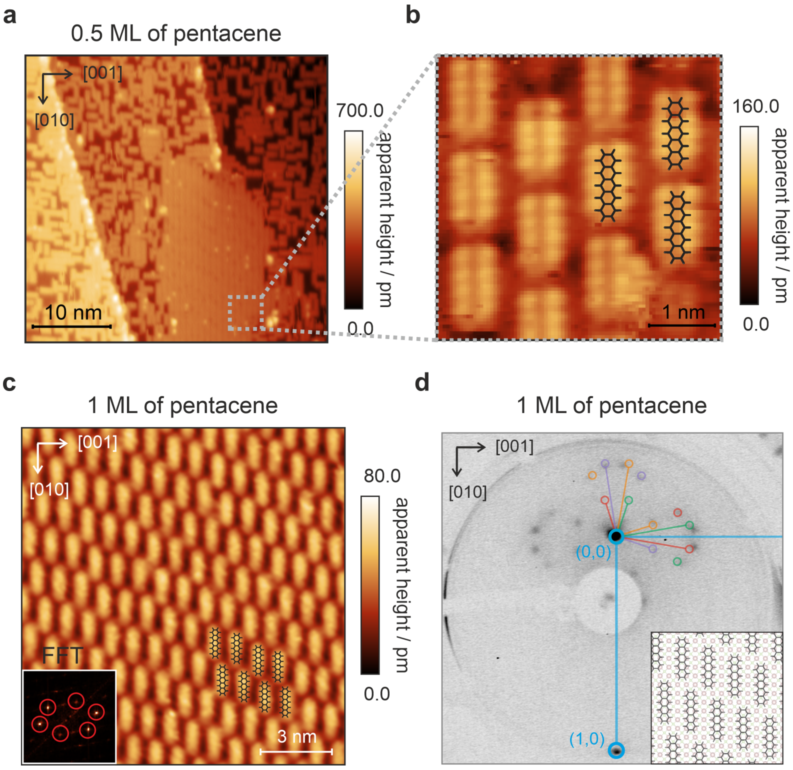

Figure 5.7: Structural evolution of 5A films on oxygen-passivated Fe(100)–$p(1 \times 1)$O, investigated using STM and LEED. **(a)** STM image of a sub-monolayer (0.5 ML) film of 5A, showing individual molecules oriented parallel to the [001] and [010] directions of the substrate. Molecules also form ordered islands. **(b)** High-resolution STM image of a molecularly ordered island within the 0.5 ML film. The molecular orientations are overlaid for clarity. **(c)** STM image of a saturated monolayer (1 ML) film, showing long-range molecular order. The inset displays the fast Fourier transform (FFT), confirming the periodicity of the molecular arrangement. **(d)** LEED image recorded for the same 1 ML film, showing diffraction spots from the molecular superstructure. A simulated LEED pattern, based on the proposed superstructure and its symmetry-equivalent rotational domains, is superimposed for comparison. The inset in (d) shows the corresponding real-space model of the superstructure. Figure from manuscript currently under review.

A close-up image of the island (Figure 5.7b), recorded at −2.5 V and 100 pA, reveals a commensurate superstructure with a unit cell that can be described by the matrix $\left(\begin{smallmatrix}5 & 4\\ 5 & -4\end{smallmatrix}\right)$, corresponding to an oblique molecular arrangement on the square substrate lattice. This unit cell covers an area of 40 Å^2 per molecule. Upon further deposition to form a saturated monolayer, the molecular packing density increases significantly. The unit cell contracts into a more compact $\left(\begin{smallmatrix} 3 & 1 \\ -1 & -6 \end{smallmatrix}\right)$ superstructure, as shown in Fig. 5.7c.

This final unit cell corresponds to an area of only 17 Å^2 per molecule, indicating that the molecular density increases by roughly a factor of two as the coverage approaches 1 ML. The STM image in Figure 5.7c, obtained at +2.0 V bias and 200 pA tunneling current, shows a single rotational domain of this fully developed monolayer, exhibiting excellent long-range order. The inset displays the corresponding *fast Fourier transform* (FFT), confirming the periodicity of the molecular arrangement.

To verify the structural assignment and account for the larger areas probed by LEED, we compare the experimental LEED pattern for 1 ML (Figure 5.7d) with a simulated pattern derived from the proposed $\left(\begin{smallmatrix} 3 & 1 \\ -1 & -6 \end{smallmatrix}\right)$ superstructure. Since the LEED data average over multiple domains, including rotational and symmetry-equivalent mirror domains imposed by the four-fold symmetry of the Fe(100) substrate, all these domains must be considered in the simulation.

The construction of the simulated LEED pattern is illustrated in Figure 5.8. Starting from the reciprocal lattice of a single molecular domain, we generate the symmetry-equivalent domains through mirroring, 90° rotation, and combined rotation and mirroring. The final simulated pattern, which is the sum of all these contributions, reproduces the experimentally observed LEED pattern with high fidelity. This agreement supports the proposed superstructure and provides a consistent picture of how 5A self-assembles on the oxygen-passivated Fe(100) surface: starting from isolated molecules aligned along substrate axes, evolving to locally ordered islands with a relatively large unit cell, to the fully developed monolayer exhibiting a denser, commensurate superstructure.

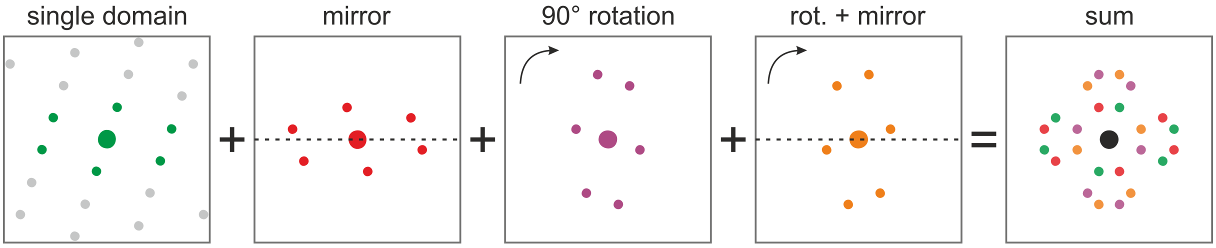

Figure 5.8: Simulation of the LEED pattern for a monolayer of 5A on Fe(100)–$p(1\times 1)$O based on a (3,1;−1,−6) superstructure. The first panel shows the diffraction pattern produced by a single ordered domain of the molecular film. The following panels illustrate the symmetry-equivalent domains generated by mirroring, 90° rotation, and combined rotation and mirroring. The final panel presents the sum of all domains, which reproduces the experimentally observed LEED pattern. This procedure reflects the coexistence of multiple rotational and mirror domains that form when 5A self-assembles on the square Fe–O surface.

5.3.3 The Occupied Electronic Structure of 5A/Fe–O in Photoemission

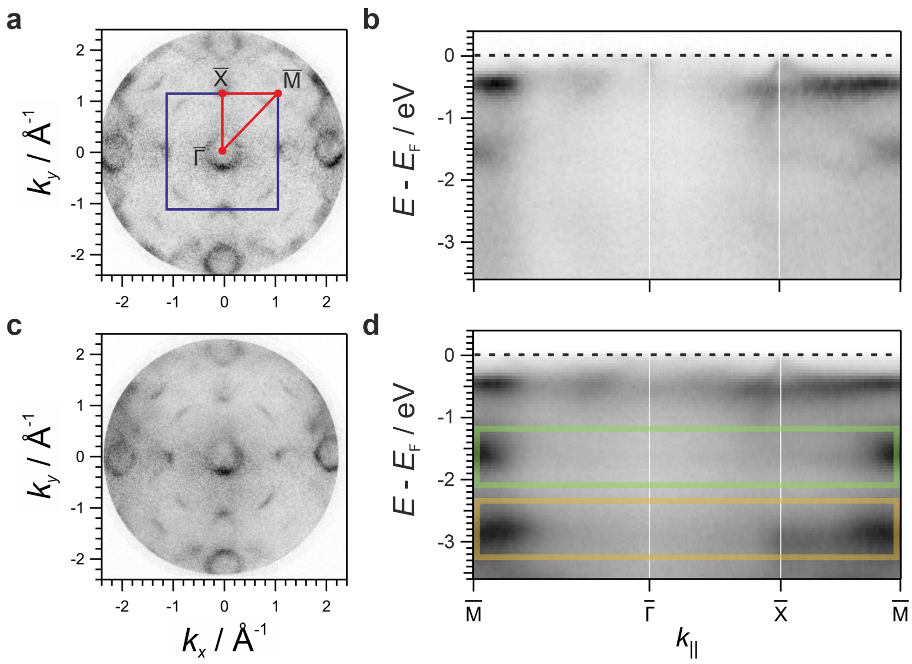

Figure 5.9: Momentum-resolved data of clean Fe–O and 1 ML 5A on Fe–O. **(a),(c)** Momentum maps at the Fermi energy are shown for **(a)** bare Fe–O and **(c)** 1 ML 5A on Fe–O. The blue square in a) marks the 1st SBZ of the Fe–O surface, and red lines indicate the corresponding high-symmetry directions. By slicing the entire 3D data cube along these high-symmetry lines, the surface band structure is derived. **(b),(d)** Resulting surface band structures of the **(b)** Fe–O substrate and the **(d)** 5A/Fe–O system. Molecular resonances are highlighted by coloured boxes. Data were acquired using *p*-polarized light at a photon energy of 40 eV. Figure from manuscript currently under review.

With the structural framework in place, we now turn to the electronic properties of the 5A/Fe–O interface, investigated using a combination of photoemission techniques (MM and POT) and scanning probe methods (STM, STS, and differential conductance ($\mathrm{d}I/\mathrm{d}V$) mapping). These complementary approaches provide detailed insights into the electronic characteristics of the metal/organic interface.

We begin by analyzing the photoemission data to determine whether the adsorption of 5A alters the electronic properties of the Fe–O substrate. Since passivation with oxygen is known to strongly modify the electronic and magnetic characteristics of the Fe surface, as discussed in the previous chapter, we must first ascertain that 5A does not induce further or revert any of these changes. However, from the previous chapter we know that in particular, states near the Fermi energy are highly susceptible to changes, making them the primary focus of our analysis. For this reason, we firstly compare momentum maps near the Fermi energy and the overall band structures of the clean Fe–O surface with those of the 5A/Fe–O system, depicted in Fig. 5.9.

Notably, the presence of 5A induces no significant changes near the Fermi level, as evidenced by the Fermi maps in Fig. 5.9a,c, which retain the characteristic fingerprints of oxygen bonding. This suggests that the magnetic and electronic properties established earlier remain valid. Given the strong influence of oxygen on the Fe(100) surface, confirming that its electronic characteristics persist upon molecular adsorption ensures a reliable reference point for modeling the hybrid interface. Likewise, the band structure comparison (see Fig. 5.9b,d) reveals no discernible variation in states near the Fermi level. However, 5A adsorption introduces distinct spectral features in the valence band at binding energies of approximately $-1.6\,\mathrm{eV}$ and $-2.8\,\mathrm{eV}$. These resonances, absent on the clean Fe–O surface, originate from the molecular layer itself. To elucidate their nature and fully resolve the molecular electronic structure at the interface, we analyze the MM data in more detail.

First, we take a look at the momentum-integrated photoemission spectra (EDCs) of the clean Fe–O substrate and the 5A-covered Fe–O interface, shown in Fig. 5.10a as black and blue curves, respectively. Consistent with the momentum-resolved data, molecular peaks emerge at approximately $-1.6\,\mathrm{eV}$ and $-2.8\,\mathrm{eV}$ below the Fermi level ($E - E_\mathrm{F}$), confirming the presence of distinct molecular states.

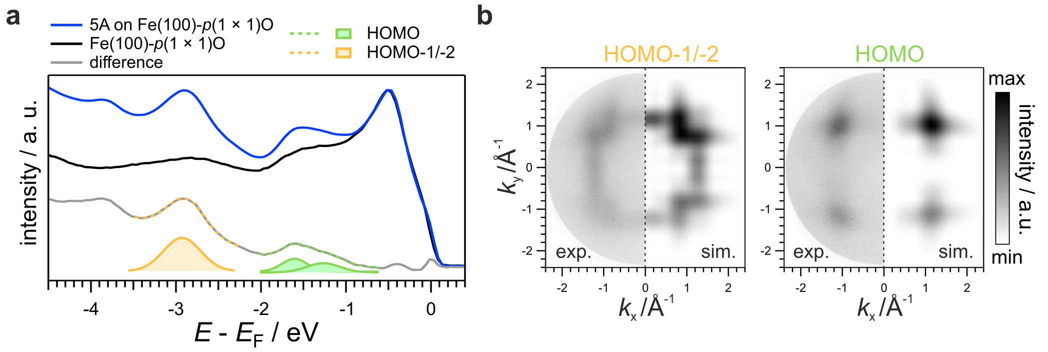

Figure 5.10: POT analysis of the 5A/Fe–O interface. **(a)** Momentum-integrated photoemission spectra of the bare Fe–O surface and the Fe–O surface after adsorption of 5A, recorded at a photon energy of 40 eV (*p*-polarized). The two prominent features at binding energies of approximately −1.6 eV and −2.8 eV are attributed to the HOMO and a sum of HOMO–1/HOMO–2 levels of 5A, respectively. **(b)** Corresponding momentum-resolved photoemission intensity maps at the energies of the HOMO–1/–2 (left) and HOMO (right) peaks. The experimental maps are shown alongside the simulated momentum distributions of the respective molecular orbitals for comparison. Figure from manuscript currently under review.

To isolate the molecular contributions from the underlying substrate features, the spectra are first normalized using and energy region where no molecular states are observed (here from 0.0 eV to $-0.5\,\mathrm{eV}$). Subsequently, the spectrum of the clean Fe–O surface is subtracted from that of the 5A/Fe–O system, yielding the difference spectrum shown as the grey curve in Fig. 5.10a.

Next, to assign these features to specific molecular orbitals, we exploit the full momentum dependence of the photoemission signal within the framework of POT [63, 114, 214]. An overview of the procedure used to generate the simulated momentum maps is provided in Section A.2.

As Fig. 5.10b demonstrates, the momentum distribution corresponding to the peak at −1.6 eV exhibits excellent agreement with the simulated photoemission signature of the HOMO of 5A.

Similarly, the momentum map at −2.8 eV matches the combined signature of the HOMO-1 and HOMO-2 orbitals, which appear energetically degenerate within the resolution of our measurement. Based on this orbital-level identification, we further examine these features quantitatively by fitting the momentum-integrated molecular peaks with Gaussian profiles and a linear background (see Section A.3) [82, 214]. This approach yields a single Gaussian peak for the combined HOMO-1/HOMO-2 feature, centered at (-2.88 ± 0.01) eV with a FWHM of (0.52 ± 0.01) eV. In contrast, the HOMO-related emission requires two Gaussian components, centered at (-1.26 ± 0.05) eV and (-1.61 ± 0.02) eV, with corresponding FWHMs of (0.46 ± 0.04) eV and (0.35 ± 0.02) eV.

Surprisingly, this detailed spectral decomposition suggests that the HOMO splits into at least two components upon adsorption, which might suggest an interaction that goes beyond a weakly interacting molecule-substrate system. Notably, despite these unusual signatures, our momentum-resolved data allow us to rule out any contributions from the LUMO in the energy window below E_F, indicating the absence of electron transfer from the substrate to the molecular layer.

5.3.4 The Local Electronic Structure of 5A in Scanning Probe Experiments

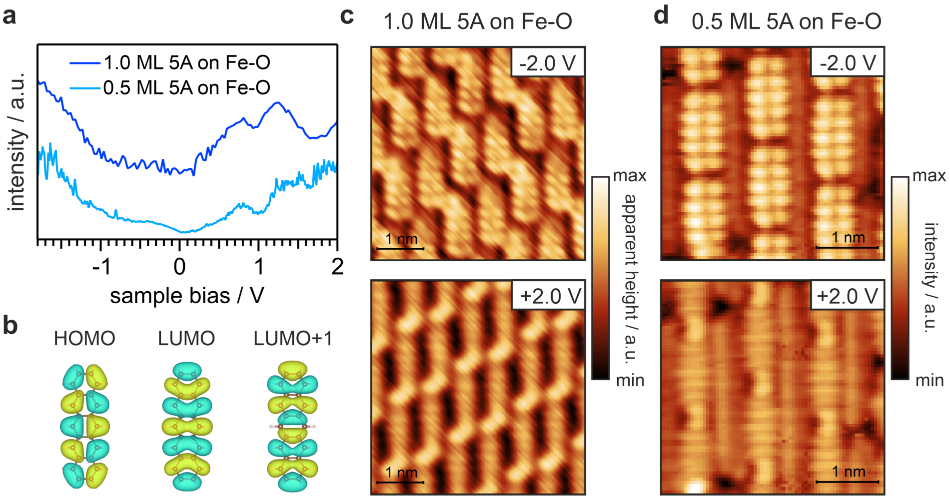

Figure 5.11: Comparison of STM and STS results for a 1 ML versus a 0.5 ML film of 5A molecules on Fe–O. **(a)** STS spectra for the 0.5 ML (light blue curve) and 1 ML (dark blue curve) films, revealing similar spectroscopic characteristics. Three peaks appear in the unoccupied states at 0.8 V, 1.2 V, and 2.0 V, while a broad resonance is centered at approximately −1.6 V in the occupied states. Additional intensity near −0.5 eV is attributed to the high substrate DOS rather than molecular features. **(b)** Gas-phase orbital plots of the HOMO, LUMO, and LUMO+1 of 5A. **(c)** STM images of a 1 ML film of 5A on Fe–O, recorded at −2.0 V (top) and +2.0 V (bottom) with tunneling currents of 500 pA and 100 pA, respectively. **(d)** dI/dV maps of an ordered island of a 0.5 ML film of 5A on Fe–O, acquired at −2.0 V (top) and +2.0 V (bottom) with a tunneling current of 300 pA. Figure from manuscript currently under review.

To complement our understanding of the electronic structure of the frontier orbitals in adsorbed 5A molecules, we extend our study to STS experiments. These measurements allow probing of both the occupied and unoccupied electronic states of the molecules, offering crucial insights into their interactions with the substrate. We first focus on the frontier orbitals closest to the Fermi energy. The STS spectra for both the 1 ML and 0.5 ML films, shown in Fig. 5.11a, exhibit similar spectral features: a prominent rising peak in the occupied region (negative bias voltages) and two distinct peaks along with a rising edge in the unoccupied region (positive bias voltages).

To understand the origin of these spectral features, we compare the gas-phase Kohn–Sham orbitals of 5A (Fig. 5.11b) with STM topography and differential conductance ($\mathrm{d}I/\mathrm{d}V$) maps recorded near these peaks (Fig. 5.11c,d). The $\mathrm{d}I/\mathrm{d}V$ mapping approximates the local electron density distribution at specific bias voltages, which enables the identification of MO fingerprints at selected energies. The analysis of $\mathrm{d}I/\mathrm{d}V$ maps at bias voltages of -2.0 V and $+2.0$ V (Fig. 5.11d) reveals a strong resemblance to the gas-phase HOMO and LUMO of 5A, respectively (see Fig. S7b), confirming that these states stem from the gas phase HOMO and LUMO.

One of the most intriguing aspects of the STS spectra is the pronounced multipeak structure in the LUMO region, which is even more prominent than in the HOMO region. The fact that no significant spectral changes occur between 0.5 ML and 1 ML films suggests that the observed electronic structure is governed by molecule-substrate interactions. This conclusion is further supported by theoretical calculations, which show that a free-standing layer of 5A arranged in the same structure as the 1 ML film does not exhibit the marked HOMO and LUMO features observed in the experiment (see Fig. 5.12). This strongly suggests that the interaction with the Fe–O substrate plays a key role in shaping the electronic structure.

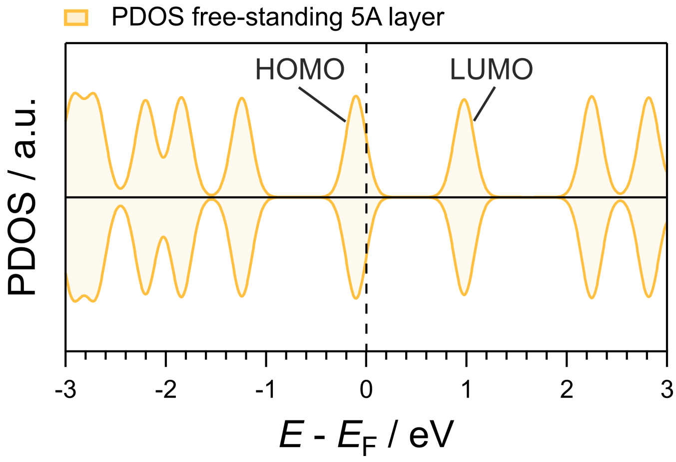

Figure 5.12: PDOS for a free-standing layer of 5A. The molecular arrangement follows the identified (3,1; -1,-6) superstructure of the saturated 1 ML film on Fe–O. Figure from manuscript currently under review.

Comparing DFT+U Results with Scanning Probe Measurements

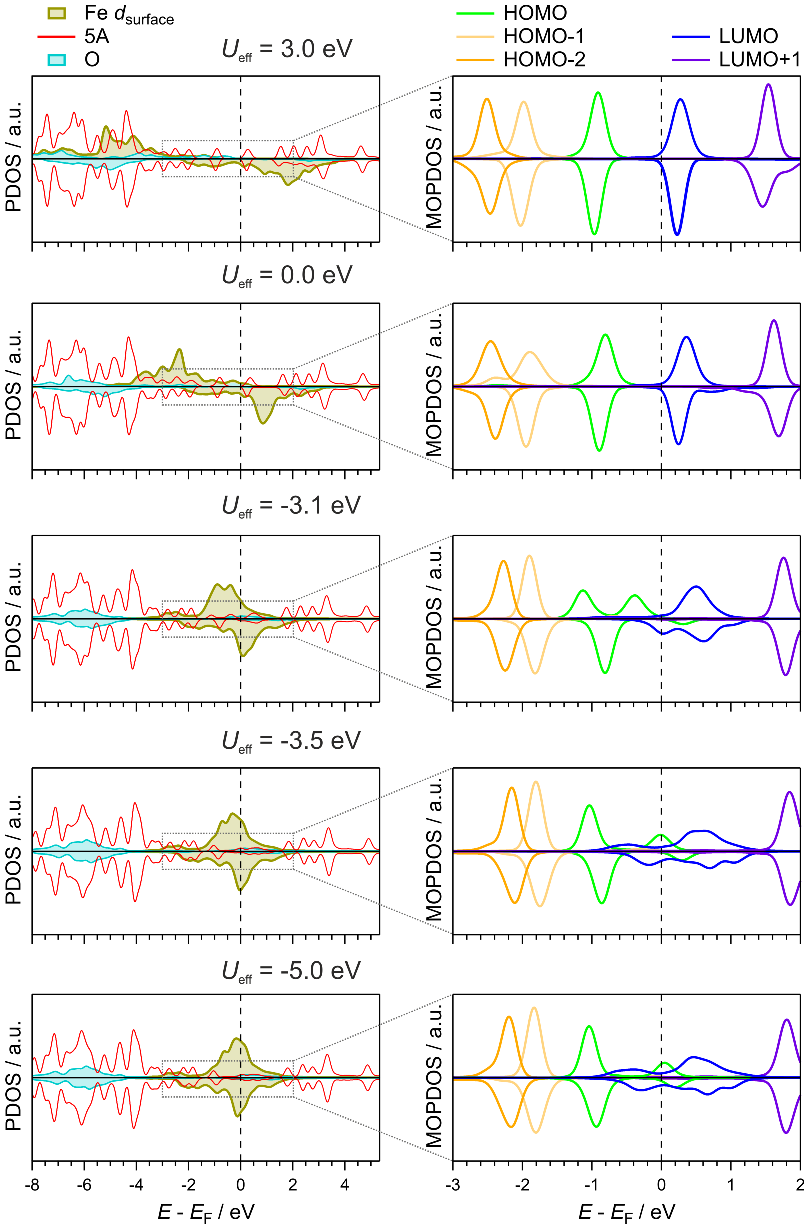

Figure 5.13: Impact of U_{eff} settings on the DOS of Fe–O and the MO-resolved PDOS (MOPDOS) of 5A. As U_{eff} becomes more negative, the exchange splitting in Fe–O decreases, while the frontier orbitals of 5A exhibit increased broadening and splitting. Figure from manuscript currently under review.

Up to this point, the findings indicate that molecule-substrate interactions go beyond a simple weak coupling. This stands in sharp contrast to commonly reported cases of weakly interacting molecules on passivated surfaces, where the LUMO typically appears as a single, well-defined peak above the Fermi energy [90, 308, 309]. Instead, the broadening of the HOMO and the emergence of multiple LUMO-related features point to more complex interactions that warrants further investigation.

Before interpreting the nature of these interactions in terms of electronic structure models, it is essential to assess whether the DFT+U approach can quantitatively reproduce the experimental signatures that have been discussed thus far. To this end, we perform DFT+U calculations based on a structural model corresponding to the experimentally observed monolayer coverage.

This step ensures that the theoretical framework is capable of capturing the relevant physical effects — particularly those arising from correlation-driven modifications of the Fe–O *d*-bands — and sets the stage for the subsequent interpretation in terms of chemisorption theory. By systematically varying the U_{eff} parameter, we can probe whether substrate-induced modifications in the *d*-band structure play a direct role in shaping the experimentally observed spectral features. This approach is particularly relevant given the distinct multipeak LUMO structure, which deviates from expectations for a weakly interacting system.

As these features arise most likely from molecule-substrate coupling rather than intrinsic molecular properties, one would expect them to be sensitive to changes in the substrate's electronic structure, particularly in the Fe *d*-bands. The following analysis, shown in Fig. 5.13, explores this relationship and evaluates to what extent DFT+U can capture the experimentally observed effects. The calculations reveal a clear correlation between U_{eff} and the observed spectral modifications. As U_{eff} becomes more negative, the exchange splitting of the Fe–O substrate decreases, leading to a significant broadening and splitting of the molecular frontier orbitals. The evolution of the LUMO into multiple distinct spectral features aligns with the characteristics of the experimental STS data. While the theoretical calculations reflect some of the key experimental trends, achieving a precise one-to-one correspondence is essential for understanding the underlying hybridization mechanisms. Without such agreement, the electronic structure remains ambiguous, and the origin behind the emerging interactions cannot be fully unraveled.

To address this, we now focus on the 1 ML film in Fig. 5.14, extending STS measurements over a broader energy range and incorporating spatially resolved conductivity ($\mathrm{d}I/\mathrm{d}V$) mapping at the previously unidentified spectral features of the LUMO. These additional features serve as the main test case to evaluate whether the theoretical model can accurately capture the experimental observations. We start by examining the occupied states (negative bias) in the extended STS spectrum of the 1 ML 5A film on Fe–O, which is displayed in Fig. 5.14a. Here the HOMO, previously visible only as an incomplete peak with its upper part extending beyond the measured range, is now fully resolved as a broad feature centered at $-1.8\,\mathrm{V}$, and a second peak is present at $-3.2\,\mathrm{V}$.

Overall, the observed peak structure closely matches the photoemission data (see Fig. 5.10), allowing for a confident assignment of the HOMO and HOMO-1/HOMO-2 states. While previous STS measurements only captured the lower part of the HOMO as a rising edge, the extended energy range now fully resolves its peak, aligning with its expected position from photoemission. Similarly, the additional peak at $-3.2\,\mathrm{V}$ matches reasonably well with the features seen in photoemission, further supporting its assignment to HOMO-1/HOMO-2. Additionally, the HOMO resonance in STS exhibits noticeable broadening, which closely resembles the shape observed in the photoemission EDC. At positive bias, where the unoccupied states are probed, the

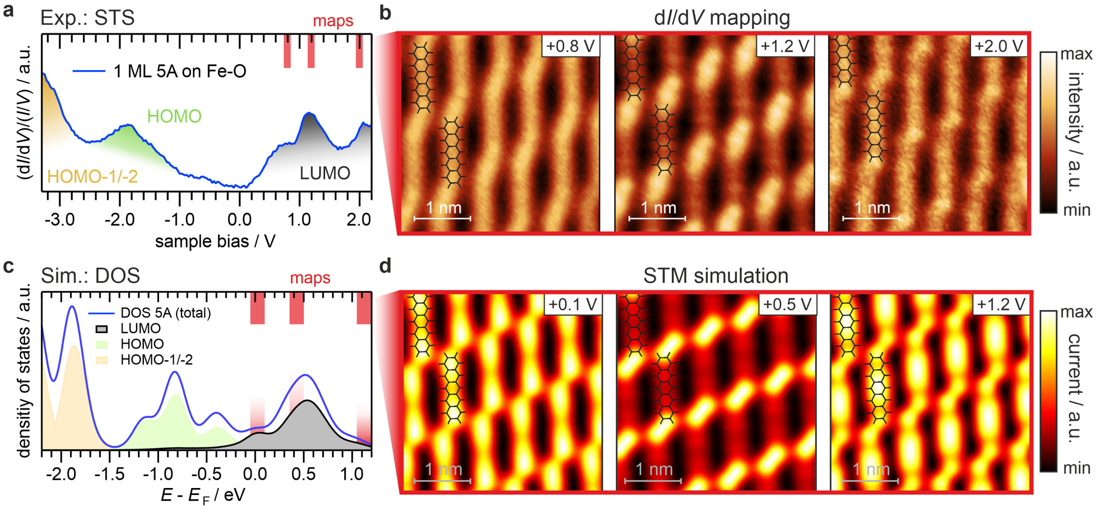

Figure 5.14: The dI/dV data of the occupied and unoccupied states of 5A atop the Fe–O surface. **(a)** Normalized dI/dV spectrum measured on top of a single 5A molecule. **(b)** dI/dV maps obtained for a tunneling current of 300 pA at different positive voltages close the peaks observed in the unoccupied region (red bars), each probing a $3.5 \times 3.5\,\mathrm{nm}^2$ area. **(c)** MOPDOS for 5A adsorbed on Fe–O derived from DFT+U calculations using a Hubbard-parameter of $U_{\mathrm{eff}} = -3.1\,\mathrm{eV}$. **(d)** Simulated STM images at a constant height of 4 Å. Figure from manuscript currently under review.

LUMO is now resolved into three distinct peaks just above the Fermi level, with two prominent features at 0.8 V and 1.2 V, accompanied by a weaker peak at 2.0 V.

Thus far, we have found no indication that any of these peaks originate from the LUMO+1 or result from intermolecular interactions. However, based on the STS spectra alone, their precise origin remains unclear. To further investigate these states, we recorded two-dimensional dI/dV maps at the peak bias voltages marked in Fig. 5.14a.

The resulting maps, shown in Fig. 5.14b, all exhibit stripe-like patterns with distinct intensity modulations, reflecting variations in their spatial electronic structure. The 0.8 V map reveals molecular states characterized by stripes with a slight dip in the center, while the 1.2 V feature exhibits a pronounced intensity profile, with a significantly attenuated central region and prominent protrusions at the molecular edges. In contrast, the 2.0 V peak produces an almost homogeneous intensity distribution across the entire 5A molecule, consistent with the clear 7-lobe structure observed in dI/dV maps of the 0.5 ML film (see Fig. 5.11).

A thorough comparison between the experimental STS spectrum and the PDOS obtained from DFT+U calculations reveals a notable agreement for the optimized $U_{\mathrm{eff}} = -3.1\mathrm{eV}$, which was established earlier. The simulated PDOS, shown in Fig. 5.14c as a blue curve, reproduces not only the broad HOMO feature but also the characteristic three-peak structure of the LUMO, mirroring the experimental findings. The only significant deviation is the underestimation of the energy gap, which is an expected consequence of the well-known electronic band gap problem in DFT [121].

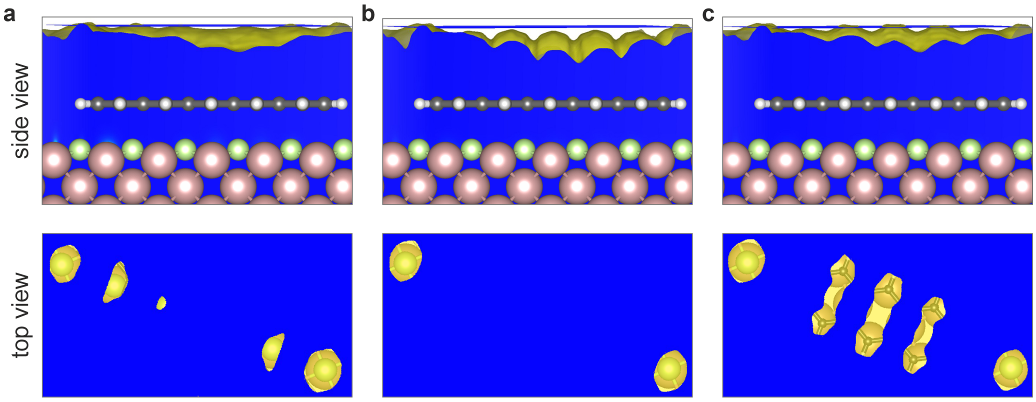

Figure 5.15: Integrated density plots for the energy regions corresponding to the identified LUMO features. **(a),(b),(c)** Density simulations near +0.1 V, +0.5 V, and +1.2 V, equivalent to the STM energy windows highlighted in Fig. 5.14d, respectively. The top row shows side views of the calculated densities, with the thin blue lines indicating the cutting plane at the estimated tip-molecule distance. The bottom row presents top-view images of the electron densities above this cutting plane, offering a direct comparison to the dI/dV images in Fig. 5.14. For clarity, the atomic positions of the molecule and the surface were superimposed on the density plots. Iso-value thresholds were optimized to best align with the STM-equivalent simulations, set at 6.0×10^{-8}, 1.2×10^{-7}, and 2.5×10^{-8} for (a), (b), and (c), respectively. Figure from manuscript currently under review.

Beyond spectral alignment, a more significant comparison between theory and experiment emerges from STM simulations. Simulated constant-height STM patterns at the three LUMO peak positions (marked by red bars in Fig. 5.14 closely replicate the intensity variations observed in the experimental dI/dV maps. This striking agreement further reinforces the assignment of these features as LUMO-derived states. Importantly, the same conclusion holds when directly comparing the measured dI/dV maps with the calculated Kohn-Sham orbitals, as shown in Fig. 5.15. This comparison not only confirms the LUMO nature of these features but also demonstrates that their origin is mainly electronic.

In contrast, such variation in intensity is not observed for the HOMO. Instead, the dI/dV maps across the identified HOMO energy range exhibit uniform distributions at all energies, with no pronounced intensity modulation across individual molecules. As shown in Fig. 5.16, the HOMO states maintain a consistent spatial profile.

Thus, by comparing the experimental scanning probe data with calculated spectral and spatial features, we have demonstrated that DFT+U provides a reliable description of the 5A/Fe–O interface. This validation confirms that the method captures the essential physical effects — most notably the influence of correlation on the substrate d-bands and the resulting interaction with the molecular frontier orbitals. Having established this agreement, we now turn to the interpretation of these results in terms of underlying bonding mechanisms and hybridization models, with the goal of uncovering how correlation-driven d-band renormalization governs chemical bond formation at the interface.

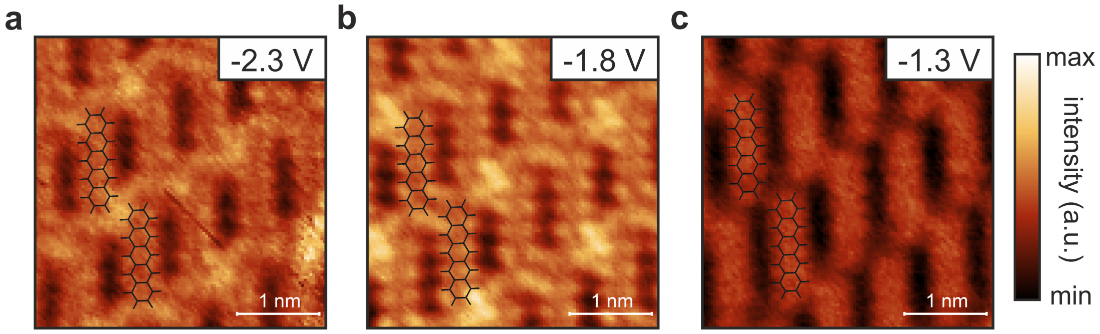

Figure 5.16: Experimental dI/dV maps for the HOMO of 5A. **(a)-(c)** Maps recorded at bias voltages of −2.3 V, −1.8 V, and −1.3 V, respectively, with a tunneling current set to 300 pA for all images. Unlike the maps obtained in the LUMO energy window, the HOMO maps show no pronounced intensity variations across individual 5A molecules. Figure from manuscript currently under review.

5.3.5 The Role of Correlation-Induced *d*-Band Modifications in Chemisorption

The agreement between experiment and DFT+U with an optimized U_{eff} underscores the importance of tuning the d-band structure to capture key aspects of the molecule–substrate interaction. While DFT+U does not fully account for many-body effects as in DFT+DMFT, it offers a practical way to approximate renormalized d-bands and their coupling to molecular states.

When the impact of correlation is neglected ($U_{\mathrm{eff}} = 0\,\mathrm{eV}$), the Fe d-bands exhibit a pronounced exchange splitting of approximately 3.0 eV (see Fig. 5.13), which places them significantly farther from the 5A molecular orbitals. As a result, little hybridization occurs. This is evident in the spin-resolved *molecular orbital projected density of states* (MOPDOS) (Fig. 5.17a, top), where the HOMO and LUMO appear only moderately broadened, and in the integrated LUMO electron density (Fig. 5.17, bottom), which closely resembles that of the gas-phase LUMO, confirming the absence of significant chemical interaction.

To interpret these observations and understand how hybridization emerges under different conditions, we now turn to established chemisorption models.

According to the Newns-Anderson model, the spin-dependent interaction between the renormalized LUMO state and the d-bands of a metal substrate can be described by intersecting the Hilbert transform of the substrate d-PDOS with the adsorbate LUMO function, given as:

$$y(\varepsilon) = \frac{1}{V^2}(\varepsilon - \varepsilon_{\mathrm{LUMO}}), \tag{5.3}$$

where $\varepsilon_{\mathrm{LUMO}}$ denotes the energy position of the renormalized LUMO, *i.e.*, its energy after interaction with the substrate sp-states. Note that strictly speaking the initial sp-coupling is not coming from the Newns-Anderson model but rather the d-band model. Yet, the central idea of utilizing the Hilbert transform stems from the Newns-Anderson approach. The term V^2 represents the adsorbate-metal d coupling strength [45, 53], which is determined by the spatial overlap between the adsorbate state and the metal d-states [310].

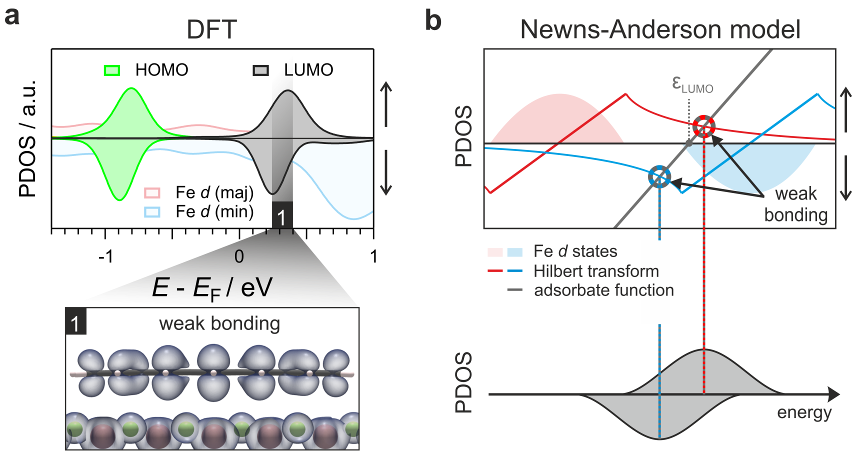

Figure 5.17: DFT-based analysis of 5A adsorption on Fe–O and the spin-resolved Newns-Anderson model. **(a)** PDOS showing the HOMO and LUMO contributions alongside the Fe d-bands resulting from DFT calculations of 5A adsorbed on top of Fe–O. The bottom panel shows a plot of the electron density stemming from the energy interval [0.2, 0.4] eV, which marks the center of the LUMO peak indicated by the black bar. **(b)** Sketch of the spin-resolved Newns-Anderson model assuming a Fe d-band structure similar to the one obtained by DFT. Solid red and blue lines indicate the Hilbert transforms of the Fe majority and minority PDOS, respectively. The grey dotted line indicates the energy position $\varepsilon_{\mathrm{LUMO}}$ of the renormalized LUMO state, from where the adsorbate function, $y(\varepsilon) = \varepsilon - \varepsilon_{\mathrm{LUMO}}$ emerges (solid grey line). The intersections between the adsorbate function and the Hilbert transforms (highlighted by circles) mark the energy positions of the hybridized adsorbate-metal states. In the presented case, the model predicts a single resonance in each of the two spin channels (see bottom panel). Figure from manuscript currently under review.

As outlined above, the slope of the adsorbate function is inversely proportional to the adsorbate-metal d-state coupling. In this framework, a steep incline of the function corresponds to low spatial overlap and, consequently, a weak coupling strength.

The intersections between the spin-dependent adsorbate functions and their respective Hilbert transforms provide two fundamental insights into the hybridization mechanism. First, the number of intersections determines whether the adsorbate state undergoes simple broadening, occurring when a single intersection is present, or whether it splits into bonding and antibonding resonances, which occurs when three intersections are found. Second, the position of these intersections dictates the energy levels of the hybridized adsorbate-metal d-states.

In cases where three intersections exist, only the two outermost ones correspond to actual electronic states, while the central intersection represents a weak, non-localized state with significantly lower density [45, 310]. By analyzing our simulations within the framework of the d-band model and assuming a coupling strength of $V^2 = 1$, we find that in the standard DFT calculation with $U_{\mathrm{eff}} = 0$, the LUMO state does not split into distinct hybridized states but instead exhibits a broadened energy distribution in both spin channels (see Fig. 5.17b).

As anticipated from the previously discussed variation of U_{eff} and its impact on the MOPDOS, the electronic structure changes significantly when an appropriate U_{eff} is applied to accurately reproduce the exchange splitting of the Fe *d*-bands. The resulting spin-resolved MOPDOS is shown in Fig. 5.18a. Consistent with the earlier finding that $U_{\mathrm{eff}} = -3.1\,\mathrm{eV}$ provides the best approximation of the DMFT-corrected band structure, this value is employed in our calculations. This adjustment leads to two pronounced energetic overlaps: first, in the spin-up channel, where the HOMO strongly interacts with the Fe majority states, and second, in the spin-down channel, where the LUMO overlaps with the Fe minority states.

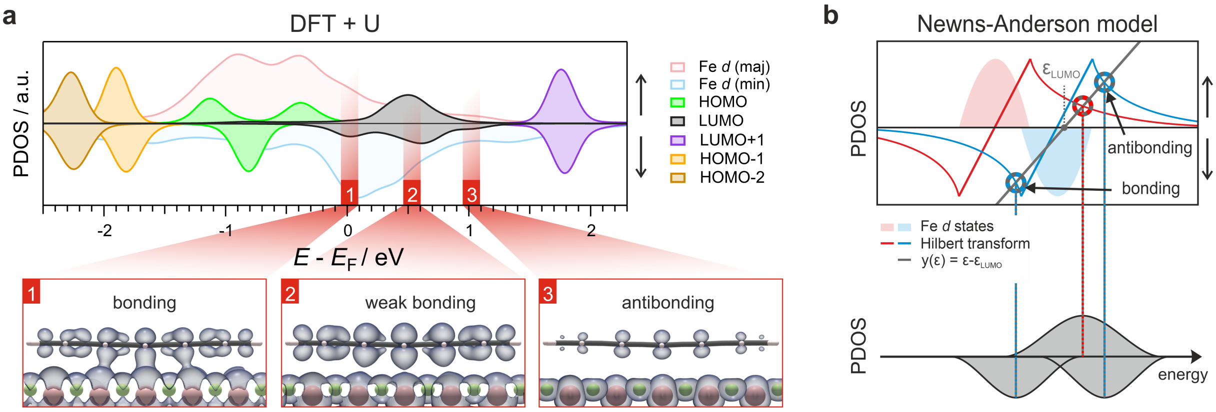

Figure 5.18: Electronic structure of the 5A/Fe–O interface calculated using DFT+U, illustrating the impact of *d*-band modifications. **(a)** Resulting MOPDOS for 5A adsorbed on Fe–O, obtained from optimized DFT+U calculations using $U_{\mathrm{eff}} = -3.1\,\mathrm{eV}$. The adsorption geometry is the same as in Fig. 5.17a. For the MOPDOS of the LUMO we identify three main peak regions, which are indicated by red bars. In the bottom part the corresponding electron densities (spin-integrated), which stem from the highlighted peak regions, are plotted. **(b)** Scheme of the spin-resolved Newns-Anderson model for a substrate DOS like the one from (a). In the top graph, the adsorbate function (solid grey line) intersects the majority Hilbert transform (solid red line) only once, while three intersections are found between the adsorbate function and the Hilbert transform of the minority states (blue line). According to the model, this results in a single broadened resonance in the spin-up PDOS, and the formation of bonding and antibonding resonances in the spin down PDOS. Figure from manuscript currently under review.

According to the predictions of simplified chemisorption models, molecular and substrate states must be energetically close to induce a non-negligible hybridization, leading to the formation of bonding and antibonding adsorbate–metal states. Applying this concept to our previous picture of the LUMO adsorbate function and its coupling to now much narrower and less-split *d*-states indeed results in the emergence of well-separated bonding and antibonding states in the spin-down channel, where $\varepsilon_{\mathrm{LUMO}}$ overlaps with the metal *d*-bands (see Fig. 5.18b). At the same time, in the spin-up channel, only a single intersection remains for the LUMO, corresponding to a broadened molecular resonance.

A closer examination of the integrated density in the LUMO region of the DFT+U calculation further supports the predictions of the *d*-band model. The spin-integrated density plots shown at the bottom of Fig. 5.18a indicate that each peak corresponds to a distinct aspect of chemical bond formation. For the peak closest to the Fermi level (1), a pronounced bonding-like interaction is observed between the three central sets of LUMO lobes and the Fe *d*-states, aligning with the predicted bonding state in the spin-down channel of the *d*-band model. Conversely, for the peak furthest from the Fermi level (3), the density distribution exhibits a distinct antibonding character, once again consistent with the simplified bonding model for the spin-down channel.

In contrast, the density plot corresponding to the central peak (2), which contributes the most significantly to the spectral weight, represents a weakly bonding state, resembling the uncorrected DFT scenario with $U_{\mathrm{eff}} = 0\,\mathrm{eV}$ that we discussed earlier in Fig. 5.17.

Hence, we conclude that while many-particle effects play a decisive role in shaping the electronic structure of the substrate, and thereby govern the degree of chemical interaction, their influence appears to be largely confined to this aspect. Accordingly, despite the enhancement of correlation effects, a description of the adsorbate-metal system in terms of single-particle approximations may remain valid. Strikingly, this opens the possibility of achieving a quantitative description of the interface using simplified chemisorption theory. In the following, we explore this prospect by directly applying the Newns-Anderson formalism to simulate the electronic structure.

5.3.6 Applying the *d*-band Formalism to the 5A/Fe–O Interface

To test the validity of the Newns–Anderson theory, we focus on molecular states that exhibit strong interaction with the substrate, while disregarding those that remain largely unaffected due to weak overlap. For this purpose, we use the expression for the adsorbate DOS derived from the Newns–Anderson model, as described in Section 1.4.5, to simulate the MOPDOS of selected molecular orbitals. This naturally leads to the HOMO in the spin-up channel as the primary benchmark, since it strongly interacts with the Fe majority *d*-states, resulting in a distinct bonding–antibonding splitting.

As shown in Fig. 5.19, the substrate DOS in the Newns–Anderson model is represented by a semi-elliptical function, shaped to approximate the Fe–O surface DOS obtained from DFT+U. The coupling strength $|V|$ is treated as an empirical parameter and slightly increased from its former value of $|V| = 1$ to $|V| = 1.4$ in order to optimize agreement with the DFT+U results for the adsorbate spectral function.

With this setup, the spectral character predicted by the Newns–Anderson model closely follows the DFT+U results across all tested U_{eff} values ($U_{\mathrm{eff}} = 0\,\mathrm{eV}$ corresponds to standard DFT). It consistently reproduces the evolution from a single resonance to distinct bonding and antibonding features, as well as the associated changes in relative peak intensities. This agreement demonstrates that the simplified model captures the key features of the hybridization. However, the absolute energies of the adsorbate resonances remain offset relative to the DFT+U results, indicating that while the model captures the correct qualitative behavior, the quantitative agreement is limited.

In contrast to the HOMO, the situation for the LUMO is more intricate. As before, we focus on the spin-down component, which shows the strongest interaction with the Fe minority *d*-states. The overall spectral character predicted by the Newns-Anderson model again reflects the key features of the DFT+U results: the molecular resonance broadens and eventually splits as U_{eff}

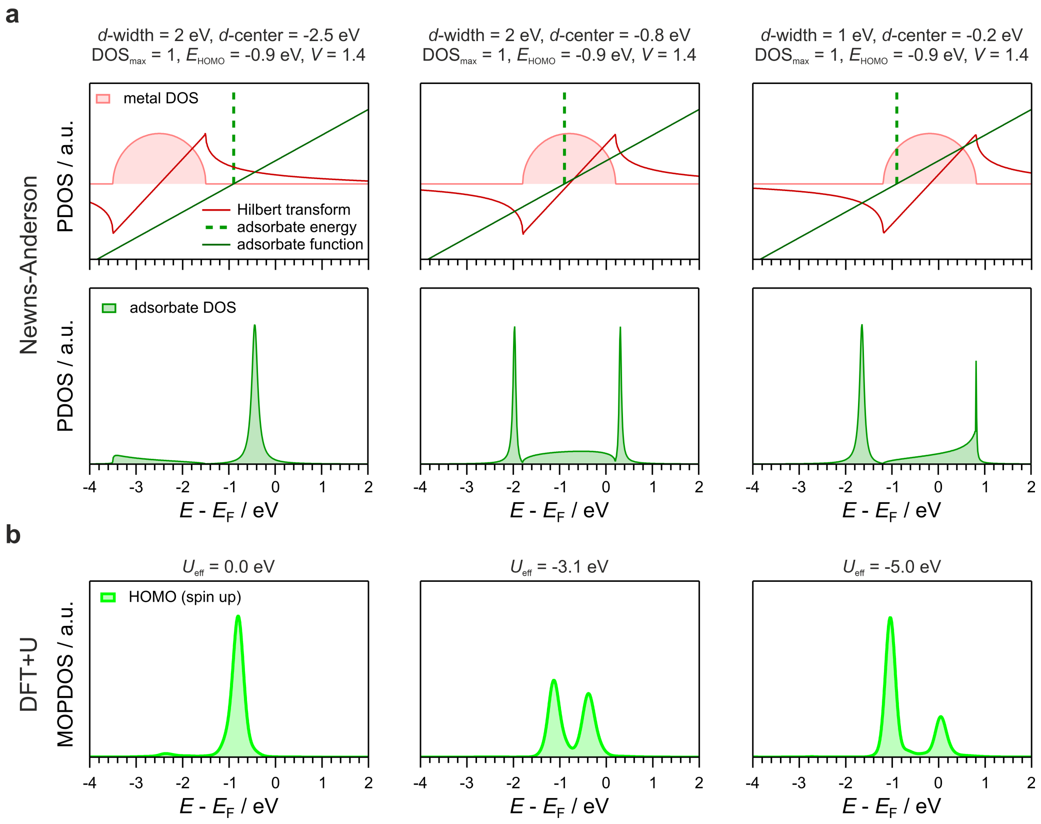

Figure 5.19: Comparison of Newns-Anderson model and DFT+U calculations for the HOMO in the spin-up channel. **(a)** Top row: Solutions obtained from the Newns-Anderson model for different d-band center positions, with parameters specified above each panel. The red curve represents the metal d-PDOS, the dark red line the corresponding Hilbert transform, and the green lines the adsorbate function. The dotted green line indicates the energy of the adsorbate state. Bottom row: Resulting adsorbate PDOS according to the Newns-Anderson model. **(b)** Corresponding spin-resolved MOPDOS of the HOMO from DFT+U calculations for different U_{eff} values.

becomes more negative (see Fig. 5.20). However, compared to the HOMO, noticeable deviations emerge in the details of the LUMO structure.

To improve agreement with the DFT+U results, the effective coupling strength was empirically adjusted from the value used for the HOMO ($|V| = 1.4$) to a slightly lower value of $|V| = 1.12$ for the LUMO. This refinement yields a noticeably better match in the overall spectral shape, particularly in capturing the distribution and relative intensity of the peaks. While the adjustment enhances the agreement, the underlying justification for the weaker coupling remains empirical, suggesting that the interaction strength may vary depending on the specific orbital character of the molecular state.

Despite this adjustment, the Newns-Anderson model still falls short of reproducing the general spectral shape of the LUMO in comparison to the results from DFT+U simulations. Most notably, while the simplified model yields two resonances — corresponding to bonding and

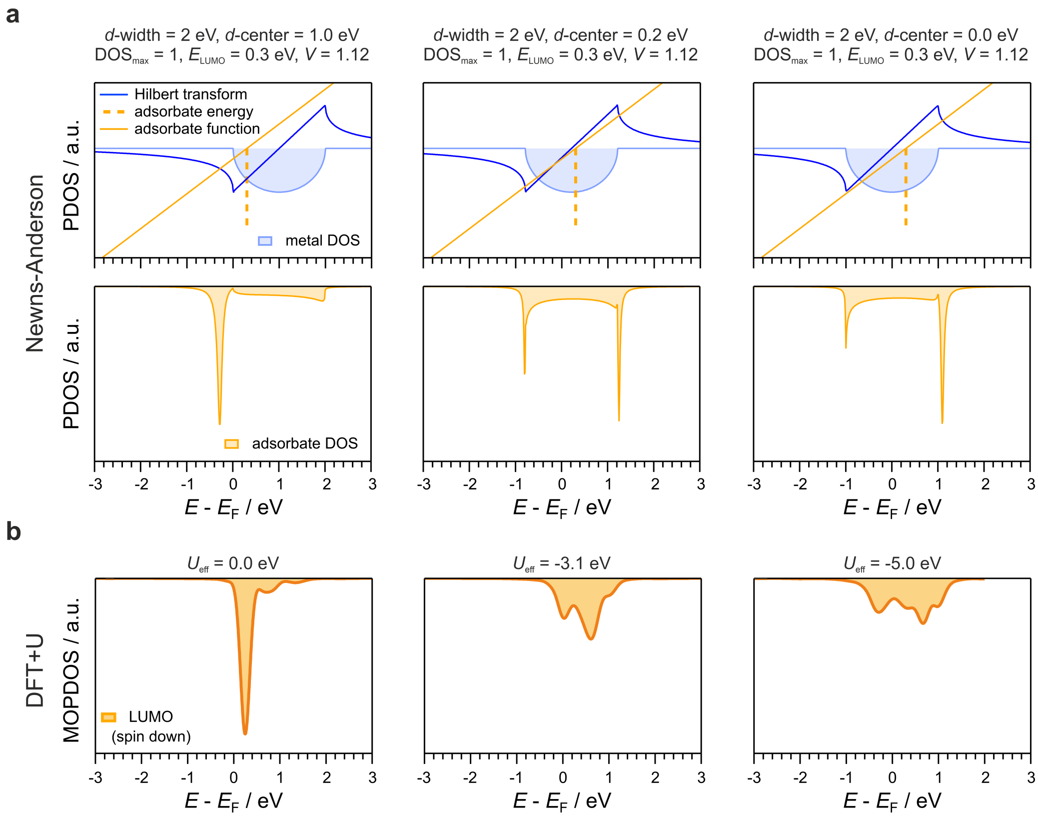

Figure 5.20: Comparison of Newns-Anderson model and DFT+U calculations for the LUMO. **(a)** Top row: Solutions obtained from the Newns-Anderson model for different d-band center positions, with parameters specified above each panel. Bottom row: Resulting adsorbate PDOS, considering only the spin-down channel.**(b)** Corresponding spin-resolved MOPDOS from DFT+U calculations for selected U_{eff} parameters.

antibonding states — the DFT+U calculations reveal a more complex structure consisting of multiple distinct peaks (see Fig. 5.18a). This contrasts with the HOMO behavior, where both the model and DFT+U consistently produce two clear resonances.

This discrepancy underscores a broader limitation of the model: even with the adjusted coupling strength, the LUMO-related resonances remain less accurately described than those of the HOMO. In addition, there is a persistent offset in absolute energies for both adsorbate states (LUMO and HOMO). This indicates that, in its current form, the Newns–Anderson model does not fully capture the electronic structure of the interface, although it reliably reproduces the onset of hybridization and its qualitative evolution with varying d-band positions.

So far, our analysis has primarily attributed the molecular level evolution to variations in the substrate d-band properties. However, this perspective implicitly assumes that spatial non-uniformities of adsorbate–substrate orbital overlap play only a secondary role. This raises a critical question:

Can the deviations observed in the LUMO resonance be traced back not merely to energetic alignment, but to variations in the coupling across the molecule?

For larger and structurally more complex adsorbates, such as acenes (see Fig. 1.2a), the assumption of a spatially uniform hybridization becomes increasingly tenuous. In the following section, we interrogate this assumption and explore how variations in the local coupling strength might alter the spectral fingerprints of hybridization, thereby offering a more complete account of the limitations observed in the standard Newns–Anderson framework.

5.3.7 Refining the *d*-Band Theory for Extended Organic Adsorbates

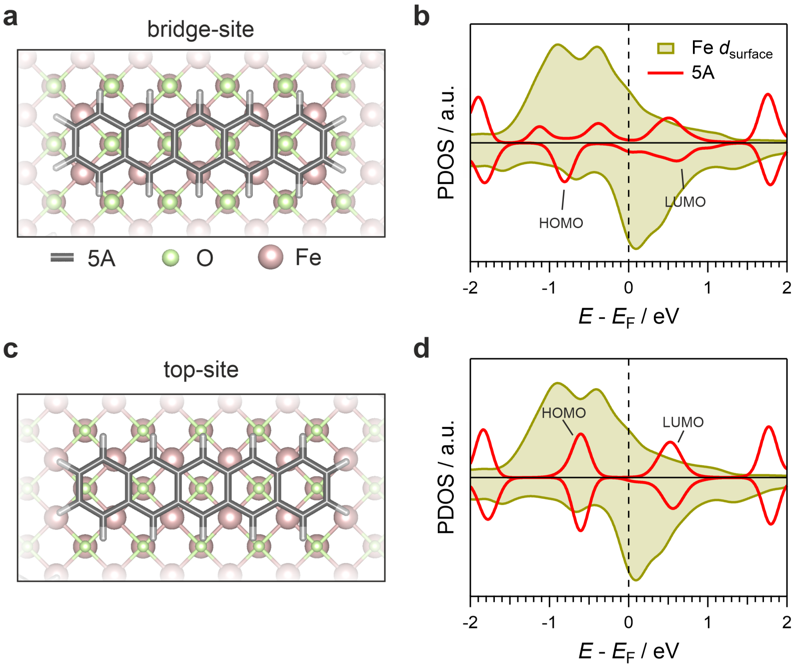

Figure 5.21: Influence of adsorption geometry on the electronic structure of 5A. **(a)** Optimized adsorption configuration for 5A molecules on the Fe–O surface and **(b)** the resulting PDOS. **(c)** Arrangement of a 5A molecule shifted by half a substrate unit cell vector along the oxygen rows relative to the optimized configuration. **(d)** PDOS obtained for the adsorption geometry shown in (c). All data were obtained using DFT+U with $U_{\mathrm{eff}} = -3.1\,\mathrm{eV}$. Figure from manuscript currently under review.

Having evaluated the role of the Fe *d*-bands in shaping the electronic structure of adsorbed 5A, we now turn to the second crucial factor influencing chemical bond formation: the spatial overlap between molecular orbitals and substrate states, which is reflected in the coupling strength, V^2. Naturally, this overlap should be highly dependent on the adsorption geometry.

To understand this dependence, we compare the optimized 5A adsorption geometry with an alternative configuration in which the molecules are displaced by half a substrate unit cell vector along the oxygen rows (see Fig. 5.21). This displacement alters the registry between the 5A backbone and the Fe lattice, moving the central carbon atoms away from directly atop Fe surface sites to positions between them.

Using the same $U_{\text{eff}} = -3.1\,\text{eV}$ value as in previous calculations, we compute the PDOS for this modified configuration and find a striking change in the electronic structure. The spin-dependent features associated with strong chemical interactions, such as molecular state splitting and broadening, almost completely vanish. Instead, both the HOMO- and LUMO-related resonances appear as single peaks in each spin channel, indicating a suppression of hybridization effects.

By directly comparing these two adsorption geometries, it is evident that the spatial arrangement of the molecule is a key parameter in determining the extent of hybridization with the Fe *d*-bands. This sets the foundation for a more detailed analysis of the spatial overlap in the optimized configuration.

To illustrate this, we visualize the electron density distributions of the gas-phase HOMO and LUMO of 5A atop the Fe–O surface in the optimized adsorption geometry (Fig. 5.22a,b). The HOMO exhibits near-perfect alignment with the Fe *d*-states due to an incidental match between its nodal structure and the periodicity of the Fe surface lattice (Fig. 5.22a). This spatial compatibility facilitates strong orbital overlap, *i.e.* coupling, leading to the pronounced bonding-antibonding splitting.

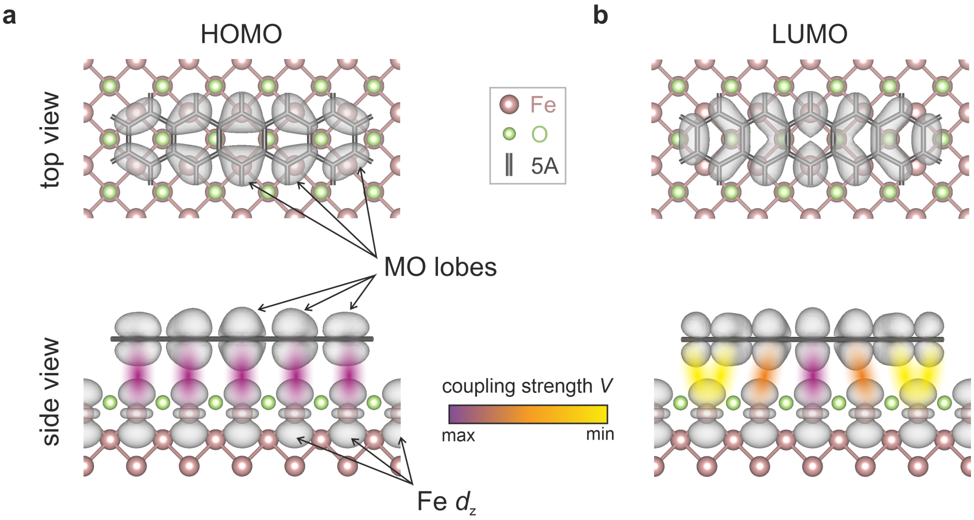

Figure 5.22: Illustration of the orbital overlap between the 5A frontier orbitals and the Fe *d*-states. Plots of the gas phase **(a)** HOMO and **(b)** LUMO of 5A placed atop the Fe–O surface for the optimized adsorption geometry. In the bottom panels, the assumed degree of spatial overlap between the MO lobes and idealized Fe *d* orbitals corresponds to a certain coupling strength highlighted by the indicated color code. Figure from manuscript currently under review.

In contrast, the LUMO, which features a shorter spatial periodicity, exhibits significant overlap only in its central lobes, while the outer lobes extending toward the molecular edges overlap much more weakly with the Fe states (Fig. 5.22b). The resulting non-uniform coupling across the molecular backbone challenges the conventional *d*-band model, which assumes a uniform interaction throughout the entire molecule.

Staying within the conceptual framework of the *d*-band model, we propose an empirical approach to cope with such non-uniformities in the overlap between individual MOs of 5A and the Fe *d*-states. By assuming that different regions of the molecular orbitals interact locally with the underlying Fe atoms, we suggest that the *d*-band model can be applied, however, using local coupling strengths. To this end, we spatially partition the LUMO into separate regions and estimate differences in the coupling strengths from the variations in the orbital overlap with the Fe *d* states.

In essence, the idea is to introduce varying coupling strengths based on differences in the overlap between single lobes of MOs with the subjacent Fe *d*-states, in order to take into account the local nature of the interaction.

Thereby, we may explain the difference in behavior between the HOMO and LUMO level splitting with the different spatial distribution of the frontier orbitals, *i.e.* the shape of their lobes, and their relative position to the Fe atoms of the surface below.

In the following, we demonstrate this influence of the orbital distribution on the *d*-band model, specifically on the coupling parameter $V_{\mathrm{C-Fe}}$[‡] — by means of an illustrative model calculation. In our model, we divide the LUMO of 5A along its long axis according to its nodal structure into four separate regions ($V1$ - $V4$), as illustrated in Fig. 5.23a (the regions are doubled by symmetry).

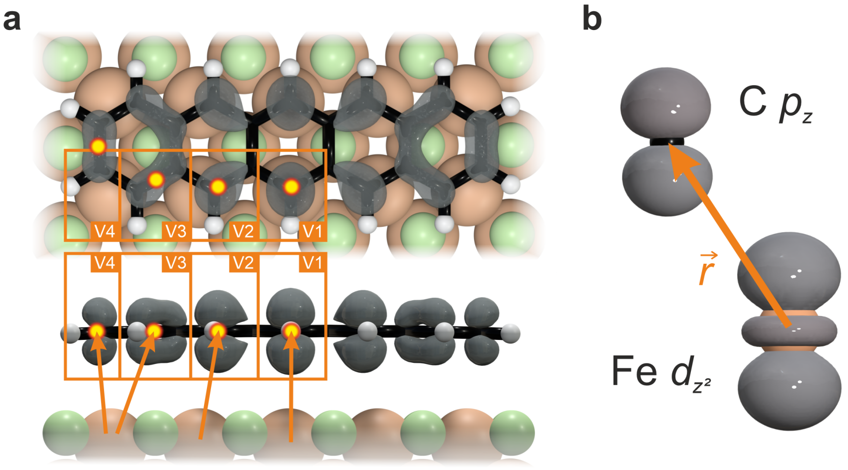

Figure 5.23: Approach to treat non-uniform coupling at the 5A/Fe–O interface. **(a)** Schematic of the four different coupling regions ($V1$-$V4$) representing distinct orbital lobes according to the nodal structure of the LUMO of 5A. The respective lobes are then approximated by p_z orbitals positioned at the yellow circles. The red arrows indicate the position vectors $\vec{r}$. **(b)** Illustration of the geometric arrangement of the approximated p_z adsorbate and the Fe d_{z^2} substrate states.

[‡] The term $V_{\mathrm{C-Fe}}$ refers to the coupling between states from Fe and C atoms

As the frontier orbitals of 5A are dominated by π-bonding character, *i.e.* with a nodal plane in the molecular plane, we then approximate each region by a single p_z orbital. The assumed p_z orbital is positioned such that the center of the density of the p_z orbital coincides with the center of the density of the respective LUMO region (marked by yellow dots in Fig. 5.23a).

In the next step, we assume that the major contribution to the molecule–surface interaction consists of σ-type bonding between the LUMO and Fe d-states. Among the d-orbitals, the d_{z^2} orbital exhibits the best symmetry match for this interaction. Hence, for each region, we approximate the molecule-surface interaction as an interaction between a C p_z state, located at the center of the respective LUMO lobe, and a d_{z^2} orbital, located at the nearest Fe atom of the surface. An illustration of this approach is depicted in Fig. 5.23b.

This approach simplifies the complex LUMO distribution into several two-center problems, which we now analyze separately. The resulting position vectors, $\vec{r}$, for the four regions are summarized in Table 5.1. Notably, the p_z location shifts from being nearly on top of a Fe atom in region $V1$ to a significantly displaced position in regions $V3$ and $V4$.

Additionally, we assume that the energies of the p_z states still correspond to the energy of the respective molecular orbital, ensuring that their interaction with the Fe surface does not alter the internal electronic structure of the LUMO itself. Moreover, since these p_z states belong to the same molecular orbital, no additional direct interaction between them is considered. Given the delocalized nature of the molecular orbital, this is a reasonable assumption, as any internal coupling is already accounted for in the molecular electronic structure.

Table 5.1: Distance $|\vec{r}|$ and position vector $\vec{r}(x, y, z)$ of the C(p_z) orbitals approximating the individual LUMO lobes relative to the respective Fe atom below. Values are given in Å. Table from manuscript currently under review.

Region	x / Å	y / Å	z / Å	$\|\vec{r}\|$ / Å
$V1$	-0.055	0.024	3.092	3.093
$V2$	-0.128	0.557	3.186	3.237
$V3$	-0.382	1.290	3.274	3.539
$V4$	-0.872	-0.594	3.269	3.435

Based on these approximations, the coupling strength for each LUMO region is given by

$$V_{\mathrm{C-Fe}} = \eta \frac{M_C M_{\mathrm{Fe}}}{|\vec{r}|^{(l_{\mathrm{C}}+l_{\mathrm{Fe}}+1)}} \tag{5.4}$$

where $|\vec{r}|$ is the absolute distance between the C and Fe atom in question, and η is a structure factor accounting for their relative positioning [48, 311, 312]. For η, we use the Slater-Koster geometry factor for a σ-bond between a p_z and d_{z^2} state [313]:

$$\eta = n_z \left(n_z^2 - \frac{1}{2}(l_x^2 + m_y^2) \right), \tag{5.5}$$

where

$$l_x = \cos\alpha_x, \quad m_y = \cos\alpha_y, \quad n_z = \cos\alpha_z \tag{5.6}$$

correspond to directional cosines. The resulting structure factors for each region are given in Table 5.2.

Table 5.2: Directional cosines (l_x, m_y, n_z) and structure factors η for a C(p_z)-Fe(d_{z^2}) σ-bond. Table from manuscript currently under review.

Region	l_x	m_y	n_z	η
$V1$	-0.017	0.007	0.999	1.000
$V2$	-0.040	0.172	0.984	0.938
$V3$	-0.108	0.364	0.925	0.725
$V4$	-0.254	-0.173	0.952	0.817

The coupling further depends on the angular quantum number l of the adsorbate state (p_z: $l_\text{C} = 1$) and the metal state (d_z^2: $l_\text{Fe} = 2$). The values M_C and M_Fe describe the potential around the atoms, however, these parameters are usually considered independent of the atomic positions. To illustrate the variation in $V_\text{C-Fe}$ with respect to the C-Fe position, we compare the coupling strength of each region relative to $V1$, where both atoms are directly aligned. This reference case corresponds to the idealized situation discussed in Fig. 5.18.

For our positional analysis, the change in coupling strength depends on the C-Fe separation as $1/|\mathbf{r}|^4$ and on the relative positioning via η. The resulting relative reduction factors for regions $V2$–$V4$ are summarized in Table 5.3. Notably, according to this modeling the coupling strength is reduced by up to a factor of ~5 for the most displaced LUMO regions.

Table 5.3: Relative reduction of the coupling strength ΔV^2 due to C-Fe (Δr) separation and the structure factor ($\Delta\eta$). Table from manuscript currently under review.

Region	Δr	$\Delta\eta$	ΔV^2
$V1$	Reference	1.000	1.000
$V2$	0.833	0.938	0.611
$V3$	0.583	0.725	0.178
$V4$	0.657	0.817	0.288

Despite the approximations involved, this analysis formally integrates the local and non-uniform nature of the bonding by introducing a set of position-dependent coupling strengths. These variations reflect how the interaction strength changes across different regions of the molecule and must now be incorporated into the d-band model to assess their impact on the electronic structure.

To convert the relative coupling strengths into absolute values, we anchor the maximum coupling constant, $V1$, to the value we formerly established for the HOMO. This calibration is physically motivated by the spatial coincidence between the central lobes of the HOMO and the LUMO, which define the region associated with $V1$. In this way, we ensure continuity with our earlier parameterization while introducing spatial resolution. The resulting effective coupling strengths are set to $V^2 = 2.0$, 1.6, and 0.4 for the central ($V1^2$), intermediate ($V2^2$), and outer ($V3^2 + V4^2$) LUMO regions, respectively. These values fall within the typical range expected for molecular adsorbates on transition metal surfaces such as Fe [48, 311, 312].

Since the coupling strength enters the *d*-band and Newns–Anderson framework as $1/V^2$, it directly influences the slope of the corresponding lobe-functions[§]. As indicated in the last row of Table 5.3, the coupling strength is substantially reduced for the outer LUMO regions, implying that the associated lobe-functions for regions $V3$ and $V4$ would exhibit much steeper slopes compared to those for $V1$ and $V2$. To qualitatively examine the consequences of this spatial

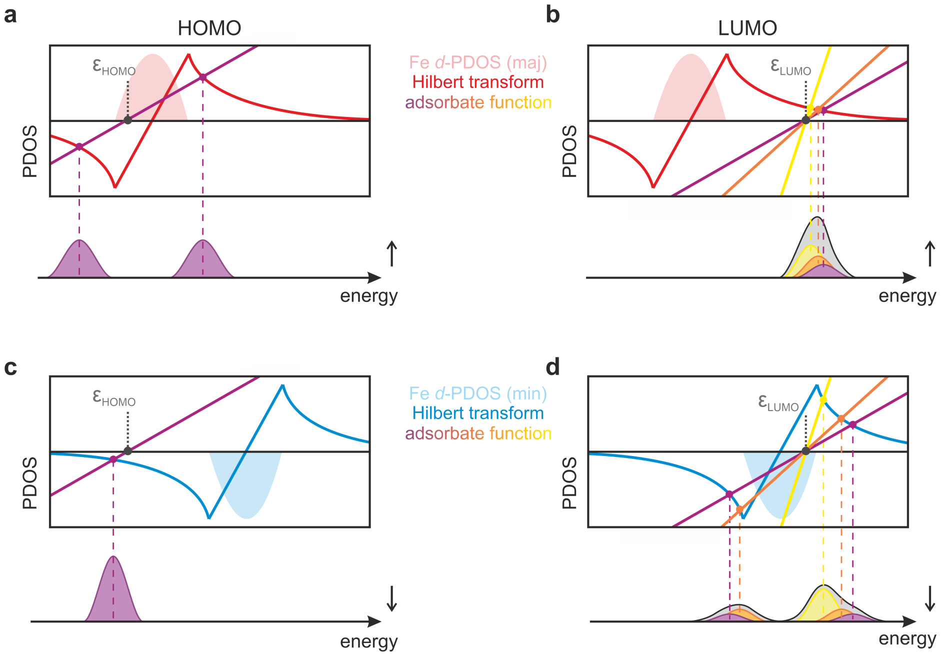

Figure 5.24: Modeling the interaction between the 5A frontier orbitals and the Fe *d*-states within the Newns-Anderson framework. **(a),(b)** Newns-Anderson model for the interaction of the 5A **(a)** HOMO and **(b)** LUMO with the Fe majority *d*-states. In accordance with the model, the interaction of the HOMO is approximated by a single adsorbate function with a slope of $s = 1/V^2 = 0.5$, while the non-uniform overlap between the Fe and LUMO orbital lobes results in a set of adsorbate functions with varying slopes of $s = 0.5$, $s = 0.8$, and $s = 2.4$. The bottom panels present estimations of the resulting MOPDOSs. **(c),(d)** Schematic representation of the Newns-Anderson model describing the interaction between the minority Fe *d*-states and the **(c)** HOMO or **(d)** LUMO. Figure from manuscript currently under review.

[§] The term lobe-function refers to a localized component of the full adsorbate function, obtained by spatially partitioning the molecular orbital into distinct lobes.

variation in the coupling, we construct a schematic version of the d-band model in which the determined lobe-function slopes ($s = 1/V^2$), are assigned to the corresponding parts of the molecular orbital. The results, shown in Fig. 5.24a–d for both spin channels and for the HOMO and LUMO, are not based on numerical evaluation but serve as illustrative diagrams to highlight how local variations in coupling strength might affect the position and nature of the resulting resonances via altered intersections with the Hilbert transform.

For the HOMO, the uniform spatial overlap with the Fe atoms, arising from its periodicity matching that of the substrate, results in a particularly simple case. It effectively behaves as a single, delocalized adsorbate function, requiring only one lobe-function to describe its interaction with the d-band. As expected, this yields two resonances in the spin-up channel and a single one in the spin-down channel (see Fig. 5.24a,c), consistent with the DFT+U results and our $\mathrm{d}I/\mathrm{d}V$ measurements. This outcome aligns with the predictions of the standard Newns–Anderson model, as the uniform coupling eliminates the need for further spatial considerations.

In contrast to the HOMO, the LUMO exhibits a more intricate interaction pattern due to its spatially varying overlap with the Fe atoms. The three distinct local coupling strengths translate into lobe-functions with different slopes, leading to multiple intersection points with the Hilbert transform. In the spin-up channel, these resonances lie close in energy and effectively merge into a single broadened feature (Fig. 5.24b), while in the spin-down channel, the larger energy separation yields a structure with three distinguishable contributions (Fig. 5.24d).

This qualitative behavior reflects the MOPDOS obtained from DFT+U calculations and underscores how spatial variations in the coupling, arising from the registry between molecular lobes and substrate atoms, can govern the spectral response. Notably, no such variation is observed for the HOMO, whose uniform spatial overlap leads to homogeneous coupling and a resonance structure consistent with the standard Newns–Anderson prediction.

5.3.8 Introducing the d_{z^2}-Band Center Model of Organic Chemisorption

So far, we have demonstrated good agreement between experimental data and theoretical calculations, supported by a possible qualitative understanding based on simplified chemisorption models. However, a precise quantitative match, particularly in the MO resonance energies, remains elusive (see Fig. 5.20 and Fig. 5.19). While the introduction of non-uniform coupling improves the LUMO lineshape by reproducing its multi-peak structure, it would not resolve the energy offset. For both the HOMO and LUMO, the model continues to overestimate the resonance splitting, possibly indicating that some interaction-specific details are not fully captured in the current description, pointing to limitations of simplified models.

A central approximation in the previous models was the treatment of the Fe d-states as a single, collective manifold. While this simplification enabled a straightforward application of the Newns–Anderson scheme, it neglects the orbital-specific nature of the hybridization. Among the five d-orbitals, the d_{z^2} orbitals of the surface Fe atoms not only extend significantly out of the plane but also exhibits the appropriate symmetry to effectively overlap with p_z-type adsorbate molecular orbitals. Given this spatial and symmetry-based compatibility, one can expect the d_{z^2} orbital to dominate the coupling mechanism. We therefore refine the model by restricting the interaction to the surface PDOS of the Fe d_{z^2} states. Accordingly, we refer to this approach as the d_{z^2}-center model.

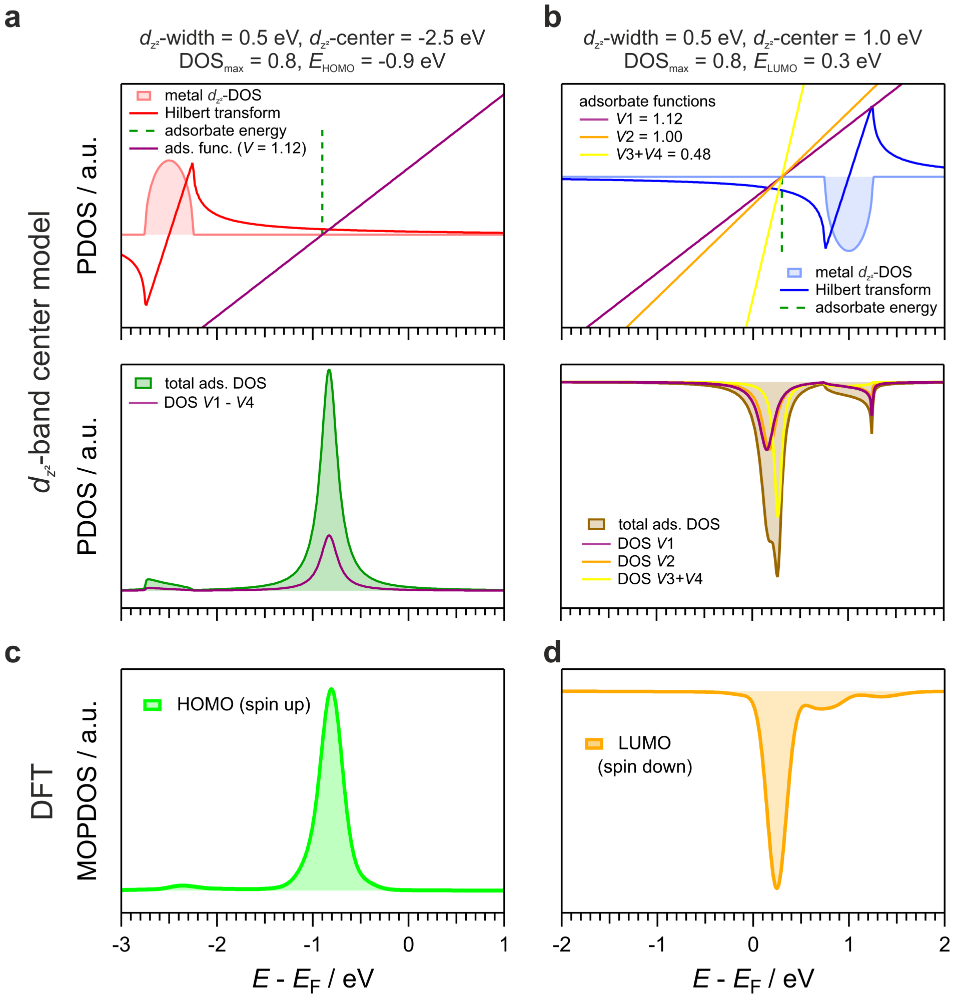

Figure 5.25: Comparison of the d_{z^2}-center model and DFT results for the spin-up HOMO and spin-down LUMO components. **(a)** Newns–Anderson-like model for the HOMO, based on the Fe d_{z^2}-projected DOS from DFT. The coupling is assumed to be spatially homogeneous across regions $V1$–$V4$, resulting in the HOMO being represented by a single adsorbate function. **(b)** Newns–Anderson-like model for the LUMO, using three distinct lobe functions for regions $V1$, $V2$, and $V3/V4$ (weighted accordingly) to simulate spatially varying coupling. **(c)** Spin-up DFT MOPDOS for the HOMO. **(d)** Spin-down DFT MOPDOS for the LUMO.

To account for the lower DOS associated with the d_{z^2} orbitals (in comparison to the total d-PDOS), the maximum width of metal DOS in the model is narrowed from 2 eV to 0.5 eV and scaled in amplitude to yield approximately one-fifth of the original total d-band DOS peak area. This is consistent with the five-fold degeneracy of the d-manifold. Using this adjusted DOS, we recompute the adsorbate PDOS for both HOMO and LUMO states by applying the Newns–Anderson procedure, now also incorporating the previously determined, region-specific coupling strengths.

The results, shown in Fig. 5.25 and Fig. 5.26, exhibit excellent agreement with the MOPDOSs obtained from DFT and DFT+U, respectively. For the HOMO, which exhibits uniform coupling across its spatial extent, the d_{z^2}-center model reproduces both the position and shape of the hybridized states with high accuracy. In the case of the LUMO, where spatial overlap with the substrate varies across the molecule, we incorporate three distinct adsorbate functions for regions $V1$, $V2$, and $V3/V4$ (weighted accordingly). Even in this more complex scenario, the model captures the spectral features of the spin-down MOPDOS remarkably well.

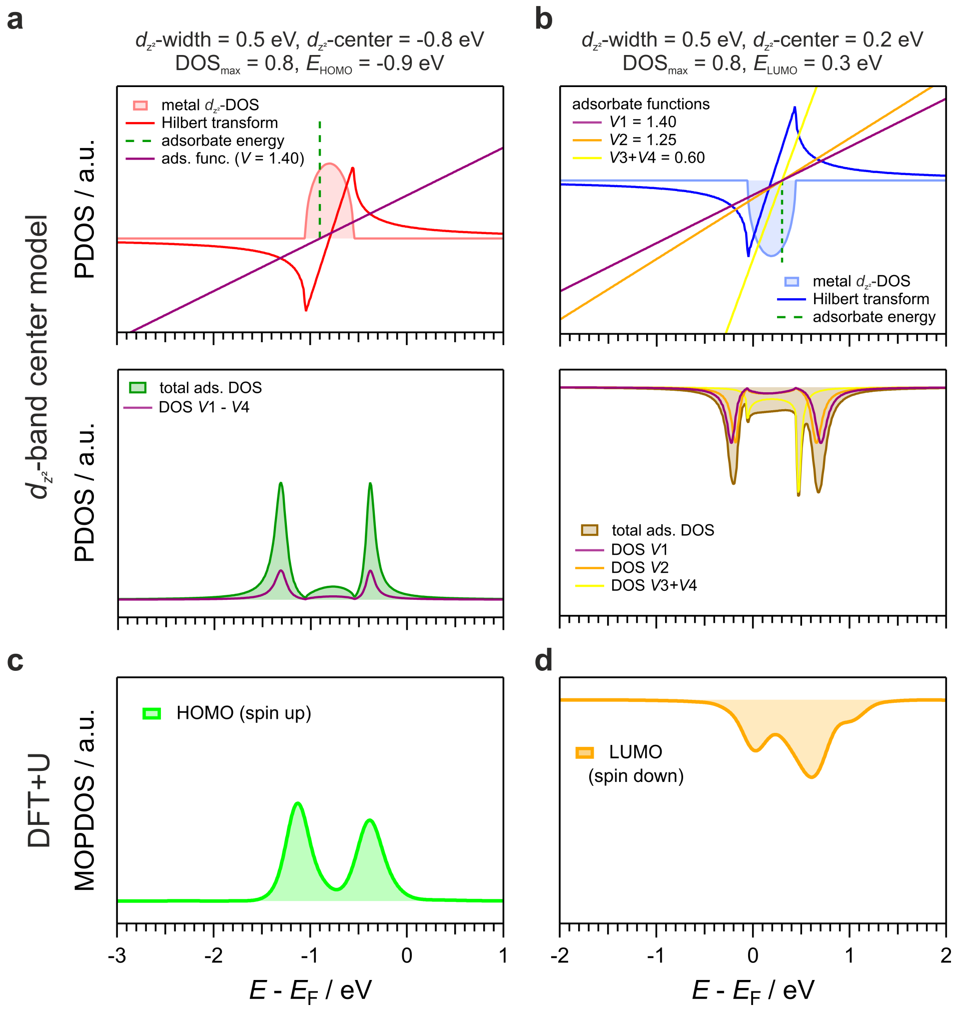

Figure 5.26: Comparison of the d_{z^2}-center model and DFT+U results ($U_{\mathrm{eff}} = -3.1\,\mathrm{eV}$) for the spin-up HOMO and spin-down LUMO components. **(a)** Newns–Anderson-like model for the HOMO, based on the spin-up Fe d_{z^2}-projected DOS from DFT+U. **(b)** Newns–Anderson-like model for the LUMO, using three distinct lobe functions corresponding to regions $V1$, $V2$, and $V3/V4$. **(c)** Spin-up DFT+U MOPDOS for the HOMO. **(d)** Spin-down DFT+U MOPDOS for the LUMO.

Hence, the refined framework not only improves the quantitative predictive power of the d-band model but also suggests a more dominant role of the surface d_{z^2} orbitals in mediating bonding at organic–metal interfaces. In contrast to small atomic adsorbates, which can embed into surface sites and couple to the full d-state manifold, large organic molecules such as 5A typically reside at distances of 2–4, Å above the surface, significantly limiting their overlap with in-plane d-orbitals. Consequently, the out-of-plane, protruding d_{z^2} orbitals are expected to become the principal channel for hybridization.

We therefore propose the d_{z^2}-center model as an efficient and physically motivated extension of the traditional d-band framework, specifically tailored to large organic adsorbates. With minimal input — requiring only the surface d_{z^2}-projected DOS and qualitative knowledge of the adsorbate's frontier orbitals — it offers a computationally inexpensive yet powerful approach to estimate and rationalize the electronic structure of complex metal–organic interfaces.

5.4 Conclusion: A Correlation-Aware Framework for Chemisorption on Ferromagnets

In this chapter, we have shown that a renormalization of the Fe d-bands, driven by electron correlation, strongly influences the bonding chemistry of 5A molecules on the oxygen-passivated Fe(100)–$p(1 \times 1)$O surface. We find that these effects can be effectively captured by treating the correlation-induced d-band reshaping as an intermediate step within simplified chemisorption models, as illustrated in Fig. 5.27.

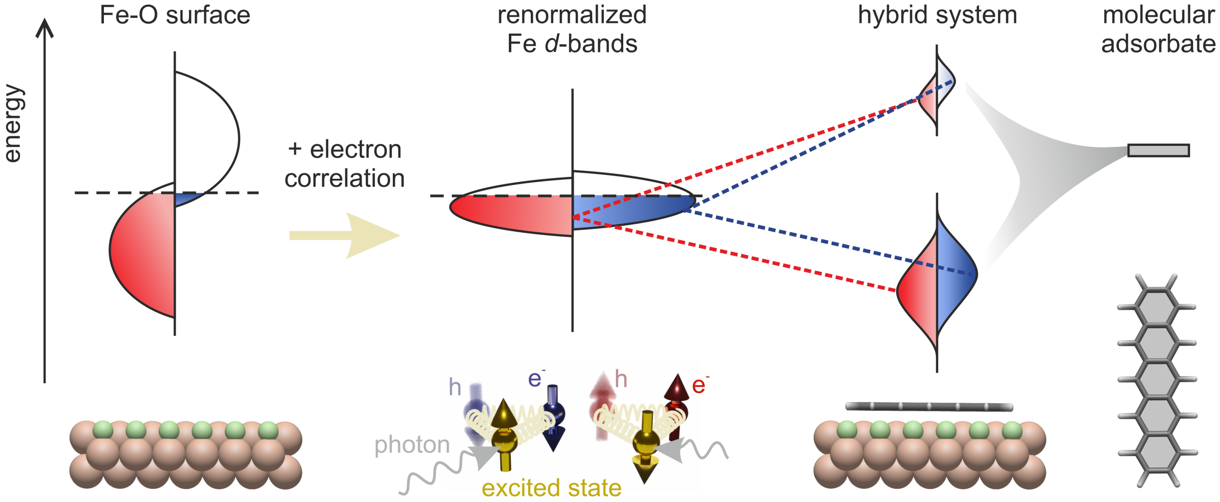

Figure 5.27: Schematic illustration of how electronic correlations reshape the Fe–O surface DOS and alter chemisorption behavior. The left shows the d-projected DOS in the single-particle picture. Upon oxygen adsorption, many-body effects narrow the d-bands, reduce exchange splitting. This renormalization directly controls the hybridization with organic adsorbates, enabling strong bonding interactions and the formation of distinct bonding and antibonding states. Figure from manuscript currently under review.

The investigation commenced with a structural characterization of the 5A/Fe–O interface using STM and LEED. These measurements revealed that the molecules adsorb in an ordered fashion, aligning preferentially with the substrate's [001] and [010] directions. At sub-monolayer coverage, 5A tends to form islands with low packing density, while at saturation, extended domains of long-range ordered molecular domains, with roughly twice the packing-density, emerge. This behavior underscores the tendency of 5A to adopt an ordered configuration on the Fe–O surface, facilitated by molecule–substrate and intermolecular interactions.

To describe the electronic structure, we first established a theoretical framework based on DFT+U, tailored to weakly to moderately correlated ferromagnetic materials. While DFT+U is not typically employed for such systems, we justified its use by demonstrating that it can reproduce key correlation-induced features of the Fe *d*-band, such as band narrowing and reduced exchange splitting, as known from more sophisticated many-body treatments like DMFT. On this basis, we applied the DFT+U framework to interpret experimental data obtained from STM and POT, finding good agreement with respect to both the structural arrangement and the electronic signatures of the adsorbed molecules.

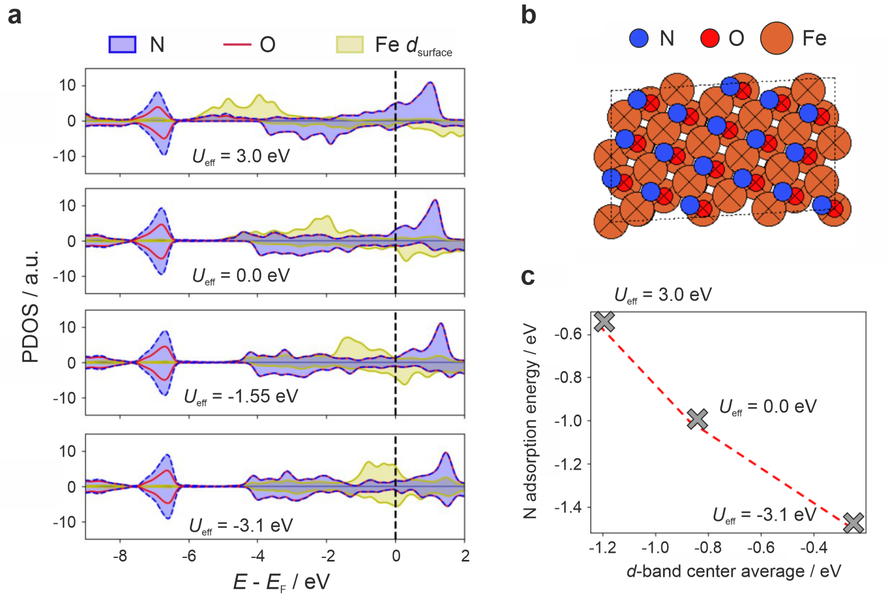

Figure 5.28: Influence of exchange splitting on the electronic structure and adsorption properties of nitrogen on Fe–O. **(a)** PDOS for nitrogen (N) adsorbed on the Fe–O surface, displaying the Fe *d*-bands and N states across four different U_{eff} parameter settings. The top curve corresponds to the highest U_{eff} value, while the bottom curve represents the lowest one (highly negative). **(b)** Adsorption site for N on the Fe–O surface, determined through structural optimization. **(c)** Dependence of the adsorption energy of N on the average surface *d*-band center, which shifts as the U_{eff} parameter is varied. The upward shift of the *d*-band center is accompanied by a reduction of the exchange splitting. Figure from manuscript currently under review.

Building on these insights, we emphasized how electronic correlation — through *d*-band narrowing and reduced exchange splitting — can fundamentally alter molecule–metal interactions. In the case of 5A on Fe–O, this renormalization switches the interface from a weakly to a strongly interacting system, contrary to the expectations of conventional single-particle theories. These effects are not only relevant for understanding spin-dependent hybridization, but also bear implications for surface reactivity, particularly in the context of heterogeneous catalysis, where *d*-band structure plays a decisive role in determining adsorption energies.

As a first conceptual outlook for this established framework, we examine the chemisorption of atomic nitrogen (N) on the same Fe–O surface Fig. 5.28. In contrast to 5A, N is a species that is highly relevant in catalytic processes. Using the same DFT+U approach employed for 5A, we find that the inclusion of correlation-driven changes in the Fe *d*-band leads to a substantial increase in N chemisorption energy relative to the standard single-particle description (see Fig. 5.28). This effect reflects recent observations of enhanced catalytic activity on 3*d* ferromagnetic surfaces upon suppression of their magnetic order, and suggests that electron correlation itself — through its impact on the *d*-band width and spin polarization — can serve as a critical lever in tuning surface reactivity.

While this broader relevance of correlation is promising, our detailed analysis of the 5A/Fe–O interface revealed an additional limitation of standard chemisorption theory: models assuming uniform molecule–substrate coupling fail to reproduce fundamental features of the adsorbate DOS. For large, structurally extended molecules such as pentacene, the assumption of spatially homogeneous hybridization breaks down. Both experimental data and DFT calculations reveal pronounced inhomogeneities in the frontier orbital spectra, indicating that the interaction strength varies across the molecular backbone.

To address this, we introduced a spatially resolved coupling scheme, wherein different regions of the molecular orbital couple locally to the substrate with varying strengths. This extension of the *d*-band model reproduces the observed registry-dependent hybridization patterns and demonstrates that even complex molecular systems can be described within a locally refined coupling framework. That pentacene exhibits strong spatial variations in bonding yet remains consistent with the extended *d*-band approach underscores the scalability and physical robustness of this model.

As a final refinement, we tested the d_{z^2}-center model, which captures the dominant role of the Fe d_{z^2} orbital in mediating coupling to planar organic molecules. Motivated by both geometric considerations and symmetry arguments, this orbital-specific extension focuses on the spatial overlap between out-of-plane d_{z^2} states and p_z-like molecular orbitals. By combining local coupling with an orbital-selective substrate DOS, the model reproduces the spectral structure of hybridized states with quantitative accuracy, closely matching DFT and DFT+U results.

In summary, this chapter has demonstrated that electron correlation fundamentally reshapes the *d*-band structure and, with it, the nature of molecule–metal interactions at ferromagnetic surfaces. By extending the *d*-band model to account for correlation-induced modifications of the *d*-band and spatially resolved coupling, we introduced a correlation-aware framework capable of capturing both the complexity of organic adsorption and the underlying physics of correlated substrates. While the results for pentacene and atomic nitrogen highlight the model's potential, its broader applicability remains to be tested across different adsorbates and materials. Such validation will be essential for establishing a general, predictive theory of chemisorption at correlated interfaces.

6 Metalloporphyrins on Fe–O: Adsorption, Conformation, and Electronic Structure

6.1 Introduction: Decoupling, Conformation, and Functional Diversity in Surface-Adsorbed Metalloporphyrins

The previous chapters have shown how the surface electronic structure of Fe(100) is modified by oxygen passivation, and how this passivated Fe–O interface still allows for strong molecule-substrate coupling in the case of entirely flat π-conjugated molecules such as 5A. In this chapter, we turn to the opposite end of the interaction spectrum: metalated porphyrin molecules that are electronically decoupled from the Fe–O surface. This weak interaction regime allows us to study the intrinsic properties of these fascinating and versatile molecules — such as the relationship between their conformation, structural symmetry, and orbital structure — in a controlled environment, largely unaffected by hybridization with the substrate.

Porphyrins are aromatic macrocycles composed of four pyrrole subunits connected via methine bridges*, forming a rigid and highly conjugated planar framework [314]. Their ability to coordinate metal cations at the central cavity, combined with extensive chemical tunability at the periphery, makes porphyrins both structurally diverse and functionally rich.

In biology, porphyrins and their derivatives — metalloporphyrins — play a foundational role [314]. Iron-containing porphyrins (hemes) serve as the reactive centers of hemoglobin and myoglobin, enabling oxygen transport and storage in blood and muscle tissue (see Fig. 6.1) [315, 316]. Similarly, cytochromes use porphyrins for electron transfer, while chlorins (closely related molecules) form the active sites in chlorophyll, responsible for capturing sunlight during photosynthesis [317]. This centrality to essential life processes has earned porphyrins the nicknames *nature's workhorses* [65] and *pigments of life* [66]. Their biochemical significance is reflected in the history of chemistry itself: Richard Willstätter was awarded the Nobel Prize in Chemistry in 1915 for his elucidation of the structure of plant pigments, including chlorophyll [319]. Hans Fischer followed in 1930, receiving the Nobel Prize in Chemistry for his pioneering work on the synthesis of haemin, a close analogue of heme [316]. A generation later, Robert Woodward was awarded the Nobel Prize in 1965 for the total synthesis of chlorophyll—one of the most complex achievements in synthetic organic chemistry [320]. These are just some of the milestones that highlight the enduring scientific fascination with tetrapyrrolic pigments.

This multifunctionality of tetrapyrroles has inspired the development of various synthetic porphyrins for biomimetic and technological applications [321]. These range from catalysis [322] and chemosensing [323] to molecular electronics [324], photovoltaics [325], and even photodynamic

---

[*] A methine bridge is a single carbon atom that is bound by two single and one double bond, where one single bond is formed with a hydrogen atom.

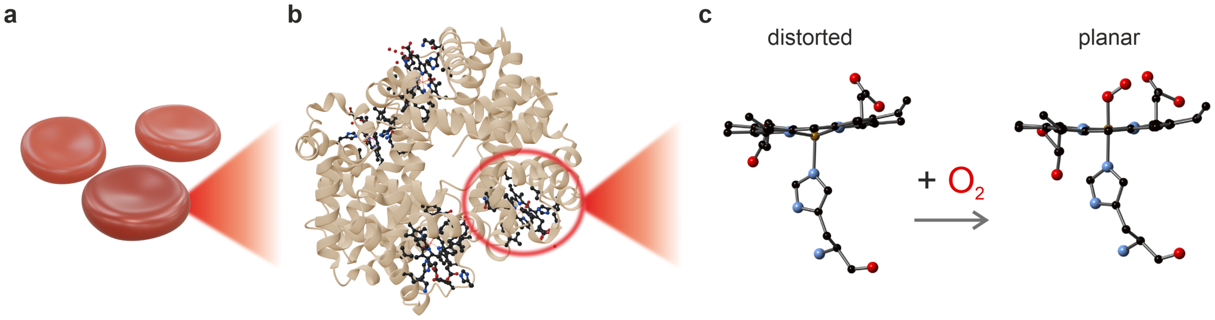

Figure 6.1: **(a)** Red blood cells, responsible for oxygen transport in the bloodstream. **(b)** Structure of hemoglobin, highlighting the embedded heme units. The molecular structure was taken from the Protein Data Bank (PDB: 1GZX). **(c)** Molecular structure of heme in its deoxygenated (distorted) and oxygenated (planar) forms, adapted from [318], licensed under CC BY 4.0.

cancer therapy [326]. Moreover, artificial porphyrins can be embedded in larger frameworks — such as *metal-organic frameworks* (MOFs) — to enhance structural stability and promote cooperative phenomena through covalent or coordinative linking of individual molecular units [327, 328]. The modularity of synthetic porphyrins extends from electronic structure (through metal center choice) to steric effects (via peripheral substitutions) [314], and even spin states (through axial coordination) [329–331], making them ideal molecular platforms for tuning function on demand.

Among the numerous synthetic derivatives, *tetraphenylporphyrins* (TPPs) have emerged as model systems in surface science. These molecules consist of a porphyrin core functionalized with four phenyl groups, as illustrated in Fig. 6.2. While the figure depicts the free-base species (2H-TPP), in their metalated state (in so-called *metalated tetraphenylporphyrins* (MTPPs)), the molecules coordinate a central transition metal ion within the macrocycle (see also Fig. 1.2b).

The phenyl substituents improve solubility [332] and steer the packing and ordering on surfaces [333], while the metal center strongly modulates the electronic and magnetic characteristics of the molecule [314]. When deposited onto surfaces, MTPPs tend to form self-assembled structures or even extended 2D arrays [334–336], providing well-defined platforms for biomimetic studies [337] and for exploring catalytic functionalities in single-atom-catalyst-like configurations [322, 338].

Importantly, the interaction of MTPPs with metal surfaces not only governs their self-assembly but also profoundly alters their electronic structure [339]. For instance, charge transfer processes from the substrate to the porphyrin layer, as observed on Cu and Ag surfaces, can populate the gas phase LUMOs [114, 186], often resulting in a reduction of the hosted metal ion [337, 340, 341]. At the same time, adsorption-induced macrocycle deformations — typically manifesting as saddle-shaped distortions — can shift the frontier orbital energies [318], modify the optical response [342], and regulate the ability of the metal center to coordinate external ligands, a key requirement for catalytic activity [343]. For example, saddling of the macrocycle has been shown to facilitate the coordination of CO molecules in either cis- or trans-configurations [344], while a planar porphyrin may suppress such coordination entirely [345]. Understanding these

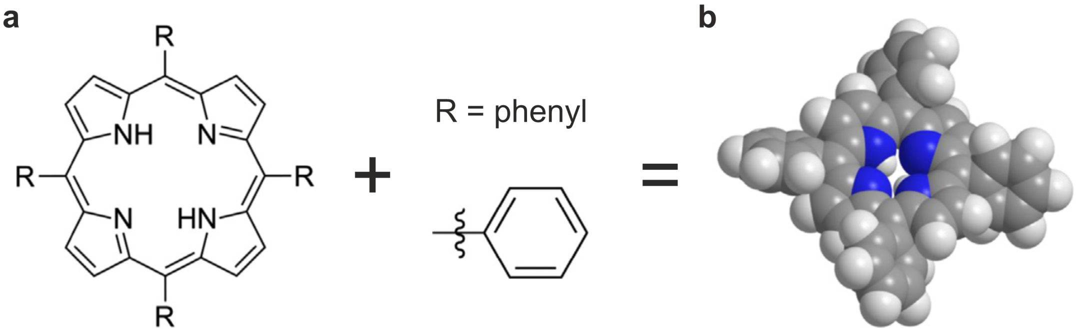

Figure 6.2: **(a)** Porphyrin macrocycle with tunable peripheral substituents (R); here, R = phenyl. **(b)** Resulting tetraphenylporphyrin (2H-TPP) shown as a ball-and-stick model. Reproduced from [314]. © 2015 Elsevier.

subtle interplays between conformation, electronic structure, and chemical reactivity in on-surface porphyrins thus presents a promising route towards the rational design of next-generation functional organic–inorganic interfaces [13, 339].

Here, we focus on ZnTPP and NiTPP — two prototypical metalloporphyrins — adsorbed on the oxygen-passivated Fe(100)–$p(1 \times 1)$O surface. This substrate provides a well-defined template with reduced reactivity compared to bare Fe(100) [346], allowing for the controlled adsorption of intact molecular layers that self-assemble into ordered films. The Fe–O surface thus facilitates stable monolayer formation with weak interaction strength, making it an ideal platform to study the delicate balance between molecular conformation and the frontier electronic structure of porphyrins [214].

To establish a basic understanding, we begin by reviewing the fundamental adsorption characteristics of ZnTPP and NiTPP on the Fe–O surface, such as their preferred adsorption sites, azimuthal orientations, and molecular conformations, as reported in the literature. Building on this foundation, we then focus on two key questions:

> First, to what extent can POT (used here in combination with DFT) be reliably employed to detect complex molecular distortions in adsorbed porphyrins?

Although such distortions have been previously reported at this interface, their manifestation in momentum-resolved photoemission data remains unexplored. It is therefore necessary to firstly carify whether POT can be systematically used to quantify them. By examining both monolayer and multilayer films of NiTPP, we aim to further elucidate the role of the substrate in driving these conformational changes.

> Second, how do adsorption-induced structural modifications influence the electronic structure of the porphyrin layer?

To answer this, we leverage the orbital sensitivity of POT, combined with the predictive power of DFT, to establish a direct link between molecular conformation and electronic properties.

6.2 Preparation and Characterization of Metalloporphyrins on Fe–O

The preparation of the ZnTPP and NiTPP molecular layers builds directly on the Fe–O substrate described in Section 4.2 and Section 5.2. Surface cleanliness and oxygen-reconstruction were routinely verified by LEED, Auger, and photoemission (UPS and MM).

Following substrate preparation, the deposition of ZnTPP and NiTPP was carried out in-situ using calibrated Knudsen cells. The deposition rates were initially estimated via a quartz crystal microbalance and further refined by monitoring the development of the characteristic (5×5) and $(5 \times 5)R37^\circ$ LEED patterns reported in the literature for monolayer coverages of ZnTPP and NiTPP, respectively [336]. The corresponding emergence of the (5×5) LEED pattern for ZnTPP is illustrated in Fig. 6.3, confirming the formation of a well-ordered monolayer on the Fe(100)–$p(1 \times 1)$O surface.

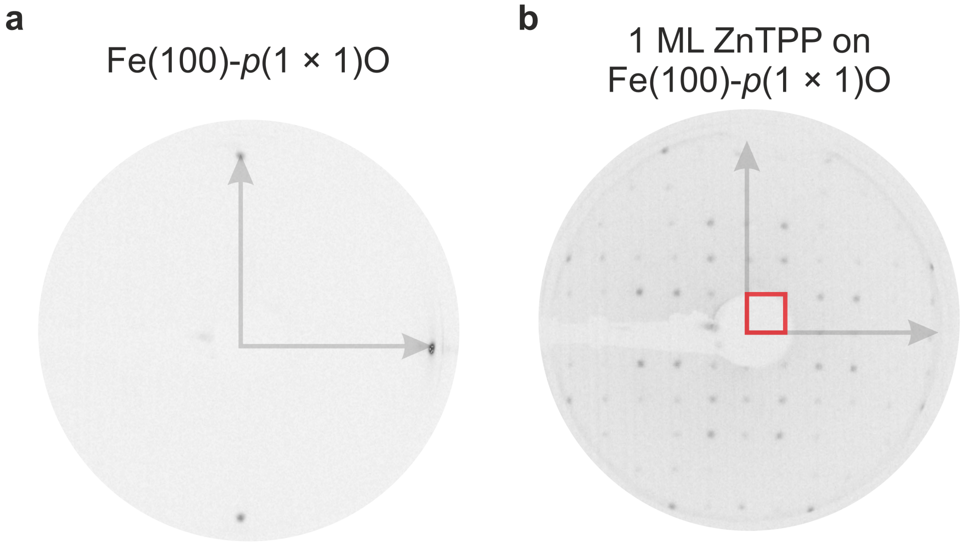

Figure 6.3: LEED patterns measured at a kinetic energy of 32 eV. **(a)** Clean Fe(100)–$p(1 \times 1)$O surface showing the characteristic square symmetry. **(b)** After deposition of 1 ML ZnTPP, a sharp (5×5) superstructure emerges, indicative of a well-ordered molecular layer. Grey arrows mark the substrate lattice vectors; the red box in (b) highlights the corresponding unit cell of the superstructure.

The deposition temperature was held at 543 K for ZnTPP and 531 K for NiTPP, with a growth rate of approximately 0.1 ML per min. For multilayer NiTPP growth, the rate was increased to 0.4 ML per min to match conditions from ref. [347].

Momentum-resolved photoemission measurements of the ZnTPP monolayer were conducted at room temperature (300 K) using a KREIOS 150 MM PEEM system (Specs GmbH), operated in momentum mode. The system was coupled to a high-harmonic generation light source providing p-polarized fs-XUV pulses at 29.7 eV, yielding 2D momentum maps over $k_x, k_y \in [-2.0, +2.0]$ 1/Å with an energy resolution better than 200 meV. Photoemission experiments on NiTPP films were performed at the NanoESCA beamline of the Elettra synchrotron using a NanoESCA momentum microscope and p-polarized synchrotron light at 40 eV. The sample temperature was maintained at 100 K, and the energy resolution was below 100 meV.

The experimental results were supported by DFT calculations performed by Dr. Andreas Windischbacher from the group of Prof. Peter Puschnig at the university of Graz. These were used to assess the geometric and electronic structure of the porphyrin molecules both in the gas phase and when adsorbed on the Fe–O substrate. For the interface systems, periodic slab models were employed at the GGA level, while for gas-phase calculations, the reduced computational cost allowed for the use of more advanced hybrid functionals. This approach provided valuable insight into the molecular orbital structure and supported the interpretation of momentum-resolved photoemission data via POT. The theoretical momentum maps were generated using the *kMap.py* tool [211].

6.3 Conformation and Electronic Structure in Weakly Coupled Porphyrins on Fe–O

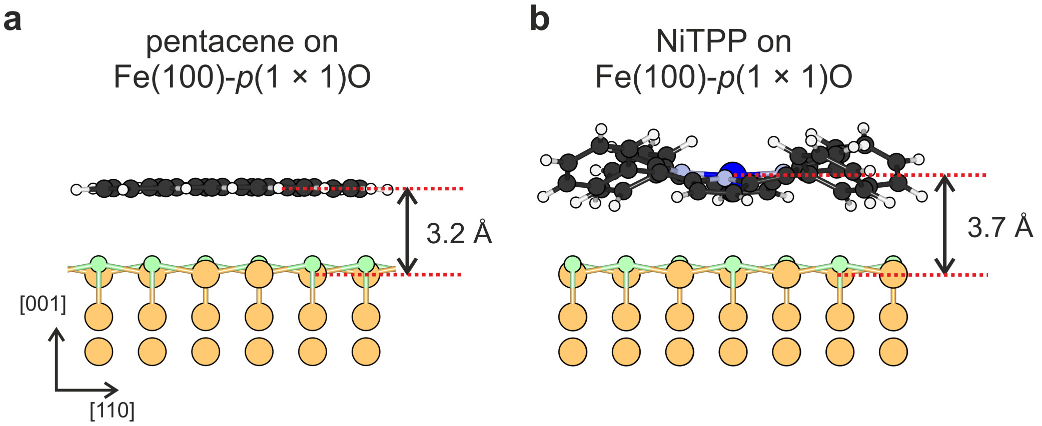

Figure 6.4: **(a)** Side view of pentacene adsorbed on Fe(100)–$p(1 \times 1)$O. **(b)** Corresponding adsorption geometry of NiTPP. Structures stem from DFT optimizations performed by Dr. Andreas Windischbacher.

Compared to fully planar, conjugated molecules such as 5A, ZnTPP and NiTPP fall into the weakly coupled regime of the interaction spectrum. This contrast is illustrated in Fig. 6.4, where DFT-optimized adsorption geometries of both 5A and NiTPP are directly compared. As shown, 5A adsorbs in a flat geometry at a distance of 3.2 Å, enabling non-negligible overlap with Fe d-orbitals and giving rise to hybrid interface states (see Chapter 5). In contrast, NiTPP lies at a significantly greater distance (3.7 Å), with no sign of electronic coupling — although an out-of-plane distortion of the macrocycle is evident.

This weak coupling of ZnTPP and NiTPP to the Fe–O surface arises from a combination of steric and electronic factors:

1. Steric decoupling by peripheral phenyl groups: The four phenyl substituents elevate the porphyrin macrocycle above the surface, acting as built-in spacers that reduce orbital overlap between macrocycle and substrate states.
2. Electronic structure of the central metal ion: The d_{z^2} orbital, which extends most prominently out of the molecular plane, is fully occupied in both NiTPP and ZnTPP. While it lies close to the Fermi level in NiTPP and significantly farther below in ZnTPP, its filled character suppresses back-donation in both cases — *i.e.*, electron transfer from the substrate into the molecule.

Despite their structural similarity, ZnTPP and NiTPP adopt different adsorption sites and self-assembled geometries on the Fe–O surface [336]. STM and LEED measurements, corroborated by DFT, show that ZnTPP preferentially adsorbs on oxygen sites and forms a commensurate (5×5) superstructure without azimuthal rotation. In contrast, NiTPP prefers Fe-top sites and adopts a rotated $(5 \times 5)\mathrm{R}37^\circ$ arrangement, as shown in Fig. 6.5.

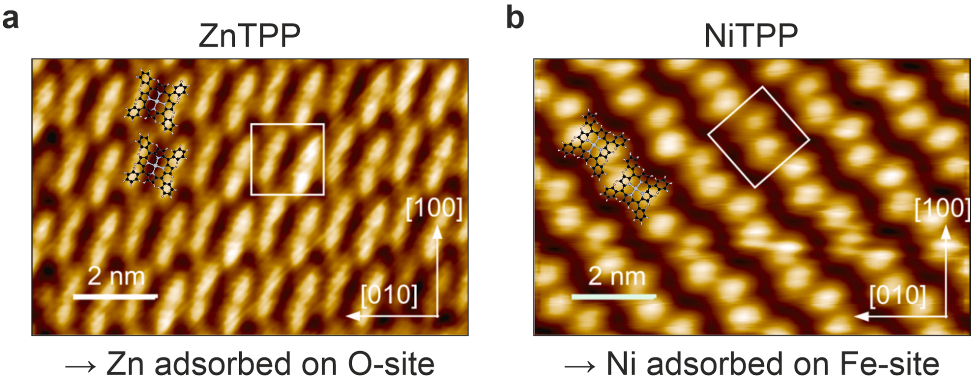

Figure 6.5: STM images of monolayers of **(a)** ZnTPP and **(b)** NiTPP on Fe(100)–$p(1 \times 1)$O. ZnTPP adsorbs on O sites; NiTPP is more stable on Fe sites. The apparent two-fold symmetry in STM arises from saddle-shape distortion, which lowers the symmetry of the macrocycle. Molecular models are overlaid to guide the eye. Adapted from [336]. © 2020 Elsevier.

These trends can be rationalized by examining the MOs with major d_{z^2} character, as illustrated in Fig. 6.6. ZnTPP, with a closed $3d^{10}$ shell, exhibits deeply bound d_{z^2} states located well below E_F, energetically close to the oxygen $2p$ states of the substrate. NiTPP, by contrast, has a $3d^8$ configuration with a filled d_{z^2} orbital situated just below E_F, closer in energy to the Fe d-bands. The energetic proximity of the d_{z^2} orbital to either O $2p$- or Fe d-states strongly influences the preferred adsorption site, while the filled character of the d_{z^2} level prevents any significant charge transfer or hybridization in both cases, resulting in comparably large macrocycle–surface distances.

The azimuthal alignment relative to the substrate lattice and the overall conformation of individual molecules also vary considerably. As shown in Fig. 6.7, the N–metal–N axis is rotated by approximately 17° in ZnTPP and by 35° in NiTPP. Notably, these differing orientations are accompanied by distinct degrees of saddle-shape distortion: ZnTPP exhibits a moderate deformation of the porphyrin core, whereas NiTPP shows a significantly more pronounced distortion. These observations suggest that the final adsorption geometry — including adsorption

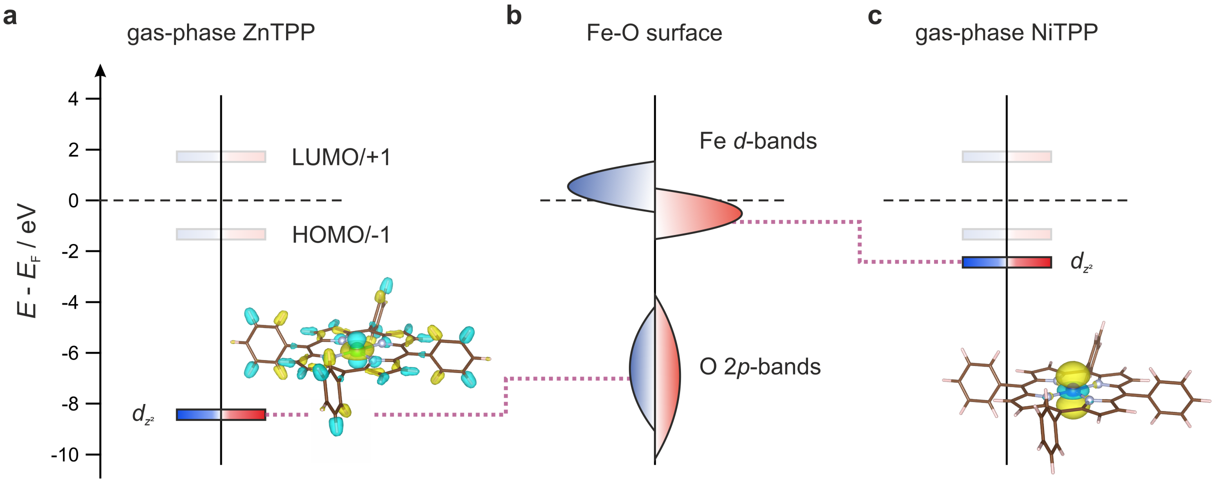

Figure 6.6: Schematic electronic structure of **(a)** ZnTPP, **(b)** the Fe–O surface, and **(c)** NiTPP, focusing on d_{z^2} orbitals of the chelated metal ions. HOMO and LUMO levels are nearly identical in both molecules. Gas-phase calculations for ZnTPP and NiTPP were carried out using ORCA 6 [348, 349] with the B3LYP hybrid functional [172, 173], a 6-31G* basis set [350, 351], and Grimme's D3 dispersion correction [352]. Visualizations were generated with VESTA [353].

site, vertical bonding distance, azimuthal orientation, and molecular conformation — arises from a complex, non-covalent interplay of electronic and steric factors. Thus, even in the absence of strong hybridization, the central metal ion dictates the preferred adsorption site, while the molecule–substrate registry and the phenyl substituents modulate lateral alignment and the extent of macrocyclic distortion.

Notably, the study underlying this chapter was conducted prior to the introduction of a negative Hubbard correction (U_{eff}) for describing correlation-induced effects in the Fe–O substrate. Consequently, the surface was modeled at the standard GGA level, without additional treatment of correlation-driven modifications in the Fe *d*-states. In this context, the simplification is fully justified: due to the weak molecule–substrate interaction, strong hybridization is absent, and even standard GGA adequately captures the essential features of the system. As demonstrated by Fratesi *et al.* [336], such weakly coupled systems can be described adequately without explicit corrections to the Fe *d*-bands.

A Hubbard U_{eff} correction was applied only to the central metal ion in the porphyrins, to improve the treatment of on-site electron correlation in the chelated metal center [299]. This choice follows prior studies on the same system [336] and is not intended to model substrate-related effects.

The weak interaction between ZnTPP/NiTPP and the Fe–O surface, combined with their distinct conformational distortions, makes these molecules ideal model systems for exploring the intrinsic relationship between porphyrin geometry and orbital electronic structure.

To probe this relationship, we employ POT in conjunction with DFT calculations. While POT is already well established for identifying and disentangling frontier orbital energies, it also shows

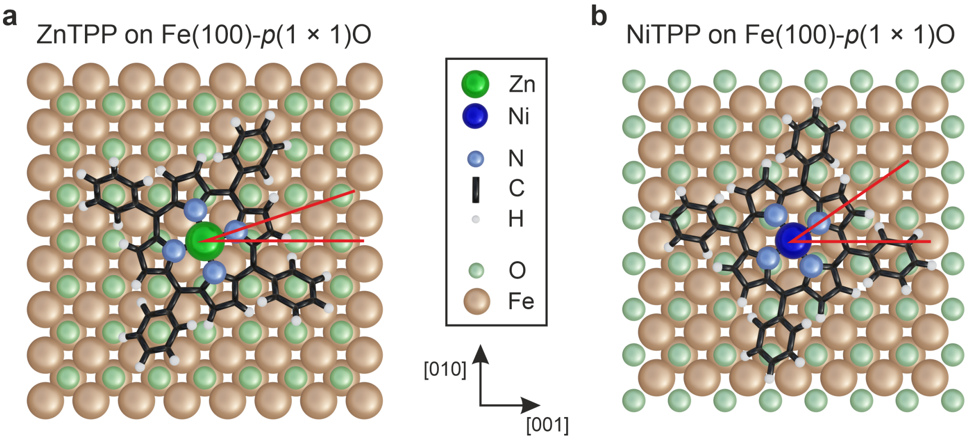

Figure 6.7: Top views of **(a)** ZnTPP and **(b)** NiTPP adsorbed on Fe(100)–$p(1 \times 1)$O, showing azimuthal orientation and adsorption site. Based on DFT calculations by Dr. Andreas Windischbacher.

promise for extracting structural information — including azimuthal orientation and more subtle conformational changes induced by surface adsorption. As we will demonstrate, POT grants access to MOs and structural features with a level of detail that not only complements but, in some respects, even rivals traditional surface-sensitive techniques such as STM and LEED.

In the following, we outline the principles underlying structural analysis using POT and clarify the conditions under which this method can reliably resolve conformational distortions in surface-supported porphyrins.

6.4 Sensitivity of POT to Molecular Distortion

The ability to identify and characterize conformational changes of surface-adsorbed molecules is a central challenge in interface science that is far from trivial. For porphyrin-based systems, distortions of the macrocyclic backbone — such as saddling or ruffling — play a critical role in defining their electronic structure, optical response, and their interaction with small axial ligands. While techniques like STM can image individual porphyrins and provide insights into their adsorption geometry, their interpretative power is limited in several respects. Peripheral groups such as phenyl rings are often flexible, complicating the identification of macrocyclic distortions [114]. In multilayer systems, STM primarily probes the outermost layer, where molecules may be mobile and interact strongly with the tip, while structurally well-defined subjacent layers remain inaccessible. Other methods, such as *near-edge x-ray absorption fine structure* (NEXAFS) [337, 354, 355] or *x-ray standing wave* (XSW) measurements [356, 357], can provide valuable complementary information, but are typically limited in their orbital specificity.

In contrast, photoemission techniques offer a more direct link to the electronic structure. The energy positions of molecular orbitals, as revealed by UPS, often serve as a reliable reference for comparing theoretical predictions with experiment. POT, in particular, goes a step further by

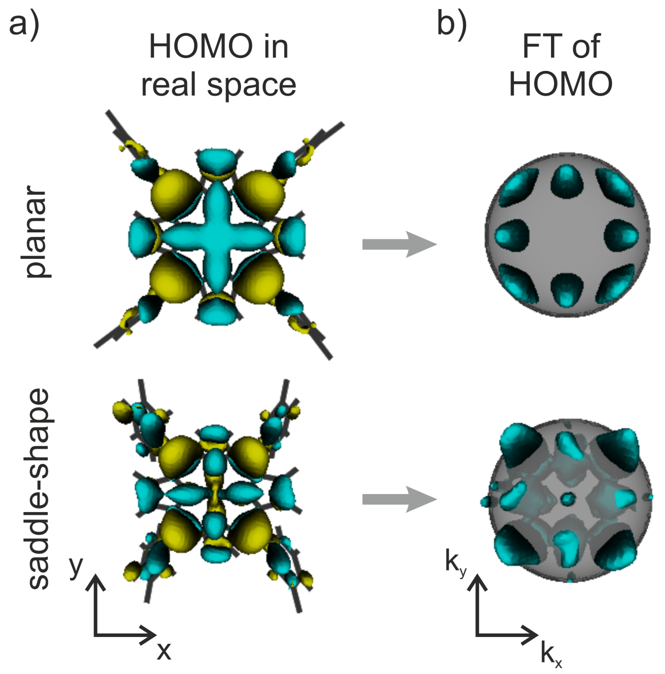

Figure 6.8: Influence of saddle-shaped distortion on the real-space and momentum-space orbital structure of ZnTPP. **(a)** Real-space isosurface of the HOMO in planar (top) and saddle-shaped (bottom) conformations. **(b)** Corresponding momentum-space distributions (FT[$\psi(\mathbf{r})$]), obtained by Fourier transforming the real-space orbitals. The grey shell illustrates an isoenergetic cut corresponding to a photoelectron kinetic energy of 25 eV, from which momentum maps are extracted to match the experimental photoemission conditions. Published in [214].

providing momentum-resolved information that is directly related to the spatial distribution of individual molecular orbitals and the molecular alignment on the substrate surface.

As such, POT has proven to be a valuable tool for analyzing the electronic structure of surface-adsorbed molecules, enabling the unambiguous assignment of molecular orbitals and offering insight into the presence of structural distortions. It has already demonstrated sensitivity to geometric changes such as tilts [63, 64], twists [358, 359], and bending [219, 360]. However, it remains unclear whether POT can also resolve more complex conformational changes in larger aromatic systems. Saddle-shaped deformations of the porphyrin macrocycle, in particular, are known to influence orbital symmetry and energy level alignment, but have not yet been quantitatively probed using POT. We therefore first assess to which degree POT is sensitive for resolving such conformational changes.

Figure 6.8 illustrates the expected impact of saddle-shaped distortions on the real-space orbitals and their corresponding momentum-space distributions. Simulations were performed for the HOMO of ZnTPP in two distinct conformations: perfectly planar (top) and saddle-distorted (bottom). The real-space isosurfaces of the MO are shown on the left, and the Fourier transforms FT[$\psi(\mathbf{r})$] are plotted on the right.

Despite the modest visual difference between the real-space orbitals, the impact on the momentum-space distribution is striking: the saddle-shaped conformation exhibits asymmetric lobes and the emergence of central intensity, which is absent in the planar case. This simulation indicates that POT is not only sensitive to the fingerprint of individual orbitals but also to subtle degrees of conformational distortions in tetrapyrrole complexes.

These findings provide a theoretical basis for using POT to distinguish between planar and saddle-shaped porphyrins at interfaces. In the following sections, this approach is applied to experimentally investigate the conformation of ZnTPP and NiTPP monolayers on Fe(100)–$p(1 \times 1)$O, and subsequently extended to explore multilayer growth in the NiTPP system.

6.5 Monolayer Adsorption of ZnTPP on Fe–O

With the sensitivity of POT to molecular conformation established, we now turn to the case of 1 ML ZnTPP adsorbed on the oxygen-passivated Fe(100) surface. Figure 6.9a shows the momentum-integrated valence band, comparing spectra of the clean Fe–O substrate (black) and the ZnTPP-covered surface (green). Both curves are normalized to the intensity near the Fermi edge, where no molecular emission is expected. Upon adsorption, two broad resonances appear at binding energies of approximately $E_\mathrm{b} = 1.5\,\mathrm{eV}$ and $3.5\,\mathrm{eV}$. While the higher-E_b feature is commonly attributed to phenyl-related states, the lower-energy structure arises from the porphyrin macrocycle moiety and exhibits a clear double-peak shape. To fully resolve this region, a high-statistics spectrum was recorded in the E_b range from -0.8 to 2.3 eV. As shown in the right panel of Fig. 6.9a, the spectrum is well described by a sum of two Gaussian functions centered at $E_\mathrm{b} = (1.3 \pm 0.1)\,\mathrm{eV}$ and $(1.6 \pm 0.1)\,\mathrm{eV}$, with FWHMs of $(0.3 \pm 0.1)\,\mathrm{eV}$ and $(0.4 \pm 0.1)\,\mathrm{eV}$, respectively.

To interpret these features, we calculated the PDOS for 1 ML ZnTPP adsorbed on Fe–O, using a relaxed saddle-shaped geometry. As shown in Fig. 6.9b, the total molecular PDOS (MOPDOS), as well as the individual contributions from the HOMO and HOMO-1, reproduce the observed double-peak structure. A Gaussian broadening of 350 meV was applied to simulate the experimental resolution. The agreement in energy position and relative intensity supports the assignment of the two peaks to the HOMO and HOMO-1 orbitals of the adsorbed molecule. The theoretically derived energy splitting of 370 meV, matches the experimentally obtained FWHM of $(300 \pm 100)\,\mathrm{meV}$. In contrast to the planar gas-phase case, where these orbitals are degenerate according to DFT, the observed splitting indicates a breaking of this degeneracy.

Having assigned the observed peaks to the HOMO and HOMO-1 based on DFT calculations of the adsorbed system, we now turn to the momentum-resolved photoemission data to experimentally verify this assignment. Using the energy windows indicated by the arrows in Fig. 6.9a, momentum maps are extracted that selectively emphasize the individual orbital contributions. This targeted energy selection avoids mixing of the two frontier orbitals in k-space and ensures that each map corresponds to a distinct electronic state.

To account for the fourfold symmetry of the Fe(100)–$p(1 \times 1)$O substrate and to compensate for experimentally induced asymmetries due to the polarization factor, the momentum maps were symmetrized with respect to the D_4 point group. The resulting patterns are shown in the upper panels of Fig. 6.10. This processing step facilitates a direct one-to-one comparison with

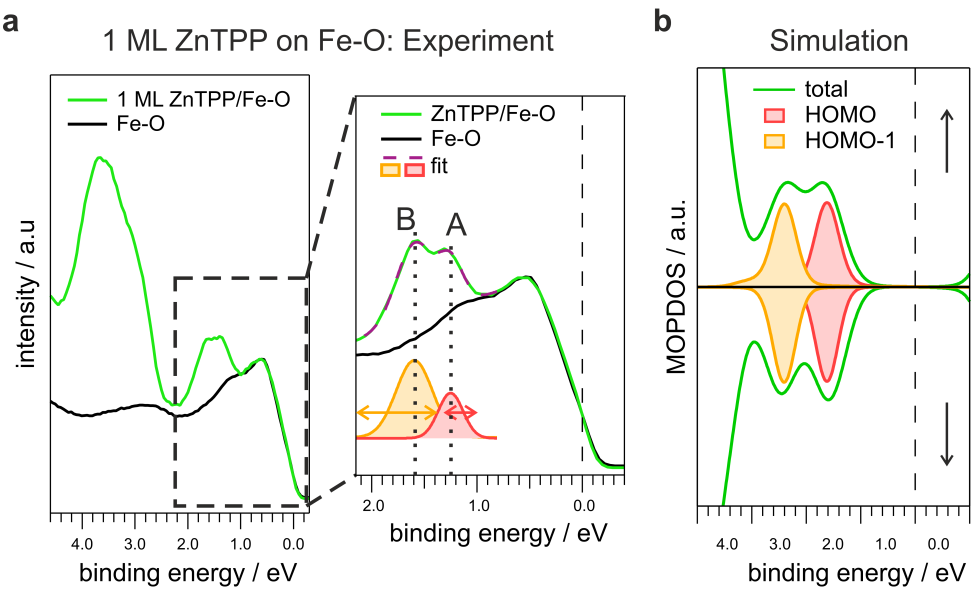

Figure 6.9: **(a)** Valence band photoemission spectra for clean Fe(100)–$p(1 \times 1)$O (black) and after deposition of 1 ML ZnTPP (green). The emergence of two molecular resonances centered at $E_\mathrm{b} = 1.5\,\mathrm{eV}$ and 3.5 eV indicates emission from the HOMO and HOMO-1 orbitals of the adsorbed molecules. Spectra are integrated over k_x, k_y in [-2.0, +2.0] 1/Å and normalized at the Fermi edge. The panel on the right displays a measurement with increased integration time, focusing on the first prominent peak at 1.5 eV. The evident double-peak structure can be captured by fitting with two Gaussians (orange and red curves) and a linear background (not shown). The arrows indicate energy windows, which were used to generate averaged momentum maps that are presented in Fig. 6.10. **(b)** ZnTPP MOPDOS calculated by means of DFT for the 1 ML ZnTPP/Fe–O system in an optimized saddle-shape adsorption geometry. The red and orange curves correspond to the MOPDOS*s* of HOMO and HOMO-1, respectively. Published in [214].

simulated momentum maps obtained from the Fourier transforms of Kohn–Sham orbitals. The entire symmetrization procedure, as well as its application to both experimental and theoretical maps, is detailed in Appendix A.4.

The comparison of experiment and theory within the POT framework confirms the orbital character previously inferred from the molecular DOS: the lower-E_b map corresponds to the HOMO, while the one at higher energies reflects the HOMO-1. Beyond spectral assignment, these momentum maps also encode information about the adsorption geometry in the deposited monolayer. In the following, we analyze their shape in detail to determine the conformation and azimuthal alignment of the ZnTPP macrocycle on the surface.

We begin by comparing the experimental momentum maps with simulations based on a planar ZnTPP molecule in the gas phase, a geometry frequently used to describe porphyrins on surfaces [114, 361]. The corresponding real-space representations of the HOMO and HOMO-1 are shown in Fig. 6.10b. Simulated momentum maps derived from these orbitals are presented in the lower halves of Fig. 6.10c, directly compared to the symmetrized experimental maps shown in the upper

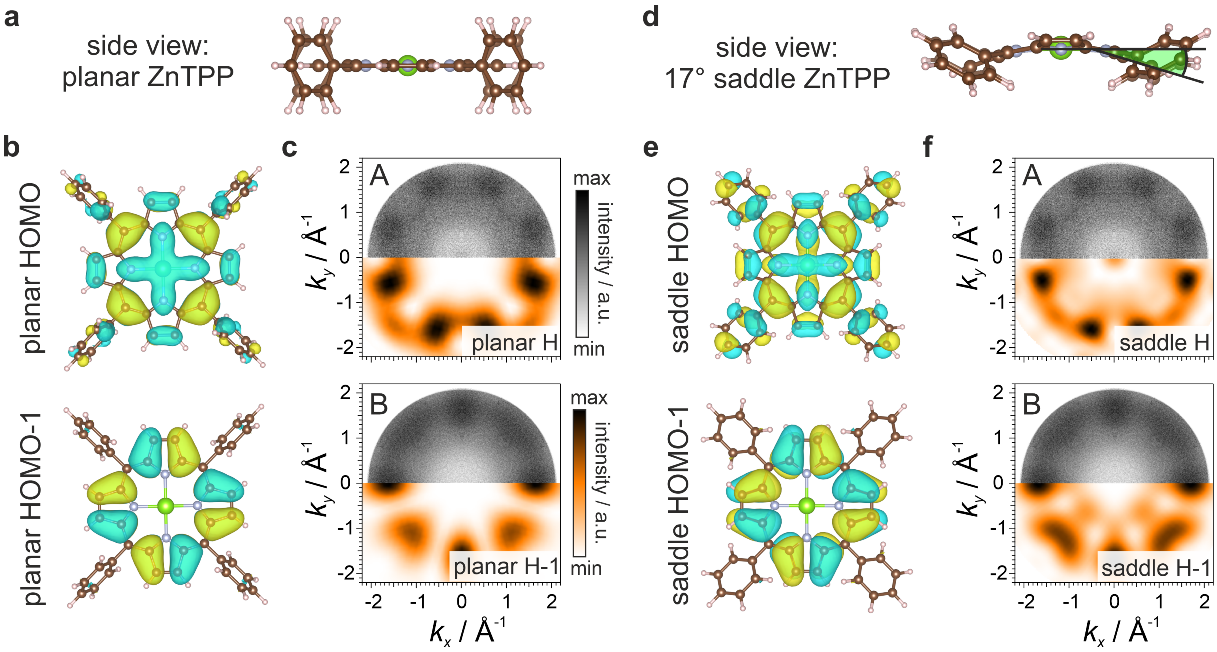

Figure 6.10: Comparison between experimental and simulated POT maps for 1 ML ZnTPP on Fe(100)–$p(1 \times 1)$O. **(a)** Ball-and-stick model of a planar ZnTPP molecule. **(b)** Real-space isosurfaces of the HOMO and HOMO-1 orbitals for the planar geometry. **(c)** Simulated momentum maps (bottom) for the planar orbitals shown in (b), compared to the symmetrized experimental maps (top) extracted from the energy windows indicated in Fig. 6.9a. **(d)** Ball-and-stick model of a saddle-shaped ZnTPP molecule with a distortion angle of approximately 17°, obtained from periodic DFT optimization on Fe–O. **(e)** Real-space isosurfaces of the HOMO and HOMO-1 orbitals for the saddle-shaped geometry. **(f)** Simulated momentum maps (bottom) for the distorted orbitals shown in (e), compared to the corresponding experimental maps (top). Published in [214].

halves. For the simulation, the molecular orientation was chosen according to the adsorption geometry proposed by Fratesi *et al.* [336], which is supported by our DFT calculations. In this configuration, the N–Zn–N axis is rotated by approximately 17° relative to the Fe[001] direction (see Fig. 6.7a).

The agreement in the nodal structures between experiment and simulation confirms the assignment of the lower-E_b feature as the HOMO and the higher-E_b feature as the HOMO-1. It further confirms the assumed azimuthal orientation of the molecules in the monolayer.

Nonetheless, subtle deviations remain: most notably, the experimental HOMO map displays intensity near the map center and features at higher k values that appear more confined and circular compared to those in the planar simulation. Strikingly, these differences are reproduced in our simulations when a saddle-shaped distortion of the macrocycle is introduced.

To explore this effect, we simulated momentum maps for ZnTPP molecules with varying degrees of saddling, as illustrated in Fig. 6.11. Notably, even moderate out-of-plane distortions produce distinct changes in the momentum-space features. We define the saddling angle as the average tilt between the macrocycle plane and the planes of the individual pyrrole units, as visualized in Fig. 6.10d. Systematic comparison of simulated patterns for different saddling angles with the experimental data reveals the best match for an angle of approximately 17°, in excellent agreement with the relaxed structure obtained from periodic DFT calculations (see Fig. 6.10e), including the corresponding Kohn–Sham orbitals.

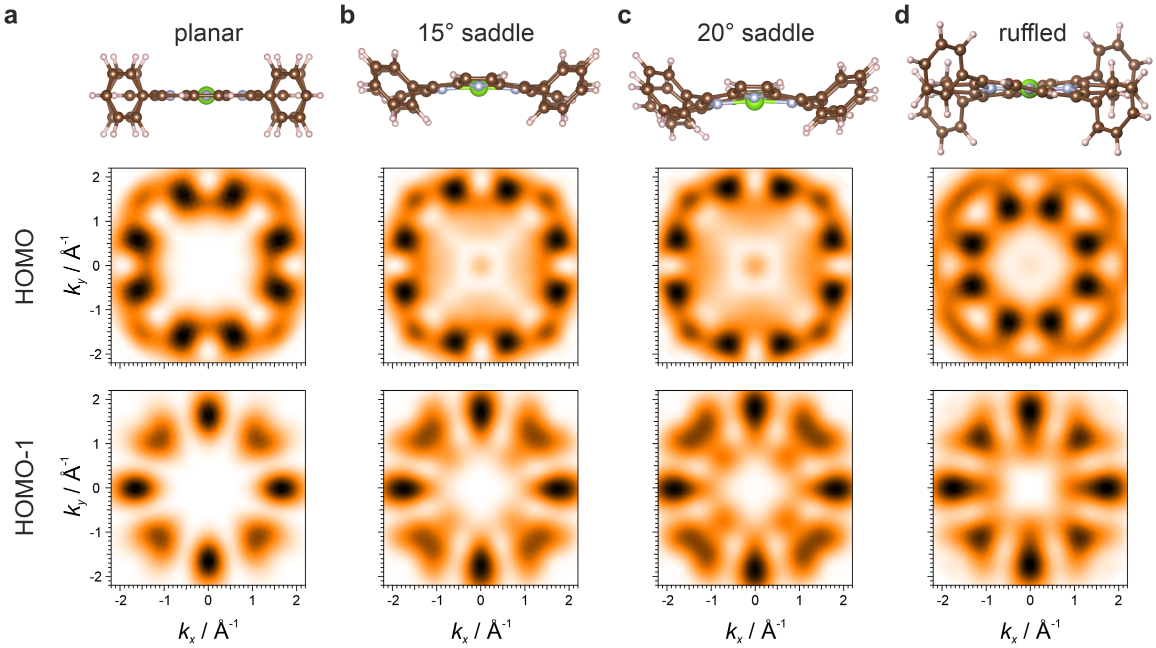

Figure 6.11: Influence of different macrocycle distortions on the simulated momentum maps of the ZnTPP HOMO and HOMO-1. Panels **(a)**–**(d)** show ball-and-stick models (top) representing different conformations of the ZnTPP macrocycle, along with the corresponding simulated photoemission momentum maps (bottom) for the HOMO and HOMO-1 orbitals. Published in [214].

The lower panels of Fig. 6.10f show the HOMO and HOMO-1 momentum maps derived from the relaxed, saddle-shaped ZnTPP structure. The HOMO-1, with its charge density residing almost exclusively on the carbon atoms of the conjugated backbone, remains largely unaffected by the distortion — aside from a predictable tilting of the orbital lobes induced by the inclination of the pyrrole units. The HOMO, in contrast, displays a markedly higher sensitivity to structural deformations. Owing to its significant contributions from the nitrogen atoms and the central metal ion, the HOMO exhibits pronounced changes in electron density near the macrocycle center upon saddling. Our calculations (see Fig. 6.9b) show that these geometric modifications are accompanied by a downward shift in HOMO binding energy, consistent with the experimentally observed lifting of the HOMO/HOMO-1 degeneracy in Fig. 6.9a.

This shift manifests in an evident double-peak structure in the MOPDOS, shown in Fig. 6.9b, which closely mirrors the spectral features observed in the UPS spectrum (Fig. 6.9a). The resulting splitting mirrors the influence of molecular conformation on the spatial and energetic character of the frontier orbitals.

Taken together, these findings demonstrate that ZnTPP forms an ordered monolayer on the

Fe–O surface, adopts a saddle-shaped macrocycle geometry, and exhibits well-separated HOMO and HOMO-1 features that are clearly distinguishable both in energy and momentum space. The excellent agreement between experiment and simulation underscores the power of POT as a conformation-sensitive probe of molecular thin films. The theoretically predicted energy splitting of 370, meV is in good agreement with the experimental estimate of (300 ± 100), meV. Importantly, this orbital splitting is also observed when the distorted ZnTPP geometry is calculated in the gas phase, confirming that the effect originates from the intrinsic electronic response to the molecular deformation, rather than from molecule–substrate interactions — although the latter are likely responsible for inducing the distortion.

As outlined in the introduction, the ability to exchange the central metal ion in the porphyrin macrocycle offers a route to systematically tune the chemical, electronic, and interfacial properties of the system. We therefore extend the POT analysis to the related system of NiTPP on Fe–O, where analogous questions of molecular conformation and orbital structure are studied.

6.6 Conformation of NiTPP on Fe–O: From Monolayer to Multilayer Films

Before turning to the actual analysis of the NiTPP monolayer on Fe–O, we first address a crucial experimental parameter that influences the visibility of conformation-specific features in POT: the photon energy. As demonstrated in the case of ZnTPP, out-of-plane distortions such as saddling have a pronounced impact on the orbital symmetry in momentum space. However, the contrast and nodal structure observed in POT maps are not solely governed by molecular geometry, they are also strongly modulated by the kinetic energy of the emitted photoelectrons. Understanding this dependence is essential for reliably identifying and quantifying these molecular distortions.

6.6.1 Photon Energy Dependence in Probing Conformation via POT

Figure 6.12a shows simulated momentum maps of the HOMO and HOMO-1 orbitals of a saddle-shaped NiTPP molecule for three different kinetic energies: 15 eV, 25 eV, and 35 eV. At lower energies (15 eV), the characteristic features of the distortion, especially the emerging features along the diagonal direction are suppressed. Only at higher photon energies (*e.g.*, 35 eV) do the maps clearly reflect the saddle-shape-specific redistribution of intensity. This dependence is critical when interpreting experimental data, as an inadequate choice of photon energy may mask conformational signatures. In contrast, the maps of planar molecules consistently exhibit the pattern presented in Fig. 6.12b, here exemplary shown for a kinetic energy of 35 eV.

In light of this, all POT measurements on NiTPP were performed using 40 eV synchrotron radiation, which is taken into account for the simulated maps ensuring a good ratio between k-space contrast to capture shape-specific features, while providing high molecular photoemission cross section.

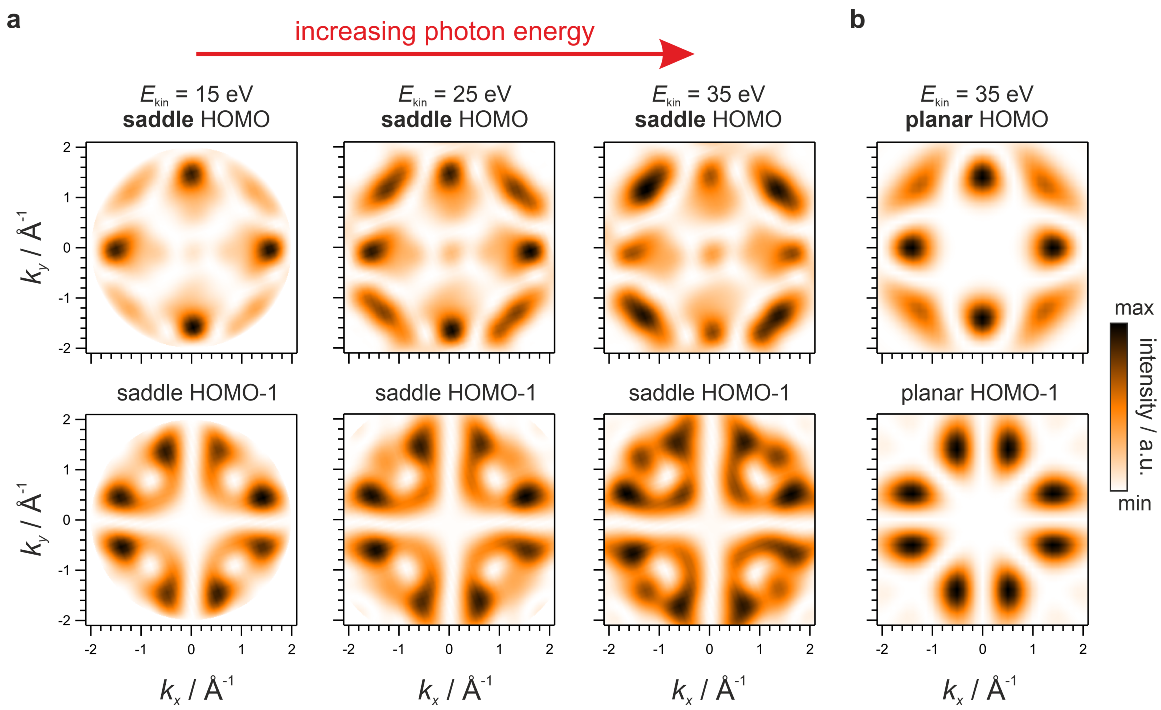

Figure 6.12: Simulated momentum maps of the HOMO and HOMO-1 orbitals of NiTPP illustrating the relation between photon energy and molecular conformation. **(a)** Saddle-shaped conformation at $E_{\mathrm{kin}} = 15$, 25, and 35 eV. Distortion-induced features emerge strongest at high kinetic energy. **(b)** Planar conformation at 35 eV, showing less-patterned intensity distributions. The comparison highlights the importance of photon energy selection in POT for resolving conformational changes.

6.6.2 Momentum-Resolved Electronic Structure of the NiTPP Monolayer

Figure 6.13 shows the momentum-integrated valence band spectrum of a 1 ML NiTPP film on Fe(100)–$p(1 \times 1)$O. In contrast to the ZnTPP case, the first molecular resonance appears as a single, broad peak centered around $E_{\mathrm{b}} = 1.5$ eV, with a Gaussian FWHM of (0.5 ± 0.1) eV. This width slightly exceeds the individual FWHMs of the HOMO and HOMO-1 features in ZnTPP and suggests that these frontier orbitals are nearly degenerate in the case of NiTPP. This interpretation is consistent with earlier findings on NiTPP/Cu(100) [114], where HOMO and HOMO-1 were treated as degenerate.

To enhance the signal-to-noise ratio, the corresponding momentum map was obtained by integrating over the energy range defined by the FWHM, indicated by the red arrow in Fig. 6.13a. Due to the higher photon energy used in the NiTPP measurement compared to ZnTPP, the contribution from the Fe–O substrate is more pronounced and requires background correction (see Section A.4 for details). The resulting background-corrected and symmetrized momentum map is shown in Fig. 6.13b.

To further analyze the azimuthal alignment and the possible degree of macrocycle distortion, we

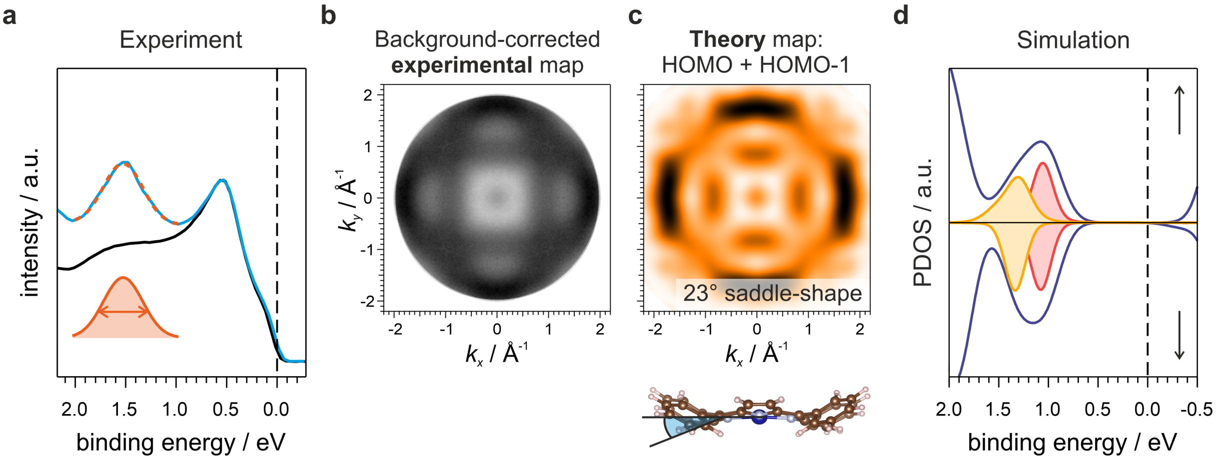

Figure 6.13: **(a)** Valence band spectrum of 1 ML NiTPP on Fe(100)–$p(1 \times 1)$O, showing a broad HOMO feature near 1.5 eV. **(b)** Experimental momentum map integrated over the energy range marked by the red arrow in (a). **(c)** Simulated momentum map for the summed HOMO and HOMO-1 of a NiTPP molecule with a 23° saddle-shaped distortion; bottom: ball-and-stick model of the corresponding geometry. **(d)** Comparison of experiment and DFT-calculated PDOS for the distorted geometry. The HOMO aligns well, while the HOMO-1 is weak and unresolved. The calculated splitting is smaller than in ZnTPP, despite the larger distortion. Published in [214].

compare the experimental map to simulations of NiTPP molecules. These simulations adopt the adsorption geometry proposed by Fratesi *et al.* [336], in which the N–Ni–N axis forms an angle of 35° with respect to the substrate [001] direction (see Fig. 6.7b). The saddle distortion series shown in Fig. 6.14 is used to evaluate the sensitivity of the momentum maps to the degree of out-of-plane deformation.

The best agreement between experiment and simulation is obtained for saddle distortion angles in the range of 20° to 30°, consistent with earlier STM-based estimates. In contrast, planar geometries fail to reproduce the observed nodal structure, reinforcing the conclusion that the NiTPP monolayer adopts a strongly distorted shape. Compared to ZnTPP, the saddling appears even more pronounced, although the consequences for the energy level alignment of the frontier orbitals are more subtle.

Periodic DFT calculations for NiTPP adsorbed on Fe–O yield a relaxed geometry with a saddling angle of 23°, as illustrated in the ball-and-stick model in Fig.6.13c (bottom). The corresponding simulated momentum map, obtained by averaging the $|\mathrm{FT}|^2$ of the HOMO and HOMO-1 for this distorted geometry (Fig. 6.13c, top), is in excellent agreement with the experimental distribution. Moreover, the MOPDOS calculated for the same structure (Fig. 6.13d) closely matches the valence band spectrum shown in Fig.6.13a. The theoretical description predicts an energy splitting of approximately 220 meV between the HOMO and HOMO-1. However, this separation is insufficient to resolve the two levels spectroscopically, resulting instead in a single, broadened resonance, as observed in the experiment.

The pronounced saddle-shaped conformation observed for NiTPP is consistent with previous

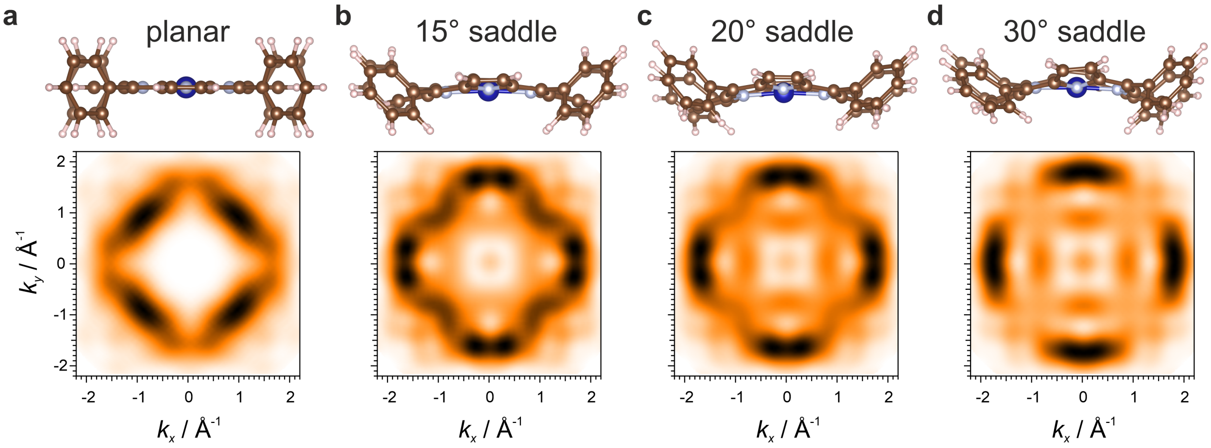

Figure 6.14: Simulated sum of HOMO and HOMO-1 momentum maps of NiTPP for increasing degrees of saddle distortion, ranging from planar to 15°, 20°, and 30°, shown left to right in panels **(a)**–**(d)**. Each panel displays the molecular geometry (top) and the corresponding summed momentum map (bottom). Published in [214].

studies reporting a more severe macrocycle distortion compared to ZnTPP [336]. Interestingly, while our DFT calculations confirm that such geometric deformations lift the degeneracy between the HOMO and HOMO-1, they also reveal that the magnitude of the resulting splitting, ΔE, is strongly dependent on the central metal ion. Even in the planar gas-phase geometry, ZnTPP exhibits a significantly larger orbital separation of 170 meV, compared to only 60 meV for NiTPP. This trend persists in the saddle-shaped configuration on the surface, where the splitting increases to 370 meV for ZnTPP but remains comparatively modest at 220 meV for NiTPP.

Notably, the enhanced splitting observed upon distortion arises predominantly from a shift of the HOMO to lower E_b, while the energetic position of the HOMO-1 remains largely unchanged. These findings underscore the dual role of metal substitution: not only does it modulate the degree of molecular deformation, but it also directly influences the electronic level alignment of the frontier orbitals.

In the following, we extend our investigation to the geometric and electronic structure of a NiTPP multilayer film, aiming to determine whether the reduced molecule–substrate interaction leads to observable changes in molecular conformation or frontier orbital alignment.

6.6.3 Growth and Electronic Structure of the NiTPP Bilayer

We begin this section by examining the LEED patterns of NiTPP/Fe–O as a function of molecular coverage, specifically for 1.0, 2.0, and 2.4 ML. The corresponding images are shown in Fig. 6.15. For the 2 ML film, the LEED pattern exhibits sharp diffraction spots that coincide with those observed for the monolayer [114], confirming the persistence of the same (5×5)R37° superstructure. Upon further increasing the coverage to 2.4 ML, additional diffraction spots emerge, accompanied by a slight blurring of the overall pattern. These new features correspond to a (5×5) overlayer structure.

In Fig. 6.15, the symmetry-equivalent unit cells of the (5×5)R37° reconstruction are indicated by green and blue squares, while the (5×5) unit cell is marked in red. The coexistence of both superstructures suggests that the molecular film remains ordered even beyond the first layer, supported by non-negligible intermolecular interactions that steer the multilayer growth.

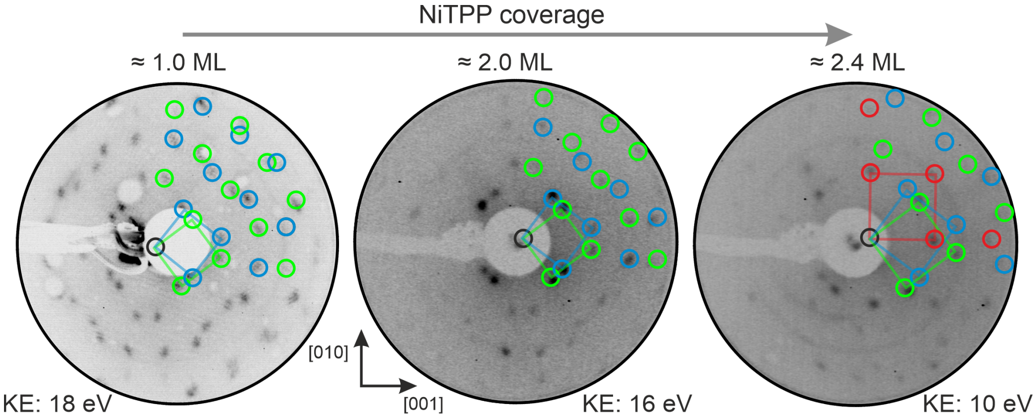

Figure 6.15: LEED patterns of NiTPP on Fe(100)–$p(1\times1)$O at different coverages. 1 ML: sharp (5×5)R37° pattern indicates an ordered monolayer. 2 ML: same pattern persists, confirming structural order in the bilayer. 2.4 ML: additional spots emerge, assigned to a (5×5) superstructure, suggesting long-range ordering beyond the second layer. Kinetic energies are noted below each image. Published in [214].

Having established the structural ordering of NiTPP beyond monolayer coverage, we now turn to the evolution of the electronic structure with increasing film thickness. Figure 6.16a compares the valence band spectra of the clean Fe–O substrate, a 1 ML NiTPP film, and a 2 ML film. Upon going from 1 ML to 2 ML, two key changes are observed: 1) the appearance of an additional peak at $E_\mathrm{b} = 2.6$ eV, and 2) a shift of the main molecular feature from 1.5 eV to higher binding energy. Furthermore, the 2 ML spectrum exhibits a kink at around 1.6 eV, indicating that this feature comprises an additional shoulder at slightly lower E_b.

The most prominent features are marked in the EDC in Fig. 6.16a, and their corresponding momentum maps are displayed in the upper halves of Fig. 6.16b. The presence of distinct nodal patterns in these maps suggests that a well-defined azimuthal orientation is preserved even in the second molecular layer, allowing for a meaningful POT analysis of the 2 ML NiTPP/Fe–O system.

The momentum map associated with the low-E_b shoulder at 1.5 eV (map A in Fig. 6.16b) exhibits striking similarity to the HOMO/HOMO-1 pattern of the saddle-shaped NiTPP monolayer previously shown in Fig. 6.13b. It features the same characteristic distribution near the center of the k-map. Given the near-perfect match in energy with the HOMO/HOMO-1 feature of the 1 ML spectrum, we attribute this signal to the first molecular layer, implying that the molecules in direct contact with the substrate retain their distorted geometry even upon subsequent molecular depositions.

In contrast, peak B at approximately 1.7 eV, although also derived from the HOMO/HOMO-1 manifold, yields a momentum map (map B) that no longer shows distortion-related nodal features.

Instead, its pattern resembles the simulated momentum map of planar NiTPP. The same applies to peaks C and D, which appear at higher E_b and whose corresponding maps (C and D) likewise match the planar orbital simulations. All the theoretical patterns for the HOMO levels are displayed below their experimental counterparts in Fig. 6.16b and show excellent agreement.

From this comparison, we conclude that once the first monolayer is complete, NiTPP molecules in subsequent layers adopt an undistorted, planar configuration. This structural relaxation reflects the absence of molecule–substrate interactions beyond the first layer. We note that in generating the planar simulations, a slight adjustment to the azimuthal orientation was applied, with the angle between the N–Ni–N axis and the [001] substrate direction tuned to 38° in order to optimize agreement with experiment. A comparison with maps at 35°, like the alignment used for the first layer of NiTPP molecules, is shown in the appendix, Fig. A.8b.

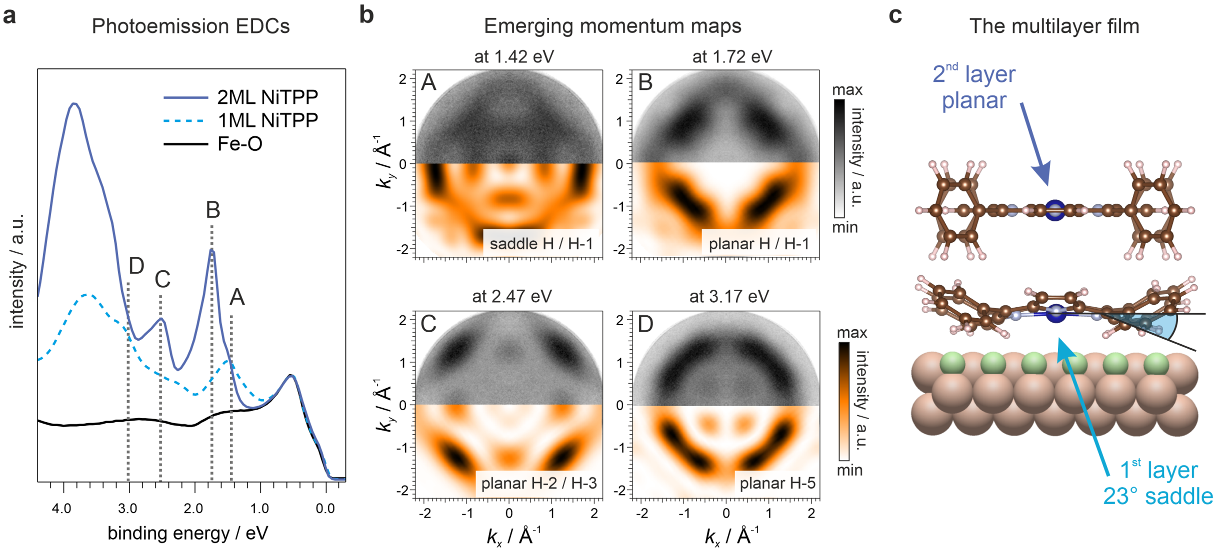

Figure 6.16: Valence band photoemission data of NiTPP on Fe–O as a function of coverage. **(a)** Momentum-integrated spectra of the clean Fe–O substrate, the 1 ML, and the 2 ML NiTPP films. Dotted vertical lines labeled A–D mark the energies at which the corresponding momentum maps were extracted. **(b)** Experimental momentum maps (top rows) for features A–D, with the respective simulated maps shown below. Comparison reveals a transition from distorted to planar orbital signatures between the first and second layer. **(c)** Deduced structure of the multilayer film: the first adsorbed layer remains strongly saddle-shaped, while the second layer relaxes into a planar configuration. Published in [214].

To assess how the planar conformation in the second molecular layer affects the energy splitting between the HOMO and HOMO-1, we analyze the peak at approximately 1.7 eV (peak B) in the EDC of the 2 ML NiTPP/Fe–O system (see Fig. 6.17), which is associated with the second molecular adlayer. To estimate its FWHM, we use the same fitting approach as for the monolayer, including a linear background and an additional Gaussian to account for the small shoulder at around 1.45 eV from the first layer (feature A). Although the fit does not perfectly reproduce the shape in this lower-energy region, it still provides a reasonable estimate for the main peak. Thereby, we extract a FWHM of (300 ± 100) meV, as shown in Fig. 6.17. The uncertainty of

100 meV is generously rounded up to reflect the imperfect agreement between fit and data and is used uniformly for all other FWHM values reported in this chapter.

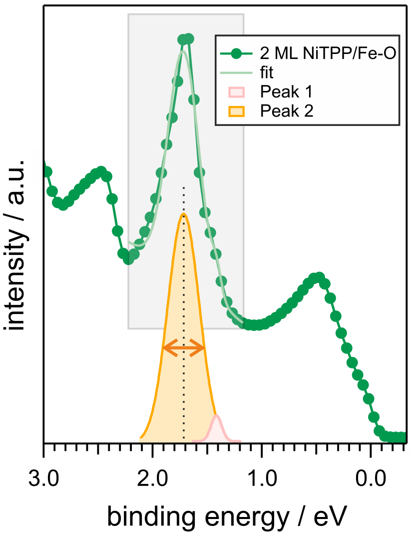

Figure 6.17: Fitting of the valence band spectrum for 2 ML NiTPP on Fe–O. The experimental energy distribution curve (dark green) is fitted within the grey-shaded region using a sum of two Gaussian functions and a linear background. The individual Gaussian contributions are shown in orange and light red, with the resulting total fit overlaid in light green. Published in [214].

The extracted peak width of (300 ± 100) meV is considerably smaller by approximately 40% than the (500 ± 100) meV obtained earlier for the main molecular feature in the 1 ML NiTPP spectrum. This supports the theoretical prediction that the energy splitting between HOMO and HOMO-1 is sensitive to molecular conformation: for a given MTPP species, a less pronounced saddle-shape distortion results in a reduced splitting, while stronger distortion increases the separation. It should be noted that this splitting is not necessarily governed by the overall deformation of the macrocycle alone, but appears to be particularly sensitive to the out-of-plane displacement of the metal ion from the porphyrin plane. However, this structural feature is typically enhanced in more strongly distorted adsorption geometries.

Finally, we compare the energy positions of the molecular peaks for first- and second-layer NiTPP. A shift of approximately 300 meV is observed, with the second-layer feature appearing at slightly higher E_b. Given the relatively small magnitude of this shift, we attribute it to attenuated surface screening effects, rather than distortion-induced changes in the electronic structure, as also discussed by Fratesi *et al.* [347].

In summary, the spectral evolution observed during NiTPP multilayer growth demonstrates that POT, in combination with spectral fitting, provides detailed access to layer-dependent variations in molecular conformation, azimuthal alignment, and electronic structure. While the first NiTPP layer adopts a strongly saddle-shaped geometry induced by the Fe–O substrate, accompanied by broader spectral features due to enhanced orbital splitting, the second layer relaxes into a near-planar geometry. As a result, its electronic structure approaches that of isolated molecules, exhibiting narrow and practically degenerate HOMO and HOMO–1 levels.

To further explore the origin of the HOMO/HOMO–1 splitting in saddle-shaped MTPPs, and to test whether this behavior extends beyond the specific case of NiTPP on Fe–O, we performed additional gas-phase DFT calculations for NiTPP and ZnTPP in both planar gas-phase and their distorted on-surface geometries. These calculations were carried out by the author using the ORCA 6 software package [348, 349]. Although the planar and saddle-shaped geometries were originally obtained using different computational settings (for example, different functionals or basis sets) all four structures were here recalculated within a uniform framework. This ensures a consistent comparison of their electronic structure and enables a closer inspection of how molecular distortion and metal ion displacement influence the HOMO/HOMO–1 splitting.

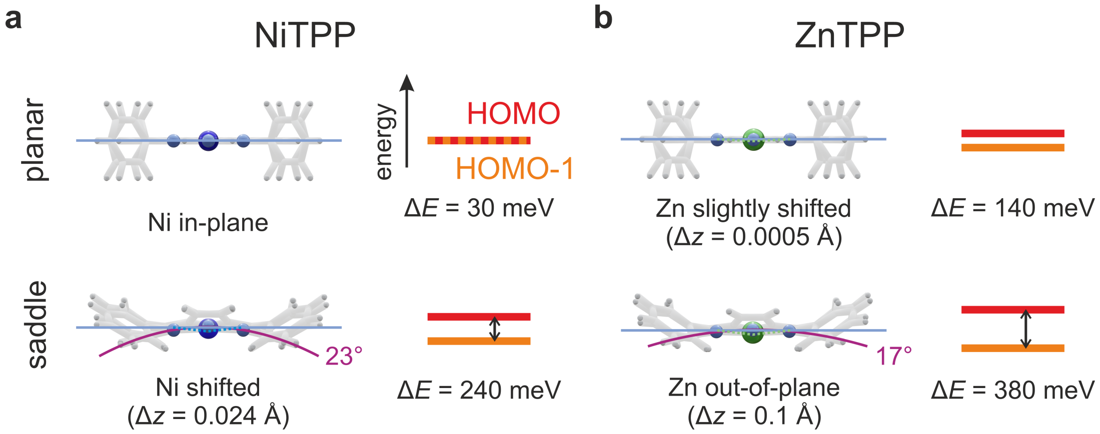

Figure 6.18: Summary of DFT results for **(a)** NiTPP and **(b)** ZnTPP, comparing planar and saddle-shaped geometries. The planar structures were taken from the Molecular Orbital Database [362], while the saddle-shaped geometries correspond to the optimized adsorption structures on Fe(100)–$p(1 \times 1)$O, as discussed throughout this thesis. All calculations shown here were performed in the gas phase using the B3LYP functional [172, 173] with Grimme's D3 dispersion correction [352] and the 6-31G* basis set [350, 351]. This computational setup differs slightly from the one used for the structure optimizations presented earlier, which may lead to minor deviations in absolute values; however, the overall trends remain fully consistent. Shown are the molecular geometries, the displacement Δz of the metal ion relative to the N_4 plane, and the corresponding energy splitting ΔE between the HOMO and HOMO–1 levels. The data reveal a clear correlation: larger out-of-plane displacements of the metal ion are accompanied by an increased HOMO–HOMO–1 splitting.

The results reveal a clear correlation between the degree of molecular distortion and the energy separation of HOMO and HOMO–1. A closer inspection shows that the splitting increases with the displacement of the metal ion (Δz) out of the plane defined by the four nitrogen atoms. This behavior suggests that the structural distortion of the macrocycle indirectly affects the HOMO/HOMO–1 splitting by promoting an out-of-plane shift of the central ion. However, the final magnitude of Δz is governed not only by the distortion itself but also by the size of the metal ion. While such distortions generally tend to displace the metal center out of the molecular plane, its absolute position is strongly influenced by the ionic radius of the metal species, which plays a significant role in determining the optimized geometry.

Interestingly, replacing Ni by Zn (or vice versa) in the same geometry yields virtually identical HOMO/HOMO–1 splittings. This observation emphasizes that it is the final molecular structure (including the Δz displacement) — rather than the specific identity of the metal center — that determines the electronic structure. Nevertheless, the choice of metal ion plays an essential role in guiding the structural relaxation during optimization, thereby indirectly shaping the electronic properties of the system. Overall, these findings underline that macrocycle distortions and metal ion displacements are intimately linked and jointly control the energetic separation of frontier orbitals in MTPP monolayers. In general, it appears likely that any reduction of molecular symmetry, such as that introduced by saddle-shaped distortions, will facilitate an out-of-plane displacement of the metal ion, further reinforcing its influence on the electronic structure.

6.7 Conclusion: Conformation, Orbital Splitting, and Optical Implications

This chapter has explored the interplay between molecular conformation and electronic structure in ZnTPP and NiTPP films on Fe(100)–$p(1 \times 1)$O, with particular focus on how saddle-shaped distortions of the porphyrin macrocycle affect the momentum-resolved photoemission signatures of frontier orbitals. Using POT in combination with DFT-based simulations, we have demonstrated that even subtle conformational changes imprint discernible fingerprints in the momentum maps of HOMO and HOMO-1 orbitals.

While POT has previously been used to identify simple geometric perturbations such as tilting, twisting, and bending, its ability to resolve more complex, delocalized conformational changes had not been quantitatively tested. Our simulations revealed that saddle-shaped distortions produce marked modifications in momentum space, as illustrated in Fig. 6.19, most notably a redistribution of intensity and the emergence of central features that are absent in the planar case. These theoretical insights laid the foundation for our experimental investigation of ZnTPP and NiTPP layers.

Importantly, the photon energy was shown to critically influence the visibility of these conformational signatures in POT. At low kinetic energies, characteristic momentum-space features of saddled molecules appear washed out or suppressed, whereas higher kinetic energies (*e.g.*, 35 eV) enhance the contrast. This dependence is crucial for experimental design and interpretation when targeting subtle orbital asymmetries.

In ZnTPP, we observed a clear splitting between HOMO and HOMO-1 in both energy and momentum, consistent with a moderate saddle distortion of 17°. NiTPP displayed an even stronger saddling of 23° in the monolayer, albeit with a smaller orbital splitting. This suggests a general link between molecular distortion and orbital energy separation — but it also indicates that the saddling angle alone does not fully determine the electronic response. While orbital splitting generally increases with saddle distortion, the crucial factor is the out-of-plane displacement of the central metal ion, which depends on the specific ion and its relaxed position. Larger metal ions tend to sit further out of plane, leading to stronger perturbations despite similar distortion angles.

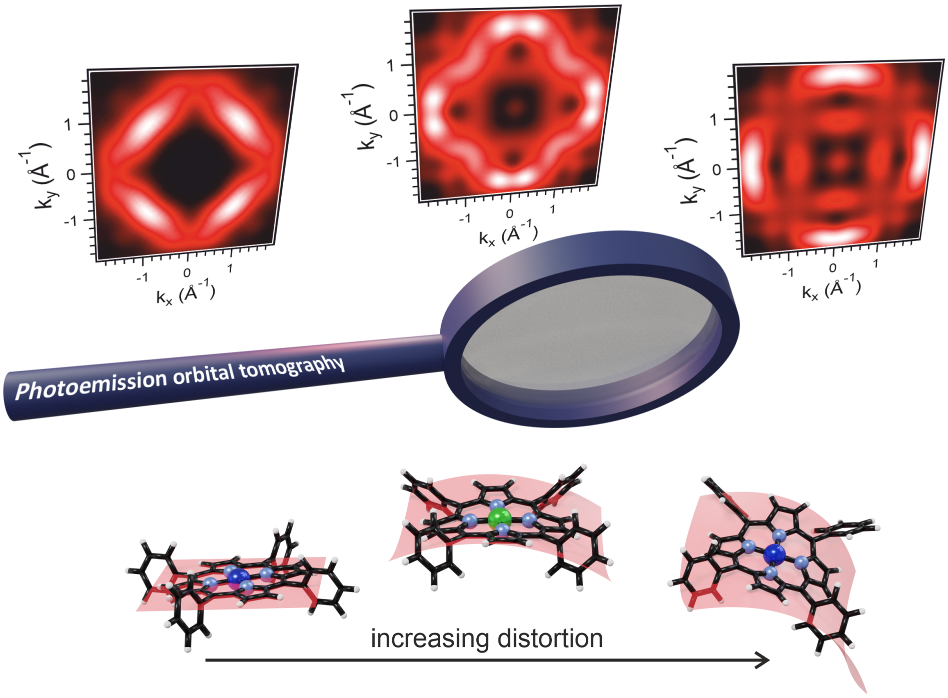

Figure 6.19: Graphical summary of how POT can assess the degree of saddle-shaped distortions by analyzing the momentum distributions of photoelectrons emitted from porphyrin films. The ability of POT to identify distinct molecular orbitals based on their momentum-space fingerprints provides direct insight into the relationship between conformation and electronic structure in porphyrins.

Upon deposition of a second layer, NiTPP molecules remain ordered but adopt a planar conformation, as evidenced by narrower photoemission features in the EDC, and strong changes in the measured momentum distributions. This layer-dependent transition underscores the power of POT to disentangle interfacial effects from intrinsic molecular behavior — offering a nanoscale probe of conformational evolution in molecular films. In this planar geometry, the HOMO and HOMO-1 become fully degenerate, highlighting the intimate connection between molecular shape and the electronic structure of porphyrins.

This link between conformation and orbital alignment has direct consequences for the optical and electronic properties of these systems. The splitting of HOMO and HOMO-1 levels reshapes the effective HOMO–LUMO gap, influencing light absorption and charge transport characteristics. As such, control over molecular geometry becomes a key design parameter in porphyrin-based optoelectronic applications, where performance often hinges on subtle shifts in energy level alignment.

Beyond synthetic materials, this structure–function relationship is of fundamental importance for understanding biomolecular processes. In nature, porphyrin derivatives such as heme rely on precisely such geometric–electronic couplings to fulfill their function. For instance, in heme complexes, oxygen binding flattens the macrocycle, modifies the orbital structure, and alters the optical response, leading to the characteristic color change between deoxygenated and oxygenated blood (Fig. 6.20). While chemically distinct from the synthetic porphyrins studied here, this biological analogy exemplifies a more general principle: molecular geometry modulates electronic structure, which in turn governs optical and chemical properties.

Table 6.1: Summary of extracted FWHM values and HOMO–HOMO-1 splittings (ΔE) for ZnTPP and NiTPP in different adsorption geometries.

system	**FWHM**	ΔE	**conformation**
1 ML ZnTPP	650 meV	370 meV	saddle
1 ML NiTPP	500 meV	170 meV	saddle
2 ML NiTPP (2nd layer)	300 meV	60 meV	planar

In summary, this chapter demonstrates that POT enables an unprecedented view into the conformational landscape and electronic structure of surface-adsorbed porphyrins. The ability to correlate orbital energies, momentum maps, and molecular geometry opens new pathways for the rational design of porphyrin-based systems in sensing, catalysis, and molecular optoelectronics. At the same time, the parallels with biologically relevant systems suggest that this level of orbital-scale insight may offer a fresh perspective on biochemical function through the lens of momentum-resolved photoemission.

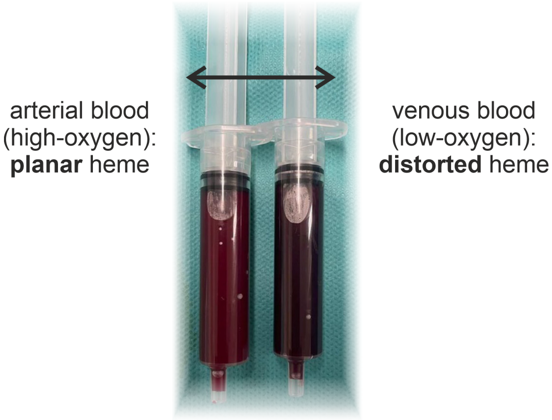

Figure 6.20: Comparison between arterial (left) and venous (right) blood. Oxygen binding to heme alters the electronic structure resulting in a visible color change. While structurally more complex than the synthetic porphyrins studied here, this biological phenomenon illustrates the broader principle that molecular geometry governs orbital energies, reactivity, and optical properties. Reproduced from [363]. © 2024 Sage Publications.

7 Conclusion and Outlook

7.1 Conclusion

This thesis has examined the interaction between different adsorbates and a model ferromagnetic $3d$ transition metal surface, namely Fe(100). Through a combined approach of spin- and momentum-resolved photoemission spectroscopy, scanning probe microscopy, and advanced electronic structure calculations (DFT+U, DMFT), we have shown that electron correlation can fundamentally determine the nature of hybrid interfaces, with far-reaching consequences for spintronics, catalysis, and organic electronics.

In the first part, we demonstrated that the chemisorption of atomic oxygen on Fe(100) strongly enhances electronic correlations in the Fe surface layer. This enhancement results in a narrowing of the Fe d-bands, suppression of exchange splitting, and the emergence of spin-dependent energy broadening in oxygen-related electronic bands due to the presence of satellite features — hallmarks of many-body interactions. These findings challenge the assumptions of conventional single-particle models and establish that adsorbates can significantly reshape the substrate's electronic structure. Electron correlation, therefore, is not a passive property of the metal but a dynamic quantity that can be modulated by interfacial chemistry.

Building on this insight, the second part of the thesis examined the adsorption of pentacene (5A) on the oxygen-passivated Fe–O surface. The correlation-induced renormalization of the Fe d-band was shown to switch the molecule–metal interaction from weak to strong coupling. To capture this behavior, we employed an empirically tuned DFT+U approach as a computationally inexpensive approximation to the DMFT substrate electronic structure. Specifically, a negative U_{eff} value was introduced to emulate the key correlation-driven modifications predicted by DMFT — namely, the narrowing of the d-band and the reduction in exchange splitting. This calibration enabled us to reproduce the experimental signatures observed for the adsorbed 5A layer, validating DFT+U as a practical substitution for describing correlation-activated coupling at hybrid interfaces.

Based on these results, we introduced a refined d-band model that treats electron correlation as an explicit intermediate step in the adsorption process. Rather than considering hybridization on top of an unmodified substrate band structure, the model accounts for the reshaping of the Fe d-states due to correlation effects prior to molecule–metal coupling. It further emphasizes the central role of the Fe d_{z^2} orbital in mediating vertical coupling to extended π-systems and incorporates the spatial inhomogeneity of the interaction across large molecular adsorbates. By capturing registry-dependent bonding with near-quantitative accuracy, this model extends traditional chemisorption theory to correlated systems with both conceptual clarity and physical relevance.

The final chapter focused on metalated tetraphenylporphyrins (ZnTPP and NiTPP) on Fe–O, where the interaction remains electronically weak but geometrically rich. Photoemission orbital tomography (POT) was established as a highly sensitive technique for resolving complex conformational distortions in molecular adsorbates. Its combined sensitivity to the momentum-space structure of frontier orbitals and to subtle molecular geometries enabled us to disentangle the interplay between energy level alignment and conformational variations. In particular, the momentum-resolved photoemission maps revealed saddle-shaped distortions of the porphyrin macrocycle at the monolayer level, allowing for a direct link between molecular geometry and orbital structure. By comparing monolayer and multilayer films with DFT simulations, we traced how molecular structure evolves under the influence of the substrate. We showed that interaction with the Fe–O surface induces pronounced molecular distortions, which lift the degeneracy between the HOMO and HOMO–1 orbitals, while such deformations are absent in subsequent molecular layers. Furthermore, by comparing porphyrins with different central metal ions, we found indications that the extent of this degeneracy lifting is highly sensitive to the precise position of the metal center — underscoring that even subtle changes in coordination geometry can decisively affect the electronic structure.

Ultimately, this thesis demonstrates that correlation and hybridization are interwoven phenomena that, when understood together, provide a richer, more accurate picture of the physics at adsorbate–metal interfaces.

7.2 Outlook

The findings presented in this thesis open several promising directions for future research. On the methodological side, time-resolved photoemission orbital tomography (POT) offers a powerful means of accessing dynamic processes such as excited-state relaxation. This is particularly relevant for unoccupied states such as the LUMO of 5A, where the relaxation dynamics of its bonding and antibonding components may provide insight into how coupling to the substrate influences the lifetime and decay pathways of excited states. Moreover, applying time-resolved POT to porphyrin systems may uncover how electronic excitations dynamically influence molecular conformation. Understanding this coupling between excited-state population and structural response would be especially valuable for photocatalysis and organic photovoltaics, where device performance depends primarily on geometric distortions and electronic structure, respectively. In these contexts, the systems presented in this thesis serve as well-defined model platforms, and future studies stand to benefit directly from the insights gained here.

Furthermore, extending the investigation to related π-conjugated systems, such as longer or shorter acenes or planar macrocyclic molecules like phthalocyanines, would provide a broader testing ground for the generalized d_{z^2}-band model developed in this work.

Another promising direction is the concept of correlation engineering, using adsorbates to tune electronic correlations at ferromagnetic surfaces, which could be pursued through systematic studies involving chemically diverse adsorbates. Carbon-based species such as atomic carbon, 5A, and C_{60} exhibit markedly different interaction strengths with Fe(100). Atomic carbon forms a $c(2 \times 2)$ superstructure and introduces a new electronic state near E_F, whose spin-resolved character remains to be determined. Pentacene shows significant charge transfer and partial LUMO occupation accompanied by spin polarization [364, 365], making it an excellent candidate for spin-resolved POT. C_{60}, by contrast, is known to induce substantial surface reconstructions [117], which may strongly influence both hybridization and correlation effects.

To disentangle these interfacial effects, experiments at variable photon energies, should be employed to tune the photoemission cross-section and selectively enhance contributions from either the molecular layer or the substrate. This strategy, which relies on synchrotron-based light sources, enables spatially and chemically resolved correlation studies at molecule–metal interfaces.

Tuning the interaction strength and nature of the coupling via substrate modification remains another powerful approach. Removing the oxygen passivation layer, or replacing it with an alternative decoupling material such as ultrathin MgO, could allow for more finely controlled charge and spin interactions. In particular, the low work function of MgO facilitates spontaneous charge transfer into organic adlayers [82]. Exploring such systems is especially promising in light of the well-established spin-filtering properties of MgO/Fe interfaces [366], which could enable the development of novel organic spin valve technologies that combine efficient spin injection with molecular-level tunability. In parallel, introducing molecular chirality could give rise to spin-selective transport via the chirality-induced spin selectivity (CISS) effect [367, 368]. In this regard, the Fe–O interface represents an attractive and versatile platform, offering both sufficient chemical reactivity to support bonding and the structural order required for controlled molecular self-assembly.

A Appendix

A.1 Additional DMFT Analysis of the Fe-O Surface

To complement the discussion in the main text Fig. A.1a shows the projected density of states (PDOS) for Fe(100)-$p(1 \times 1)$O calculated using both DFT and DFT+DMFT with correlation parameters $U = 1.8\,\mathrm{eV}$ and $J = 0.5\,\mathrm{eV}$, *i.e.*, the values commonly used for the clean Fe(100) surface. In Fig. A.1b, the resulting DFT+DMFT spectrum is compared with the experimentally measured valence band spectrum, obtained via momentum-integrated photoemission using $h\nu = 64\,\mathrm{eV}$ p-polarized synchrotron light. The blue-shaded region highlights the dominant spectral feature originating from Fe d states. As evident from the comparison, the calculated spectrum underestimates the spectral weight near the Fermi level, underscoring the necessity of increasing the correlation parameters to reproduce the experimental lineshape.

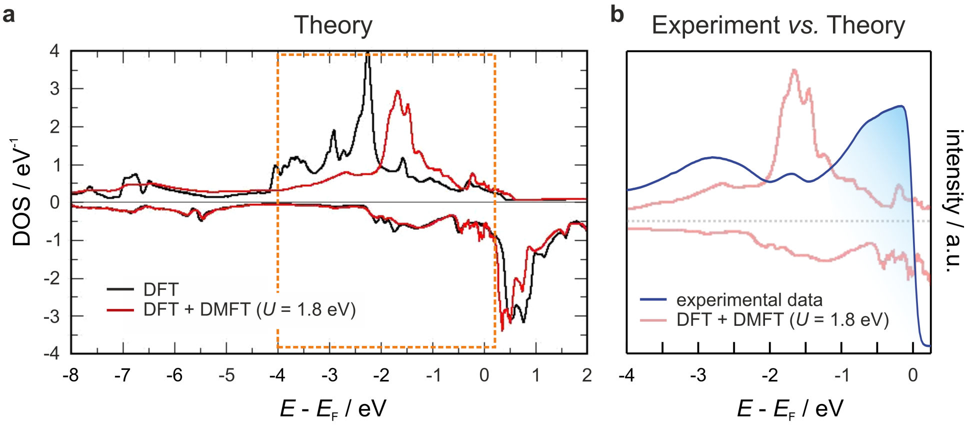

Figure A.1: (a) Projected density of states (PDOS) for Fe(100)-$p(1 \times 1)$O computed using DFT and DFT+DMFT with $U = 1.8\,\mathrm{eV}$ and $J = 0.5\,\mathrm{eV}$. **(b)** Comparison of DFT+DMFT PDOS (red) with the experimental valence band spectrum (blue). Published in [190].

A.2 Simulating the Photoemission Maps of Pentacene

Theoretical momentum maps were generated based on gas-phase DFT calculations of the pentacene (5A) HOMO. The momentum distribution was obtained from the orbital's Fourier transform, evaluated on an isoenergetic sphere corresponding to the kinetic energy of the photoelectrons (35 eV), as described in Section 3.2. This procedure yields the base momentum map shown in Fig. A.2b.

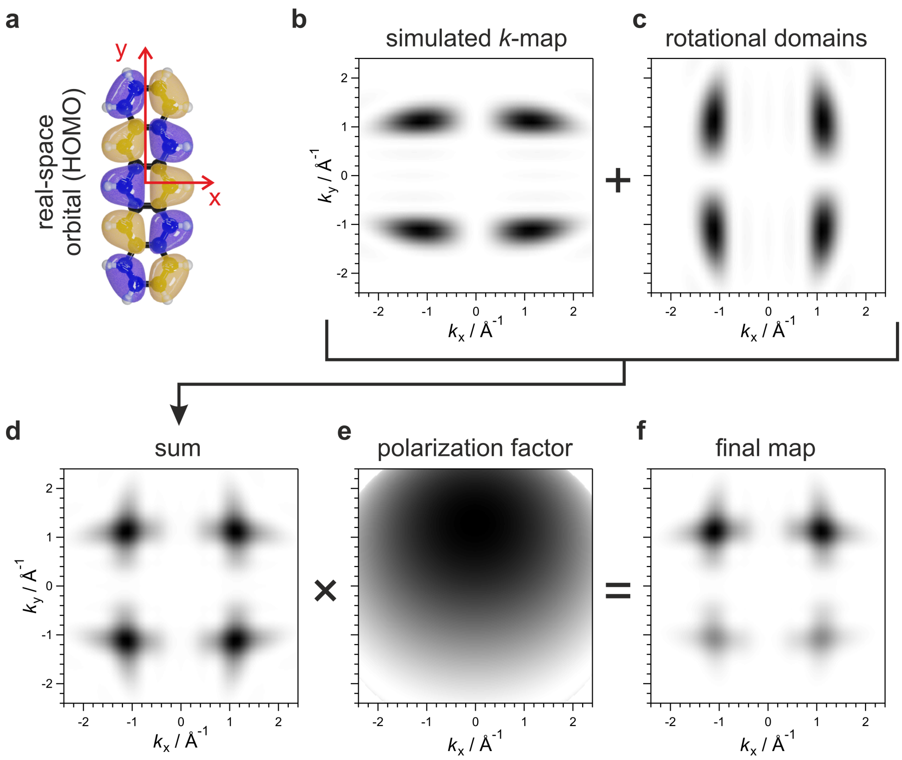

Figure A.2: Workflow for generating theoretical momentum maps of pentacene. **(a)** Real-space representation of the HOMO of 5A, obtained from gas-phase DFT calculations. **(b)** Corresponding momentum map extracted from the Fourier transform of the orbital. **(c)** Simulated map for molecules arranged in rotationally equivalent domains. **(d)** Sum of the individual domain contributions, accounting for spatial averaging inherent in ARPES measurements. **(e)** Polarization factor that reflects the experimental light incidence and polarization geometry. **(f)** Final theoretical momentum map resulting from the multiplication of the summed domain map with the polarization factor. This final image serves as the theoretical counterpart to the experimentally measured photoemission intensity distributions. Figure from manuscript currently under review.

Because MM (and ARPES in general) probes relatively large surface areas, it inherently averages over multiple rotational domains of adsorbed molecules. On the Fe–O surface, the presence of azimuthally rotated domains must therefore be taken into account. In this case, the fourfold (D_4) symmetry of the substrate allows for a straightforward treatment: a simple 90° rotation of the base map (Fig. A.2b) yields the equivalent domain shown in Fig. A.2c. Other symmetry operations such as mirroring or further rotation would reproduce features already contained in either map (b) or (c). The sum of these two rotationally equivalent maps (Fig. A.2d) effectively represents the domain-averaged momentum distribution expected in the experiment. Finally, a polarization factor reflecting the experimental geometry, specifically the photon energy and light incidence angle, was applied (Fig. A.2e) to incorporate matrix element effects. The resulting momentum map (Fig. A.2f) reproduces the characteristic symmetry and intensity variations of the experimental photoemission data and serves as a reference for orbital identification.

A.3 Characterizing the Valence Band Peaks of 5A/Fe-O

In this appendix, we present a detailed analysis of the valence band features observed in the photoemission spectra of the 5A/Fe–O interface. In particular, we focus on the peaks corresponding to the highest occupied molecular orbital (HOMO) and its adjacent orbitals (HOMO−1, HOMO−2).

Fitting Procedure and Error Estimation

To analyze the spectra, we employed a phenomenological fitting model consisting of a linear background and a sum of Gaussian functions. While this approach provides a straightforward method for modeling broad photoemission peaks, it cannot fully resolve the microscopic origin of each feature. Consequently, the precise number of contributing states remains ambiguous. However, the quality of the fits provides insights into the minimal number of spectral components required to describe the data.

To estimate the experimental noise, a flat region of the valence band spectrum (Fig. A.3a–b) was fitted with a linear function. The residuals of this fit yield a standard deviation of 3.6 (arbitrary units), which we take as the error margin for a single photoemission spectrum. As our analysis is based on the difference between two spectra, the total uncertainty is multiplied by $\sqrt{2}$, in accordance with Gaussian error propagation.

HOMO Peak Fitting Analysis

We performed fits of the HOMO peak using one, two, and three Gaussian functions (Fig. A.4a–c). The residuals clearly indicate that a single Gaussian is insufficient to model the data, exhibiting strong and systematic deviations. To quantify the fit quality, we compute the reduced chi-squared parameter

$$\chi^2_\nu = \frac{1}{\nu}\sum_{i=1}^{N}\left(\frac{y_i - y(x_i)}{\alpha}\right)^2,$$

where y_i denotes the measured intensity, $y(x_i)$ the fit value at point x_i, and $\alpha = 5.1$ is the propagated error. The number of degrees of freedom $\nu = N - N_{\text{cons.}}$ corresponds to the total number of data points minus the number of fit parameters [369].

The resulting reduced chi-squared values were $\chi^2_{\nu,\text{HOMOa}} = 7.3$ for the single-Gaussian fit, $\chi^2_{\nu,\text{HOMOb}} = 1.3$ for two Gaussians, and $\chi^2_{\nu,\text{HOMOc}} = 1.0$ for three Gaussians. These results suggest that the HOMO peak comprises at least two, and likely three, spectral components.

HOMO-1 and HOMO-2 Peak Analysis

An analogous analysis was performed for the HOMO−1 and HOMO−2 features (Fig. A.5). Here, we compared fits using one and two Gaussians, both combined with a linear background. The resulting reduced chi-squared values were $\chi^2_{\nu,\text{HOMO-1/−2a}} = 1.6$ and $\chi^2_{\nu,\text{HOMO-1/−2b}} = 1.4$.

These results indicate a marginal improvement when using two components, though both models describe the data reasonably well.

We also tested Lorentzian peak shapes, but in all cases the resulting fits were inferior, exhibiting larger residuals and higher χ^2 values.

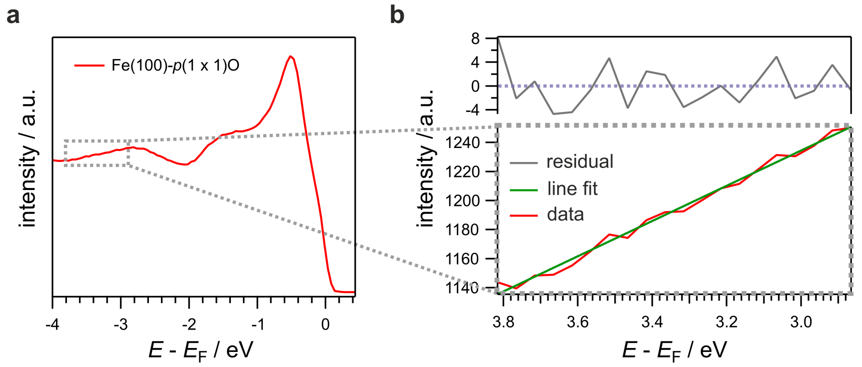

Figure A.3: Determination of the noise level in the photoemission data. **(a)** Momentum-integrated valence band spectrum of a freshly prepared Fe–O surface. The grey box indicates the region selected for background fitting. **(b)** Close-up of the linear region (red curve) and its linear fit (green line). The residual (grey) is shown in the inset, with the mean residual value (violet dashed line) defining the error margin. Figure from manuscript currently under review.

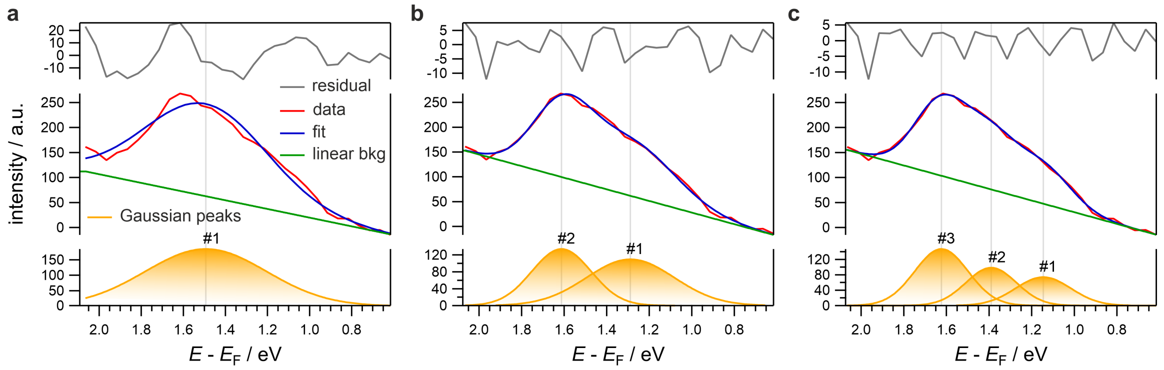

Figure A.4: Fitting analysis of the HOMO-related photoemission peak at the 5A/Fe–O interface. **(a)** Fit with a single Gaussian, showing structured residuals. **(b)** Fit with two Gaussians. **(c)** Fit with three independent Gaussians. The progression shows improved fit quality with increased model complexity. Figure from manuscript currently under review.

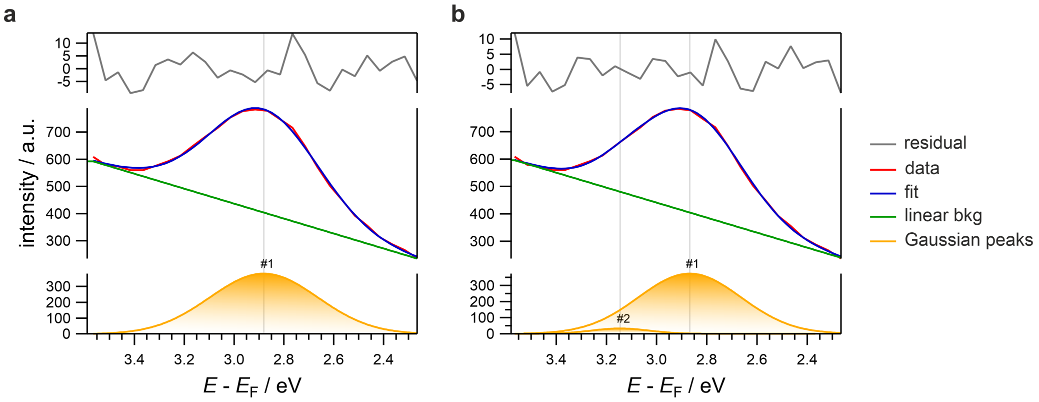

Figure A.5: Fitting analysis of the HOMO−1 and HOMO−2 peaks. **(a)** Fit using one Gaussian and a linear background. **(b)** Fit with two Gaussians. The residuals improve modestly with the additional peak, but the simpler model still performs reasonably well. Figure from manuscript currently under review.

A.4 Momentum Map Processing for POT Analysis of MTPPs

All momentum-resolved photoemission maps presented in Chapter 6 were symmetrized according to the D_4 symmetry of the Fe(100)-$p(1 \times 1)$O surface to improve the signal-to-noise ratio and thereby enhance molecule-related features. Symmetrization was performed by averaging over equivalent rotational domains, assuming azimuthal alignment along the crystallographic axes. This procedure severely improves signal quality and was applied uniformly to all ZnTPP and NiTPP datasets.

Momentum Map Alignment and Background Subtraction

In order to identify the molecular orbitals in POT it is often required to remove the signal stemming from the substrate, in order to isolate the molecular intensity. However, due to instrumental variations (*e.g.*, slight changes in PEEM lens settings), the field of view in k-space can differ slightly between measurements. Hence, before subtracting substrate-related background features, we applied a rescaling procedure based on line profiles taken from control maps. This allowed the clean Fe-O maps to be accurately resized by bilinear interpolation, aligning them with the molecular-layer maps.

Subtraction was then performed at binding energies of molecular resonance energies (1.5 eV for NiTPP) to isolate orbital features. In addition, subtraction was also performed on control maps where only substrate emission is expected (typically close to the Fermi energy). An example of this procedure is shown in Fig. A.7.

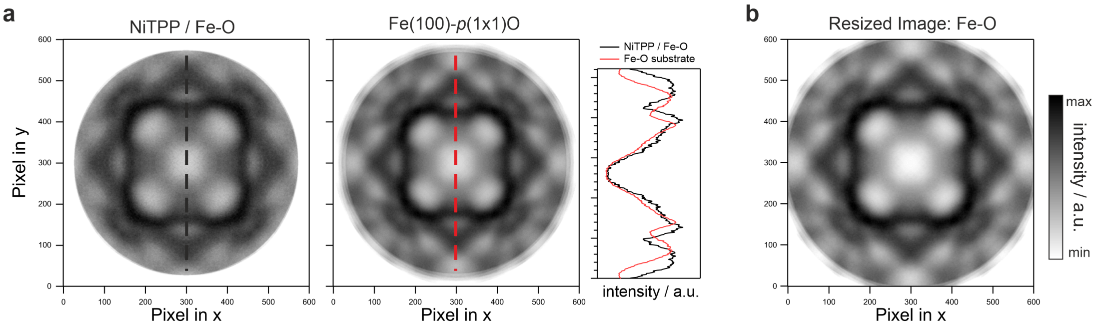

Figure A.6: Adjustment of momentum map scaling before subtraction. **(a)** Momentum-resolved PEEM images of NiTPP/Fe–O (left) and the bare Fe–O substrate (middle), integrated over the 0.5–0.8 eV binding energy range. Dashed lines denote the directions used for extracting line profiles (right panel). **(b)** Interpolated and cropped Fe–O reference map, scaled to match the NiTPP/Fe–O field-of-view. Published in [214].

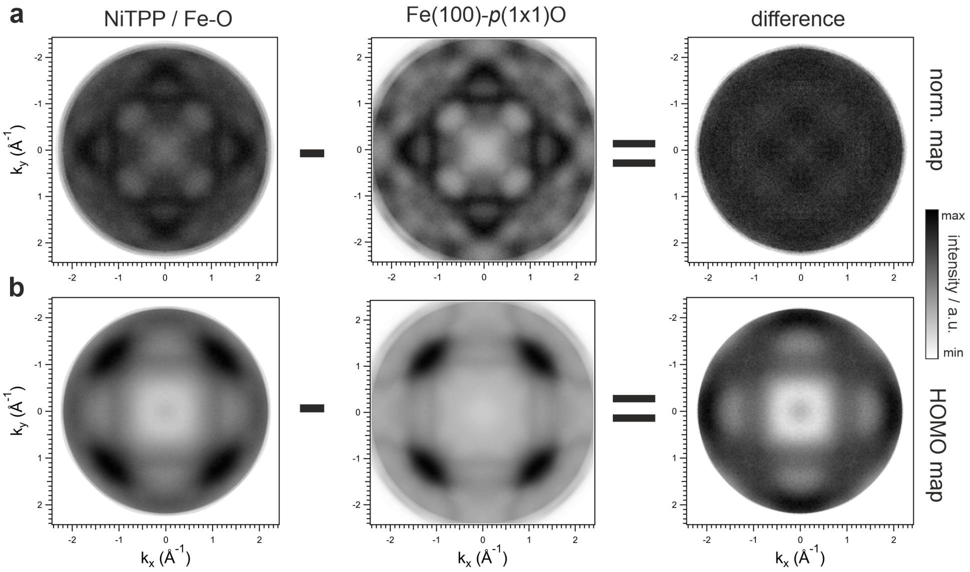

Figure A.7: Subtraction of background maps. **(a)** Control subtraction at 0.6 eV, showing the NiTPP/Fe–O image (left), scaled Fe–O reference (middle), and difference map (right). **(b)** Subtraction result at 1.5 eV, where molecular emission features emerge. This corresponds to the data shown in Fig. 6.13. Published in [214].

Simulation of Momentum Maps

To compare these experimental photoemission maps to theoretical orbital patterns, simulated maps were generated from the squared Fourier transforms ($|\mathrm{FT}|^2$) of the relevant molecular orbitals. These maps were then rotated according to the assumed azimuthal adsorption geometry found in literature and in our simulations (17° for ZnTPP and 35° for NiTPP), and averaged in cases of degenerate orbitals (*e.g.*, HOMO/HOMO-1 in Fig. A.8a). Next, to account for the existence of symmetry-equivalent domains, the final maps were symmetrized assuming the D_4 symmetry of the substrate surface. An exemplary resulting averaged HOMO/HOMO–1 map of NiTPP is displayed in Fig. A.8b, while additional symmetrized maps for the corresponding HOMO–2/HOMO–3 and HOMO–5 orbitals are presented in Fig. A.8c,d.

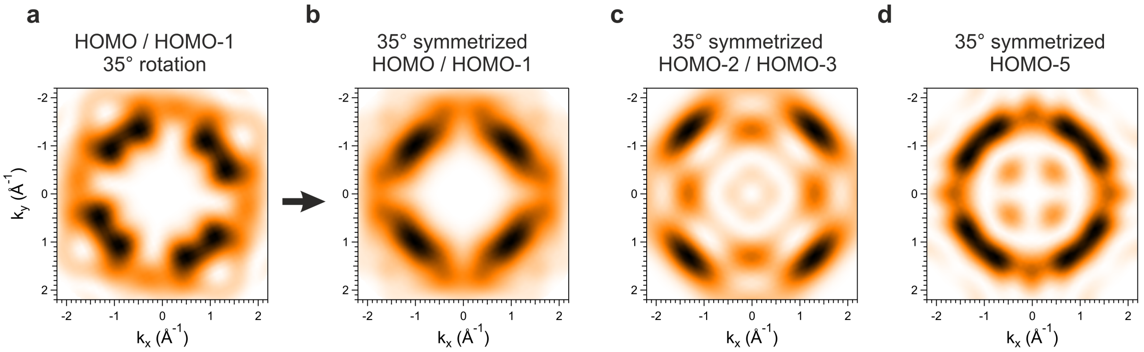

Figure A.8: Simulated photoemission momentum maps of NiTPP orbitals in a planar structure. **(a)** Average of the HOMO and HOMO–1 maps for a molecular azimuth of 35° with respect to the substrate [100] direction. **(b)** Resulting symmetrized map assuming D_4 symmetry of the Fe(100) surface. **(c),(d)** Symmetrized orbital maps corresponding to the HOMO–2/HOMO–3 and HOMO–5 states, respectively. Published in [214].

Bibliography

[1] C. Herring, "The State of d Electrons in Transition Metals," *Journal of Applied Physics* **31**, S3–S11 (1960).

[2] M. N. Baibich, J. M. Broto, A. Fert, F. N. Van Dau, F. Petroff, P. Etienne, G. Creuzet, A. Friederich, and J. Chazelas, "Giant Magnetoresistance of (001)Fe/(001)Cr Magnetic Superlattices," *Physical Review Letters* **61**, 2472–2475 (1988).

[3] G. Binasch, P. Grünberg, F. Saurenbach, and W. Zinn, "Enhanced magnetoresistance in layered magnetic structures with antiferromagnetic interlayer exchange," *Physical Review B* **39**, 4828–4830 (1989).

[4] J. Mathon and A. Umerski, "Theory of tunneling magnetoresistance of an epitaxial Fe/MgO/Fe(001) junction," *Physical Review B* **63**, 220403 (2001).

[5] S. S. P. Parkin, C. Kaiser, A. Panchula, P. M. Rice, B. Hughes, M. Samant, and S.-H. Yang, "Giant tunnelling magnetoresistance at room temperature with MgO (100) tunnel barriers," *Nature Materials* **3**, 862–867 (2004).

[6] S. Yuasa, T. Nagahama, A. Fukushima, Y. Suzuki, and K. Ando, "Giant room-temperature magnetoresistance in single-crystal Fe/MgO/Fe magnetic tunnel junctions," *Nature Materials* **3**, 868–871 (2004).

[7] S. S. P. Parkin, K. P. Roche, M. G. Samant, P. M. Rice, R. B. Beyers, R. E. Scheuerlein, E. J. O'Sullivan, S. L. Brown, J. Bucchigano, D. W. Abraham, Y. Lu, M. Rooks, P. L. Trouilloud, R. A. Wanner, and W. J. Gallagher, "Exchange-biased magnetic tunnel junctions and application to nonvolatile magnetic random access memory (invited)," *Journal of Applied Physics* **85**, 5828–5833 (1999).

[8] A. Fert, "Nobel Lecture: Origin, development, and future of spintronics," *Reviews of Modern Physics* **80**, 1517–1530 (2008).

[9] S. Parkin and S.-H. Yang, "Memory on the racetrack," *Nature Nanotechnology* **10**, 195–198 (2015).

[10] A. R. Rocha, V. M. García-suárez, S. W. Bailey, C. J. Lambert, J. Ferrer, and S. Sanvito, "Towards molecular spintronics," *Nature Materials* **4**, 335–339 (2005).

[11] Z. H. Xiong, D. Wu, Z. Valy Vardeny, and J. Shi, "Giant magnetoresistance in organic spin-valves," *Nature* **427**, 821–824 (2004).

[12] C. Barraud, P. Seneor, R. Mattana, S. Fusil, K. Bouzehouane, C. Deranlot, P. Graziosi, L. Hueso, I. Bergenti, V. Dediu, F. Petroff, and A. Fert, "Unravelling the role of the interface for spin injection into organic semiconductors," *Nature Physics* **6**, 615–620 (2010).

[13] M. Cinchetti, V. A. Dediu, and L. E. Hueso, "Activating the molecular spinterface," *Nature Materials* **16**, 507–515 (2017).

[14] N. Atodiresei, J. Brede, P. Lazić, V. Caciuc, G. Hoffmann, R. Wiesendanger, and S. Blügel, "Design of the Local Spin Polarization at the Organic-Ferromagnetic Interface," *Physical Review Letters* **105**, 066601 (2010).

[15] K. Bairagi, A. Bellec, V. Repain, C. Chacon, Y. Girard, Y. Garreau, J. Lagoute, S. Rousset, R. Breitwieser, Y.-C. Hu, Y. C. Chao, W. W. Pai, D. Li, A. Smogunov, and C. Barreteau, "Tuning the Magnetic Anisotropy at a Molecule-Metal Interface," *Physical Review Letters* **114**, 247203 (2015).

[16] A. Quesada, G. Chen, A. T. N'Diaye, P. Wang, Y. Z. Wu, and A. K. Schmid, "Non-monotonic magnetic anisotropy behavior as a function of adsorbate coverage in Fe ultrathin films near the spin reorientation transition," *Journal of Materials Chemistry C* **9**, 2801–2805 (2021).

[17] F. Al Ma'Mari, T. Moorsom, G. Teobaldi, W. Deacon, T. Prokscha, H. Luetkens, S. Lee, G. E. Sterbinsky, D. A. Arena, D. A. Maclaren, M. Flokstra, M. Ali, M. C. Wheeler, G. Burnell, B. J. Hickey, and O. Cespedes, "Beating the Stoner criterion using molecular interfaces," *Nature* **524**, 69–74 (2015).

[18] P. Sharangi, P. Gargiani, M. Valvidares, and S. Bedanta, "Magnetism at the interface of non-magnetic Cu and C 60," *Physical Chemistry Chemical Physics* **23**, 6490–6495 (2021).

[19] S. Sanvito, "The rise of spinterface science," *Nature Physics* **6**, 562–564 (2010).

[20] I. Bergenti and V. Dediu, "Spinterface: A new platform for spintronics," *Nano Materials Science* **1**, 149–155 (2019).

[21] S. Pramanik, C.-G. Stefanita, S. Patibandla, S. Bandyopadhyay, K. Garre, N. Harth, and M. Cahay, "Observation of extremely long spin relaxation times in an organic nanowire spin valve," *Nature Nanotechnology* **2**, 216–219 (2007).

[22] S. Sanvito and A. R. Rocha, "Molecular-Spintronics: The Art of Driving Spin Through Molecules," *Journal of Computational and Theoretical Nanoscience* **3**, 624–642 (2006).

[23] I. Žutić, J. Fabian, and S. Das Sarma, "Spintronics: Fundamentals and applications," *Reviews of Modern Physics* **76**, 323–410 (2004).

[24] M. Cinchetti, K. Heimer, J.-P. Wüstenberg, O. Andreyev, M. Bauer, S. Lach, C. Ziegler, Y. Gao, and M. Aeschlimann, "Determination of spin injection and transport in a ferromagnet/organic semiconductor heterojunction by two-photon photoemission," *Nature Materials* **8**, 115–119 (2009).

[25] S. Schmaus, A. Bagrets, Y. Nahas, T. K. Yamada, A. Bork, M. Bowen, E. Beaurepaire, F. Evers, and W. Wulfhekel, "Giant magnetoresistance through a single molecule," *Nature Nanotechnology* **6**, 185–189 (2011).

[26] K. V. Raman, A. M. Kamerbeek, A. Mukherjee, N. Atodiresei, T. K. Sen, P. Lazić, V. Caciuc, R. Michel, D. Stalke, S. K. Mandal, S. Blügel, M. Münzenberg, and J. S. Moodera, "Interface-engineered templates for molecular spin memory devices," *Nature* **493**, 509–513 (2013).

[27] M. Callsen, V. Caciuc, N. Kiselev, N. Atodiresei, and S. Blügel, "Magnetic hardening induced by nonmagnetic organic molecules," *Physical Review Letters* **111**, 106805 (2013).

[28] I. Dzyaloshinsky, "A thermodynamic theory of "weak" ferromagnetism of antiferromagnetics," *Journal of Physics and Chemistry of Solids* **4**, 241–255 (1958).

[29] T. Moriya, “Anisotropic Superexchange Interaction and Weak Ferromagnetism,” *Physical Review* **120**, 91–98 (1960).

[30] G. Chen, A. Mascaraque, H. Jia, B. Zimmermann, M. Robertson, R. L. Conte, M. Hoffmann, M. A. G. Barrio, H. Ding, R. Wiesendanger, E. G. Michel, S. Blügel, A. K. Schmid, and K. Liu, “Large Dzyaloshinskii-Moriya interaction induced by chemisorbed oxygen on a ferromagnet surface,” *Science Advances* **6**, eaba4924 (2020).

[31] P.-J. Hsu, L. Rózsa, A. Finco, L. Schmidt, K. Palotás, E. Vedmedenko, L. Udvardi, L. Szunyogh, A. Kubetzka, K. von Bergmann, and R. Wiesendanger, “Inducing skyrmions in ultrathin Fe films by hydrogen exposure,” *Nature Communications* **9**, 1571 (2018).

[32] A. Cao and J. K. Nørskov, “Spin Effects in Chemisorption and Catalysis,” *ACS Catalysis* **13**, 3456–3462 (2023).

[33] J. K. Nørskov, F. Studt, F. Abild-Pedersen, and T. Bligaard, *Fundamental Concepts in Heterogeneous Catalysis* (Wiley, Sept. 2014).

[34] K. Zhang, A. Cao, L. H. Wandall, J. Vernieres, J. Kibsgaard, J. K. Nørskov, and I. Chorkendorff, “Spin-mediated promotion of Co catalysts for ammonia synthesis,” *Science* **383**, 1357–1363 (2024).

[35] Z. W. She, J. Kibsgaard, C. F. Dickens, I. Chorkendorff, J. K. Nørskov, and T. F. Jaramillo, “Combining theory and experiment in electrocatalysis: Insights into materials design,” *Science* **355**, `10.1126/science.aad4998` (2017).

[36] A. Mittasch, *Geschichte der ammoniaksynthese*, German (Verlag Chemie, Weinheim, 1951).

[37] C. Bosch, *The development of the chemical high pressure method*, Nobel Lecture, Nobel Lecture, December 11, 1931, 1932.

[38] L. Pauling, *The nature of the chemical bond and the structure of molecules and crystals*, 3rd ed., The George Fisher Baker Non-Resident Lectureship in Chemistry at Cornell University (Cornell University Press, Ithaca, NY, Jan. 1960).

[39] F. Bozso, G. Ertl, and M. Weiss, “Interaction of nitrogen with iron surfaces: II. Fe(110),” *Journal of Catalysis* **50**, 519–529 (1977).

[40] F. Bozso, G. Ertl, M. Grunze, and M. Weiss, “Interaction of nitrogen with iron surfaces I. Fe(100) and Fe(111),” *Journal of Catalysis* **49**, 18–41 (1977).

[41] G. Ertl, M. Weiss, and S. Lee, “The role of potassium in the catalytic synthesis of ammonia,” *Chemical Physics Letters* **60**, 391–394 (1979).

[42] G. Ertl, “Reactions at surfaces: From atoms to complexity (nobel lecture),” *Angewandte Chemie - International Edition* **47**, 3524–3535 (2008).

[43] G. Ertl, “Surface Science and Catalysis—Studies on the Mechanism of Ammonia Synthesis: The P. H. Emmett Award Address,” *Catalysis Reviews* **21**, 201–223 (1980).

[44] T. N. Rhodin and G. Ertl, eds., *The nature of the surface chemical bond*, Vol. 2, North-Holland Surface Science Series (North-Holland, Amsterdam, 1979).

[45] D. M. Newns, “Self-consistent model of hydrogen chemisorption,” *Physical Review* **178**, 1123–1135 (1969).

[46] P. W. Anderson, “Localized Magnetic States in Metals,” *Physical Review* **124**, 41–53 (1961).

[47] B. Hammer and J. K. Norskov, “Why gold is the noblest of all the metals,” *Nature* **376**, 238–240 (1995).

[48] B. Hammer and J. Nørskov, “Electronic factors determining the reactivity of metal surfaces,” *Surface Science* **343**, 211–220 (1995).

[49] M. Andersen, “Revelations of the d band,” *Nature Catalysis* **6**, 460–461 (2023).

[50] Z.-J. Zhao, S. Liu, S. Zha, D. Cheng, F. Studt, G. Henkelman, and J. Gong, “Theory-guided design of catalytic materials using scaling relationships and reactivity descriptors,” *Nature Reviews Materials* **4**, 792–804 (2019).

[51] V. Pallassana and M. Neurock, “Electronic Factors Governing Ethylene Hydrogenation and Dehydrogenation Activity of Pseudomorphic PdML/Re(0001), PdML/Ru(0001), Pd(111), and PdML/Au(111) Surfaces,” *Journal of Catalysis* **191**, 301–317 (2000).

[52] J. K. Norsko, “Chemisorption on metal surfaces,” *Reports on Progress in Physics* **53**, 1253–1295 (1990).

[53] B. Hammer and J. Nørskov, “Theoretical surface science and catalysis—calculations and concepts,” in *Advances in catalysis*, Vol. 45 (2000), pp. 71–129.

[54] A. Nilsson, L. G. M. Pettersson, and J. K. Nørskov, eds., *Chemical bonding at surfaces and interfaces* (Elsevier, 2008).

[55] J. Kanamori, “Electron Correlation and Ferromagnetism of Transition Metals,” *Progress of Theoretical Physics* **30**, 275–289 (1963).

[56] M. M. Steiner, R. C. Albers, and L. J. Sham, “Quasiparticle properties of Fe, Co, and Ni,” *Physical Review B* **45**, 13272–13284 (1992).

[57] A. Grechnev, I. Di Marco, M. I. Katsnelson, A. I. Lichtenstein, J. Wills, and O. Eriksson, “Theory of bulk and surface quasiparticle spectra for Fe, Co, and Ni,” *Physical Review B* **76**, 035107 (2007).

[58] A. Liebsch, “Effect of self-energy corrections on the valence-band photoemission spectra of Ni,” *Physical Review Letters* **43**, 1431–1434 (1979).

[59] B. Hammer, Y. Morikawa, and J. K. Nørskov, “CO Chemisorption at Metal Surfaces and Overlayers,” *Physical Review Letters* **76**, 2141–2144 (1996).

[60] V. I. Anisimov, J. Zaanen, and O. K. Andersen, “Band theory and Mott insulators: Hubbard U instead of Stoner I,” *Physical Review B* **44**, 943–954 (1991).

[61] M. Cococcioni and S. de Gironcoli, “Linear response approach to the calculation of the effective interaction parameters in the LDA+U method,” *Physical Review B* **71**, 035105 (2005).

[62] G. Kotliar, S. Y. Savrasov, K. Haule, V. S. Oudovenko, O. Parcollet, and C. A. Marianetti, “Electronic structure calculations with dynamical mean-field theory,” *Reviews of Modern Physics* **78**, 865–951 (2006).

[63] P. Puschnig, S. Berkebile, A. J. Fleming, G. Koller, K. Emtsev, T. Seyller, J. D. Riley, C. Ambrosch-Draxl, F. P. Netzer, and M. G. Ramsey, “Reconstruction of Molecular Orbital Densities from Photoemission Data,” *Science* **326**, 702–706 (2009).

[64] P. Puschnig, G. Koller, C. Draxl, and M. G. Ramsey, “The structure of molecular orbitals investigated by angle-resolved photoemission,” in *Small organic molecules on surfaces* (Springer Berlin Heidelberg, 2013), pp. 3–23.

[65] P. Krzyszowska and E. Pacholska-Dudziak, “Porphyrins are nature’s workhorse,” *Nature Chemistry* **17**, 156–156 (2025).

[66] M. Knapp and J. Bridwell-Rabb, “The green pigment of life,” *Nature Chemistry* **14**, 1202–1202 (2022).

[67] R. S. Mulliken, “Spectroscopy, Molecular Orbitals, and Chemical Bonding,” *Science* **157**, 13–24 (1967).

[68] L. Pauling, “THE NATURE OF THE CHEMICAL BOND. APPLICATION OF RESULTS OBTAINED FROM THE QUANTUM MECHANICS AND FROM A THEORY OF PARAMAGNETIC SUSCEPTIBILITY TO THE STRUCTURE OF MOLECULES,” *Journal of the American Chemical Society* **53**, 1367–1400 (1931).

[69] J. Heckötter, D. Janas, R. Schwartz, M. Aßmann, and M. Bayer, “Experimental limitation in extending the exciton series in Cu_2O towards higher principal quantum numbers,” *Physical Review B* **101**, 235207 (2020).

[70] *Organic electronics for a better tomorrow: innovation, accessibility, sustainability, A white paper from the chemical sciences and society summit (cs3)*, White paper, Accessed: 2025-05-22 (Chemical Sciences and Society Summit (CS3), San Francisco, California, United States, Sept. 2012).

[71] S. Braun, W. R. Salaneck, and M. Fahlman, “Energy-Level Alignment at Organic/Metal and Organic/Organic Interfaces,” *Advanced Materials* **21**, 1450–1472 (2009).

[72] E. Goiri, P. Borghetti, A. El-Sayed, J. E. Ortega, and D. G. de Oteyza, “Multi-Component Organic Layers on Metal Substrates,” *Advanced Materials* **28**, 1340–1368 (2016).

[73] A. J. Heeger, S. Kivelson, J. R. Schrieffer, and W. .-. Su, “Solitons in conducting polymers,” *Reviews of Modern Physics* **60**, 781–850 (1988).

[74] J. L. Bredas and G. B. Street, “Polarons, bipolarons, and solitons in conducting polymers,” *Accounts of Chemical Research* **18**, 309–315 (1985).

[75] H. Sato, S. A. Abd. Rahman, Y. Yamada, H. Ishii, and H. Yoshida, “Conduction band structure of high-mobility organic semiconductors and partially dressed polaron formation,” *Nature Materials* **21**, 910–916 (2022).

[76] A. Köhler and H. Bässler, *Electronic Processes in Organic Semiconductors* (Wiley, May 2015).

[77] P. J. Benning, J. L. Martins, J. H. Weaver, L. P. F. Chibante, and R. E. Smalley, “Electronic States of K x C 60 : Insulating, Metallic, and Superconducting Character,” *Science* **252**, 1417–1419 (1991).

[78] G. K. Wertheim, J. E. Rowe, D. N. E. Buchanan, E. E. Chaban, A. F. Hebard, A. R. Kortan, A. V. Makhija, and R. C. Haddon, “Photoemission Spectra and Electronic Properties of K x C 60,” *Science* **252**, 1419–1421 (1991).

[79] M. Mitrano, A. Cantaluppi, D. Nicoletti, S. Kaiser, A. Perucchi, S. Lupi, P. Di Pietro, D. Pontiroli, M. Riccò, S. R. Clark, D. Jaksch, and A. Cavalleri, “Possible light-induced superconductivity in K3C60 at high temperature,” *Nature* **530**, 461–464 (2016).

[80] E. Rowe, B. Yuan, M. Buzzi, G. Jotzu, Y. Zhu, M. Fechner, M. Först, B. Liu, D. Pontiroli, M. Riccò, and A. Cavalleri, “Resonant enhancement of photo-induced superconductivity in K3C60,” *Nature Physics* **19**, 1821–1826 (2023).

[81] F. Bussolotti, S. Kera, and N. Ueno, “Pentacene Becomes Mott–Hubbard Insulator by Potassium Doping,” in *Electronic processes in organic electronics* (Springer Japan, 2015), pp. 69–87.

[82] M. Hollerer, D. Lüftner, P. Hurdax, T. Ules, S. Soubatch, F. S. Tautz, G. Koller, P. Puschnig, M. Sterrer, and M. G. Ramsey, “Charge Transfer and Orbital Level Alignment at Inorganic/Organic Interfaces: The Role of Dielectric Interlayers,” *ACS Nano* **11**, 6252–6260 (2017).

[83] G. Reecht, N. Krane, C. Lotze, and K. J. Franke, “π-Radical Formation by Pyrrolic H Abstraction of Phthalocyanine Molecules on Molybdenum Disulfide,” *ACS Nano* **13**, 7031–7035 (2019).

[84] S. Erker and O. T. Hofmann, “Fractional and Integer Charge Transfer at Semiconductor/Organic Interfaces: The Role of Hybridization and Metallicity,” *The Journal of Physical Chemistry Letters* **10**, 848–854 (2019).

[85] I. Hill, A. Kahn, Z. Soos, and R. Pascal, Jr, “Charge-separation energy in films of π-conjugated organic molecules,” *Chemical Physics Letters* **327**, 181–188 (2000).

[86] J. B. Neaton, M. S. Hybertsen, and S. G. Louie, “Renormalization of Molecular Electronic Levels at Metal-Molecule Interfaces,” *Physical Review Letters* **97**, 216405 (2006).

[87] E. Tsiper, Z. Soos, W. Gao, and A. Kahn, “Electronic polarization at surfaces and thin films of organic molecular crystals: PTCDA,” *Chemical Physics Letters* **360**, 47–52 (2002).

[88] D. Hernangómez-Pérez, J. Schlör, D. A. Egger, L. L. Patera, J. Repp, and F. Evers, “Reorganization energy and polaronic effects of pentacene on NaCl films,” *Physical Review B* **102**, 115419 (2020).

[89] M. Frankerl, L. L. Patera, F. Giselbrecht, T. Frederiksen, J. Repp, and A. Donarini, “Substrate Polarization Alters the Jahn-Teller Effect in a Single Molecule,” *Physical Review Letters* **134**, 176203 (2025).

[90] J. Repp, G. Meyer, S. M. Stojković, A. Gourdon, and C. Joachim, “Molecules on Insulating Films: Scanning-Tunneling Microscopy Imaging of Individual Molecular Orbitals,” *Physical Review Letters* **94**, 026803 (2005).

[91] D. R. Zahn, G. N. Gavrila, and M. Gorgoi, “The transport gap of organic semiconductors studied using the combination of direct and inverse photoemission,” *Chemical Physics* **325**, 99–112 (2006).

[92] B. Stadtmüller, S. Emmerich, D. Jungkenn, N. Haag, M. Rollinger, S. Eich, M. Maniraj, M. Aeschlimann, M. Cinchetti, and S. Mathias, “Strong modification of the transport level alignment in organic materials after optical excitation,” *Nature Communications* **10**, 1470 (2019).

[93] S. R. Forrest, “Excitons and the lifetime of organic semiconductor devices,” *Philosophical Transactions of the Royal Society A: Mathematical, Physical and Engineering Sciences* **373**, 20140320 (2015).

[94] J. Muscat and D. Newns, “Chemisorption on metals,” *Progress in Surface Science* **9**, 1–43 (1978).

[95] P. Lazić, V. Caciuc, N. Atodiresei, M. Callsen, and S. Blügel, "First-principles insights into the electronic and magnetic structure of hybrid organic-metal interfaces," *Journal of Physics: Condensed Matter* **26**, 263001 (2014).

[96] Q. Ge and D. A. King, "The chemisorption and dissociation of ethylene on Pt111 from first principles," *The Journal of Chemical Physics* **110**, 4699–4702 (1999).

[97] N. D. Lang and W. Kohn, "Theory of metal surfaces: charge density and surface energy," *Physical Review B* **1**, 4555–4568 (1970).

[98] N. D. Lang and W. Kohn, "Theory of metal surfaces: induced surface charge and image potential," *Physical Review B* **7**, 3541–3550 (1973).

[99] N. D. Lang, "The density-functional formalism and the electronic structure of metal surfaces," in *Solid state physics* (Elsevier, 1974), pp. 225–300.

[100] A. W. Dweydari and C. H. B. Mee, "Work function measurements on (100) and (110) surfaces of silver," *Physica Status Solidi (a)* **27**, 223–230 (1975).

[101] M. T. Greiner, M. G. Helander, W.-M. Tang, Z.-B. Wang, J. Qiu, and Z.-H. Lu, "Universal energy-level alignment of molecules on metal oxides," *Nature Materials* **11**, 76–81 (2012).

[102] S. Rangan, C. Ruggieri, R. Bartynski, J. I. Martínez, F. Flores, and J. Ortega, "Adsorption Geometry and Energy Level Alignment at the PTCDA/TiO 2 (110) Interface," *The Journal of Physical Chemistry B* **122**, 534–542 (2018).

[103] S. Rangan, C. Ruggieri, R. Bartynski, J. I. Martínez, F. Flores, and J. Ortega, "Densely Packed ZnTPPs Monolayer on the Rutile TiO 2 (110)-(1 × 1) Surface: Adsorption Behavior and Energy Level Alignment," *The Journal of Physical Chemistry C* **120**, 4430–4437 (2016).

[104] J. I. Martínez, F. Flores, J. Ortega, S. Rangan, C. Ruggieri, and R. Bartynski, "Chemical Interaction, Space-Charge Layer, and Molecule Charging Energy for a TiO 2 /TCNQ Interface," *The Journal of Physical Chemistry C* **119**, 22086–22091 (2015).

[105] M. Gruenewald, L. K. Schirra, P. Winget, M. Kozlik, P. F. Ndione, A. K. Sigdel, J. J. Berry, R. Forker, J.-L. Brédas, T. Fritz, and O. L. A. Monti, "Integer Charge Transfer and Hybridization at an Organic Semiconductor/Conductive Oxide Interface," *The Journal of Physical Chemistry C* **119**, 4865–4873 (2015).

[106] Y. Xu, O. T. Hofmann, R. Schlesinger, S. Winkler, J. Frisch, J. Niederhausen, A. Vollmer, S. Blumstengel, F. Henneberger, N. Koch, P. Rinke, and M. Scheffler, "Space-Charge Transfer in Hybrid Inorganic-Organic Systems," *Physical Review Letters* **111**, 226802 (2013).

[107] O. T. Hofmann and P. Rinke, "Band Bending Engineering at Organic/Inorganic Interfaces Using Organic Self-Assembled Monolayers," *Advanced Electronic Materials* **3**, `10.1002/aelm.201600373` (2017).

[108] P. Hurdax, M. Hollerer, P. Puschnig, D. Lüftner, L. Egger, M. G. Ramsey, and M. Sterrer, "Controlling the Charge Transfer across Thin Dielectric Interlayers," *Advanced Materials Interfaces* **7**, 2000592 (2020).

[109] P. Hurdax, M. Hollerer, L. Egger, G. Koller, X. Yang, A. Haags, S. Soubatch, F. S. Tautz, M. Richter, A. Gottwald, P. Puschnig, M. Sterrer, and M. G. Ramsey, "Controlling the electronic and physical coupling on dielectric thin films," *Beilstein Journal of Nanotechnology* **11**, 1492–1503 (2020).

[110] H. Vázquez, Y. J. Dappe, J. Ortega, and F. Flores, “Energy level alignment at metal/organic semiconductor interfaces: “Pillow” effect, induced density of interface states, and charge neutrality level,” *The Journal of Chemical Physics* **126**, 144703 (2007).

[111] F. Flores, J. Ortega, and H. Vázquez, “Modelling energy level alignment at organic interfaces and density functional theory,” *Physical Chemistry Chemical Physics* **11**, 8658 (2009).

[112] H. Vázquez, F. Flores, R. Oszwaldowski, J. Ortega, R. Pérez, and A. Kahn, “Barrier formation at metal–organic interfaces: dipole formation and the charge neutrality level,” *Applied Surface Science* **234**, 107–112 (2004).

[113] R. Otero, A. Vázquez de Parga, and J. Gallego, “Electronic, structural and chemical effects of charge-transfer at organic/inorganic interfaces,” *Surface Science Reports* **72**, 105–145 (2017).

[114] G. Zamborlini, D. Lüftner, Z. Feng, B. Kollmann, P. Puschnig, C. Dri, M. Panighel, G. Di Santo, A. Goldoni, G. Comelli, M. Jugovac, V. Feyer, and C. M. Schneider, “Multi-orbital charge transfer at highly oriented organic/metal interfaces,” *Nature Communications* **8**, 335 (2017).

[115] X. Zhang, W. He, A. Zhao, H. Li, L. Chen, W. W. Pai, J. Hou, M. M. T. Loy, J. Yang, and X. Xiao, “Geometric and electronic structure of a C_{60} monolayer on Ag(100),” *Physical Review B* **75**, 235444 (2007).

[116] G. Xu, X.-Q. Shi, R. Q. Zhang, W. W. Pai, H. T. Jeng, and M. A. Van Hove, “Detailed low-energy electron diffraction analysis of the (4×4) surface structure of C_{60} on Cu(111): Seven-atom-vacancy reconstruction,” *Physical Review B* **86**, 075419 (2012).

[117] Z.-H. Yang, R. Pang, and X.-Q. Shi, “Engineering Magnetic Hybridization at Organic–Ferromagnetic Interfaces by C 60 -Adsorption-Induced Fe(001) Surface Reconstruction,” *The Journal of Physical Chemistry C* **119**, 10532–10537 (2015).

[118] X. Yang, M. Jugovac, G. Zamborlini, V. Feyer, G. Koller, P. Puschnig, S. Soubatch, M. G. Ramsey, and F. S. Tautz, “Momentum-selective orbital hybridisation,” *Nature Communications* **13**, 5148 (2022).

[119] S. Berkebile, T. Ules, P. Puschnig, L. Romaner, G. Koller, A. J. Fleming, K. Emtsev, T. Seyller, C. Ambrosch-Draxl, F. P. Netzer, and M. G. Ramsey, “A momentum space view of the surface chemical bond,” *Physical Chemistry Chemical Physics* **13**, 3604 (2011).

[120] A. Droghetti, S. Steil, N. Großmann, N. Haag, H. Zhang, M. Willis, W. P. Gillin, A. J. Drew, M. Aeschlimann, S. Sanvito, and M. Cinchetti, “Electronic and magnetic properties of the interface between metal-quinoline molecules and cobalt,” *Physical Review B - Condensed Matter and Materials Physics* **89**, 094412 (2014).

[121] J. P. Perdew and M. Levy, “Physical Content of the Exact Kohn-Sham Orbital Energies: Band Gaps and Derivative Discontinuities,” *Physical Review Letters* **51**, 1884–1887 (1983).

[122] P. Mori-Sánchez and A. J. Cohen, “The derivative discontinuity of the exchange–correlation functional,” *Phys. Chem. Chem. Phys.* **16**, 14378–14387 (2014).

[123] A. J. Cohen, P. Mori-Sánchez, and W. Yang, “Insights into Current Limitations of Density Functional Theory,” *Science* **321**, 792–794 (2008).

[124] A. Droghetti, M. M. Radonjić, A. Halder, I. Rungger, and L. Chioncel, "DFT+Σ_2 method for electron correlation effects at transition metal surfaces," *Physical Review B* **105**, 115129 (2022).

[125] T. B. Grimley, "The indirect interaction between atoms or molecules adsorbed on metals," *Proceedings of the Physical Society* **90**, 751–764 (1967).

[126] A. Kokalj, "Molecular modeling of organic corrosion inhibitors: Calculations, pitfalls, and conceptualization of molecule–surface bonding," *Corrosion Science* **193**, 109650 (2021).

[127] E. Kawabe, H. Yamane, R. Sumii, K. Koizumi, Y. Ouchi, K. Seki, and K. Kanai, "A role of metal d-band in the interfacial electronic structure at organic/metal interface: PTCDA on Au, Ag and Cu," *Organic Electronics* **9**, 783–789 (2008).

[128] G. Moore, "Cramming More Components Onto Integrated Circuits," *Proceedings of the IEEE* **86**, 82–85 (1998).

[129] M. M. Waldrop, "The chips are down for Moore's law," *Nature* **530**, 144–147 (2016).

[130] M. Faraday, "X. The Bakerian Lecture. —Experimental relations of gold (and other metals) to light," *Philosophical Transactions of the Royal Society of London* **147**, 145–181 (1857).

[131] R. J. Martín-Palma and A. Lakhtakia, "Vapor-Deposition Techniques," in *Engineered biomimicry* (Elsevier, 2013), pp. 383–398.

[132] K. Sree Harsha, *Principles of Vapor Deposition of Thin Films* (Elsevier, 2006).

[133] A. K. Eessaa and A. El-Shamy, "Review on fabrication, characterization, and applications of porous anodic aluminum oxide films with tunable pore sizes for emerging technologies," *Microelectronic Engineering* **279**, 112061 (2023).

[134] P. Auger, "Sur l'effet photoélectrique composé," *Journal de Physique et le Radium* **6**, 205–208 (1925).

[135] L. Meitner, "Über die β-Strahl-Spektra und ihren Zusammenhang mit der γ-Strahlung," *Zeitschrift für Physik* **11**, 35–54 (1922).

[136] S. Hofmann, *Auger- and X-Ray Photoelectron Spectroscopy in Materials Science*, Vol. 49, Springer Series in Surface Sciences (Springer Berlin Heidelberg, Berlin, Heidelberg, 2013).

[137] M. Klaua and G. Oertel, "Auger-Elektronenspektroskopie," in *Handbuch festkörperanalyse mit elektronen, ionen und röntgenstrahlen* (Vieweg+Teubner Verlag, Wiesbaden, 1979), pp. 295–314.

[138] T. Fauster, L. Hammer, K. Heinz, and M. A. Schneider, *Oberflächenphysik*, 2nd ed. (De Gruyter, Oct. 2019).

[139] K. Robbie, S. T. Jemander, N. Lin, C. Hallin, R. Erlandsson, G. V. Hansson, and L. D. Madsen, "Formation of Ni-graphite intercalation compounds on SiC," *Physical Review B* **64**, 155401 (2001).

[140] V. Le Roux, G. Machicoane, S. Kerdiles, R. Laffitte, N. Béchu, L. Vallier, G. Borsoni, M. L. Korwin-Pawlowski, P. Roman, C.-T. Wu, and J. Ruzyllo, "Etching of Silicon Native Oxide Using Ultraslow Multicharged Ar^{q+} Ions," *Journal of The Electrochemical Society* **151**, G76 (2004).

[141] M. A. Van Hove, W. H. Weinberg, and C.-M. Chan, *Low-Energy Electron Diffraction*, Vol. 6, Springer Series in Surface Sciences (Springer Berlin Heidelberg, Berlin, Heidelberg, 1986).

[142] G. Binnig and H. Rohrer, “Scanning tunneling microscopy—from birth to adolescence,” *Reviews of Modern Physics* **59**, 615–625 (1987).

[143] K. Bian, C. Gerber, A. J. Heinrich, D. J. Müller, S. Scheuring, and Y. Jiang, “Scanning probe microscopy,” *Nature Reviews Methods Primers* **1**, 36 (2021).

[144] P. Willke, K. Yang, Y. Bae, A. J. Heinrich, and C. P. Lutz, “Magnetic resonance imaging of single atoms on a surface,” *Nature Physics* **15**, 1005–1010 (2019).

[145] L. L. Patera, F. Queck, P. Scheuerer, and J. Repp, “Mapping orbital changes upon electron transfer with tunnelling microscopy on insulators,” *Nature* **566**, 245–248 (2019).

[146] S. Fatayer, F. Albrecht, Y. Zhang, D. Urbonas, D. Peña, N. Moll, and L. Gross, “Molecular structure elucidation with charge-state control,” *Science* **365**, 142–145 (2019).

[147] A. Köbke, F. Gutzeit, F. Röhricht, A. Schlimm, J. Grunwald, F. Tuczek, M. Studniarek, D. Longo, F. Choueikani, E. Otero, P. Ohresser, S. Rohlf, S. Johannsen, F. Diekmann, K. Rossnagel, A. Weismann, T. Jasper-Toennies, C. Näther, R. Herges, R. Berndt, and M. Gruber, “Reversible coordination-induced spin-state switching in complexes on metal surfaces,” *Nature Nanotechnology* **15**, 18–21 (2020).

[148] F. Albrecht, S. Fatayer, I. Pozo, I. Tavernelli, J. Repp, D. Peña, and L. Gross, “Selectivity in single-molecule reactions by tip-induced redox chemistry,” *Science* **377**, 298–301 (2022).

[149] S. Baumann, W. Paul, T. Choi, C. P. Lutz, A. Ardavan, and A. J. Heinrich, “Electron paramagnetic resonance of individual atoms on a surface,” *Science* **350**, 417–420 (2015).

[150] T. L. Cocker, D. Peller, P. Yu, J. Repp, and R. Huber, “Tracking the ultrafast motion of a single molecule by femtosecond orbital imaging,” *Nature* **539**, 263–267 (2016).

[151] T. Siday, J. Hayes, F. Schiegl, F. Sandner, P. Menden, V. Bergbauer, M. Zizlsperger, S. Nerreter, S. Lingl, J. Repp, J. Wilhelm, M. A. Huber, Y. A. Gerasimenko, and R. Huber, “All-optical subcycle microscopy on atomic length scales,” *Nature* **629**, 329–334 (2024).

[152] T. M. Ajayi, N. Shirato, T. Rojas, S. Wieghold, X. Cheng, K. Z. Latt, D. J. Trainer, N. K. Dandu, Y. Li, S. Premarathna, S. Sarkar, D. Rosenmann, Y. Liu, N. Kyritsakas, S. Wang, E. Masson, V. Rose, X. Li, A. T. Ngo, and S.-W. Hla, “Characterization of just one atom using synchrotron X-rays,” *Nature* **618**, 69–73 (2023).

[153] C. J. Chen, *Introduction to Scanning Tunneling Microscopy* (Oxford University PressOxford, Mar. 2021).

[154] P. K. Hansma and J. Tersoff, “Scanning tunneling microscopy,” *Journal of Applied Physics* **61**, R1–R24 (1987).

[155] J. Tersoff and D. R. Hamann, “Theory of the scanning tunneling microscope,” *Physical Review B* **31**, 805–813 (1985).

[156] A. Selloni, P. Carnevali, E. Tosatti, and C. D. Chen, “Voltage-dependent scanning-tunneling microscopy of a crystal surface: Graphite,” *Physical Review B* **31**, 2602–2605 (1985).

[157] J. A. Stroscio, R. M. Feenstra, and A. P. Fein, “Electronic Structure of the Si(111)2 × 1 Surface by Scanning-Tunneling Microscopy,” *Physical Review Letters* **57**, 2579–2582 (1986).

[158]V. A. Ukraintsev, “Data evaluation technique for electron-tunneling spectroscopy,” *Physical Review B* **53**, 11176–11185 (1996).

[159]F. Donati, S. Piccoli, C. E. Bottani, and M. Passoni, “Three-dimensional approach to scanning tunneling spectroscopy and application to Shockley states,” *New Journal of Physics* **13**, 053058 (2011).

[160]R. S. Becker, J. A. Golovchenko, D. R. Hamann, and B. S. Swartzentruber, “Real-Space Observation of Surface States on Si(111) 7×7 with the Tunneling Microscope,” *Physical Review Letters* **55**, 2032–2034 (1985).

[161]R. J. Hamers, R. M. Tromp, and J. E. Demuth, “Surface Electronic Structure of Si (111)-(7×7) Resolved in Real Space,” *Physical Review Letters* **56**, 1972–1975 (1986).

[162]W.-H. Soe, C. Manzano, A. De Sarkar, N. Chandrasekhar, and C. Joachim, “Direct Observation of Molecular Orbitals of Pentacene Physisorbed on Au(111) by Scanning Tunneling Microscope,” *Physical Review Letters* **102**, 176102 (2009).

[163]S. Heinze, S. Blügel, R. Pascal, M. Bode, and R. Wiesendanger, “Prediction of bias-voltage-dependent corrugation reversal for STM images of bcc (110) surfaces: W(110), Ta(110), and Fe(110),” *Physical Review B* **58**, 16432–16445 (1998).

[164]F. Donati, P. Sessi, S. Achilli, A. Li Bassi, M. Passoni, C. S. Casari, C. E. Bottani, A. Brambilla, A. Picone, M. Finazzi, L. Duò, M. I. Trioni, and F. Ciccacci, “Scanning tunneling spectroscopy of the Fe(001)-p(1×1)O surface,” *Physical Review B* **79**, 195430 (2009).

[165]N. Krane, C. Lotze, and K. J. Franke, “Moiré structure of MoS2 on Au(111): Local structural and electronic properties,” *Surface Science* **678**, 136–142 (2018).

[166]Y. Nomura and R. Akashi, “Density functional theory,” in *Encyclopedia of condensed matter physics* (Elsevier, 2024), pp. 867–878.

[167]W. Kohn, “Nobel Lecture: Electronic structure of matter—wave functions and density functionals,” *Reviews of Modern Physics* **71**, 1253–1266 (1999).

[168]P. Hohenberg and W. Kohn, “Inhomogeneous Electron Gas,” *Physical Review* **136**, B864–B871 (1964).

[169]D. S. Sholl and J. A. Steckel, *Density Functional Theory* (Wiley, Mar. 2009).

[170]W. Kohn and L. J. Sham, “Self-Consistent Equations Including Exchange and Correlation Effects,” *Physical Review* **140**, A1133–A1138 (1965).

[171]R. O. Jones, “Density functional theory: Its origins, rise to prominence, and future,” *Reviews of Modern Physics* **87**, 897–923 (2015).

[172]P. J. Stephens, F. J. Devlin, C. F. Chabalowski, and M. J. Frisch, “Ab Initio Calculation of Vibrational Absorption and Circular Dichroism Spectra Using Density Functional Force Fields,” *The Journal of Physical Chemistry* **98**, 11623–11627 (1994).

[173]A. D. Becke, “Density-functional thermochemistry. III. The role of exact exchange,” *The Journal of Chemical Physics* **98**, 5648–5652 (1993).

[174]A. I. Lichtenstein and M. I. Katsnelson, “Ab initio calculations of quasiparticle band structure in correlated systems: LDA++ approach,” *Physical Review B* **57**, 6884–6895 (1998).

[175] D. Nabok, S. Blügel, and C. Friedrich, "Electron–plasmon and electron–magnon scattering in ferromagnets from first principles by combining GW and GT self-energies," *npj Computational Materials* **7**, 178 (2021).

[176] H. Hertz, "Ueber einen Einfluss des ultravioletten Lichtes auf die electrische Entladung," *Annalen der Physik* **267**, 983–1000 (1887).

[177] W. Hallwachs, "Ueber die Electrisirung von Metallplatten durch Bestrahlung mit electrischem Licht," *Annalen der Physik* **270**, 731–734 (1888).

[178] P. Lenard, "Ueber die lichtelektrische Wirkung," *Annalen der Physik* **313**, 149–198 (1902).

[179] A. Einstein, "Über einen die Erzeugung und Verwandlung des Lichtes betreffenden heuristischen Gesichtspunkt," *Annalen der Physik* **322**, 132–148 (1905).

[180] E. Schrödinger, "An Undulatory Theory of the Mechanics of Atoms and Molecules," *Physical Review* **28**, 1049–1070 (1926).

[181] A. Goldmann, ed., *Magnetic transition metals* (Springer-Verlag, 1999).

[182] K. Siegbahn, "Electron Spectroscopy for Atoms, Molecules, and Condensed Matter," *Science* **217**, 111–121 (1982).

[183] K. Oura, V. Lifshits, A. Saranin, A. Zotov, and M. Katayama, *Surface science: an introduction*, Advanced Texts in Physics (Springer Berlin Heidelberg, 2003).

[184] S. Hüfner, *Photoelectron Spectroscopy*, Advanced Texts in Physics (Springer Berlin Heidelberg, Berlin, Heidelberg, 2003).

[185] G. Wan, A. Croot, N. A. Fox, and M. Cattelan, "Empty-State Band Mapping Using Momentum-Resolved Secondary Electron Emission," *Advanced Functional Materials* **31**, 2007319 (2021).

[186] I. Cojocariu, S. Carlotto, G. Zamborlini, M. Jugovac, L. Schio, L. Floreano, M. Casarin, V. Feyer, and C. M. Schneider, "Reversible redox reactions in metal-supported porphyrin: The role of spin and oxidation state," *Journal of Materials Chemistry C* **9**, 12559–12565 (2021).

[187] C. J. Nelin, F. Uhl, V. Staemmler, P. S. Bagus, Y. Fujimori, M. Sterrer, H. Kuhlenbeck, and H.-J. Freund, "Surface core-level binding energy shifts for MgO(100)," *Phys. Chem. Chem. Phys.* **16**, 21953–21956 (2014).

[188] W. Eberhardt and F. J. Himpsel, "Dipole selection rules for optical transitions in the fcc and bcc lattices," *Physical Review B* **21**, 5572–5576 (1980).

[189] S. Moser, "An experimentalist's guide to the matrix element in angle resolved photoemission," *Journal of Electron Spectroscopy and Related Phenomena* **214**, 29–52 (2017).

[190] D. M. Janas, A. Droghetti, S. Ponzoni, I. Cojocariu, M. Jugovac, V. Feyer, M. M. Radonjić, I. Rungger, L. Chioncel, G. Zamborlini, and M. Cinchetti, "Enhancing Electron Correlation at a 3d Ferromagnetic Surface," *Advanced Materials* **35**, 2205698 (2023).

[191] M. Helander, M. Greiner, Z. Wang, and Z. Lu, "Pitfalls in measuring work function using photoelectron spectroscopy," *Applied Surface Science* **256**, 2602–2605 (2010).

[192] M. Hentschel, R. Kienberger, C. Spielmann, G. A. Reider, N. Milosevic, T. Brabec, P. Corkum, U. Heinzmann, M. Drescher, and F. Krausz, "Attosecond metrology," *Nature* **414**, 509–513 (2001).

[193] R. Kienberger, E. Goulielmakis, M. Uiberacker, A. Baltuska, V. Yakovlev, F. Bammer, A. Scrinzi, T. Westerwalbesloh, U. Kleineberg, U. Heinzmann, M. Drescher, and F. Krausz, “Atomic transient recorder,” *Nature* **427**, 817–821 (2004).

[194] J. E. Nitschke, L. Sternemann, M. Gutnikov, K. Schiller, E. Coronado, A. Omar, G. Zamborlini, C. Saraceno, M. Stupar, A. M. Ruiz, D. L. Esteras, J. J. Baldoví, F. Anders, and M. Cinchetti, “Tracing the ultrafast buildup and decay of d-d transitions in FePS3,” *Newton* **1**, 100019 (2025).

[195] K. J. Schiller, L. Sternemann, M. Stupar, A. Omar, M. Hoffmann, J. E. Nitschke, V. Mischke, D. M. Janas, S. Ponzoni, G. Zamborlini, C. J. Saraceno, and M. Cinchetti, “Time-resolved momentum microscopy with fs-XUV photons at high repetition rates with flexible energy and time resolution,” *Scientific Reports* **15**, 3611 (2025).

[196] S. Ponzoni, F. Paßlack, M. Stupar, D. M. Janas, G. Zamborlini, and M. Cinchetti, “Dirac Bands in the Topological Insulator Bi 2 Se 3 Mapped by Time-Resolved Momentum Microscopy,” *Advanced Physics Research* **2**, 2200016 (2023).

[197] J. Madéo, M. K. L. Man, C. Sahoo, M. Campbell, V. Pareek, E. L. Wong, A. Al-Mahboob, N. S. Chan, A. Karmakar, B. M. K. Mariserla, X. Li, T. F. Heinz, T. Cao, and K. M. Dani, “Directly visualizing the momentum-forbidden dark excitons and their dynamics in atomically thin semiconductors,” *Science* **370**, 1199–1204 (2020).

[198] D. Schmitt, J. P. Bange, W. Bennecke, A. AlMutairi, G. Meneghini, K. Watanabe, T. Taniguchi, D. Steil, D. R. Luke, R. T. Weitz, S. Steil, G. S. M. Jansen, S. Brem, E. Malic, S. Hofmann, M. Reutzel, and S. Mathias, “Formation of moiré interlayer excitons in space and time,” *Nature* **608**, 499–503 (2022).

[199] F. Boschini, M. Zonno, and A. Damascelli, “Time-resolved ARPES studies of quantum materials,” *Reviews of Modern Physics* **96**, 015003 (2024).

[200] C. N. Berglund and W. E. Spicer, “Photoemission studies of copper and silver: theory,” *Physical Review* **136**, A1030–A1044 (1964).

[201] C. N. Berglund and W. E. Spicer, “Photoemission studies of copper and silver: experiment,” *Physical Review* **136**, A1044–A1064 (1964).

[202] P. J. Feibelman and D. E. Eastman, “Photoemission spectroscopy—Correspondence between quantum theory and experimental phenomenology,” *Physical Review B* **10**, 4932–4947 (1974).

[203] J. Hermanson, “Final-state symmetry and polarization effects in angle-resolved photoemission spectroscopy,” *Solid State Communications* **22**, 9–11 (1977).

[204] M. P. Seah and W. A. Dench, “Quantitative electron spectroscopy of surfaces: A standard data base for electron inelastic mean free paths in solids,” *Surface and Interface Analysis* **1**, 2–11 (1979).

[205] E. T. Jensen, “Surface Physics,” in *Springer handbook of atomic, molecular, and optical physics* (2023), pp. 1349–1358.

[206] W. Schattke and M. A. Van Hove, eds., *Solid-State Photoemission and Related Methods* (Wiley, Oct. 2003).

[207] S. Suga, A. Sekiyama, and C. Tusche, *Photoelectron Spectroscopy*, Vol. 72, Springer Series in Surface Sciences (Springer International Publishing, Cham, 2021).

[208] A. Damascelli, Z. Hussain, and Z.-X. Shen, “Angle-resolved photoemission studies of the cuprate superconductors,” *Reviews of Modern Physics* **75**, 473–541 (2003).

[209] J. A. Sobota, Y. He, and Z.-X. Shen, “Angle-resolved photoemission studies of quantum materials,” *Reviews of Modern Physics* **93**, 025006 (2021).

[210] J. He, *Angle-resolved photoemission spectroscopy on high-temperature superconductors* (Springer Berlin Heidelberg, 2016).

[211] D. Brandstetter, X. Yang, D. Lüftner, F. S. Tautz, and P. Puschnig, “kMap.py: A Python program for simulation and data analysis in photoemission tomography,” *Computer Physics Communications* **263**, 107905 (2021).

[212] A. Haags, X. Yang, L. Egger, D. Brandstetter, H. Kirschner, F. C. Bocquet, G. Koller, A. Gottwald, M. Richter, J. M. Gottfried, M. G. Ramsey, P. Puschnig, S. Soubatch, and F. S. Tautz, “Momentum space imaging of σ orbitals for chemical analysis,” *Science Advances* **8**, eabn0819 (2022).

[213] A. Haags, D. Brandstetter, X. Yang, L. Egger, H. Kirschner, A. Gottwald, M. Richter, G. Koller, F. C. Bocquet, C. Wagner, M. G. Ramsey, S. Soubatch, P. Puschnig, and F. S. Tautz, “Tomographic identification of all molecular orbitals in a wide binding-energy range,” *Physical Review B* **111**, 165402 (2025).

[214] D. M. Janas, A. Windischbacher, M. S. Arndt, M. Gutnikov, L. Sternemann, D. Gutnikov, T. Willershausen, J. E. Nitschke, K. Schiller, D. Baranowski, V. Feyer, I. Cojocariu, K. Dave, P. Puschnig, M. Stupar, S. Ponzoni, M. Cinchetti, and G. Zamborlini, “Metalloporphyrins on oxygen-passivated iron: Conformation and order beyond the first layer,” *Inorganica Chimica Acta* **557**, 121705 (2023).

[215] R. Wallauer, M. Raths, K. Stallberg, L. Münster, D. Brandstetter, X. Yang, J. Güdde, P. Puschnig, S. Soubatch, C. Kumpf, F. C. Bocquet, F. S. Tautz, and U. Höfer, “Tracing orbital images on ultrafast time scales,” *Science* **371**, 1056–1059 (2021).

[216] A. Adamkiewicz, M. Raths, M. Stettner, M. Theilen, L. Münster, S. Wenzel, M. Hutter, S. Soubatch, C. Kumpf, F. C. Bocquet, R. Wallauer, F. S. Tautz, and U. Höfer, “Coherent and Incoherent Excitation Pathways in Time-Resolved Photoemission Orbital Tomography of CuPc/Cu(001)-2O,” *The Journal of Physical Chemistry C* **127**, 20411–20418 (2023).

[217] W. Bennecke, A. Windischbacher, D. Schmitt, J. P. Bange, R. Hemm, C. S. Kern, G. D’Avino, X. Blase, D. Steil, S. Steil, M. Aeschlimann, B. Stadtmüller, M. Reutzel, P. Puschnig, G. S. M. Jansen, and S. Mathias, “Disentangling the multiorbital contributions of excitons by photoemission exciton tomography,” *Nature Communications* **15**, 1804 (2024).

[218] A. Neef, S. Beaulieu, S. Hammer, S. Dong, J. Maklar, T. Pincelli, R. P. Xian, M. Wolf, L. Rettig, J. Pflaum, and R. Ernstorfer, “Orbital-resolved observation of singlet fission,” *Nature* **616**, 275–279 (2023).

[219] P. Hurdax, C. S. Kern, T. G. Boné, A. Haags, M. Hollerer, L. Egger, X. Yang, H. Kirschner, A. Gottwald, M. Richter, F. C. Bocquet, S. Soubatch, G. Koller, F. S. Tautz, M. Sterrer, P. Puschnig, and M. G. Ramsey, “Large Distortion of Fused Aromatics on Dielectric Interlayers Quantified by Photoemission Orbital Tomography,” *ACS Nano* **16**, 17435–17443 (2022).

[220] E. Brüche, “Elektronenmikroskopische Abbildung mit lichtelektrischen Elektronen,” *Zeitschrift für Physik* **86**, 448–450 (1933).

[221] O. Hayes Griffith and W. Engel, “Historical perspective and current trends in emission microscopy, mirror electron microscopy and low-energy electron microscopy,” *Ultramicroscopy* **36**, 1–28 (1991).

[222] A. Sala, “Imaging at the Mesoscale (LEEM, PEEM),” in *Springer handbook of surface science* (2020), pp. 387–425.

[223] C. Tusche, A. Krasyuk, and J. Kirschner, “Spin resolved bandstructure imaging with a high resolution momentum microscope,” *Ultramicroscopy* **159**, 520–529 (2015).

[224] A. Locatelli and T. O. Menteş, “Chemical and Magnetic Imaging with X-Ray Photoemission Electron Microscopy,” in *Synchrotron radiation* (Springer Berlin Heidelberg, Berlin, Heidelberg, 2015), pp. 571–591.

[225] M. Kim, M. Bertram, M. Pollmann, A. von Oertzen, A. S. Mikhailov, H. H. Rotermund, and G. Ertl, “Controlling Chemical Turbulence by Global Delayed Feedback: Pattern Formation in Catalytic CO Oxidation on Pt(110),” *Science* **292**, 1357–1360 (2001).

[226] J. Wolff, A. G. Papathanasiou, I. G. Kevrekidis, H. H. Rotermund, and G. Ertl, “Spatiotemporal Addressing of Surface Activity,” *Science* **294**, 134–137 (2001).

[227] M. Bär, N. Gottschalk, M. Eiswirth, and G. Ertl, “Spiral waves in a surface reaction: Model calculations,” *The Journal of Chemical Physics* **100**, 1202–1214 (1994).

[228] K. Medjanik, O. Fedchenko, S. Chernov, D. Kutnyakhov, M. Ellguth, A. Oelsner, B. Schönhense, T. R. F. Peixoto, P. Lutz, C.-H. Min, F. Reinert, S. Däster, Y. Acremann, J. Viefhaus, W. Wurth, H. J. Elmers, and G. Schönhense, “Direct 3D mapping of the Fermi surface and Fermi velocity,” *Nature Materials* **16**, 615–621 (2017).

[229] M. Kotsugi, W. Kuch, F. Offi, L. I. Chelaru, and J. Kirschner, “Microspectroscopic two-dimensional Fermi surface mapping using a photoelectron emission microscope,” *Review of Scientific Instruments* **74**, 2754–2758 (2003).

[230] G. Zamborlini, M. Jugovac, I. Cojocariu, D. Baranowski, S. Mearini, Y. Y. Grisan Qiu, V. Feyer, and C. M. Schneider, “Exploring Spin- and Momentum-Resolved Phenomena at the NanoESCA Beamline of Elettra Synchrotron,” *Synchrotron Radiation News* **37**, 24–29 (2024).

[231] M. Escher, N. Weber, M. Merkel, C. Ziethen, P. Bernhard, G. Schönhense, S. Schmidt, F. Forster, F. Reinert, B. Krömker, and D. Funnemann, “Nanoelectron spectroscopy for chemical analysis: a novel energy filter for imaging x-ray photoemission spectroscopy,” *Journal of Physics: Condensed Matter* **17**, S1329–S1338 (2005).

[232] F. Matsui, S. Makita, H. Matsuda, T. Yano, E. Nakamura, K. Tanaka, S. Suga, and S. Kera, “Photoelectron Momentum Microscope at BL6U of UVSOR-III synchrotron,” *Japanese Journal of Applied Physics* **59**, 067001 (2020).

[233] C. Tusche, Y.-J. Chen, C. M. Schneider, and J. Kirschner, “Imaging properties of hemispherical electrostatic energy analyzers for high resolution momentum microscopy,” *Ultramicroscopy* **206**, 112815 (2019).

[234] M. Patt, “Bulk and surface sensitive energy-filtered photoemission microscopy using synchrotron radiation for the study of resistive switching memories,” PhD thesis (Universität Duisburg-Essen, 2016).

[235] D. Pierce, R. Celotta, M. Kelley, and J. Unguris, "Electron spin polarization analyzers for use with synchrotron radiation," *Nuclear Instruments and Methods in Physics Research Section A: Accelerators, Spectrometers, Detectors and Associated Equipment* **266**, 550–559 (1988).

[236] D. Yu, C. Math, M. Meier, M. Escher, G. Rangelov, and M. Donath, "Characterisation and application of a SPLEED-based spin polarisation analyser," *Surface Science* **601**, 5803–5808 (2007).

[237] A. Winkelmann, D. Hartung, H. Engelhard, C.-T. Chiang, and J. Kirschner, "High efficiency electron spin polarization analyzer based on exchange scattering at Fe/W(001)," *Review of Scientific Instruments* **79**, 083303 (2008).

[238] M. Kolbe, P. Lushchyk, B. Petereit, H. J. Elmers, G. Schönhense, A. Oelsner, C. Tusche, and J. Kirschner, "Highly Efficient Multichannel Spin-Polarization Detection," *Physical Review Letters* **107**, 207601 (2011).

[239] J. Kirschner and R. Feder, "Spin Polarization in Double Diffraction of Low-Energy Electrons from W(001): Experiment and Theory," *Physical Review Letters* **42**, 1008–1011 (1979).

[240] C. Tusche, M. Ellguth, A. A. Ünal, C.-T. Chiang, A. Winkelmann, A. Krasyuk, M. Hahn, G. Schönhense, and J. Kirschner, "Spin resolved photoelectron microscopy using a two-dimensional spin-polarizing electron mirror," *Applied Physics Letters* **99**, 032505 (2011).

[241] C. Tusche, M. Ellguth, A. Krasyuk, A. Winkelmann, D. Kutnyakhov, P. Lushchyk, K. Medjanik, G. Schönhense, and J. Kirschner, "Quantitative spin polarization analysis in photoelectron emission microscopy with an imaging spin filter," *Ultramicroscopy* **130**, 70–76 (2013).

[242] M. Escher, N. Weber, T.-J. Kühn, and M. Patt, "2D imaging spin-filter for NanoESCA based on Au/Ir(001) or Fe(001)-p(1×1)O," *Ultramicroscopy* **253**, 113814 (2023).

[243] E. C. Stoner, "Collective electron ferronmagnetism," *Proceedings of the Royal Society of London. Series A. Mathematical and Physical Sciences* **165**, 372–414 (1938).

[244] J. Stöhr and H. Siegmann, *Magnetism: from fundamentals to nanoscale dynamics*, Springer Series in Solid-State Sciences (Springer Berlin Heidelberg, 2016).

[245] S. Bhattacharjee, U. V. Waghmare, and S.-C. Lee, "An improved d-band model of the catalytic activity of magnetic transition metal surfaces," *Scientific Reports* **6**, 35916 (2016).

[246] R. G. Parr and Y. Weitao, *Density-functional theory of atoms and molecules* (Oxford University Press, Jan. 1995).

[247] E. P. Wohlfarth, "The Theoretical and Experimental Status of the Collective Electron Theory of Ferromagnetism," *Reviews of Modern Physics* **25**, 211–219 (1953).

[248] A. I. Lichtenstein, M. I. Katsnelson, and G. Kotliar, "Finite-Temperature Magnetism of Transition Metals: An ab initio Dynamical Mean-Field Theory," *Physical Review Letters* **87**, 67205–1–67205–4 (2001).

[249] R. Gotter, A. Verna, M. Sbroscia, R. Moroni, F. Bisio, S. Iacobucci, F. Offi, S. R. Vaidya, A. Ruocco, and G. Stefani, "Unexpectedly Large Electron Correlation Measured in Auger Spectra of Ferromagnetic Iron Thin Films: Orbital-Selected Coulomb and Exchange Contributions," *Physical Review Letters* **125**, 067202 (2020).

[250] U. von Barth and L. Hedin, "A local exchange-correlation potential for the spin polarized case. i," *Journal of Physics C: Solid State Physics* **5**, 1629–1642 (1972).

[251] S. H. Vosko, L. Wilk, and M. Nusair, “Accurate spin-dependent electron liquid correlation energies for local spin density calculations: a critical analysis,” *Canadian Journal of Physics* **58**, 1200–1211 (1980).

[252] R. Zeller, J. Grotendorst, S. Blügel, and D. Marx, “Spin-Polarized DFT Calculations and Magnetism,” *Magnetism, in Computational Nanoscience: Do It Yourself!* **31**, 419–445 (2006).

[253] D. E. Eastman, F. J. Himpsel, and J. A. Knapp, “Experimental band structure and temperature-Dependent magnetic exchange splitting of nickel using angle-Resolved photoemission,” *Physical Review Letters* **40**, 1514–1517 (1978).

[254] S. Monastra, F. Manghi, C. A. Rozzi, C. Arcangeli, E. Wetli, H.-J. Neff, T. Greber, and J. Osterwalder, “Quenching of Majority-Channel Quasiparticle Excitations in Cobalt,” *Physical Review Letters* **88**, 236402 (2002).

[255] J. Braun, J. Minár, H. Ebert, M. I. Katsnelson, and A. I. Lichtenstein, “Spectral Function of Ferromagnetic 3*d* Metals: A Self-Consistent LSDA+DMFT Approach Combined with the One-Step Model of Photoemission,” *Physical Review Letters* **97**, 227601 (2006).

[256] L. Chioncel, C. Morari, A. Östlin, W. H. Appelt, A. Droghetti, M. M. Radonjić, I. Rungger, L. Vitos, U. Eckern, and A. V. Postnikov, “Transmission through correlated $\mathrm{Cu}_n\mathrm{CoCu}_n$ heterostructures,” *Physical Review B* **92**, 054431 (2015).

[257] L. Sponza, P. Pisanti, A. Vishina, D. Pashov, C. Weber, M. van Schilfgaarde, S. Acharya, J. Vidal, and G. Kotliar, “Self-energies in itinerant magnets: A focus on Fe and Ni,” *Physical Review B* **95**, 041112 (2017).

[258] C. Guillot, Y. Ballu, J. Paigné, J. Lecante, K. P. Jain, P. Thiry, R. Pinchaux, Y. Pétroff, and L. M. Falicov, “Resonant Photoemission in Nickel Metal,” *Physical Review Letters* **39**, 1632–1635 (1977).

[259] A. Clarke, N. B. Brookes, P. D. Johnson, M. Weinert, B. Sinković, and N. V. Smith, “Spin-polarized photoemission studies of the adsorption of O and S on Fe(001),” *Physical Review B* **41**, 9659–9667 (1990).

[260] P. D. Johnson, A. Clarke, N. B. Brookes, S. L. Hulbert, B. Sinkovic, and N. V. Smith, “Exchange-Split Adsorbate Bands: The Role of Substrate Hybridization,” *Physical Review Letters* **61**, 2257–2260 (1988).

[261] M. Getzlaff, J. Bansmann, and G. Schönhense, “Oxygen on Fe(100) and Fe(110),” *Fresenius’ Journal of Analytical Chemistry* **353**, 743–747 (1995).

[262] A. Tange, C. L. Gao, B. Y. Yavorsky, I. V. Maznichenko, C. Etz, A. Ernst, W. Hergert, I. Mertig, W. Wulfhekel, and J. Kirschner, “Electronic structure and spin polarization of the Fe(001)-p(1×1)O surface,” *Physical Review B* **81**, 195410 (2010).

[263] M. Zheng, E. F. Schwier, H. Iwasawa, and K. Shimada, “High-resolution angle-resolved photoemission study of oxygen adsorbed Fe/MgO(001),” *Chinese Physics B* **29**, 067901 (2020).

[264] R. Bertacco and F. Ciccacci, “Oxygen-induced enhancement of the spin-dependent effects in electron spectroscopies of Fe(001),” *Physical Review B* **59**, 4207–4210 (1999).

[265] M. Escher, N. B. Weber, M. Merkel, L. Plucinski, and C. M. Schneider, “FERRUM: A new highly efficient spin detector for electron spectroscopy,” *e-Journal of Surface Science and Nanotechnology* **9**, 340–343 (2011).

[266] S. Borek, J. Braun, J. Minár, and H. Ebert, “Ab initio calculation of spin-polarized low-energy electron diffraction pattern for the systems Fe(001) and Fe(001)- p (1 × 1) O,” *Physical Review B* **92**, 075126 (2015).

[267] A. Picone, G. Fratesi, A. Brambilla, P. Sessi, F. Donati, S. Achilli, L. Maini, M. I. Trioni, C. S. Casari, M. Passoni, A. Li Bassi, M. Finazzi, L. Duò, and F. Ciccacci, “Atomic corrugation in scanning tunneling microscopy images of the Fe(001)−p(1×1)O surface,” *Physical Review B* **81**, 115450 (2010).

[268] C. Schneider and J. Kirschner, “Magnetism at Surfaces and in Ultrathin Films,” in *Handbook of surface science* (2000), pp. 511–668.

[269] G. D. Mahan, “Homogeneous Electron Gas,” in *Many-particle physics* (Springer US, Boston, MA, 2000), pp. 295–374.

[270] F. Manghi, V. Bellini, J. Osterwalder, T. J. Kreutz, P. Aebi, and C. Arcangeli, “Correlation effects in the low-energy region of nickel photoemission spectra,” *Physical Review B* **59**, R10409–R10412 (1999).

[271] D. Golze, M. Dvorak, and P. Rinke, “The GW Compendium: A Practical Guide to Theoretical Photoemission Spectroscopy,” *Frontiers in Chemistry* **7**, `10.3389/fchem.2019.00377` (2019).

[272] A. Yamasaki and T. Fujiwara, “Electronic Structure of Transition Metals Fe, Ni and Cu in the G W Approximation,” *Journal of the Physical Society of Japan* **72**, 607–610 (2003).

[273] R. M. Martin, L. Reining, and D. M. Ceperley, *Interacting Electrons* (Cambridge University Press, May 2016).

[274] A. Droghetti, M. M. Radonjić, L. Chioncel, and I. Rungger, “Dynamical mean-field theory for spin-dependent electron transport in spin-valve devices,” *Physical Review B* **106**, 075156 (2022).

[275] M. Imada, A. Fujimori, and Y. Tokura, “Metal-insulator transitions,” *Reviews of Modern Physics* **70**, 1039–1263 (1998).

[276] Y. Tokura and N. Nagaosa, “Orbital Physics in Transition-Metal Oxides,” *Science* **288**, 462–468 (2000).

[277] J. Zaanen, G. A. Sawatzky, and J. W. Allen, “Band gaps and electronic structure of transition-metal compounds,” *Physical Review Letters* **55**, 418–421 (1985).

[278] R. Zimmermann, P. Steiner, R. Claessen, F. Reinert, and S. Hüfner, “Electronic structure systematics of 3d transition metal oxides,” *Journal of Electron Spectroscopy and Related Phenomena* **96**, 179–186 (1998).

[279] J. Callaway and C. S. Wang, “Energy bands in ferromagnetic iron,” *Physical Review B* **16**, 2095–2105 (1977).

[280] E. Młyńczak, M. C. T. D. Müller, P. Gospodarič, T. Heider, I. Aguilera, G. Bihlmayer, M. Gehlmann, M. Jugovac, G. Zamborlini, C. Tusche, S. Suga, V. Feyer, L. Plucinski, C. Friedrich, S. Blügel, and C. M. Schneider, “Kink far below the Fermi level reveals new electron-magnon scattering channel in Fe,” *Nature Communications* **10**, 505 (2019).

[281] E. Młyńczak, I. Aguilera, P. Gospodarič, T. Heider, M. Jugovac, G. Zamborlini, C. Tusche, S. Suga, V. Feyer, S. Blügel, L. Plucinski, and C. M. Schneider, “Spin-polarized quantized electronic structure of Fe(001) with symmetry breaking due to the magnetization direction,” *Physical Review B* **103**, 035134 (2021).

[282] A. M. Turner and J. L. Erskine, “Surface electronic properties of Fe(100),” *Physical Review B* **30**, 6675–6688 (1984).

[283] E. Młyńczak, M. Eschbach, S. Borek, J. Minár, J. Braun, I. Aguilera, G. Bihlmayer, S. Döring, M. Gehlmann, P. Gospodarič, S. Suga, L. Plucinski, S. Blügel, H. Ebert, and C. M. Schneider, “Fermi Surface Manipulation by External Magnetic Field Demonstrated for a Prototypical Ferromagnet,” *Physical Review X* **6**, 041048 (2016).

[284] L. Plucinski, Y. Zhao, C. M. Schneider, B. Sinkovic, and E. Vescovo, “Surface electronic structure of ferromagnetic Fe(001),” *Physical Review B* **80**, 184430 (2009).

[285] T. Moorsom, M. Wheeler, T. Mohd Khan, F. Al Ma’Mari, C. Kinane, S. Langridge, D. Ciudad, A. Bedoya-Pinto, L. Hueso, G. Teobaldi, V. K. Lazarov, D. Gilks, G. Burnell, B. J. Hickey, and O. Cespedes, “Spin-polarized electron transfer in ferromagnet/C60 interfaces,” *Physical Review B* **90**, 125311 (2014).

[286] C. Tusche, M. Ellguth, V. Feyer, A. Krasyuk, C. Wiemann, J. Henk, C. M. Schneider, and J. Kirschner, “Nonlocal electron correlations in an itinerant ferromagnet,” *Nature Communications* **9**, 3727 (2018).

[287] A. Droghetti, P. Thielen, I. Rungger, N. Haag, N. Großmann, J. Stöckl, B. Stadtmüller, M. Aeschlimann, S. Sanvito, and M. Cinchetti, “Dynamic spin filtering at the Co/Alq3 interface mediated by weakly coupled second layer molecules,” *Nature Communications* **7**, 12668 (2016).

[288] J. Yeh and I. Lindau, “Atomic subshell photoionization cross sections and asymmetry parameters: 1   Z   103,” *Atomic Data and Nuclear Data Tables* **32**, 1–155 (1985).

[289] R. Imbihl, R. Behm, G. Ertl, and W. Moritz, “The structure of atomic nitrogen adsorbed on Fe(100),” *Surface Science* **123**, 129–140 (1982).

[290] F. Himpsel and J. Ortega, “Unoccupied orbitals of C and O on Fe(100),” *Surface Science* **268**, L279–L283 (1992).

[291] K. Fukui and H. Fujimoto, “An MO-theoretical Interpretation of the Nature of Chemical Reactions. I. Partitioning Analysis of the Interaction Energy,” *Bulletin of the Chemical Society of Japan* **41**, 1989–1997 (1968).

[292] K. Fukui, “Role of Frontier Orbitals in Chemical Reactions,” *Science* **218**, 747–754 (1982).

[293] H. S. Lee, D. H. Kim, J. H. Cho, M. Hwang, Y. Jang, and K. Cho, “Effect of the phase states of self-assembled monolayers on pentacene growth and thin-film transistor characteristics,” *Journal of the American Chemical Society* **130**, 10556–10564 (2008).

[294] B. Himmetoglu, A. Floris, S. de Gironcoli, and M. Cococcioni, “Hubbard-corrected DFT energy functionals: The LDA+U description of correlated systems,” *International Journal of Quantum Chemistry* **114**, 14–49 (2014).

[295] R. Tesch and P. M. Kowalski, “Hubbard U parameters for transition metals from first principles,” *Physical Review B* **105**, 195153 (2022).

[296] K. Harun, N. A. Salleh, B. Deghfel, M. K. Yaakob, and A. A. Mohamad, "DFT + U calculations for electronic, structural, and optical properties of ZnO wurtzite structure: A review," *Results in Physics* **16**, 102829 (2020).

[297] J. E. Nitschke, D. L. Esteras, M. Gutnikov, K. Schiller, S. Mañas-Valero, E. Coronado, M. Stupar, G. Zamborlini, S. Ponzoni, J. J. Baldoví, and M. Cinchetti, "Valence band electronic structure of the van der Waals antiferromagnet FePS3," *Materials Today Electronics* **6**, 100061 (2023).

[298] J. E. House, "Ligand fields and molecular orbitals," in *Inorganic chemistry* (Elsevier, 2020), pp. 687–715.

[299] P. M. Panchmatia, B. Sanyal, and P. M. Oppeneer, "GGA+U modeling of structural, electronic, and magnetic properties of iron porphyrin-type molecules," *Chemical Physics* **343**, 47–60 (2008).

[300] A. Windischbacher and P. Puschnig, "Computational study on the adsorption of small molecules to surface-supported Ni-porphyrins," *Inorganica Chimica Acta* **558**, 121719 (2023).

[301] J. Girovsky, K. Tarafder, C. Wäckerlin, J. Nowakowski, D. Siewert, T. Hählen, A. Wäckerlin, A. Kleibert, N. Ballav, T. A. Jung, and P. M. Oppeneer, "Antiferromagnetic coupling of Cr-porphyrin to a bare Co substrate," *Physical Review B* **90**, 220404 (2014).

[302] N. Ballav, C. Wäckerlin, D. Siewert, P. M. Oppeneer, and T. A. Jung, "Emergence of On-Surface Magnetochemistry," *The Journal of Physical Chemistry Letters* **4**, 2303–2311 (2013).

[303] A. G. Petukhov, I. I. Mazin, L. Chioncel, and A. I. Lichtenstein, "Correlated metals and the LDA +U method," *Physical Review B* **67**, 153106 (2003).

[304] Y. Fu and D. J. Singh, "Density functional methods for the magnetism of transition metals: SCAN in relation to other functionals," *Physical Review B* **100**, 045126 (2019).

[305] E. Abad, J. Ortega, Y. J. Dappe, and F. Flores, "Dipoles and band alignment for benzene/Au(111) and C60/Au(111) interfaces," *Applied Physics A* **95**, 119–124 (2009).

[306] P. Darancet, J. R. Widawsky, H. J. Choi, L. Venkataraman, and J. B. Neaton, "Quantitative Current–Voltage Characteristics in Molecular Junctions from First Principles," *Nano Letters* **12**, 6250–6254 (2012).

[307] P. Martin, B. Dlubak, R. Mattana, P. Seneor, M.-B. Martin, T. Henner, F. Godel, A. Sander, S. Collin, L. Chen, S. Suffit, F. Mallet, P. Lafarge, M. L. Della Rocca, A. Droghetti, and C. Barraud, "Combined spin filtering actions in hybrid magnetic junctions based on organic chains covalently attached to graphene," *Nanoscale* **14**, 12692–12702 (2022).

[308] X. Yang, I. Krieger, D. Lüftner, S. Weiß, T. Heepenstrick, M. Hollerer, P. Hurdax, G. Koller, M. Sokolowski, P. Puschnig, M. G. Ramsey, F. S. Tautz, and S. Soubatch, "On the decoupling of molecules at metal surfaces," *Chemical Communications* **54**, 9039–9042 (2018).

[309] J. Gall, P. Zeppenfeld, L. Sun, L. Zhang, Y. Luo, Z. Dong, C. Hu, and P. Puschnig, "Spectroscopic STM studies of single pentacene molecules on Cu(110)- c(6×2) O," *Physical Review B* **94**, 195441 (2016).

[310] M. T. Greiner, T. E. Jones, S. Beeg, L. Zwiener, M. Scherzer, F. Girgsdies, S. Piccinin, M. Armbrüster, A. Knop-Gericke, and R. Schlögl, "Free-atom-like d states in single-atom alloy catalysts," *Nature Chemistry* **10**, 1008–1015 (2018).

[311] J. K. Nørskov, "Effective medium potentials for molecule–surface interactions: H2 on Cu and Ni surfaces," *The Journal of Chemical Physics* **90**, 7461–7471 (1989).

[312] A. Vojvodic, J. K. Nørskov, and F. Abild-Pedersen, "Electronic Structure Effects in Transition Metal Surface Chemistry," *Topics in Catalysis* **57**, 25–32 (2014).

[313] J. C. Slater and G. F. Koster, "Simplified LCAO method for the periodic potential problem," *Physical Review* **94**, 1498–1524 (1954).

[314] J. M. Gottfried, "Surface chemistry of porphyrins and phthalocyanines," *Surface Science Reports* **70**, 259–379 (2015).

[315] K. Oohora and T. Hayashi, "Hemoprotein-based supramolecular assembling systems," *Current Opinion in Chemical Biology* **19**, 154–161 (2014).

[316] H. Fischer, "Synthese des Hämins," *Die Naturwissenschaften* **17**, 611–617 (1929).

[317] M. Chen, "Chlorophyll Modifications and Their Spectral Extension in Oxygenic Photosynthesis," *Annual Review of Biochemistry* **83**, 317–340 (2014).

[318] C. J. Kingsbury and M. O. Senge, "The shape of porphyrins," *Coordination Chemistry Reviews* **431**, 213760 (2021).

[319] R. Willstätter, "Zur Kenntniss der Zusammensetzung des Chlorophylls," *Justus Liebigs Annalen der Chemie* **350**, 48–82 (1906).

[320] R. B. Woodward, W. A. Ayer, J. M. Beaton, F. Bickelhaupt, R. Bonnett, P. Buchschacher, G. L. Closs, H. Dutler, J. Hannah, F. P. Hauck, S. Itô, A. Langemann, E. Le Goff, W. Leimgruber, W. Lwowski, J. Sauer, Z. Valenta, and H. Volz, "THE TOTAL SYNTHESIS OF CHLOROPHYLL," *Journal of the American Chemical Society* **82**, 3800–3802 (1960).

[321] J. Chen, Y. Zhu, and S. Kaskel, "Porphyrin-Based Metal–Organic Frameworks for Biomedical Applications," *Angewandte Chemie International Edition* **60**, 5010–5035 (2021).

[322] M. Stredansky, S. Moro, M. Corva, H. Sturmeit, V. Mischke, D. Janas, I. Cojocariu, M. Jugovac, A. Cossaro, A. Verdini, L. Floreano, Z. Feng, A. Sala, G. Comelli, A. Windischbacher, P. Puschnig, C. Hohner, M. Kettner, J. Libuda, M. Cinchetti, C. M. Schneider, V. Feyer, E. Vesselli, and G. Zamborlini, "Disproportionation of Nitric Oxide at a Surface-Bound Nickel Porphyrinoid," *Angewandte Chemie International Edition* **61**, e202201916 (2022).

[323] N. A. Rakow and K. S. Suslick, "A colorimetric sensor array for odour visualization," *Nature* **406**, 710–713 (2000).

[324] K. R. Graham, Y. Yang, J. R. Sommer, A. H. Shelton, K. S. Schanze, J. Xue, and J. R. Reynolds, "Extended Conjugation Platinum(II) Porphyrins for use in Near-Infrared Emitting Organic Light Emitting Diodes," *Chemistry of Materials* **23**, 5305–5312 (2011).

[325] L. Schmidt-Mende, W. M. Campbell, Q. Wang, K. W. Jolley, D. L. Officer, M. K. Nazeeruddin, and M. Grätzel, "Zn-porphyrin-sensitized nanocrystalline TiO2 heterojunction photovoltaic cells," *ChemPhysChem* **6**, 1253–1258 (2005).

[326] A. S. Brandis, Y. Salomon, and A. Scherz, "Chlorophyll Sensitizers in Photodynamic Therapy," in *Chlorophylls and bacteriochlorophylls* (Springer Netherlands, Dordrecht), pp. 461–483.

[327] L. Grill, M. Dyer, L. Lafferentz, M. Persson, M. V. Peters, and S. Hecht, "Nano-architectures by covalent assembly of molecular building blocks," *Nature Nanotechnology* **2**, 687–691 (2007).

[328] F. Armillotta, D. Bidoggia, P. Biasin, A. Annese, A. Cossaro, A. Verdini, L. Floreano, M. Peressi, and E. Vesselli, “Spectroscopic fingerprints of iron-coordinated cobalt and iron porphyrin layers on graphene,” *Cell Reports Physical Science* **4**, 101378 (2023).

[329] H. M. Sturmeit, I. Cojocariu, A. Windischbacher, P. Puschnig, C. Piamonteze, M. Jugovac, A. Sala, C. Africh, G. Comelli, A. Cossaro, A. Verdini, L. Floreano, M. Stredansky, E. Vesselli, C. Hohner, M. Kettner, J. Libuda, C. M. Schneider, G. Zamborlini, M. Cinchetti, and V. Feyer, “Room-Temperature On-Spin-Switching and Tuning in a Porphyrin-Based Multifunctional Interface,” *Small* **17**, 2104779 (2021).

[330] C. Wäckerlin, K. Tarafder, J. Girovsky, J. Nowakowski, T. Hählen, A. Shchyrba, D. Siewert, A. Kleibert, F. Nolting, P. M. Oppeneer, T. A. Jung, and N. Ballav, “Ammonia Coordination Introducing a Magnetic Moment in an On-Surface Low-Spin Porphyrin,” *Angewandte Chemie International Edition* **52**, 4568–4571 (2013).

[331] C. Wäckerlin, D. Chylarecka, A. Kleibert, K. Müller, C. Iacovita, F. Nolting, T. A. Jung, and N. Ballav, “Controlling spins in adsorbed molecules by a chemical switch,” *Nature Communications* **1**, 61 (2010).

[332] C. Li, Q. Wang, B. Shen, Z. Xiong, and C. Chen, “Solubilities of 5,10,15,20-Tetraphenylporphyrin and 5,10,15,20-Tetra(p -chlorophenyl)porphyrin in Binary N , N -Dimethylformamide + Water Solvent Mixtures,” *Journal of Chemical & Engineering Data* **60**, 2834–2842 (2015).

[333] J. Brede, M. Linares, S. Kuck, J. Schwöbel, A. Scarfato, S.-H. Chang, G. Hoffmann, R. Wiesendanger, R. Lensen, P. H. J. Kouwer, J. Hoogboom, A. E. Rowan, M. Bröring, M. Funk, S. Stafström, F. Zerbetto, and R. Lazzaroni, “Dynamics of molecular self-ordering in tetraphenyl porphyrin monolayers on metallic substrates,” *Nanotechnology* **20**, 275602 (2009).

[334] Z. H. Cheng, L. Gao, Z. T. Deng, N. Jiang, Q. Liu, D. X. Shi, S. X. Du, H. M. Guo, and H.-J. Gao, “Adsorption Behavior of Iron Phthalocyanine on Au(111) Surface at Submonolayer Coverage,” *The Journal of Physical Chemistry C* **111**, 9240–9244 (2007).

[335] H. Huang, W. Chen, and A. T. S. Wee, “Low-Temperature Scanning Tunneling Microscopy Investigation of Epitaxial Growth of F 16 CuPc Thin Films on Ag(111),” *The Journal of Physical Chemistry C* **112**, 14913–14918 (2008).

[336] G. Fratesi, S. Achilli, A. Ugolotti, A. Lodesani, A. Picone, A. Brambilla, L. Floreano, A. Calloni, and G. Bussetti, “Nontrivial central-atom dependence in the adsorption of M-TPP molecules (M = Co, Ni, Zn) on Fe(001)- $p(1 \times 1)$O,” *Applied Surface Science* **530**, 147085 (2020).

[337] G. Zamborlini, M. Jugovac, A. Cossaro, A. Verdini, L. Floreano, D. Lüftner, P. Puschnig, V. Feyer, and C. M. Schneider, “On-surface nickel porphyrin mimics the reactive center of an enzyme cofactor,” *Chemical Communications* **54**, 13423–13426 (2018).

[338] X.-f. Yang, A. Wang, B. Qiao, J. Li, J. Liu, and T. Zhang, “Single-Atom Catalysts: A New Frontier in Heterogeneous Catalysis,” *Accounts of Chemical Research* **46**, 1740–1748 (2013).

[339] W. Auwärter, D. Écija, F. Klappenberger, and J. V. Barth, “Porphyrins at interfaces,” *Nature Chemistry* **7**, 105–120 (2015).

[340] Y. Bai, F. Buchner, I. Kellner, M. Schmid, F. Vollnhals, H.-P. Steinrück, H. Marbach, and J. Michael Gottfried, “Adsorption of cobalt (II) octaethylporphyrin and 2H-octaethylporphyrin on Ag(111): new insight into the surface coordinative bond,” *New Journal of Physics* **11**, 125004 (2009).

[341] M. Stredansky, S. Moro, M. Corva, M. Jugovac, G. Zamborlini, V. Feyer, C. M. Schneider, I. Cojocariu, H. M. Sturmeit, M. Cinchetti, A. Verdini, A. Cossaro, L. Floreano, and E. Vesselli, “Vibronic Fingerprints of the Nickel Oxidation States in Surface-Supported Porphyrin Arrays,” *The Journal of Physical Chemistry C* **124**, 6297–6303 (2020).

[342] R. E. Haddad, S. Gazeau, J. Pécaut, J.-C. Marchon, C. J. Medforth, and J. A. Shelnutt, “Origin of the Red Shifts in the Optical Absorption Bands of Nonplanar Tetraalkylporphyrins,” *Journal of the American Chemical Society* **125**, 1253–1268 (2003).

[343] I. Cojocariu, S. Carlotto, M. Jugovac, L. Floreano, M. Casarin, V. Feyer, and C. M. Schneider, “Distortion-driven spin switching in electron-doped metal porphyrins,” *Journal of Materials Chemistry C* **10**, 9748–9757 (2022).

[344] K. Seufert, M.-L. Bocquet, W. Auwärter, A. Weber-Bargioni, J. Reichert, N. Lorente, and J. V. Barth, “Cis-dicarbonyl binding at cobalt and iron porphyrins with saddle-shape conformation,” *Nature Chemistry* **3**, 114–119 (2011).

[345] P. Knecht, J. Reichert, P. S. Deimel, P. Feulner, F. Haag, F. Allegretti, M. Garnica, M. Schwarz, W. Auwärter, P. T. P. Ryan, T.-L. Lee, D. A. Duncan, A. P. Seitsonen, J. V. Barth, and A. C. Papageorgiou, “Conformational Control of Chemical Reactivity for Surface-Confined Ru-Porphyrins,” *Angewandte Chemie International Edition* **60**, 16561–16567 (2021).

[346] A. Picone, D. Giannotti, M. Riva, A. Calloni, G. Bussetti, G. Berti, L. Duò, F. Ciccacci, M. Finazzi, and A. Brambilla, “Controlling the Electronic and Structural Coupling of C 60 Nano Films on Fe(001) through Oxygen Adsorption at the Interface,” *ACS Applied Materials & Interfaces* **8**, 26418–26424 (2016).

[347] G. Albani, A. Calloni, A. Picone, A. Brambilla, M. Capra, A. Lodesani, L. Duò, M. Finazzi, F. Ciccacci, and G. Bussetti, “An In-Depth Assessment of the Electronic and Magnetic Properties of a Highly Ordered Hybrid Interface: The Case of Nickel Tetra-Phenyl-Porphyrins on Fe(001)–p(1×1)O,” *Micromachines* **12**, 191 (2021).

[348] F. Neese, “The ORCA program system,” *WIREs Computational Molecular Science* **2**, 73–78 (2012).

[349] F. Neese, “Software update: The ORCA program system—Version 5.0,” *WIREs Computational Molecular Science* **12**, e1606 (2022).

[350] P. C. Hariharan and J. A. Pople, “The influence of polarization functions on molecular orbital hydrogenation energies,” *Theoretica Chimica Acta* **28**, 213–222 (1973).

[351] W. J. Hehre, R. Ditchfield, and J. A. Pople, “Self—Consistent Molecular Orbital Methods. XII. Further Extensions of Gaussian—Type Basis Sets for Use in Molecular Orbital Studies of Organic Molecules,” *The Journal of Chemical Physics* **56**, 2257–2261 (1972).

[352] S. Grimme, J. Antony, S. Ehrlich, and H. Krieg, “A consistent and accurate ab initio parametrization of density functional dispersion correction (DFT-D) for the 94 elements H-Pu,” *The Journal of Chemical Physics* **132**, 154104 (2010).

[353] K. Momma and F. Izumi, “VESTA 3 for three-dimensional visualization of crystal, volumetric and morphology data,” *Journal of Applied Crystallography* **44**, 1272–1276 (2011).

[354] I. Cojocariu, H. M. Sturmeit, G. Zamborlini, A. Cossaro, A. Verdini, L. Floreano, E. D’Incecco, M. Stredansky, E. Vesselli, M. Jugovac, M. Cinchetti, V. Feyer, and C. M. Schneider, “Evaluation of molecular orbital symmetry via oxygen-induced charge transfer quenching at a metal-organic interface,” *Applied Surface Science* **504**, 144343 (2020).

[355] A. Calloni, M. Jagadeesh, G. Bussetti, G. Fratesi, S. Achilli, A. Picone, A. Lodesani, A. Brambilla, C. Goletti, F. Ciccacci, L. Duò, M. Finazzi, A. Goldoni, A. Verdini, and L. Floreano, “Cobalt atoms drive the anchoring of Co-TPP molecules to the oxygen-passivated Fe(0 0 1) surface,” *Applied Surface Science* **505**, 144213 (2020).

[356] D. Wechsler, M. Franke, Q. Tariq, L. Zhang, T.-L. Lee, P. K. Thakur, N. Tsud, S. Bercha, K. C. Prince, H.-P. Steinrück, and O. Lytken, “Adsorption Structure of Cobalt Tetraphenylporphyrin on Ag(100),” *The Journal of Physical Chemistry C* **121**, 5667–5674 (2017).

[357] J. Knippertz, L. L. Kelly, M. Franke, C. Kumpf, M. Cinchetti, M. Aeschlimann, and B. Stadtmüller, “Vertical bonding distances and interfacial band structure of PTCDA on a Sn-Ag surface alloy,” *Physical Review B* **102**, 075447 (2020).

[358] E. M. Reinisch, T. Ules, P. Puschnig, S. Berkebile, M. Ostler, T. Seyller, M. G. Ramsey, and G. Koller, “Development and character of gap states on alkali doping of molecular films,” *New Journal of Physics* **16**, 023011 (2014).

[359] E. M. Reinisch, P. Puschnig, T. Ules, M. G. Ramsey, and G. Koller, “Layer-resolved photoemission tomography: The *p*-sexiphenyl bilayer upon Cs doping,” *Physical Review B* **93**, 155438 (2016).

[360] P. Kretz, K. Waltar, Y. Geng, C. Metzger, M. Graus, A. Schöll, F. Reinert, S.-X. Liu, S. Decurtins, M. Hengsberger, J. Osterwalder, and L. Castiglioni, “Adsorption geometry and electronic structure of a charge-transfer-complex: TTF-PYZ 2 on Ag(110),” *New Journal of Physics* **23**, 013002 (2021).

[361] L. Egger, M. Hollerer, C. S. Kern, H. Herrmann, P. Hurdax, A. Haags, X. Yang, A. Gottwald, M. Richter, S. Soubatch, F. S. Tautz, G. Koller, P. Puschnig, M. G. Ramsey, and M. Sterrer, “Charge-Promoted Self-Metalation of Porphyrins on an Oxide Surface,” *Angewandte Chemie International Edition* **60**, 5078–5082 (2021).

[362] P. Puschnig, *Organic molecule database*, Karl-Franzens-Universität Graz, 2025.

[363] G. Ávila, P. Matias, L. Marques, I. Laranjinha, T. Carvalho, A. Mendes, and C. Gil, “Malpositioning of a dialysis catheter: One lumen with arterial blood and the other with venous blood?” *The Journal of Vascular Access* **25**, 681–684 (2024).

[364] T. Suzuki, M. Kurahashi, X. Ju, and Y. Yamauchi, “Adsorption structure and spin polarization of pentacene on a magnetized Fe(100) substrate: SPMDS and ERDA study,” *Surface Science* **549**, 97–102 (2004).

[365] X. Sun, T. Suzuki, Y. Yamauchi, M. Kurahashi, Z. Wang, and S. Entani, “Ab initio study of pentacene on the Fe(100) surface,” *Surface Science* **602**, 1191–1198 (2008).

[366] W. H. Butler, “Tunneling magnetoresistance from a symmetry filtering effect,” *Science and Technology of Advanced Materials* **9**, 014106 (2008).

[367] A. Chiesa, A. Privitera, E. Macaluso, M. Mannini, R. Bittl, R. Naaman, M. R. Wasielewski, R. Sessoli, and S. Carretta, "Chirality-Induced Spin Selectivity: An Enabling Technology for Quantum Applications," *Advanced Materials* **35**, 2300472 (2023).

[368] A. Chiesa, A. Privitera, E. Garlatti, G. Allodi, R. Bittl, M. R. Wasielewski, R. Sessoli, and S. Carretta, "Chirality-Induced Spin Selectivity at the Molecular Level: A Different Perspective to Understand and Exploit the Phenomenon," *The Journal of Physical Chemistry Letters* **16**, 5358–5372 (2025).

[369] I. Hughes and T. Hase, *Measurements and their Uncertainties A practical guide to modern error analysis* (Oxford University Press, 2010), p. 160.

List of Publications

- D. M. Janas, A. Droghetti, S. Ponzoni, I. Cojocariu, M. Jugovac, V. Feyer, M. M. Radonjić, I. Rungger, L. Chioncel, G. Zamborlini, M. Cinchetti, "Enhancing electron correlation at a $3d$ ferromagnetic surface", *Advanced Materials*, **35** (2023), 2205698. https://doi.org/10.1002/adma.202205698
- D. M. Janas, A. Windischbacher, M. S. Arndt, M. Gutnikov, L. Sternemann, D. Gutnikov, T. Willershausen, J. E. Nitschke, K. Schiller, D. Baranowski, V. Feyer, I. Cojocariu, K. Dave, P. Puschnig, M. Stupar, S. Ponzoni, M. Cinchetti, G. Zamborlini, "Metalloporphyrins on oxygen-passivated iron: Conformation and order beyond the first layer", *Inorganica Chimica Acta*, **557** (2023), 121705. https://doi.org/10.1016/j.ica.2023.121705
- D. M. Janas, A. Windischbacher, A. Sala, V. Feyer, I. Cojocariu, M. Gruber, M. Bouatou, A. Droghetti, P. Puschnig, G. Zamborlini, M. Cinchetti, "Correlation-driven d-band modifications promote chemical bonding at $3d$-ferromagnetic surfaces", under review (submitted 2025).
- D. M. Janas, M. S. Arndt, J. E. Nitschke, L. Sternemann, V. M. M. Mischke, V. Feyer, I. Cojocariu, D. Baranowski, A. Sala, A. Windischbacher, P. Puschnig, J. Dreiser, S. Ponzoni, G. Zamborlini, M. Cinchetti, "Spin-selective interface engineering in oxide–ferromagnetic junctions via atomic-scale oxygen control", under review (submitted 2025).
- D. M. Janas, A. Windischbacher, J. E. Nitschke, L. Sternemann, M. S. Arndt, V. M. M. Mischke, V. Feyer, I. Cojocariu, D. Baranowski, V. Romankov, J. Dreiser, S. Ponzoni, P. Puschnig, G. Zamborlini, M. Cinchetti, "Charge and spin control in organic molecules on MgO/Fe(100) tunneling junctions", manuscript in preparation.
- G. Zamborlini, D. M. Janas, S. Ponzoni, M. Cinchetti, "Charge transfer at molecular interfaces – the key to multifunctionality", manuscript in preparation.
- J. Heckötter, D. Janas, M. Aßmann, and M. Bayer, "Rydberg excitons in Cu_2O at millikelvin temperatures", *arXiv preprint* (2025). https://doi.org/10.48550/arXiv.2510.26966
- J. E. Nitschke, P. Bhumla, T. Willershausen, P. Merisescu, D. Janas, L. Sternemann, M. Gutnikov, K. Schiller, V. Mischke, M. Capra, M. Arndt, S. Botti, M. Cinchetti, "Electronic structure reorganization in MPS_3 via d-shell-selective alkali metal doping", *arXiv preprint* (2025). https://doi.org/10.48550/arXiv.2506.01527
- J. E. Nitschke, D. M. Janas, S. Ponzoni, M. Capra, E. Molteni, A. Picone, A. Giampietri, A. Ferretti, S. Ma, A. Brambilla, G. Zamborlini, G. Fratesi, M. Cinchetti, "Electronic and structural coupling of pentacene on NiO(001)", *Nanoscale*, **17** (2025), 17137–17145. https://doi.org/10.1039/D5NR00700C

- L. Sternemann, D. M. Janas, J. E. Nitschke, K. Schiller, T. Willershausen, L. Becker, A. Isaeva, G. Zamborlini, S. Tappertzhofen, M. Cinchetti, ”Fabrication of large-area 2D magnetic semiconductor films for low-temperature ARPES”, *2D Materials* (2025). https://iopscience.iop.org/article/10.1088/2053-1583/add7ea
- K. J. Schiller, L. Sternemann, M. Stupar, A. Omar, M. Hoffmann, J. E. Nitschke, V. Mischke, D. M. Janas, S. Ponzoni, G. Zamborlini, C. J. Saraceno, M. Cinchetti, ”Time-resolved momentum microscopy with fs-XUV photons at high repetition rates with flexible energy and time resolution”, *Scientific Reports*, **15** (2025), 3611. https://www.nature.com/articles/s41598-025-86660-1
- S. Ponzoni, F. Paßlack, M. Stupar, D. M. Janas, G. Zamborlini, M. Cinchetti, ”Dirac bands in the topological insulator Bi_2Se_3 mapped by time-resolved momentum microscopy”, *Advanced Physics Research*, **2** (2023), 2200016. https://doi.org/10.1002/apxr.202200016
- M. Stredansky, S. Moro, M. Corva, H. Sturmeit, V. Mischke, D. Janas, I. Cojocariu, M. Jugovac, A. Cossaro, A. Verdini, L. Floreano, Z. Feng, A. Sala, G. Comelli, A. Windischbacher, P. Puschnig, C. Hohner, M. Kettner, J. Libuda, M. Cinchetti, C. M. Schneider, V. Feyer, E. Vesselli, G. Zamborlini, ”Disproportionation of nitric oxide at a surface-bound nickel porphyrinoid”, *Angewandte Chemie International Edition*, **61** (2022), e202201916. https://doi.org/10.1002/anie.202201916
- J. Heckötter, D. Janas, R. Schwartz, M. Aßmann, M. Bayer, ”Experimental limitation in extending the exciton series in Cu_2O towards higher principal quantum numbers”, *Physical Review B*, **101** (2020), 235207. https://doi.org/10.1103/PhysRevB.101.235207

List of Abbreviations

2H-TPP	Free-base tetraphenylporphyrin	120
5A	Pentacene	82
AES	Auger electron spectroscopy	30
ARPES	Angle-resolved photoelectron spectroscopy	42
ASIC	Atomic self-interaction correction	71
BFP	Back-focal plane	49
BZ	Brillouin zone	35
CB	Conduction band	5
CNL	Charge neutrality level	21
DFT	Density functional theory	10
DFT+U	Density functional theory with Hubbard U_{eff} correction	38
DMFT	Dynamical mean-field theory	25
DOS	Density of states	13
e-beam	Electron beam	28
EDC	Energy distribution curve	40
ESCA	Electron spectroscopy for chemical analysis	39
Fe–O	Fe(100)–$p(1 \times 1)$O	3
FFT	Fast Fourier transform	92
FM	Ferromagnetic	56
FWHM	Full width at half maximum	75
GGA	Generalized gradient approximation	38
GMR	Giant magnetoresistance	1
HHG	High-harmonic generation	50
HIS	Hybrid interface state	12
HOMO	Highest occupied molecular orbital	6
ICT	Integer charge transfer	14

IDIS	Induced density of interface states	21
IMFP	Inelastic mean free path	43
IPES	Inverse photoelectron spectroscopy	10
LDA	Local density approximation	38
LDOS	Local density of states	35
LEED	Low energy electron diffraction	31
LSDA	Local spin density approximation	71
LT	Low-temperature	85
LT STM	Low-temperature scanning tunneling microscope	85
LUMO	Lowest unoccupied molecular orbital	6
MM	Momentum microscopy	49
MO	Molecular orbital	4
MOF	Metal-organic framework	120
MOPDOS	Molecular orbital projected density of states	101
MTPP	Metalated tetraphenylporphyrin	120
NEXAFS	Near-edge x-ray absorption fine structure	126
NiTPP	Nickel(II)-tetraphenylporphyrin	121
OLED	Organic light-emitting diode	5
OSC	Organic semiconductor	5
PDOS	Projected density of states	58
PEEM	Photoelectron emission microscopy	48
PES	Photoelectron spectroscopy	39
POT	Photoemission orbital tomography	46
SBZ	Surface Brillouin zone	57
SCLS	Surface core-level shift	41
SOMO	Singly occupied molecular orbital	9
SP-LEED	Spin-polarized low-energy electron diffraction	52
STM	Scanning tunneling microscopy	10
STS	Scanning tunneling spectroscopy	10
SUMO	Singly unoccupied molecular orbital	9

TMR	Tunneling magnetoresistance	1
TPP	Tetraphenylporphyrin	120
UHV	Ultra-high vacuum	28
UPS	Ultraviolet photoelectron spectroscopy	10
VB	Valence band	5
XAS	X-ray absorption spectroscopy	32
XSW	X-ray standing wave	126
XUV	Extreme ultraviolet	50
ZnTPP	Zinc(II)-tetraphenylporphyrin	121

List of Symbols

$\varDelta$	interface dipole
$\varDelta_{\text{ex}}$	exchange energy splitting in ferromagnetic materials (e.g., Fe, Co)
$\downarrow$	spin-down (minority spin)
η	Slater–Koster geometry factor (structure factor accounting for the relative positioning of atomic orbitals)
$\hat{\vec{p}}$	momentum operator
$\hbar$	reduced Planck constant, $\hbar = h/2\pi = 1.055 \times 10^{-34}\,\mathrm{J\,s}$
λ	inelastic mean free path (average distance electrons travel before energy loss), unit: nm
μ	chemical potential
μ_B	Bohr magneton, $\mu_B = \frac{e\hbar}{2m_e} \approx 9.274 \times 10^{-24}\,\mathrm{J/T}$
$\varPhi$	work function (minimum energy to remove an electron from a material)
ϕ	azimuthal angle
$\varPhi_{\text{eB}}$	electron injection barrier
$\varPhi_{\text{hB}}$	hole injection barrier
τ	lifetime
EA	electron affinity (energy required to add an electron to the LUMO)
IP	ionization potential (energy required to remove an electron from the HOMO)
θ	polar (inclination) angle
$\uparrow$	spin-up (majority spin)
$\Sigma(E)$	electronic self-energy, describes interaction of an electron or hole with its many-body environment
ε_0	vacuum permittivity, $8.854 \times 10^{-12}\,\mathrm{F/m}$

ε_r	relative permittivity (dimensionless dielectric constant)
$\vec{A}$	electromagnetic vector potential
$\vec{G}_{hk}$	reciprocal lattice vector associated with Miller indices (h, k)
$\vec{k}_{\parallel}$	parallel component of the electron wave vector (in-plane with the surface)
$\vec{k}_{\perp}$	perpendicular component of the electron wave vector (normal to the surface)
$\vec{M}$	magnetization vector (direction and magnitude of magnetic moment per unit volume)
c	speed of light in vacuum, $2.998 \times 10^8\,\mathrm{m/s}$
E_b	binding energy
E_F	Fermi energy
E_gap	band gap energy
E_kin	kinetic energy
E_t	transport gap
E_vac	vacuum energy
F	figure of merit in spin-resolved measurements, defined as $F = S_\mathrm{Sh}^2 \cdot \frac{I}{I_0}$
G	electrical conductance, unit: S
$h\nu$	photon energy (Planck constant times frequency), unit: eV
I	electric current, unit: A
l	orbital angular momentum quantum number of the electronic state
l_C	orbital angular momentum quantum number of the carbon (p_z) state, $l_\mathrm{C} = 1$
l_Fe	orbital angular momentum quantum number of the iron (d_{z^2}) state, $l_\mathrm{Fe} = 2$
m^*/m	mass enhancement factor (effective mass relative to DFT band mass, quantifying many-body renormalization)
P_+	polarization cloud surrounding anions
P_-	polarization cloud surrounding cations
S	screening parameter

S_{Sh}	Sherman function (spin sensitivity factor)
V	electric potential (voltage), unit: V
V_0	inner potential (effective potential inside the crystal), unit: eV
V_{g}	external "gate" potential applied to simulate the effect of varying adsorbates
C_{60}	buckminsterfullerene (fullerene molecule with 60 carbon atoms)
EA^*	renormalized electron affinity (modified by interfacial effects)
IP^*	renormalized ionization potential (modified by interfacial effects)
L	Langmuir, unit of gas exposure, $1\,\mathrm{L} = 1 \times 10^{-6}\,\mathrm{Torr{\cdot}s}$
ML	monolayer; defined as one saturated molecular layer

Acknowledgments

I would like to thank all the many people who supported me in one way or another throughout this exciting journey during my PhD.

First and foremost, I am deeply grateful to Prof. Mirko Cinchetti for giving me the opportunity to pursue this research within his group. I especially appreciate the numerous opportunities to participate in beamtimes, conferences, and collaborative projects over the past years. His steady support — both scientific and organizational — enabled the diverse and rewarding work that culminated in this thesis. Moreover, he provided access to an outstanding laboratory infrastructure, offering some of the finest equipment a researcher could wish for.

I also thank Prof. Carsten Westphal for kindly agreeing to serve as the second examiner and for taking the time to read and evaluate this thesis.

Over the course of my doctoral research, I had the privilege of working alongside many great researchers whose guidance and collaboration were essential to my development. I am particularly thankful to Dr. Giovanni Zamborlini, who mentored me over the past years and taught me not only the essentials of project development and scientific writing, but also what it means to cultivate a thoughtful and collaborative lab culture. Dr. Stefano Ponzoni taught me to approach challenges with curiosity and courage, always open to discussion and experimentation. Dr. Matija Stupar, with his unmatched knowledge of lasers, had the incredible ability to align the beam in almost no time.

My sincere thanks also go to the many collaborators who supported the experimental aspects of this work. At the Elettra NanoESCA beamline, I had the pleasure of working with Dr. Vitaliy Feyer, Dr. Iulia Cojocariu, Dr. Matteo Jugovac, and Dr. Daniel Baranowski. At the SLS X-Treme beamline, I gratefully acknowledge the support of Dr. Jan Dreiser. I would also like to thank Dr. Alessandro Sala for performing STM and STS measurements and for encouraging us to submit an NFFA proposal — an instructive and rewarding experience. I also thank Prof. Manuel Gruber and Dr. Mehdi Bouatou for their contributions to the STM/STS work.

On the theoretical side, I am indebted to Dr. Andrea Droghetti for performing the DMFT calculations and for giving substance to many emerging ideas. I also had the rare privilege of working in parallel with two theory groups — a collaboration that was both intellectually stimulating and scientifically productive. I thank Dr. Andreas Windischbacher for his brilliant insights, sharp analytical mind, and relentless pursuit of truth, all of which proved invaluable to the success of our joint efforts. I am also grateful to Prof. Peter Puschnig for his openness and generosity in enabling the calculations on the organic systems and for his readiness to participate in fruitful discussions, which played a central role in this work.

Special thanks go to those who shared the office with me over extended periods: Sophie Bork, Jonah Nitschke, and Lasse Sternemann, who created a supportive, enjoyable, and humorous

working atmosphere that never took itself too seriously. I also thank Felix Paßlack and Michael Gutnikov for their intermittent but entertaining presence in the office.

I am especially grateful to the many students who worked with me during their bachelor's and master's theses. Among them, Mira Arndt deserves special mention — not only for enduring working with me twice (during both her bachelor's and master's theses), but also for creating the beautiful cover art that now accompanies this thesis. I also wish to thank Marcel Karas, David Pachurka, Valentin Mischke, Katharina Müller, and Benedikt Lütke Lanfer for their valuable contributions during their respective theses. I would further like to thank Khush Dave, who joined for just a brief three-month internship, yet brought remarkable motivation and enthusiasm. I am truly glad we have remained in touch, even if only occasionally.

I would also like to acknowledge all other members of the photoemission group. Karl Schiller was always a pleasure to be around, and the new student assistants — Timo and Amelie — helped keep the atmosphere in our office lively and dynamic. I also thank the members of the magneto-optics group, in particular Dr. Umut Parlak, to whom I wish a successful time in Konstanz, as well as Richard Leven and David Gutnikov (who has since joined the photoemission team) for their kindness and for contributing to a friendly environment. My thanks also go to Julian Hochaus from our neighboring chair for the instructive discussions on LEED $I(V)$, and Dr. Andreas Farenbruch for sharing his motivation and passion during our numerous highly productive library working sessions.

I would like to acknowledge former group members who left a lasting impression. Henning Sturmeit, Marc Wehling (formerly Terschanski), Fabian Mertens, and David Mönkebüscher created a great working atmosphere during the early phase of my doctorate, which was highly motivating. More recently, I have had the pleasure of engaging with Mattia Benini (mainly at conferences and during coffee breaks) and Michele Capra, whose knowledge and humorous character quickly left a strong impression despite their recent arrival.

I would also like to thank the people who keep everything running behind the scenes: Monika Voits-Besli, Nina Sesemann-Collette, Nicole Bialik, Lena Bobon — the secretaries over the years — for managing countless administrative tasks with efficiency and kindness. A heartfelt thank-you goes to Patrick Mc Lelland, whose technical expertise, unwavering support, and approachable nature have always been a pleasure.

Finally, I would like to thank those who supported me on a personal level. My father, who stood by me during difficult times and when it mattered most. I also wish to express my deep gratitude to Irmgard Köchling, who sadly passed away at the end of 2023. Her presence and care after my mother's passing were a profound source of strength, and I miss her dearly. Today, her daughter Yvonne Köchling and granddaughter Pia Köchling carry that same sense of connection and trust — for which I am deeply thankful.

And, of course, I thank all my friends, especially Jendrik Kettling, one of the most remarkable people I know. Despite my near-total neglect of social life over the past years, none of you ever let go; your friendship and constancy brought immeasurable stability and support.

Thank you!